

國立交通大學
材料科學與工程學系
博士論文

設計與製備具顯影與磁場刺激藥物釋放之
多功能型奈米藥物輸送載體元件

Design and Fabricate Multifunctional Nanocapsules for Imaging
and Magnetically-triggered Drug Release

研究生：胡尚秀

指導教授：陳三元 博士

中華民國九十九年七月

設計與製備具顯影與磁場刺激藥物釋放之

多功能型奈米藥物輸送載體元件

研究生：胡尚秀

指導老師：陳三元

國立交通大學材料科學與工程學系

摘要

在控制藥物釋放的系統中，尤其是在是及外力場刺激下作用之智慧型藥物釋放系統，在全球已經引起各學界與業界人士的注意。在本論文中，利用材料與藥物的結合，設計與製備一種具多功能性的磁性藥物奈米載體，除了具有利用外部磁場控制釋放藥物之功能，並可以同步監測藥物釋放的情形。然而，傳統的藥物釋放，僅利用藥物載體的特性與所在的環境變化來運作，在人體中並未真正達到完善地控制釋放的目標。故本論文根據此創新的研究構想，使用"磁場"的非接觸力特性，達到遙控藥物載體快速藥物釋放的效果。首先，用奈米級氧化鐵與明膠/幾丁聚醣製備複合材料水膠，該水膠可以利用外加高頻磁場驅動水膠內部氧化鐵生熱與轉動，進而使該溫度敏感型水膠高分子結構鬆散，達到快速藥物釋放的效果。為達到可應用於體內之藥物載體，因此將藥物載體奈米化，提出利用新穎製程控制，先將 poly-(N-vinyl-2-pyrrolidone) (PVP) 做為奈米核之結構，其表面具有螯合鐵離子的特性，再利用共沈法，將單晶奈米氧化鐵殼層成長於表面上，發展具有磁敏感性的奈米核殼膠囊結構，將藥物完美的包覆於該奈米膠囊當中，在未加磁場的狀態下，該奈米膠囊藥物自然釋放量趨近於零，如此可大幅降低高毒性藥物在體內的副作用，然而當此奈米膠囊抵達治療位置時，可以利用外部的磁場刺激磁奈米載體，控制藥物快速的局部釋放，有效的控制藥物釋放於定點。此外，利用奈米晶體成長技術，架接具光學特性的量子點於奈米膠囊的表面上，此

具光學特性量子點，可以利用其螢光顯影，來追蹤該奈米膠囊於體內的位置，並且搭配磁場的控制下，可監測藥物於定點釋放的情形，可用來評估釋放量對於疾病的影響。並且奈米膠囊的表面經由化學表面改質，可帶有標靶癌細胞的分子，在體內中大量提升奈米膠囊進入癌細胞的效率。此奈米複合膠囊搭配外加磁場的控制的結構元件，期望在未來可達到快速有效率的局部釋藥於腫瘤細胞，並同時於體內偵測藥物釋放情形。

同時，為了達到包覆油相藥物與提升包藥率，設計另一種多功能性的磁性奈米膠囊藥物載體，尺度約為 100 奈米，將油相藥物與氧化鐵作為奈米核，並在載體外部包覆奈米二氧化矽殼層，達到大幅降低藥物自然釋放的效果；並藉由螢光染劑標定二氧化矽殼層，可使該載體可同時具有控制釋放藥物與顯影之功能。未加磁場的狀態下，由於二氧化矽為堅固緊密之結構，此奈米膠囊藥物利用奈米殼層，將藥物包覆於載體當中，可大幅降低載體漏藥性與高毒性抗癌藥物在體內的副作用，然而當此奈米膠囊抵達需要特定位置時，再施加外部的磁場刺激磁奈米載體，控制藥物快速的局部釋放，將大量的藥物釋放於治療之位置，達到治療的效果。此外，磁性奈米粒子還能利用 MRI 來作為細胞追蹤的標的，在磁性奈米粒子表面接枝特定抗體，使此特殊架接的奈米粒子可以與特定細胞之抗原結合，以達到標定式之藥物釋放。本研究後期將利用靜脈注射的方式，將奈米膠囊藥物載體注射入老鼠的血管內，來作一些體內之標定式藥物釋放之測試，並觀察體內腫瘤細胞的治療效果，期望達到新一代的治療效果。

關鍵字：藥物控制釋放，磁性奈米粒子，藥物載體，影像顯影

Design and Fabricate Multifunctional Nanocapsules for Imaging and Magnetically-triggered Drug Release

Student: Shang-Hsiu Hu

Advisor: San-Yuan Chen

Department of Materials Science and Engineering

Nation Chiao Tung University

Abstract

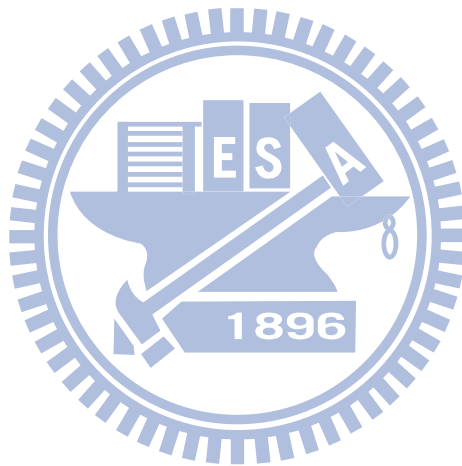
Controlled drug release has been received greatest attention worldwide, especially stimuli-responsive drug-delivery systems. In order to accelerate the response of an adaptive nanocarrier to stimuli, the use of the magnetic-sensitive nanomedical platforms as a new type of actuator has been developed in this thesis. In first part, ferrogels composed of thermosensitive polymers, gelatin and chitosan, and iron oxide nanoparticles were triggered by a high frequency magnetic field to achieve pulsatile drug release. Under cyclic exposures to the high frequency magnetic stimuli, a highly controllable and repeatable burst release were exhibited with desirable precision from the ferrogels. In second part, the drug carriers were designed and narrowed down to nanosize. A novel core-shell nanosphere which was constructed by a poly-(N-vinyl-2-pyrrolidone) (PVP)-modified silica core with an outer layer of single-crystal iron oxide shell was fabricated. This drug delivery nano-device capable of providing controlled release of precise dose of therapeutic molecules when body needs and in particular, zero release when no need in the host, is critically important for clinical practices. The nanosphere showed outstanding release-and-zero-release characteristic via the addition and removal of an external manipulation of high-frequency magnetic field, respectively. Upon magnetic stimulus, the single

crystal iron oxide shell with a thickness in a few nanometers demonstrated atomic re-arrangement, forming lattice of varying orientations, where inter-crystal boundary were developed, allowing drug eluted or no released in a reversible behavior. Further stimulation causes rupturing, i.e., permanent damage, of the shell, where drug eluted rapidly and can hardly be ceased, even after removal of the stimulus. Such novel core-shell nanospheres showed a fast cancerous cell (human cervical cancer cell line) uptake behavior, which implies a highly efficient potential to achieve anti-cancer therapy when anti-cancer drug is delivered. On the other hand, constructing with other functional nanoparticles like quantum dots can form the multifunctional magnetic nanocarriers that could be applicable to a variety of fields as a new driving mechanism. Combining with fluorescent quantum dots, the nanocarriers can be tracked in the human body. The optical properties also can be tunable while applying the magnetic field for sensing the drug release. Drug release rate at on-off operation of AC magnetic fields (hyperthermia effects) and the conditions of killing-tumor cells also would be investigated.

Finally, the magnetic nanocapsules capable of carrying hydrophobic drug molecules were synthesized as the bifunctional magnetic vectors that can be triggered for control release of therapeutic agent by an external magnetic field. The drug release profiles of capsules can be well-regulated through an ultra thin layer of silica shell. Remote control of drug release from the nanocapsules was successfully achieved using an external magnetic field where the core phase being structurally disintegrated to a certain extent while subjecting to magnetic stimulus, resulting in a burst release of the encapsulated drug. However, a relatively slow and linear release restored immediately right after removal of the stimulus. More than surprisingly, the nanocapsules demonstrated a relatively high uptake efficiency by HeLa cell line. In addition, the magnetic nanoparticles still provides some advantages, such as magnetic

resonance image (MRI) for cell labeling and grafted probe-proteins (such as biotin or antibody) onto magnetic nanoparticles for “target” drug delivery. Therefore, the multifunctional drug-carriers is able to be triggered by thermal and magnetic changes, and especially put emphasis on “target” drug-delivery using MRI, cell labeling or others detecting technique.

Keywords: controlled drug release, magnetic nanoparticles, drug carriers, imaging



致謝

經過四年的奮鬥與努力，終於在 2010 年拿到了博士學位，雖然一路上跌跌撞撞，遇到了很多挫折與阻礙，過程難免有許多的失落、灰心與現實的壓力，不過我總是相信這是自己選擇的路，一定要堅固自己的意志將學位完成，總是不斷的提醒自己，雖然自己不是最聰明的學生，要做的最認真的學生。取得學位時，那心中的激動與喜悅，真的難以言喻。

首先要先感謝我的指導教授**陳三元老師**，在研究上，總是很有耐心的與學生討論，分析每項實驗的新穎性與創新性，找出好的研究方向，給學生很大的想像空間與彈性，並誘導學生的創造力，不斷激發學生的潛能，訓練鋼鐵般的意志，在生活上，也給學生許多的協助與鼓勵，我相信，我能遇到這麼優秀的指導老師，真的是上輩子修來的福氣。我也要感謝另一位老師**劉典謨教授**，嚴格上來說，他也是學生的指導教授，從碩士到博士班，指導學生論文的研究題目與方向，他的創新思考模式與積極研究的態度，深深的感染了學生，讓學生對於研究的思維有更深入的想法，在論文撰寫部分，也給予學生很多的指導，不厭其凡的幫助學生修改論文，學生相當的感動，會永遠銘記在心。此外，學生也要感謝在美國華盛頓大學的 Xiaohu Gao 教授，在學生於美國執行千里馬研究計畫時，給予學生很大的協助與資源，學習美國在研究上活躍與開放式的思維，訓練學生的快速思考模式，見識美國頂尖研究環境的訓練模式，雖然只在該實驗室待一年，對於研究能力與創造性的開發，有相當的助益。在此也感謝交大電控所的陳右穎老師，在核詞共振顯影與奈米載體的開發，給學生許多相當有用的建議，並給予學生相當多研究資源。也感謝來幫學生口試的宋信文教授、林峰輝教授、鐘次文教授、林志生教授、邱信程教授，給予學生許多各領域的專業建議，深入研究探討，讓學生受益良多。最後要感謝台灣國科會，給予研究經費上支持，充裕的研究經費，對於研究的速度與執行度有正面的幫助。

特別感謝劉定與學長，從碩士班就開始帶學生進入磁性材料與藥物釋放的領域，學習許多實驗的技巧與方法。感謝劉澤英學長於藥物釋放分析上的協助與指導。特別感謝蕭繼聖學長，在電子顯微鏡上分析的協助，沒有好的電鏡分析人才，我相信也做不出好的研究，學長總是很有耐心的協助我完成各項樣品分析，很懷念在路途遙遠的奈米中心一同打拼的日子。此外，感謝董維琳學妹，在細胞研究上的協助，他總是很認真負責的完成許多任務，日以繼夜的完成工作量相當大的細胞實驗，建構細胞實驗系統，讓研究順利進行。也要特別感謝同組的蔡佳惠、黃信揚、陳柏溶、廖邦傑，在研究上的討論於協助，一同抱著冒險的精神往未知的方向前進，一同解決許多難題，有了你們，研究才能順利的推進。此外，也感謝實驗室其他的成員，昆和、彥妤、冠廷、泓洲、振富、志欣、翔銓、又維、薇蓁、大方、彥博、純瑜、偉銘、俞君、博學、孟軒、衍人、簪華、輔宣、佩鈴、

岱容、立傑、嘉偉、吟芝，在研究與生活上的幫忙與協助，幫遇到打擊時，總能適時的拉我一把，讓我又有了新的力量，有了你們，研究所生活變得更加的多采多姿。

感謝我的家人，爺爺、奶奶、爸爸、媽媽、弟弟與姑姑們，在一路上無怨無悔的支持與鼓勵，在我感到迷惘疲累時，督促我必須努力勇敢的往前，給我很大的關心，此刻終於畢業了，希望與他們一同分享這份喜悅，這個學位也是屬於他們的。感謝毓瑄，陪伴我度過的日子，讓我感覺生命更有他的價值，更用心體會這個世界。感謝我的機車與電腦，陪我完成十幾篇的 SCI 論文與國科會計畫，我想我跟他們相處的時間是最長的。一個結束，也是另一個開始，我會秉持著博士班所學到的態度與精神，繼續面對未來的挑戰。

2010 年 7 月 22 日

尚秀



Contents

摘要.....	i
Abstract.....	iii
致謝.....	vi
Chapter 1 Introduction.....	1
Chapter 2 Literature Review and Theory	6
2.1 Introduction of controlled drug delivery and release.....	6
2.2 Responsive polymers for drug delivery	7
2.2.1 Temperature-responsive polymer.....	8
2.2.2 Responsive polymer incorporated magnetic nanoparticles	11
2.3 Nanotechnology on drug delivery system.....	13
2.3.1 Nanotechnology for nanoplatforms	14
2.3.2 Nano-polymer drug delivery vehicles.....	14
2.4 Magnetic nanoparticles for biomedical applications	16
2.4.1 Synthesis of magnetic nanoparticles.....	19
2.4.2 Biocompatibility of magnetic nanoparticles	21
2.4.3 Magnetic nanoparticles for high performance magnetic resonance imaging	23
2.4.4 Magnetic nanoparticles for <i>in vivo</i> molecular imaging	26
2.4.5 Surface modification of magnetic nanoparticles	28
2.5 Magnetic Nano-Carriers for drug delivery and therapy.....	31
2.5.1 Amphiphilic micellar coatings	33
2.5.2 Magnetic nanoparticles encapsulated in polymer for small molecules drug delivery	34
2.5.3 Magnetic nanoparticles encapsulated in silica for drug delivery.....	36
2.5.4 Magnetic nanoparticles for other therapy	38
2.5.5 Magnetically triggered release for composite membrane.....	40
2.5.6 Magnetic-vortex microdiscs for targeted cancer-cell destruction.....	42
Chapter 3 Experimental Procedures.....	44
3.1 Experiment overviews	44
3.2 Synthesis of magnetic nanoparticles.....	45
3.3 Characterization	46
3.4 High frequency magnetic field (HFMF)	46
3.5 Drug loading efficiency and release.....	48
3.6 Release kinetics.....	49
3.7 Cell culture.....	50
Chapter 4 Controlled Pulsatile Drug Release from a Ferrogel.....	52

4.1 Introduction.....	52
4.2 Fabrication of ferrogels.....	53
4.3 Characteristics of ferrogels	54
4.4 Drug release triggered by magnetic field from ferrogels.....	56
4.5 Cyclic drug release rates of ferrogels.....	59
Chapter 5 Core/Single-Crystal-Shell Nanospheres for Controlled Drug Release via a Magnetically Triggered Rupturing Mechanism.....	62
5.1 Introduction.....	62
5.2 Preparation of core/single-crystal-shell nanospheres.....	64
5.3 Nanostructure of core-single crystal shell nanospheres.....	66
5.4 Triggered release of fluorescence dye from nanoparticles	67
5.5 BET analysis of core-shell nanospheres	69
5.6 Nanostructural evolution.....	71
5.7 <i>in vitro</i> controlled release.....	74
5.8 Summary	85
Chapter 6 A Multifunctional Nanodevice capable of Imaging, Magnetically Controlling, and In-situ Monitoring Drug Release.....	86
6.1 Introduction.....	86
6.2 Experimental section of multifunctional nanodevices.....	88
6.3 Structures of multifunctional nanodevices.....	89
6.4 Drug release and in-situ monitoring abilities of the nanodevices.....	94
6.6 Operation mechanism of the nanodevice.....	101
6.7 In-situ-monitoring of drug release in cancerous cells.....	102
6.8 Summary	106
Chapter 7 PVA-Iron Oxide /Silica Core-Shell Nanocarriers for Magnetically Controlled Drug Release and Cancer Cell Uptake Efficiency	109
7.1 Introduction.....	109
7.2 Experimental section.....	110
7.3 Preparation of SAIO@SiO ₂ nanocarriers	114
7.4 Characterization of SAIO@SiO ₂ nanocarriers	117
7.5 Drug release of SAIO and SAIO@SiO ₂ nanocarriers	118
7.6 Magnetic-sensitive drug release behavior.....	120
7.7 Nanostructure evolution under magnetic treatment.....	122
7.8 Cell Uptake	126
7.9 Summary	129
Chapter 8 Thermosensitive Yolk/Shell Capsules for Magnetically-Triggered Drug Release	131
8.1 Introduction.....	131

8.2 Experimental section.....	133
8.3 Preparation of thermosensitive yolk/shell capsules	136
8.4 Characterization of yolk/shell capsules	139
8.5 Drug release of yolk/shell capsules and F68/PVA nanocomposites	141
8.6 Thermosensitive behavior of the yolk/shell capsules	142
8.7 Magnetically-triggered drug release from yolk/shell capsules	145
8.8 Nanostructure evolution under magnetic treatment.....	147
8.9 Cell uptake and MR imaging	149
8.10 Summary	151
Chapter 9 Conclusion	153
9.1 Ferrogels for magnetically-triggered drug release	153
9.2 Core/single-crystal iron oxide shell nanospheres for drug delivery	153
9.3 Self-assemble iron oxide/silica (SAIO) core-shell carriers	154
9.4 Thermosensitive yolk/shell capsules.....	155
Reference	156
CURRICULUM VITAE	163

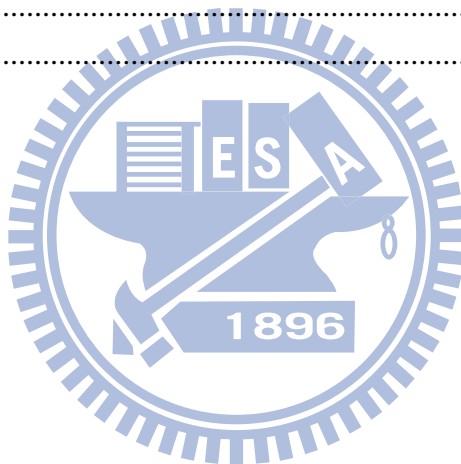


Figure Captions

- Figure 2.1** (a) Drug concentration at site of therapeutic action under a controlled drug release system (solid line) and a conventional injection (dash line). (b) An ideal distribution of drug concentration from a controlled drug release system..... 7
- Figure 2.2** Thermosensitive behaviors of poly (ethylene oxide)-poly (propylene oxide)-poly (ethylene oxide) (PEO-PPO-PEO) tri-block polymer..... 9
- Figure 2.3** Gelatin possesses a triple helix structure at room temperature and forms a stable gels (middle). While increasing above the breaking temperature of hydrogen bonds, the gelatin becomes solution states (right). 10
- Figure 2.4** Magnetic Targeted Carriers (MTCs) has been designed which could adsorb pharmaceutical agents through application of an externally magnetic field for site-specific targeting and sustained release of drugs. 12
- Figure 2.5** Representative nanoparticles that can serve as nanoplatforms and polymeric vehicles for targeted molecular imaging in living subjects. 16
- Figure 2.6** Magnetic nanoparticles for biomedical applications: (a) drug delivery, (b) diagnosis, and (c) therapy by hyperthermia..... 18
- Figure 2.7** TEM micrographs of iron oxide NPs with diameters of (a) 6 nm, (b) 7 nm, (c) 8 nm, (d) 9 nm, (e) 10 nm, (f) 11 nm, (g) 12 nm, (h) 13 nm. The organic phase high-temperature synthetic route enables precise control of NP size. 21
- Figure 2.8** Functionalized MNPs for molecular and cellular magnetic resonance imaging (MRI). a) Controlling the magnetism of the nanoparticle core, b) tailoring the surface ligands of the nanoparticle shell, and c) the molecular targeting capability of biomolecule-conjugated nanoparticles. d) High performance utilizations of nanoparticles for molecular and cellular MRI. 25
- Figure 2.9** (a) Surface spin canting effect of a nanoparticle upon magnetization (M magnetic moment, H external magnetic field). (b–e) Nanoscale size effects of Fe₃O₄ nanoparticles on magnetism and MR contrast effects. (b) Transmission electron microscopic (TEM) images of 4, 6, 9, and 12 nm of iron oxide nanoparticles. (c) Mass magnetization values, d) T₂-weighted MR images (top: black and white, bottom: color), and (e) relaxivity coefficient r₂ of the nanoparticles presented in (a). (f) FeCo magnetism-controlled metal-alloy MNPs. These FeCo MNPs have an exceptionally high magnetization value of 215 emu per gram metal..... 26
- Figure 2.10** (a-f) Color maps of T₂-weighted MR images of a mouse implanted with the cancer cell at different time points after injection of MnFe₂O₄-Herceptin conjugates or CLIO-Herceptin conjugates. In (a–c), gradual color changes at the tumor site, from red (low R₂) to blue (high R₂), indicate progressive targeting by MnFe₂O₄-Herceptin conjugates. (g) T₂*-weighted in vivo MR images of cancer cells implanted in mouse

model imaged at 9.4 T. Color-coded MR images to further delineate MR signal changes.

..... 27

Figure 2.11 Three types of surface modification schemes for magnetic nanoparticles. (a) Inorganic surface coating with an amorphous silica shell. (b) Amphiphilic polymer coating on the magnetic nanoparticles. (c) Ligand exchange is to replace native surface ligands. These routes exhibit polar or charged functional groups onto the outer surface of the NP for water solubility..... 30

Figure 2.12 Biomedical application of magnetic nanoparticles. 32

Figure 2.13 (a) Synthesis scheme and TEM image of polystyrene–poly(acrylic acid) (PSPAA) block copolymer micelles encapsulating several MNPs. (b) Schematic and TEM image of poly(d,l-lactide)–PEG block copolymer micelles encapsulating several MNPs and a therapeutic agent..... 34

Figure 2.14 (a) Synthetic procedure for the multifunctional polymer nanoparticles. TEM images of nanoparticles. (b) CLSM of DOXO fluorescence and optical images in KB cells treated with a) naked PLGA(MNP/DOXO), b) PLGA(MNP/DOXO)-PEG, c) PLGA(MNP/DOXO)-FOL nanoparticles, and d) PLGA(MNP/DOXO)-FOL nanoparticles under an external magnetic field, respectively. 36

Figure 2.15 (a) Schematic illustration of multifunctional nanoparticles showing iron oxide nanocrystals encapsulated within mesoporous silica, hydrophobic anticancer drugs stored inside the pores, and surface modifications with phosphonate and folic acid targeting ligands. SEM and TEM images of the iron oxide incorporated within the mesoporous silica NPs. (b) Fluorescence microscopy images showing the effect of folic acid modification on the NPs (green fluorescence). The cell nuclei were stained with DAPI (blue fluorescence), and the membranes were stained with WGA (red fluorescence)..... 38

Figure 2.16 (a) Therapeutic applications of hybrid FePt@CoS₂ metal-alloy MNPs. Left: the lethal effect of the hybrid MNPs on cells. Middle: optical detection of changes in cell morphology of untreated HeLa cells (top) and the MNP-treated HeLa cells (bottom). Right: dose-dependent cell viability, b) hybrid iron oxide nanoparticles consisting of SiO₂@Fe₃O₄@Au and anti-HER2/neu antibody for simultaneous MRI diagnosis and laser-assisted hyperthermia therapy. 39

Figure 2.17 Stimulus-responsive membrane triggering in vitro: (a) temperature-triggering, comparison of nanogel particle size in suspension (blue data, right y-axis) and differential flux of sodium fluorescein through the nanogel-loaded membranes (red data, left y-axis) as a function of temperature; (b) magnetic triggering, temperature profile in the sample chamber and differential flux of sodium fluorescein out of membrane-capped devices as a function of time over four successive on/off cycles of the external magnetic field..... 41

Figure 2.18 (a) The concept of targeted magnetomechanical cancer-cell destruction using disc-shaped magnetic particles possessing a spin-vortex ground state. The microdiscs are biofunctionalized with anti-human-IL13 2R antibody, specifically targeting human glioblastoma cells. When an alternating magnetic field is applied, the magnetic discs oscillate, compromising membrane integrity and initiating spin-vortex-mediated programmed cell death. (b,d) and MD–mAb-functionalized cells subjected to 20 Hz–90 Oe a.c. fields for 10 min and TUNEL stained 4 h after the magnetic-field exposure (c,e). The control cells with well-organized chromatin structures have a blue fluorescence, whereas the treated cells are stained with a dark orange–brown dye owing to chromatin fragmentation—an indication of apoptosis..... 43

Figure 3.1 (a) Intrinsic (Néel) and (B) extrinsic (Brown) remagnetization mechanism (schematic). Equipment of high frequency magnetic field (HFMF). 47

Figure 4.1 (a) SEM, (b) TEM and (c) XPS analyses of ferrogels composed by iron oxide nanoparticles and gelatin matrix..... 55

Figure 4.2 (a) Drug release behaviors of the ferrogels under the 10 minutes exposing of high frequency magnetic field (HFMF) and (b) The on-off switch operations of high frequency magnetic field (HFMF) manipulated the cumulative drug release of the ferrogels with different sizes of the nano-magnets..... 57

Figure 4.3 Vibrating sample magnetometry measurements for the ferrogels with various iron oxide nanoparticles sizes. 58

Figure 4.4 Schematic drawing of structures of ferrogel which exhibited a triple-helix structure to restrict the drug molecules to release. While applying the high frequency magnetic field (HFMF), the magnetic nanoparticles provides the heat energy to loose the structures, and twist and shake the polymer molecular chains to effectively accelerate drug release rate. 58

Figure 4.5 Cyclic drug release rates of 40nm@GE ferrogels under a 5-min period of HFMF stimuli and a long 180-minute switching duration, where a longer switching time period ensures the drug to reach a kinetically favorable distribution in the ferrogel for a subsequent burst release. 60

Figure 4.6 Cyclic drug release rates of 40nm@GE ferrogels (a) under a 2-minute period of HFMF stimuli and a short 2-min switching duration. 61

Figure 5.1 (a) TEM images and (b) HR-TEM of PVP-modified Silica/Fe₃O₄ core-shell nanospheres. Local Fourier transfer patterns indicate that the crystallographic structure is extremely uniform and homogenous through the shell. Some facet {1 1 0} planes are observed inside the nanosphere, and the Fourier transform pattern indicates that the shell is oriented at z = [0 0 1]. (c) Local Fourier transfer patterns indicate that the crystalline is uniform and homogenous through the particle. (d) X-ray diffractometer verified the crystallographic phase, at a scanning rate of 6° 2θ per minute, as Fe₃O₄ (magnetite,

according to JCPDS [85-1436])..... 65

Figure 5.2 (a) Photographs of the cuvettes with fluorescence-loaded PVP-modified Silica/Fe₃O₄ core-shell nanospheres dispersed in water solution. Before HFMF exposure, fluorescence-loaded PVP-modified Silica/Fe₃O₄ core-shell nanospheres displayed no sign of fluorescence under the UV light (left); after exposure, green fluorescence released from the PVP-modified Silica/Fe₃O₄ core-shell nanospheres was clearly detected (right). (b) Emission spectra of PVP-modified Silica/Fe₃O₄ core-shell nanospheres (15 mg per 10 mL water) for applying HFMF from 30 s to 180 s. (c) Emission spectra of PVP-modified Silica/Fe₃O₄ core-shell nanospheres. Negligibly small amount of the dye molecule being further released from the nanospheres for a time period of 120 seconds in the absence of the stimulus..... 68

Figure 5.3 Nitrogen-adsorption spectra for the nanospheres before and after a 20-min HFMF exposure. BET measurements of silica nanospheres treated with HFMF for 0 sec, 60 sec and 20 minute. 69

Figure 5.4 Schematic illustration of the thin shell with a proposed mechanism for control release of the fluorescence dye: (I) while applying HFMF, vibration enlarges the dimension of the nano-faults, making dye molecules easy to release out and the change in the dimension of the nano-faults is physically reversible upon a short-term field exposure. (II) under long-term exposure, the nano-faults received sufficient amount of the energy, vigorous energy (although not specifically identified yet in this communication) ruptures the thin shell permanently..... 72

Figure 5.5 TEM images of long-term HFMF exposure, the nano-faults received sufficient amount of the energy, vigorous energy (although not specifically identified yet in this communication) ruptures the thin shell permanently..... 73

Figure 5.6 Fluorescence micrographs of HeLa cells after 10 hours incubation with fluorescence-loaded PVP-modified Silica/Fe₃O₄ core-shell nanospheres. (a) without HFMF treatment; (b) after 30 seconds of HFMF stimulus, green fluorescence was clearly observed within the cell bodies of these HeLa cells upon excitation at 494 nm. 75

Figure 5.7 (a)Temperature curve of nanocapsules during application of HFMFs. (b) Drug release behaviours of nanocapsules under HFMFs, and their release rates (k). 76

Figure 5.8 A near-linear relationship between the rate constant k and SAR values, with correlation coefficient as high as 0.98 can be obtained. 79

Figure 5.9 SAR effects on the different manetic field regions. Drug release behaviors in cells are highly relative with the strength of SAR. 81

Figure 5.10 The TEM electron beam is focus on the nanocapsule for different time durations. While increasing the heating time to 40 minutes, the obvious deformation of melting was observed..... 82

Figure 5.11 (a) Field-dependent magnetization curve and (b) XPS analysis of nanocapsules

for different time of HFMF treatment..... 83

Figure 6.1 (a) Schematic of the stimuli-response nanodevice delivery system where quantum dots were deposited on the shell of the PVP/Fe₃O₄ core-shell nanospheres. Attachment of the ZCIS QDs on the surface of the nanospheres acts not only as a strong fluorescence-emitting agent, but also as a sensor to monitor the drug release in a real-time basis under magnetic induction. (b) TEM image and (c) HRTEM image of the PVP-Fe₃O₄ core-shell nanospheres. (d) HRTEM image of the ZCIS-doped nanospheres. After incorporation of the ZCIS QDs on the core-shell nanospheres, the suspension displayed a fluorescence character under the UV light (inset picture). 90

Figure 6.2 Local Fourier transfer patterns of single-crystal iron oxide shell indicate that the shell exhibits uniform and homogenous crystalline orderliness along the surface of the core phase. 91

Figure 6.3 (a) The TEM image and local Fourier transfer patterns of ZCIS QD-Single crystal Fe₃O₄ shell nanoplatfrom. The local Fourier transfer pattern also demonstrated a high crystallinity of the ZCIS QD. (b) The TEM image of CIS QD-Single crystal Fe₃O₄ shell nanoplatfrom. The EDS investigated the Fe₃O₄ shell and ZCIS QD, corresponding to the regions 1 and 2 in the HRTEM image, respectively. HRTEM image shows the solid nanoparticle attaching the ring-like shell region being ZCIS QDs in the heterodimer. The energy dispersive X-ray spectrometer (EDS) analysis confirms that the ring-like region mainly consists of Fe and the small solid particle consists of Cu and Se. 91

Figure 6.4 Field-dependent magnetization curve of nanodevices with and without quantum dots..... 92

Figure 6.5 Schematic drawing showing multi-functionalities of each compartment from as-designed nanodevices for nanoimaging, controlled drug release, and in-situ motoring of drug release. 93

Figure 6.6 Cellular uptake of the nanodevice was evaluated using HeLa cells, by incubating the cell line with both mercaptoundecanoic acid-modified nanodevice (MUA-NDs) and folic acid-modified nanodevice (FA-NDs). Both the MUA-NDs and FA-NDs were uptaken by the cells in 4 hours of period, probably through endocytosis, with different degrees of efficiency. In comparison, the majority of the FA-NDs can be clearly observed in the cytoplasm region of the cell, but only a few MUA-NDs was uptaken by HeLa cells, indicating that the folic acid-modified version promotes a stronger cell-specific intake by the HeLa cell line than that of the mercaptoundecanoic acid-modified version. The folic-acid-modified nanodevices showed excellent cell-specific uptake efficiency, through possibly endocytosis. 93

Figure 6.7 (a) Emission spectra of dye-loaded nanodevices (30 mg per 10 mL water) under HFMF treatment over a time period from 0 s to 100 s. Before HFMF exposure, the dye-loaded nanodevices displayed no sign of dye release, which causes green

fluorescence at an emission wavelength of 517 nm, as determined by fluorescence spectrophotometer. However, a strong emission signal from the QDs after exposure, red fluorescence at an emission wavelength of 581-614 nm, show that dye was released from the nanodevices. A degenerative green fluorescence appeared concurrently. (b) Model drug intensity versus quantum dot intensity curves originate from both the dye and ZCIS emitting spectra and show a near symmetrical profile under different magnetic field strengths..... 95

Figure 6.8 Temperature curve of nanodevices during application of HFMFs of different strengths..... 97

Figure 6.9 Binding energy of S 2p of the nanodevices with and without exposure to a high frequency magnetic field (HFMF) for a time period of 180 seconds. XPS results indicate the binding energy shift of the S 2p line from 162.3 eV - 166.2 eV before the stimulus to a single, strong binding-energy peak at 167 eV after the magnetic exposure. This could be attributed to S²⁻ from ZnS, CuS, In₂S₃, or SO₄²⁻, SO₂. The binding energy at 167 eV on the ZCIS surface is strongly associated with the presence of oxide groups including SO₄²⁻, SO₂, etc on the surface. This demonstrates a rapid oxidation of the ZCIS QDs after a short period of magnetic induction..... 99

Figure 6.10 PL emission spectrum at various time intervals of nanodevice incubation in PBS solution. 100

Figure 6.11 (a) Schematic illustration of the nanodevice with a proposed mechanism for controlled release of the dye molecules, as well as the degeneration of fluorescence intensity of the ZCIS QDs (b) Shell vibration causing enlargement of the dimensions of nano-crevices along the deformed single-crystal shell, rendering dye release upon short-term magnetic stimulation. (c) After long-term exposure, the deformed shell has received a sufficient amount of the energy to cause a final, permanent, mechanical rupture. Meanwhile, a rapid surface oxidation altered the surface structure of the QDs, leading to substantial degeneration of the fluorescence intensity..... 102

Figure 6.12 Cell viability of HeLa cells after 12 to 48 hours of incubation with increasing amounts of folic acid modified nanodevices (FA-NDs). Cell viability was measured using an MTT assay..... 103

Figure 6.13 Fluorescent combination of the HeLa cells with the dye-loaded nanodevices after 12 hours incubation. With increasing duration of HFMF treatment, both the controlled release of the dye molecules (green channel intensity increased) and the associated real-time, in-situ monitoring capability of the doped ZCIS QDs (red channel intensity decreased) can be manipulated simultaneously to single-cell resolution. This implies that dye release can be precisely monitored by the variation of the ZCIS QDs from the nanodevices. G_{sum}/B_{sum} represents the ratio of the green channel intensity to blue channel intensity, and is indicative of the relative concentration of the model drug in each cell.

R_{sum}/B_{sum} is then defined as the relative intensities of the nanodevices in each cell..... 105

Figure 6.14 The ratio of G_{sum}/B_{sum} and R_{sum}/B_{sum} versus the duration of magnetic stimulus in the cells gives rise to two curves. The results demonstrate the relative drug concentration, represented by G_{sum}/B_{sum} , in the cells with increasing duration of stimulus. The fluorescence intensity originating from the ZCIS QDS, represented by R_{sum}/B_{sum} , decreased in proportion at the same time..... 106

Figure 6.15 Fluorescent morphologies of HeLa cells after 12 hours incubation with drug loaded nanodevices. With increasing the time duration of HFMF treatment, the control of drug release associated with a real-time self monitoring of the ZCIS QDs from the nanodevices were manipulated simultaneously. The digital analysis software (Nikon, Japan) was use to analyze the fluorescence intensities of model drug and nanodevices. The conditions of the exposure are the same for each color channels. The analyzed areas were determined by the software which defined the fluorescence intensity from 1 to 255. The ranges of the fluorescence intensities: Blue channel (60-255), Green channel (40-255), and Red channel (30-255)..... 107

Figure 7.1 Schematic illustration of the synthesis and structure of the self-assemble iron oxide /silica core-shell (SAIO@SiO₂) nanocarriers for magnetically controlled drug release.115

Figure 7.2 TEM images of (a) iron oxide nanoparticles, (b) self-assemble iron oxide (SAIO) nanospheres, and (c, d) self-assemble iron oxide /silica core-shell (SAIO@SiO₂) nanocarriers. The thickness of silica shells coated on the SAIO nanoparticle is 4-5 nm. The inside pictures displayed the solution color for different particles. (e-g) The size distributions of iron oxide nanoparticles, SAIO nanoparticles and SAIO@SiO₂ nanocarriers were measured by dynamic light scattering (DLS).....116

Figure 7.3 The SEM images of (a) SAIO and (b) SAIO@SiO₂ nanospheres. (c)After 4 minutes, the SAIO@ SiO₂ nanospheres did not show obviously cracks under the SEM analysis.116

Figure 7.4 (a) X-ray diffraction patterns of iron oxide nanoparticles, SAIO and SAIO@SiO₂. (b) Field-dependent magnetization curve of iron oxide nanoparticles, SAIO and SAIO@SiO₂ nanocarriers. The inside pictures: the SAIO@SiO₂ nanocarriers were attracted by an external magnet.118

Figure 7.5 Cumulative drug release of SAIO and SAIO@SiO₂ nanocarriers. Coated with silica shells, the SAIO@SiO₂ nanocarriers exhibited relatively smaller amount of cumulative drug release than SAIO nanoparticles..... 120

Figure 7.6 Cumulative drug release profiles of ibuprofen (IBU) from (a) SAIO and (b) SAIO@SiO₂ nanocarriers were triggered by 1 to 4 minutes of high frequency magnetic field..... 121

Figure 7.7 TEM images of nanostructures of (a, b) SAIO@SiO₂ nanocarriers, and (c) to (f) SAIO after 4-min duration of HFMF treatment. (a, b) SAIO@SiO₂ nanocarriers

displayed no obviously crack after HFMF treatment. (c-f) SAIO without silica shells showed obvious cracks or deformation after applying HFMF..... 123

Figure 7.8 Time-course PL microscopy images of HeLa cells labeled with FITC- SAIO@SiO₂ nanocarriers, the cell skeleton was stained with rhodamine phalloidin (red), and cell nucleus with DAPI (purple). Cells were incubated with FITC- SAIO@SiO₂ nanocarriers for (a) 30 min, (b) 1 h, (c) 2 h, and (d) 4 hour. 127

Figure 7.9 (a) Cell viability of HeLa cells after 12 to 48 hours of incubation with increasing amounts of SAIO and SAIO@SiO₂ nanospheres. Cell viability was measured using an MTT assay. (b) Flow cytometry analysis for the FITC- SAIO@SiO₂ nanocarriers accumulated in HeLa cells for incubation of 30 min and 2 hours. 128

Figure 7.10 After the HeLa cells took up the SAIO@SiO₂ nanospheres, the HFMF subjected to these cells for 30 seconds to 4 minutes. The cytotoxicity with short time of HFMF treatment is small, indicating that the heat produced by nanospheres could not kill most of the cancer cells. 130

Figure 8.1 (a) Schematic illustration of the synthesis and structure of the thermosensitive yolk/shell capsules for magnetically-triggered controlled drug release. TEM images of (b) yolk/shell-1, (e) yolk/shell-2, (f) yolk/shell-3, and (g) yolk/shell-4. (c) The SEM images of yolk/shell capsules. (d) The TEM image of lattice structure of iron oxide nanoparticles in the capsules. The yolk/shell capsules with an average diameter about 76 nm possessed an ultra-thin layer of dense silica shell of about 7 nm in thickness. 137

Figure 8.2 TEM images of yolk/shell capsules without PVA. Without PVA as a stabilizer, the nanocapsules displayed a un-uniform morphologies. Some magnetic nanoparticles were not encapsulated in the nanocapsules. 138

Figure 8.3 SEM images of (a) yolk/shell-1, (b) yolk/shell-2, (c) yolk/shell-3, and (d) yolk/shell-4. 138

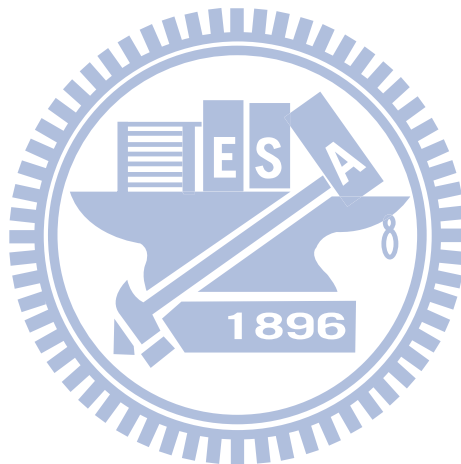
Figure 8.4 (a) Field-dependent magnetization curves of yolk/shell-1 to yolk/shell-4, showing the capsules are superparamagnetic. (b) Cumulative drug release of F68/PVA nanocomposites (NCs) and yolk/shell capsules. Coated with silica shells, the yolk/shell capsules showed relatively smaller amount of cumulative drug release than F68/PVA nanocomposites (NCs). 140

Figure 8.5 (a) Diameter of F68/PVA nanocomposites (NCs) measured by DLS decreased abruptly at about critically micellization temperature (CMT). (b) DSC cooling scans of F68 and F68/PVA nanocomposites (NCs). 144

Figure 8.6 (a) Cumulative drug release profiles of ibuprofen (IBU) from yolk/shell capsules were triggered by 1 minute of high frequency magnetic field (HFMF) at fourth minute. Schematic illustration as shown in inside picture with a proposed mechanism for controlled drug release under HFMF. After the exposure to a magnetic field, the

volume/hydrophobicity transition of cores produced a strong inner stress, making the capsules collapse or rupture as demonstrated in (b) and (c) TEM images. 145

Figure 8.7 Time-course confocal images of ARPE-19 cells incubated with 10 FITC-labeled yolk/shell capsules (green dots) for (a) 4 and (b) 24 hours. The cells were stained with rhodamine phalloidin (red), and cell nucleus with DAPI (blue). (c) The cross section images of cells viewed by laser-scanning confocal microscope exhibited that the capsules are localized in cells. (d) ARPE-19 cell viability under the incubation of capsules for 24 hours with and without 1-minute of magnetic field treatment. (e) Magnetic resonance images of rat brain before and after the intravenous injection of yolk/shell capsules. The local hyperintensity generated by capsules was visualized using a 3 T small animal MR. Image was acquired pre-injection (Left) and 2 hr post-injection (Right)..... 150



Chapter 1

Introduction

Control release of therapeutic agents from nanometric carriers has been receiving increasingly interest because it provides numerous advantages, such as high delivery efficiency and site-specific therapy, compared to traditional dosing techniques. Owing to these advantages, many researches proposed to integrate active drug molecules with host materials, aimed at manipulating drug release profile. It is desirable that drug release behavior can be optimized with either a slow, zero-order release pattern or a burst fashion mimicking natural release of biological molecules, such as hormones like insulin or thyroxine formed in endocrine glands, in the body.^[1] Therefore, many studies have been reported in response to specific stimuli, such as temperature,^[2,3] pH,^[4] electric field,^[5] ultrasound,^[6,7] and magnetic field^[8-11] to deliver drugs in a therapeutically desirable manner. Many traditional stimuli such as electric signal, mechanical force, pH, etc, were usually needed a physical contact with the drug carriers in order to trigger drug release, however, such a manner of triggering drug release may not be practically applicable in human body. Furthermore, real-time release upon a short-time stimulus is also hard to achieve for traditional stimuli-responsive polymeric materials, which is especially critical for a certain clinical complications. Therefore, a practical development of a desired drug carrier should possess real-time responsive to the stimuli when an urgent need is required for disease control and/or slow, sustained release to meet different clinical complications.

A major challenge in designing drug release systems involves the precise control of drug release, both spatially and temporally. Optimizing drug-release behavior to enable pulsatile release mimicking the natural release of biomolecules is also desirable. Many focal diseases require local drug release systems that can act at a

specific site, thus reducing the side effects of a toxic drug molecule or enhancing a drug's therapeutic efficiency. Functional nanomaterials have recently been used as an energy-induced media to trigger drug release for cancer therapy.^[12,13] For example, the photothermal effects of gold nanostructures, nanocages and carbon nanotubes can be activated by irradiation with near-infrared (NIR) light for tumor therapy.^[14-18] These materials are effective at increasing the local temperature using NIR light, but the short penetration depth of NIR lasers may require the injection of an invasive optical-fiber into the tumor tissue to treat deep-seated cancer cells. Using a magnetic field in place of these NIR systems would allow for remote management to trigger drug release from the magnetic drug carriers.^[19, 20]

A high frequency magnetic field can cause an increase in the temperature of magnetic nanoparticles, which could be useful for creating local hyperthermia and as an approach to cancer therapy. So far, to our best knowledge, little investigation has been addressed on the controlled drug release precisely from nanosized carriers under an external magnetic stimulation. However, nano-carriers with controllable drug release property is highly desirable because such small carriers can be designed to deliver drug to a specific site of disease, and then, drop the therapeutic molecules in a right position at a right time with a therapeutically effective dose. For the purpose to control release by magnetic field, this thesis was mainly designed and constructed by preparing a self-assembly iron oxide nanoparticles with drug molecules embedded in an ultra-thin nanoshell. A structurally dense shell can be acted as a physical barrier to eliminate undesirable drug release before reaching the target sites, which appears to be practically desired.

First, in Chapter 4, in order to investigate the ability of high frequency magnetic field (HFMF) to trigger drug release from magnetic composites, we synthesized smart ferrogels fabricated by gelatin/chitosan polymer in the presence of iron oxide particles

averaging from 10nm to 250 nm in diameter. Iron oxide particles embedded in the ferrogel exhibit a good affinity with carboxylic acid groups of gelatin. An external HFMF of 50k-100k Hz was applied to rotate the embedded iron oxide particles, which subsequently disturbed the polymer chains and dramatically increase the drug diffusion rate from ferrogels. Pulses of HFMF were also applied to the nanocarriers to examine the programmed drug release. The interaction of iron oxide particles and gelatin were estimated by the ESCA and SEM analysis.

In Chapter 5, we shifted our focus on nanosized magnetic drug-carriers which were designed and prepared by a poly-(N-vinyl-2-pyrrolidone) (PVP)-modified silica core covered with a thin, single-crystal iron oxide shell. The iron shell is used for outstanding on-off characteristic of controlled release of model molecule. The fluorescence dye as a model drug molecule was encapsulated in the cores and released under a stimulus of high-frequency magnetic field (HFMF). While applying HFMF, the thin oxide shells may subject to developing crevices along the spherical shell, which may be formed the “nano-faults”, where magnetically-induced vibration enlarges the dimension of the nano-faults, making drug molecules easy to diffuse out and the change in the dimension of the nano-fault is reversible upon a short-term magnetic field exposure.

To be continued, in Chapter 6, based on the core-iron oxide shell nanocarriers, the multifunctional nanodevice were fabricated by integrating nano-imaging, targeting, and controlled drug delivery. The nanodevice is composed of a polymer core/single-crystal iron oxide shell nanostructure bonded to a quantum dot. It shows outstanding release and retention characteristics via an external on/off manipulation of a high-frequency magnetic field. This allows a variation between retention and slow release of the drug. Further stimulation causes permanent rupturing of the shell, causing release of the drug in a burst-like manner. The quantum dot bonded to the

nanodevice provides optical information for in-situ monitoring of the drug release through use of a magnetic field.

In addition, in Chapter 7, to encapsulate hydrophobic drug molecules and enhance the encapsulation efficiency, self-assemble iron oxide/silica core-shell (SAIO@SiO₂) nanocarriers were synthesized as the bifunctional magnetic vectors that can be used for control release of therapeutic agent by an external magnetic field and drug release profiles can be well-regulated through an ultra thin layer of silica shell. The hydrophobic drug molecules were encapsulated within the iron oxide-PVA core and then further covered with a thin-layer silica shell to regulate release pattern. The nanostructural evolution of the nanocarriers upon the stimulus was examined and the mechanism of control release of drug is proposed for such a core-shell nanocarrier. The surfactant-free SAIO@SiO₂ nanocarriers were incubated with HeLa cell line to investigate the uptake efficiency.

Chapter 8 expanding our study from SAIO@SiO₂ nanocarriers in Chapter 7 investigate synthesis of thermosensitive yolk/shell capsules containing cores with a stimulus-responsive volume and hydrophobicity and an ultra-thin silica shell. The core of these yolk/shell capsules is composed of thermosensitive PEO-PPO-PEO copolymers with iron oxide nanoparticles and hydrophobic drug molecules incorporated via a mini-emulsion process. The core is also coated with a thin-layer silica shell to regulate the release from the capsule before application of an external magnetic field. When the magnetic field induces temperatures approaching 47 °C, the thermosensitive cores exhibit a significant shrinkage in size resulting in a greater than 10-fold decrease in diameter. The dramatic volume/hydrophobicity transition destroys the solid silica shells and causes them to collapse, leading to rapid drug release. These yolk/shell capsules can also be used to enhance magnetic resonance imaging (MRI) as demonstrated in vivo in rat brains.

We make a conclusion in Chapter 9 for each parts of our drug carriers with controllable functionalities. These carriers are simultaneously being multifunctional, compact in size, and sensitive to environmental stimulation, which are not available for conventional drug carriers. Future development of this new class of multifunctional carriers includes targeted imaging and therapy in vitro and in vivo, and we envision this enabling technology will open exciting opportunities in nanomedicine, electronics, spintronics, and catalysis.



Chapter 2

Literature Review and Theory

2.1 Introduction of controlled drug delivery and release

Controlled drug delivery and release is one of the most rapidly advancing areas of science in which material and chemical researchers are contributing to human health care. Drug delivery and release have typically focused on optimizing drug compounds, enhancing their effects, and reducing their side effect and toxicity. The role now includes diagnosis, site-specific targeting, and rapid dosing to high therapeutic concentration. The technique can also enhance the screening and evaluating new compounds. The key concept of controlled drug delivery and release is defined as "Making old drugs new."^[21] Generally, developing new drug compounds costs a lot of money ,and at least, spend several years for animal studies and clinical trials. Designing functional molecules or materials conjugated with well-developed drug molecules offers rapid and efficient way to achieve the concepts. By these wide advantages of the drug delivery and release system, a number of researches have been successfully proposed to integrate active drug molecules and host materials, where to manipulate drug release desirably. For example, through conventional bolus injection, drug concentrations at site of therapeutic actions are only a portion of the treatment period in the therapeutic window. By contrast, drug delivery from the controlled polymeric systems can maintain drug concentrations within the therapeutic window for prolonged time.^[22] As shown in **Figure 2.1a**, the concentrations of drug at the site of activity are compared 4 injections per six hours and a controlled drug release system. Drug concentrations fluctuate via the bolus injections during the 24 hours, and the drug concentrations reach the therapeutic window for only portion of

treatment period. The controlled drug release system matches the rate of drug elimination maintaining the drug concentration within the therapeutic window for the vast majority of the 24 hours periods. In distribution control, the drug release systems aim to release the drug to the targeting site of activity, in which the drug concentrations reaching the therapeutic window as well as reducing the side-effect production in **Figure 2.1b**. This literature reviews exhibit the smart drug delivery and release systems including environment-sensitive hydrogels, micro- and nano- carriers, in which the functional materials such as quantum dots, iron oxide, or gold nanoparticles incorporating for imaging, diagnosis, energy absorbing or triggering drug release. In the later sections of this review, we focus on the current applications of nanotechnology inducing and triggering the drug delivery systems, especially for magnetic field and magnetic nanoparticles.

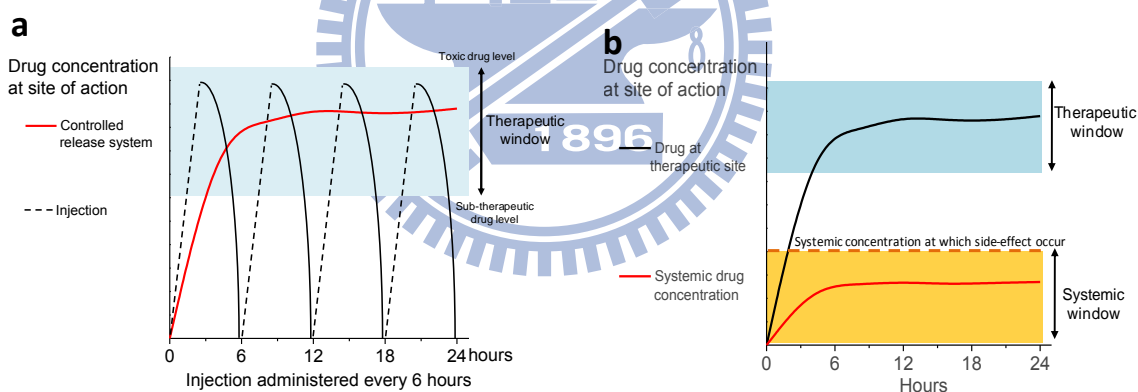


Figure 2.1 (a) Drug concentration at site of therapeutic action under a controlled drug release system (solid line) and a conventional injection (dash line). (b) An ideal distribution of drug concentration from a controlled drug release system.[22] Copyright 1999, Chemical Reviews.

2.2 Responsive polymers for drug delivery

Responsive hydrogels provide enormous advantages in various applications. Some environmental variables, such as low pH and raised temperature, are occurred in the human body. By tailoring their molecular structure, polymer chains can be

modified to interact with their environment in a preprogrammed and intelligent manner. The types of responsive hydrogels are also called 'intelligent' or 'smart' hydrogels. Many physical or chemical stimuli have been used to induce the various responses of the smart hydrogel systems. Such smart hydrogels possess such 'sensing' properties which allow to change in swelling behaviors, permeability, and elasticity upon only minute alternations in the environmental conditions. Many physical and chemical stimuli have been applied to induce various responses in response to change in temperature,^[2,3] pH,^[4] electric field^[5] and magnetic field,^[8] for the smart hydrogels which administer drug release considerably and can be potentially used in extended field. These smart hydrogels have widely been used in diverse applications, such as in artificial muscles, chemical valves, immobilization of enzymes, and concentrating dilute solutions in bioseparation. Owing to these advantages, responsive hydrogels are ideal candidates for developing self-regulating drug delivery systems.

2.2.1 Temperature-responsive polymer

Temperature-sensitive hydrogels are one of the most commonly studied class of environmentally responsive polymer systems in controlled drug release. Many polymers show a thermodynamic structures possessing a temperature-responsive phase transition property. The changes are categorized by the phase diagrams. For example, polymers are one-phase in that solution may thermodynamically separate into two distinct phases at another temperature, which is causing the presence of hydrophobic groups, such as methyl, ethyl and propyl groups. The responsive polymer is related to polymer phase separation as the temperature is raised to a critical value so-called the lower critical solution temperature (LCST), above which the solution partitions into two phases: water and polymer rich phase. The polymer chains showing a lower critical miscibility temperature tend to collapse or shrink while the

temperature increasing above the LCST. In contrast, the polymers swell upon the temperature below the LCST. Among the homopolymers that exhibit LCST, the most studied is poly(N-isopropylacrylamide) (PNIPAAm) and its derivatives. PNIPAAm showing a LCST around 33 °C has been widely studied for variety of applications, including controlled drug release and tissue engineering.^[23-25]

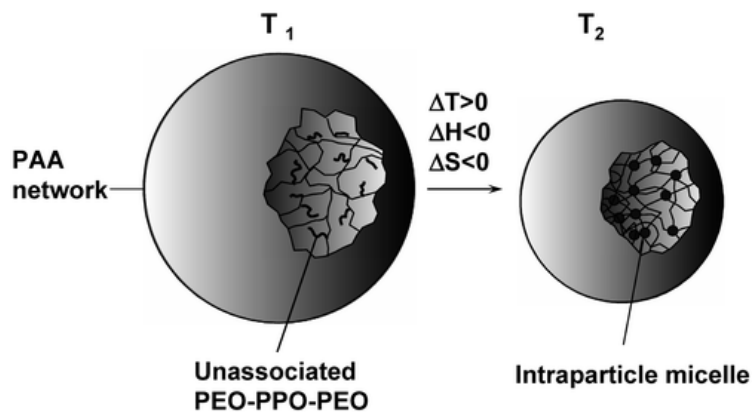


Figure 2.2 Thermosensitive behaviors of poly (ethylene oxide)-poly (propylene oxide)-poly (ethylene oxide) (PEO-PPO-PEO) tri-block polymer. Copyright 1999, American Chemical Society.[26]

Another nontoxic temperature-sensitive hydrogels is tri-block copolymers, poly (ethylene oxide)-poly (propylene oxide)- poly (ethylene oxide) (PEO-PPO-PEO) which also exhibits the reversible solution transition behaviors in aqueous solution. Commercially known as Pluronic (BASF) or poloxamers (ICI), this amphiphilic polymer is non-ionic surfactant composed of the hydrophilic PEO segments and hydrophobic PPO segments. They are approved by the US Food and Drug Administration (FDA) for clinical purposes. In **figure 2.2**, inter-chain aggregation of polymer occurs while the temperature above LCST, forming alternating PEO and PPO arranged into micelles, cylinders or other supermolecular structures.^[27,28] On the other word, the LCST also means the critical micellization temperature (CMT).^[29,30] Therefore, in this thesis, this thermosensitive polymer is proposed to the formation of nanocapsules to optimize the operating temperature of the magnetic field inducing

triggered release. Under the suitable temperature, the drug molecules or biomolecules can maintain their activities. Recently, Choi et al. reported that the nanocapsules synthesized by PEO-PPO-PEO copolymer is biocompatible (commercially known as pluronic) and manifest a range of critical micellization temperature for volume/hydrophobicity transition, showing a reversible (1000×) volume transition when cycled between 25 and 37 °C.^[31]



Figure 2.3 Gelatin possesses a triple helix structure at room temperature and forms a stable gels (middle). While increasing above the breaking temperature of hydrogen bonds, the gelatin becomes solution states (right). Copyright 2000, American Chemical Society.^[32]

Natural biomolecules such as protein or poly-peptides generally show structural transitions at increasing temperature. For example, the conformation of single strand peptides can be changed from a helix to a coil under the characteristic temperature. Such changes of secondary and tertiary structures of biopolymers demonstrate a significant effect on the biological functionalities. This conformation changes are caused by the formation or de-formation of the hydrogen bonds between amino acids and relatively immune to the entropy-dominated influences of hydrophobicity. For these biomolecules, the temperature sensitive behaviors is like the 'melting' of the hydrogen bonds. For example as shown in **Figure 2.3**, gelatin, a protein, possesses a triple helix structure at room temperature and forms a stable gels.^[32] While increasing above the breaking temperature of hydrogen bonds, the gelatin becomes solution states. Cooling the solution below the gelation temperature, the random coils of the peptides self-assemble again into triple-helix structure. In this situation, both

hydrogen bonds and hydrophobic molecular aggregation contribute to gelation.

2.2.2 Responsive polymer incorporated magnetic nanoparticles

Such smart hydrogels possess such ‘sensing’ properties which allow to change in swelling behaviors, permeability, and elasticity upon only minute alternations in the environmental conditions. So far, many kinds of magnetic sensitive hydrogels (ferrogels) have been developed and studied with regard to biomedical materials. This magnetic field sensitive gel, also known as ferrogel, finely distributed colloidal superparamagnetic magnetic nanoparticles are incorporated into the swollen network. A macroscopic change in the shapes of the resulting ferrogels in response to external magnetic stimuli can be easily manipulated, which permit these ferrogels to be employed as muscle-like soft linear actuators and drug delivery systems.^[33-35] On the other hand, the magnetic nanoparticles couple the shape of the ferrogel to external magnetic field. Shape distortion can be induced instantaneously and disappears abruptly while removing the magnetic field. A discontinuous elongation and contraction in response to infinitesimal change can be controlled by an external magnetic field. Such gels has been reported with regard to their applications to several boimedical and industrial fields. For example, magnetic-field-sensitive gelatin microspheres were reported for pulsed release of insulin via an oscillating magnetic field^[36] and the release rate of insulin in the alginate microspheres with magnetic particles is much faster than that in absence of an external magnetic field. Although magnetic nanoparticles (MNPs) were widely used for magnetic resonance contrast enhancement, tissue repair, immunoassay, hyperthermia, drug targeting and delivery and in cell separation,^[37,38] to the best of our knowledge, there has been little investigation on drug delivery under a direct current (DC) magnetic field through the use of magnetic nanoparticles in the ferrogels. Drug delivery from the magnetic

sensitive ferrogels can be triggered by a non-contact force (an external magnetic field), which is superior to the traditional stimuli response polymers, such as pH or temperature sensitive polymer. By this concept, a Magnetic Targeted Carriers (MTCs) has been designed which could adsorb pharmaceutical agents through application of an externally magnetic field for site-specific targeting and sustained release of drugs^[39] as shown in **Figure 2.4**. In addition, according to our previous study, it was demonstrated that a direct current (DC) magnetic field can be used to manipulate the drug release behaviors from a smart magnetic hydrogel through an on-off switch of a magnetic field.^[40] Zhang et al. reported that macroporous temperature-sensitive hydrogels exhibited a tremendously faster response to the external temperature changes due to their unique macroporous structures.^[41] In addition, pHEMA sponges were developed to achieve rapid and reliable delivery of bioactive substances for long-term implantable drug delivery devices,^[42] and plasmid DNA with a sustained release from polymeric scaffolds was investigated for tissue regeneration.^[43]

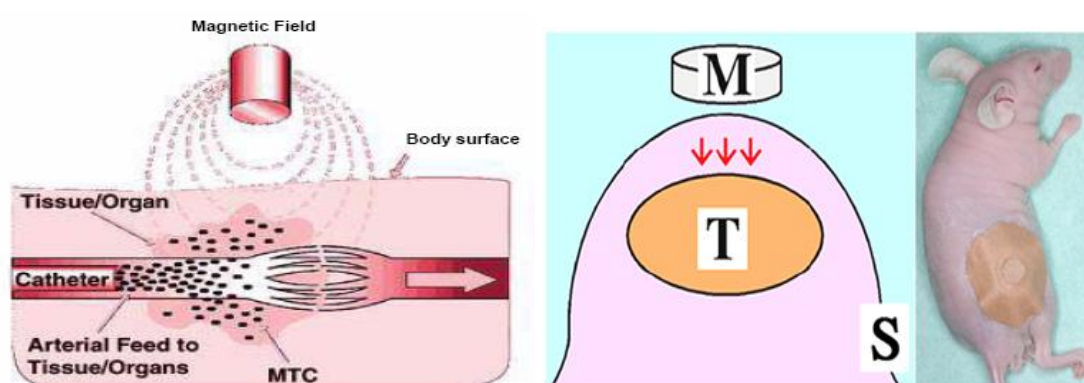


Figure 2.4 Magnetic Targeted Carriers (MTCs) has been designed which could adsorb pharmaceutical agents through application of an externally magnetic field for site-specific targeting and sustained release of drugs.

2.3 Nanotechnology on drug delivery system

The application of nanotechnology to drug delivery received a lot of attention because it is widely expected to change the landscape of pharmaceutical and biomedical industries.^[44] The development of nanotechnology products may play an important role in adding a new function of therapeutics. Applying the nanotechnology to drug delivery system, it may be possible to achieve (1) improved delivery of poorly water-soluble drugs; (2) targeted delivery of drug in a cell- or tissue-specific manner; (3) delivery of large macromolecule drugs to intracellular sites of action; (4) co-delivery of two or more drugs or therapeutic modality for combination therapy; and (5) visualization of sites of drug delivery by combining therapeutic agents with imaging modalities. Additionally, the fabricating complexity of nanotechnology therapeutics may also display a significant hurdle for generic companies to develop equivalent therapeutics readily. These are just a few of the many compelling reasons that nanotechnology holds enormous promise for drug delivery. There are a number of parameters that are important for successful development and manufacturing of drug delivery vehicles. For example, the use of biocompatible materials with simple robust processes for biomaterial assembly, conjugation chemistry, and purification steps; and developing scalable unit operations amenable to manufacturing large quantities of targeted drug delivery system. It has been shown that the development of drug delivery vehicles by self-assembly of prefunctionalized biomaterials simplifies the optimization and the potential manufacturing of these systems.^[44] The physical and chemical properties of vehicles, such as size, charge, and surface hydrophilicity, can all impact the circulating half-time of the particles and their distribution. Recently, surface properties of drug delivery nanosystem such as ordered striations of functional groups as well as their shape and size have been shown to enhance particle uptake.

2.3.1 Nanotechnology for nanoplatforms

Nanotechnology, an interdisciplinary research field involving chemistry, engineering, biology, medicine, and more, has great potential for early detection, accurate diagnosis, and personalized treatment of diseases. Nanoscale devices are typically smaller than several hundred nanometers and are comparable to the size of large biological molecules such as enzymes, receptors, and antibodies. With a size about 100 to 10000 times smaller than human cells, these nanoscale devices can offer unprecedented interactions with biomolecules both on the surface of and inside cells, which may revolutionize disease diagnosis and treatment. The most well-studied nanomaterials include quantum dots (QDs),^[45,46] carbon nanotubes,^[47,48] nanoshells,^[49] paramagnetic nanoparticles,^[50] and many others (**Figure 2.5**).^[51,52]

One of the major applications of nanotechnology is in biomedicine. Nanoparticles can be engineered as nanoplatforms for effective and targeted delivery of drugs and imaging labels by overcoming the many biological, biophysical, and biomedical barriers. For *in vitro* and *ex vivo* applications, the advantages of state-of-the-art nanodevices (nanochips, nanosensors, and so on) over traditional assay methods are obvious.^[52,53] Several barriers exist for *in vivo* applications in preclinical animal models and eventually clinical translation of nanotechnology, among which are the biocompatibility, *in vivo* kinetics, targeting efficacy, acute and chronic toxicity, and cost-effectiveness.

2.3.2 Nano-polymer drug delivery vehicles

Drugs entrapped in polymer matrices can be released via passive diffusion of the drug from a static polymer scaffold (e.g., through the pores in the polymer matrix or between polymer chains). Enhanced diffusion can be attained with swelling of the polymer matrix (via changes in pH, ionic strength, temperature, enzymatic conversion,

application of electric or magnetic field), providing a mechanism for stimuli-responsive release. Alternatively, drug release can be initiated by polymer degradation (proteolytic or hydrolytic), thus eliminating the need to remove the scaffold after drug release. A variety of hydrophilic and biocompatible hydrogels based on natural and synthetic polymers have been used for encapsulation of drugs for drug delivery or cells for repairing tissues and organs; indeed, their use dates back decades.

They withstand heat sterilization, and their mechanical properties and water content can be adjusted to meet use requirements. Since then, an enormous amount of work has been done in the development of various improved hydrogel-based polymer matrices. In particular, poly(ethylene glycol) (PEG)-based hydrogels have shown excellent properties for use as biomaterials because of their biodegradation and biocompatibility^[54] and have been regularly employed as matrices for drug delivery and cell encapsulation as well as conjugated to biomacromolecules to improve their half-lives in vivo.^[55] Park and co-workers have reported superporous hydrogels and composites from a wide range of polymers including poly-(acrylic acid) (PAA) and PNIPAAm.^[56] The polymers were produced via ATRP methods in inverse miniemulsions, and the high ethylene oxide content prevents protein adsorption to the nanogels. Cytotoxicity assays revealed that the resulting nanogels were nontoxic to cells. The nanogels can be degraded to soluble polymers in the presence of reducing agents such as the water-soluble biocompatible glutathione tripeptide, suggesting their potential use as delivery matrices that target specific cells. Thus, in the future, porous hydrogels of controlled structure and chemical composition should be useful for optimal release of drugs under various therapeutically relevant conditions.

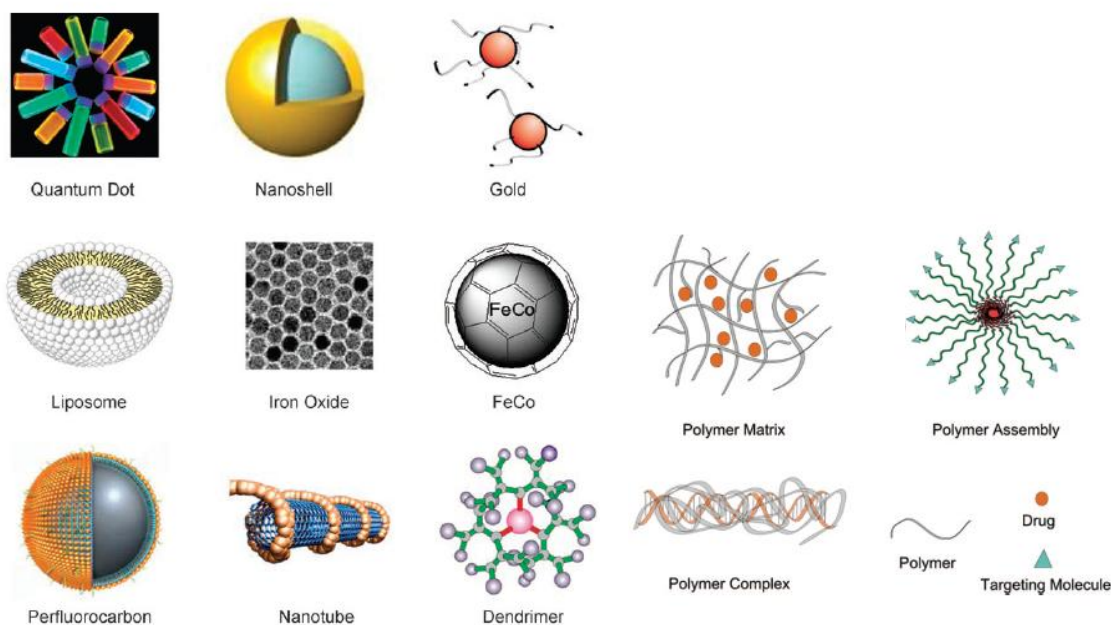


Figure 2.5 Representative nanoparticles that can serve as nanoplatforms and polymeric vehicles for targeted molecular imaging in living subjects. Copyright 2007, Wiley-VCH Verlag GmbH & Co. KGaA. 2009, American Chemical Society.[57,58]

2.4 Magnetic nanoparticles for biomedical applications

Controlled drug release from nanofunctional materials, especially magnetic nanoparticles (NPs), is attracting increasing attention due to their potentials in cancer therapy and the treatment of other ailments. The magnetic NPs stems from intrinsic properties of their magnetic properties combined with their drug loading capability and the biochemical properties that can be bestowed on them by means of a suitable coating.^[59] Preparation methods of NPs generally fall into the category of so-called 'bottom up' methods, where nanomaterials are prepared from atoms or molecules in a controlled manner that is thermodynamically regulated by means such as self-assembly. Some biomedical applications require core-shell magnetic NPs. They have a metal or metallic oxide core, which is encapsulated in an inorganic or a polymeric coating that renders the particles biocompatible, stable, and may serve as a support for drug or biomolecules. As shown in **Figure 2.6**, their magnetic properties

make these particles to be used in numerous applications, belonging to one or more than the following groups:

- (i) Magnetic contrast agents in magnetic resonance imaging (MRI);
- (ii) Hyperthermia agents, where the magnetic particles are heated selectively by application of an high frequency field. (e.g. in thermal ablation/hyperthermia of tumors); and
- (iii) Magnetic vectors that can be directed by means of a magnetic field gradient towards a certain location, such as in the case of the targeted drug delivery.

Prior to their use for drug delivery, magnetic nanoparticles were served as contrast agents for localized radiation therapy and to induce vascular occlusion of the tumors. Freeman et al. reported in 1960 that the magnetic nanoparticles could be transported through the vascular system and concentrated in a specific part of the body with the aid of a magnetic field. Since the 1970s, the magnetic particles were used to the delivery of chemotherapeutics. In 1976, Zimmermann and Pilwat applied magnetic erythrocytes for the delivery of cytotoxic drugs. And, Widder et al. proposed the targeting of magnetic albumin microspheres encapsulating an anticancer drug (doxorubicin) in animal models. In the 1980s, several studies reported his strategy to deliver different drugs using magnetic microcapsules and microspheres. However, all these initial researches were microsized. Magnetic NPs were used for the first time in animal studies by Lübke et al.. In 1996, the first Phase I clinical trial was carried out by the same group in patients with advanced and unsuccessfully pretreated cancers using magnetic NPs loaded with epirubicin. However, in that first trial, more than 50 % of NPs were accumulated in the liver. Since that, a number of groups have designed and fabricated magnetic vectors and shown potential applications. Different start-ups manufacture magnetic micro- or nano- particles, which used in MRI, hyperthermia, cell sorting and targeting, bioseparation, sensing, enzyme immobilization,

immunoassays, and gene transfection and detection systems.

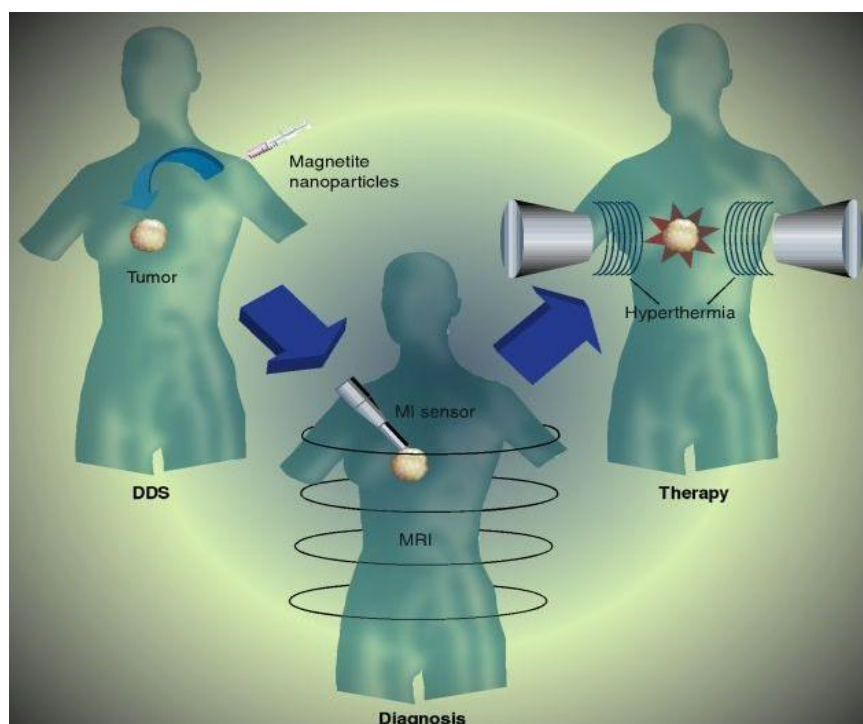


Figure 2.6 Magnetic nanoparticles for biomedical applications: (a) drug delivery, (b) diagnosis, and (c) therapy by hyperthermia. Copyright 2009, Nanomedicine, Future Medicine Ltd.

Recently, Chemicell GmbH currently commercializes TargetMAG-doxorubicin NPs involving a multidomain magnetite core and a cross-linked starch matrix with terminal cations that can be reversibly exchanged by the positively charged doxorubicin. The particles have a hydrodynamic diameter of 50 nm and are coated with 3 mg/ml doxorubicin. These NPs loaded with mitoxantrone have already been used in animal models. Chemicell also commercializes FluidMAG® for drug delivery applications. Magnetic NP hydro-gel (MagNaGel®) from Alnis Biosciences, Inc. is a material comprising chemotherapeutic agents, Fe oxide colloids, and targeting ligands. In summary, a drug or therapeutic agents with magnetic targeting are bound to a magnetic compound, introduced in the body, and then concentrated in the target area by means of a magnetic field. Depending on the application, the magnetic vectors then release the drug or therapeutic agents or give rise to a local effect (irradiation

from radioactive microspheres or hyperthermia with magnetic NPs). Drug release can be achieved by simple diffusion or changes in physiological conditions such as pH or temperature. The drug release can also be triggered by an external magnetic field.

2.4.1 Synthesis of magnetic nanoparticles

The synthesis of iron oxide NPs has been received an great attention by chemists and material scientists for nearly the last half a century. Early studies have developed a number of methods, such as physical mechanogrinding, gas phase vapor deposition, sol-gel process, and coprecipitation of ferrous and ferric salts. Recently, in the synthesis of highly uniform semiconductor quantum dots and metal oxide nanoparticles in the mid- 1990s (involving high-temperature organometallic routes) opened up new efficient synthetic routes to produce monodispersed nanoparticles. For biomedical applications, the two most common aqueous syntheses of iron oxide nanoparticles are alkaline coprecipitation and microemulsion-based precipitation/oxidation of ferrous and ferric salts (Fe^{+2} and Fe^{+3}). The coprecipitation techniques have continually been refined to yield small magnetic cores typically less than 20 nm. However, the synthesis of small monodisperse NPs is hindered by the inability to precisely control the core size. This is further compounded by the use of surface coatings which introduce large hydrodynamic size variability. Briefly, iron salts are coprecipitated under aqueous conditions with a strong base to yield the magnetic NPs which can be either complexed with surface coatings in a one-pot fashion or after purification and dispersion in a multistep procedure. Common surface coatings include phospholipids, polysaccharides such as dextran, which can be further cross-linked on the surface of magnetic NPs to produce cross-linked iron oxide (CLIO), and polymers such as PEG, polyvinyl alcohol (PVA), and poly-lactic-co-glycolic acid (PLGAs),^[60] which can be non-specifically adsorbed or

grafted onto the NP surface to produce biomedically relevant aqueous-based magnetic NPs. Although it is difficult to achieve control of NP size with nanometer precision and crystallinity with high fidelity via the aqueous based synthesis, magnetic NPs have been widely used as MRI contrast agents, bioseparation agents, and drug delivery vectors.^[61] Despite these achievements, the polydispersity and lower magnetization attributed to the large hydrodynamic size and small core may preclude such NPs from being used in certain biomedical assays which necessitate NP uniformity or thin surface coating.

A significant evolutionary in the control over size and properties of magnetic NPs occurred with movement away from low-temperature hydrolytic synthesis techniques toward organometallic procedures carried out at higher temperatures. Thermal decomposition of iron pentacarbonyl in a dilute solution of functional polymers in organic solvent at relatively elevated temperatures ($\sim 150^\circ\text{C}$) was employed by Griffiths and coworkers in 1979 to obtain single domain (10–20 nm) and single domain superparamagnetic (< 10 nm) colloidal Fe and Feoxide.^[62] Bawendi and coworkers proposed metal–alkyl precursors, surface coordinating ligands, and high-boiling point solvents for the high quality and efficient elevated-temperature organic-phase synthesis of semiconductor nanocrystals.^[62–67] Importantly, these techniques have demonstrated well-controlled size, high monodispersity, and enhanced magnetic properties. Major improvements of this approach by Hyeon et al. utilized iron pentacarbonyl precursors and oleic acid as the surfactant for the synthesis of maghemite NPs,^[68] followed by additional optimization wherein the large-scale magnetic NP synthesis with 1-nm size control was demonstrated^[69] (**Figure 2.7**). At this point, the synthesis of uniform magnetic NPs is readily obtainable for sizes ranging from 5 to 30 nm in diameter; however, further improvements are yet to be made for the synthesis of larger magnetic NPs by organometallic routes.

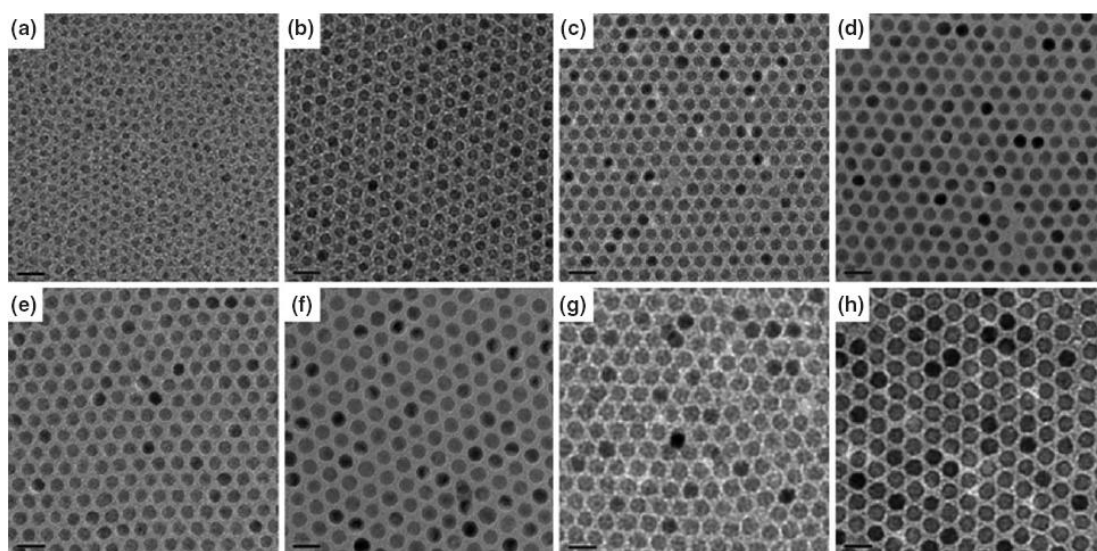


Figure 2.7 TEM micrographs of iron oxide NPs with diameters of (a) 6 nm, (b) 7 nm, (c) 8 nm, (d) 9 nm, (e) 10 nm, (f) 11 nm, (g) 12 nm, (h) 13 nm. The organic phase high-temperature synthetic route enables precise control of NP size.²⁹ Copyright 2005, Wiley-VCH Verlag GmbH & Co. KGaA

The thermolytic method is attributed to the versatility of the organic solvent at dissolving various precursors and surfactants that aid in controlling nucleation and growth.^[70-72] Reproducible large-scale synthesis is readily achievable when parameters such as choice of surfactants and precursors, heating rate, and solvent (boiling point) are carefully controlled. For example, changing precursor to surfactant ratio and/or solvent boiling point have been shown to tune NP size.^[68,69] Casula and Alivisatos reported that the nucleation is considerably slower than the subsequent growth of NPs, temporally separating the two phases, indicating that the reaction rate can be controlled by the nucleation rate.^[73] A systematic study of the reaction kinetics of magnetic NPs by Hyeon et al. has shown that the ‘heating up’ method follows a similar size distribution control mechanism as the ‘hot injection’ QD synthesis technique, wherein a sudden burst in nucleation is succeeded by rapid size distribution narrowing and a high growth rate.^[74]

2.4.2 Biocompatibility of magnetic nanoparticles

In comparison to other heavy metal-based NPs, a main advantage of iron oxide NPs for clinical applications is their natural integration into tissue physiology. Iron and its oxides are metabolized, stored and transported through human tissues by proteins including ferritin, transferritin, hemosiderin, and others, such that the resultant iron is incorporated into the iron pool.^[75] Although magnetic vectors composed of iron oxide are overall well-tolerated *in vivo*, the differences of NPs in size, composition, and surface coatings can impact physiological response. There are two clinically iron oxide MRI contrast agents, Combidex (Advanced Magnetix, employed to differentiate between cancerous and normal lymph nodes) and Feridex (Advanced Magnetix, employed to detect and evaluate liver lesions), which are physiologically benign, but have significantly different degradation profiles *in vivo*. Within 3 days post-injection (intracerebral inoculation or intraarterially after osmotic blood–brain barrier disruption), Combidex breaks down in the intracranial tissue and after 1 week becomes undetectable, whereas 4 weeks after administration, Feridex continues to remain visible by MR imaging.^[76] In contrast, MION (monocrystalline iron oxide NP) employed in the same study was demonstrated to induce seizures in rats and may not readily degrade in the brain due to a lack of response from local macrophages and reactive astrocytes. In light of these findings, it exhibits that not only the chemical composition, but the physical size and surface chemistry are important factors in determining biodistribution and physiological response.

The reticuloendothelial system (RES) which is comprised of the cells in the spleen, liver, and lymphatic system acts as a defensive system to remove foreign particulates or substances from the blood stream. Non-specific protein binding on NP surfaces can lead to changes in overall size and consequent uptake of NPs by the RES system. This results cause a significant hurdle to bypass for *in vivo* studies due to sequestration and loss of NPs. The standard strategy toward evading RES detection

involves the use of nonfouling coatings such as poly(ethyleneglycol) (PEG) and dextran (polysaccharide) to produce ‘stealthlike’ particles with reduced non-specific binding of plasma proteins and improved circulation half-lives. For example, Weissleder et al. have reported dextran coatings and have observed blood half-lives of greater than 24 h in humans.^[77] An alternative approach has applied zwitterionic surface coatings to NPs (small molecule ligands) and has demonstrated a greatly improved ability to avoid non-specific plasma protein adsorption and RES sequestration.^[78] Furthermore, this work displayed that by successfully avoiding RES sequestration, NPs with hydrodynamic radius smaller than 5.5 nm were able to be eliminated from the body through the urinary tract. However, there is no perfect approach to avoid the RES system has been found, and thus, this area remains highly investigated. It is likely that the surface engineering of compact NPs such that they appear to be ‘natural’ to the body can be future solutions to the RES problem. This may be possible by developing NP surfaces that mimic natural biomolecules such as lipids and glycoproteins.

2.4.3 Magnetic nanoparticles for high performance magnetic resonance imaging

For the past two decades, synthetic iron oxide nanoparticles such as dextran-coated superparamagnetic iron oxide (SPIO) and related nanoparticles (e.g. crosslinked iron oxide (CLIO), Feridex, Resovist, and Combidex) have served as contrast-enhancing probes for MRI.^[79,80] These magnetic nanoparticles are now clinically used for improving anatomical magnetic resonance (MR) contrast^[81,82] and have also been used in molecular imaging.^[83,84] To enhance MR contrast effects and to functionalize versatile surface groups for advanced molecular imaging, researchers have been developing next generation magnetic NPs probes. For example, rapid advances in non-hydrolytic thermal-decomposition synthetic methods for preparing

monodispersed magnetic NPs have offer to synthetically control the important features of these probes, such as size, magnetic dopants, magneto-crystalline phases, and surface states,^[85-92] resulting in the discovery of designed functional magnetic NPs. These innovative nanoparticle probes exhibit superior magnetism and MR contrast effects which have been shown to be better than that of conventional MR contrast agents.^[93-98] For instance, the two most representative types of iron oxide NPs and metal alloy MNPs. As illustrated in **Figure 2.8**, there are four factors to influence the MR contrast behaviors, (1) MR contrast enhancement by control of the magnetic core, (2) design of the ligand shell to achieve high colloidal stability and biocompatibility, (3) molecular and cellular targeting capabilities, and (4) MR imaging of cancer, angiogenesis, cell trafficking, and therapy.

The size of magnetic NPs is one important parameter for the MR contrast enhancement effect. For the bulk materials, the magnetic spins are aligned parallel to the external magnetic field. However, in the nanoscale size, surface spins tend to be slightly tilted to cause a magnetically disordered spin-glass-like surface layer (**Figure 2.9a**).^[99] Such surface spin-canting effects of MNPs influence their magnetic moments and MR contrast-enhancement effects. This effect is size dependent and is well demonstrated in the case of magnetism-engineered iron oxide (MEIO, Fe_3O_4) nanoparticles, where the variation of their size from 4 nm to 6 nm, 9 nm, and 12 nm results in massmagnetization values of 25, 43, 80, and 101 emu per gram Fe, respectively (**Figure 2.9b,c**).^[93] As the nanoparticle size decreases, the surface effect becomes more pronounced and is reflected in the reduced net magnetic moment. Such sizedependent magnetism directly influences the MR enhancement effect. The relaxivity coefficient (r_2) gradually increases from approximately 78 to 106, 130, and to 218 $\text{mm}^1 \text{ s}^{-1}$ for 4 nm, 6 nm, 9 nm, and 12 nm sized nanoparticles, respectively, which is shown by the MR contrast changing from light gray to black (or from red to

blue in color-coded images; (Figure 2.9d,e).

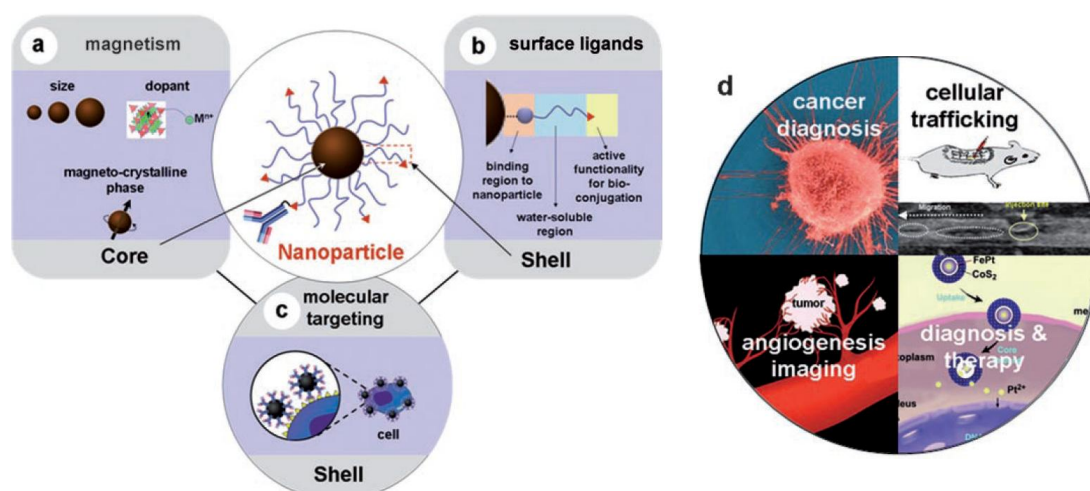


Figure 2.8 Functionalized MNPs for molecular and cellular magnetic resonance imaging (MRI). a) Controlling the magnetism of the nanoparticle core, b) tailoring the surface ligands of the nanoparticle shell, and c) the molecular targeting capability of biomolecule-conjugated nanoparticles. d) High performance utilizations of nanoparticles for molecular and cellular MRI.

Another example of MR contrast agents is metal alloys MNPs, such as FeCo and FePt.^[92,100,101] For these system, all the magnetic spins align parallel to the external magnetic field because they typically have higher magnetic moments than those of ferrimagnetic nanoparticles. Therefore, metal-alloy MNPs can be excellent candidates for MR contrast enhancement. One successful demonstration has been reported 7 nm sized FeCo MNPs passivated with a graphite shell (Figure 2.9f).^[95] Coating of the MNPs with phospholipid–poly(ethylene glycol) (PL-PEG) endows them with colloidal stability in aqueous media. These FeCo MNPs have an exceptionally high magnetization value of 215 emu per gram metal. The coefficient r_2 of FeCo MNPs has been determined to be $644 \text{ mM}^{-1}\text{s}^{-1}$. It is much larger than that of conventional iron oxide contrast agents, such as Feridex (ca. $10 \text{ mM}^{-1}\text{s}^{-1}$).^[95]

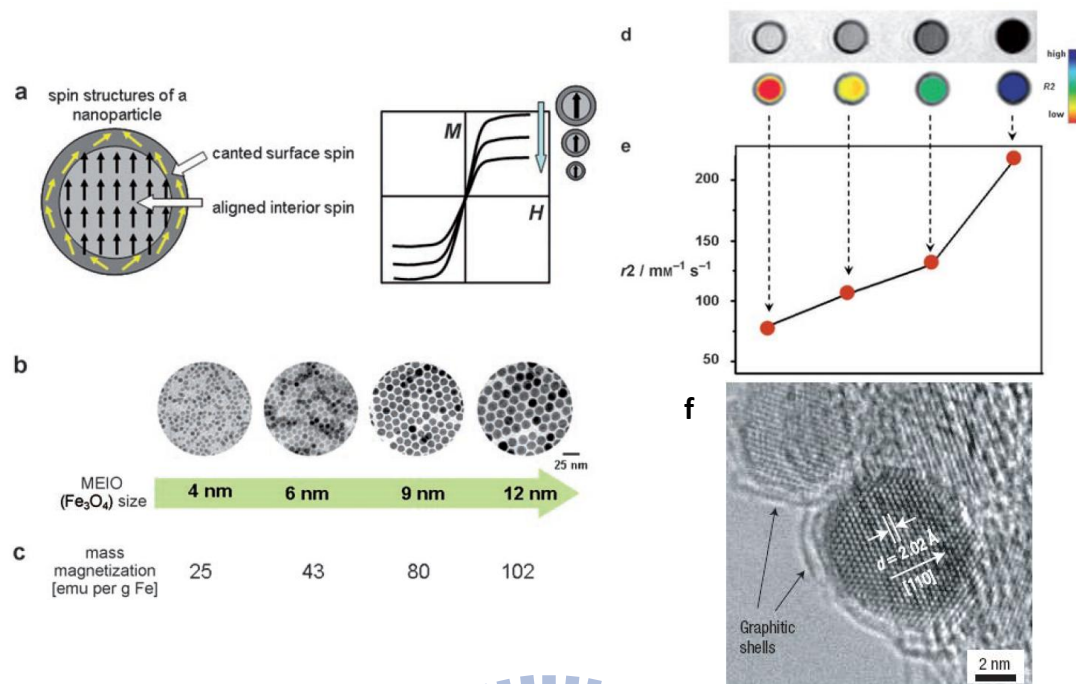


Figure 2.9 (a) Surface spin canting effect of a nanoparticle upon magnetization (M magnetic moment, H external magnetic field). (b–e) Nanoscale size effects of Fe_3O_4 nanoparticles on magnetism and MR contrast effects. (b) Transmission electron microscopic (TEM) images of 4, 6, 9, and 12 nm of iron oxide nanoparticles. (c) Mass magnetization values, (d) T2-weighted MR images (top: black and white, bottom: color), and (e) relaxivity coefficient r_2 of the nanoparticles presented in (a). (f) FeCo magnetism-controlled metal-alloy MNPs. These FeCo MNPs have an exceptionally high magnetization value of 215 emu per gram metal. Copyright 2005, American Chemical Society. 2006, Nature publisher group.

2.4.4 Magnetic nanoparticles for *in vivo* molecular imaging

Functionalized magnetic nanoparticles (NPs) are receiving a great attention in the field of *in vivo* imaging owing to their molecular information, such as the presence and relative abundance of biomarkers, preparing by magnetic NPs functionalized with a myriad of available targeting ligands. Many studies using this concept have been successfully fabricated with the variations of magnetic iron oxide NPs possessing functional ligands. Specific-site targeting can enhance the specific accumulation and intracellular uptake, which are required for tumor therapy or sufficient contrast enhancement. For example, the transferrin and folate receptors have been

extensively used as *in vivo* and *in vitro* targets for transferrin-^[102,103] and folate-labeled magnetic NPs to image cancers.^[104,105]

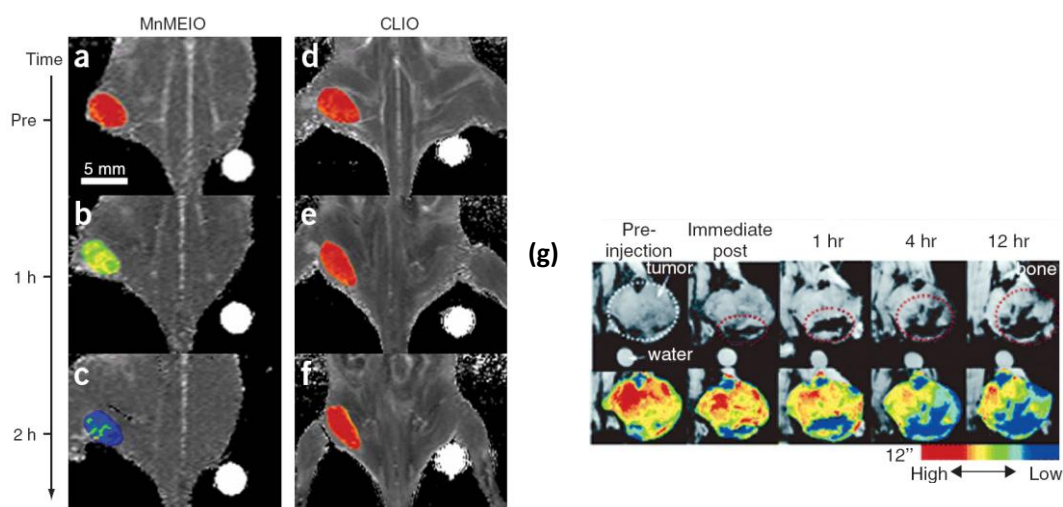


Figure 2.10 (a-f) Color maps of T2-weighted MR images of a mouse implanted with the cancer cell at different time points after injection of MnFe₂O₄–Herceptin conjugates or CLIO–Herceptin conjugates. In (a–c), gradual color changes at the tumor site, from red (low R2) to blue (high R2), indicate progressive targeting by MnFe₂O₄–Herceptin conjugates.¹³⁰ (g) T2*-weighted *in vivo* MR images of cancer cells implanted in mouse model imaged at 9.4 T. Color-coded MR images to further delineate MR signal changes. ¹⁴³ (Reprinted with permission from Ref 143. Copyright 2005, American Chemical Society. 2006, Macmillan Publishers Ltd.

The monodisperse magnetic NPs have revealed exciting new discoveries in the field of *in vivo* molecular imaging due to their uniform and special characteristics. This can be attributed to their improved magnetic relaxivities and controlled hydrodynamic size precisely, which translate into increased MR contrast sensitivity and more uniform biodistribution profiles in comparison with the non-optimal physical attributes of hydrolytically synthesized iron oxide NPs. For example, highly uniform MnFe₂O₄ NPs conjugated to anti-Her-2 receptor antibodies were recently developed by Cheon et al.^[106] These magnetic NPs with engineered magnetic properties demonstrated approximately four times stronger relaxivity and enhanced

contrast ($T_2 = 34\%$ for $MnFe_2O_4$) in comparison to CLIO ($T_2 < 5\%$). These enhancements of magnetic properties improve the potential for the sensitive detection of small or early-stage tumors (**Figure 2.10a-f**).

In a previous study, the same group utilized 9-nm Fe_3O_4 NPs synthesized via the high-temperature organic-phase route and performed ligand exchange with dimercaptosuccinic acid (DMSA) to yield highquality water-soluble iron oxide NPs.^[107] This ligand exhibits two distinct advantages. First, the disulfide crosslinking of surface-bound DMSA enhances NP stability in buffered solutions and in the pH range between 6 and 10, conditions crucial for biological applications. Second, the small molecular weight of DMSA enables NPs to exhibit a smaller hydrodynamic radius than traditional high-molecular-weight dextran systems (MW = 10,000–100,000). For *in vivo* investigations, probe size is a critical factor as biostability, diffusion, nonspecific binding, and RES sequestration can be negatively affected by an increase in size, while tumor penetration depth can be improved by a decrease in size. Applying anti-Herceptin antibodies directly conjugated to the magnetic NPs, it exhibited the new generation of magnetic NP *in vivo* probes by targeted HER2/neu receptor (overexpressed in breast cancer cells). Immediately following injection, magnetic NP-Herceptin probes were detected to accumulate *in vivo* at the static tumor site with T_2 signal drop of $\sim 10\%$ after 5 min and $\sim 20\%$ after 4 h, which is a significant increase. It was noted that the time-dependent MR signal change was indicative of the heterogeneous nature of the intratumoral vasculature and delineated the denser tumor core with reduced vasculature from the ‘leaky’ neovasculatures of the tumor periphery (**Figure 2.10g**).

2.4.5 Surface modification of magnetic nanoparticles

Before the oil-soluble magnetic nanoparticles (NPs) are used in biological

applications, their native hydrophobic surface ligands must be modified in order to make them in aqueous solutions. Based on this concept, surface ligands of magnetic NPs like those of QDs and gold NPs enables the surface-engineering methods previously developed to be easily adopted for magnetic NPs. Generally, as shown in **Figure 2.11**, there are three approaches to modify hydrophobic NPs to lead them soluble in aqueous biological buffers.

In the first method of ligand exchange, hydrophobic surface ligands is replaced with amphiphilic ligands containing head groups that bind the magnetic NP surface and hydrophilic tails that interact with aqueous solvent.^[108] There are wide available of compatible ligands which can be applied in this convenient water-solubilization procedures.^[109] However, a key drawback of this procedure is the potential for desorption of labile ligands from the magnetic NP surface as ligand adsorption is often reversible. Incomplete surface coverage probably causes NP aggregation, inefficient conjugation with biomolecules, and desorption of a bioconjugated surface ligand. The unstable properties can reduce overall biological functionality of the magnetic NP.

Another solubilization strategy in which the native hydrophobic ligands are retained on the magnetic NP surface is performed through the adsorption of amphiphilic polymers onto the NP. This general procedure has been used for hydrophobic nanoparticles encapsulation with various polymers including polyacrylic acid,⁸⁰ PEG-derivatized phospholipids,⁸¹ block copolymers,^[110] and amphiphilic polyanhydrides.^[111] Additionally, biodegradable amphiphilic polymers originally designed for drug delivery applications are used to encapsulated magnetic NPs for in vivo applications since each component of the construct is biocompatible [core material ($\text{Fe}_3\text{O}_4/\text{Fe}_2\text{O}_3$), surface ligands (oleic acid), and polymer coating (polyethylacrylic-polypropylacrylic acid)]. Amphiphilic polymers used for

encapsulation contain hydrophobic segments (mostly hydrocarbons) that intercalate and interact with the alkyl tails of the native magnetic NP surface ligands by the multivalency effect, and the hydrophilic segments (PEG or multiple charged groups) cause the overall magnetic NP–polymer constructs soluble in aqueous buffer.

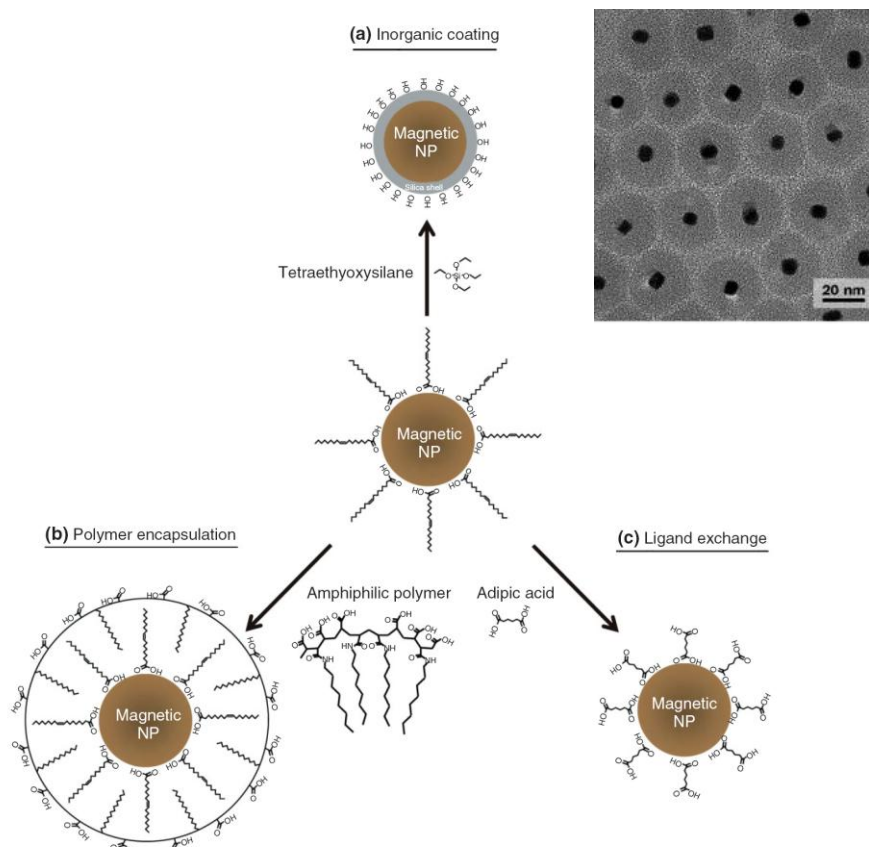


Figure 2.11 Three types of surface modification schemes for magnetic nanoparticles. (a) Inorganic surface coating with an amorphous silica shell. (b) Amphiphilic polymer coating on the magnetic nanoparticles. (c) Ligand exchange is to replace native surface ligands. These routes exhibit polar or charged functional groups onto the outer surface of the NP for water solubility. [75] Copyright 2009, John Wiley & Sons, Inc.

The third method to modify the surface of magnetic NPs is the fabrication of an inorganic shell, typically consisting of silica or gold, by one of two general schemes: precipitation and reaction at the NP surface or deposition of preformed colloids onto the NP surface.^[112] The formation of silica shells involves the base-catalyzed hydrolysis of the alkoxides of tetraethoxysilane (TEOS) followed by condensation of

the resulting silanol groups. The benefits of silica include its biocompatibility, ease of bioconjugation, and biostability in vivo. Xia and coworkers employed a sol–gel approach and demonstrated the direct surface coating of magnetic NPs with amorphous silica through the hydrolysis and condensation of TEOS with a concentration-dependent shell thickness ranging from 2 to 100 nm.^[113]

2.5 Magnetic Nano-Carriers for drug delivery and therapy

Organic materials (polymeric NPs, liposomes, micelles) have been investigated as drug delivery carriers using passive targeting, active targeting with a recognition moiety, or active targeting by a physical stimulus (e.g. magnetism in magnetoliposomes). However, these organic systems still exhibit limited chemical and mechanic stability, swelling, susceptibility to microbiological attack, inadequate control over the drug release rate, and high cost.^[114] On the other hand, polymer NPs display the problem of high polydispersity. Synthesis produces particles with a broad size distribution and irregular branching, which could lead to heterogeneous pharmacological properties. The preparation of dendritic polymers that circulate in the blood long enough to accumulate at target sites but that can also be removed from the body at a reasonable rate to avoid long-term accumulation also remains a challenge. Passive targeting using drug-conjugated dendrimers and dendritic polymers has been widely studied, mainly using the EPR effect. Therapies based on active targeting, such as antibody-conjugated dendrimers, constitute a promising alternative in view of the potential of antibodies for selective targeting.^[115] Because of the disadvantages of organic NPs for drug delivery, inorganic vectors constitute an interesting option and are the subject of intense research.

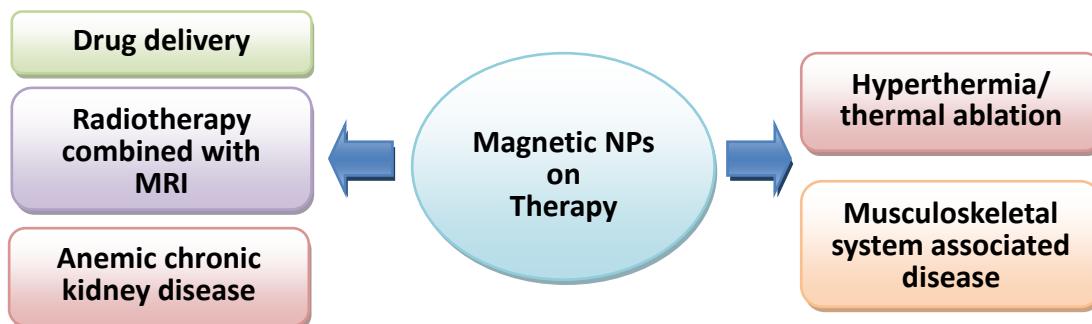


Figure 2.12 Biomedical application of magnetic nanoparticles.

The main advantages of magnetic (organic or inorganic) NPs are that they can be: (i) visualized (superparamagnetic NPs are used in MRI); (ii) guided or held in place by means of a magnetic field; and (iii) heated in a magnetic field to trigger drug release or to produce hyperthermia/ablation of tissue as shown in **Figure 2.12**. It is important to point out that the latter capability is not restricted to magnetic NPs, but also to other particles such as gold NPs or CNTs capable of absorbing near-infrared, microwave, and ultrasound radiation. Depending on the synthesis procedure, magnetic NPs or magnetic capsules can be obtained. We refer to NPs when the drug is covalently attached to the surface or entrapped or adsorbed within the pores of the magnetic carrier (polymer or mesoporous silica). Nanocapsules designate magnetic vesicular systems where the drug is confined to an aqueous or oily cavity, usually prepared by the reverse micelle procedure, and surrounded by an organic membrane (magnetoliposomes) or encapsulated within a hollow inorganic capsule.^[114]

The surface chemistry is especially important to avoid the action of the reticuloendothelial system (RES), which is part of the immune system, and increase the half-life in the blood stream. Coating the NPs with a neutral and hydrophilic compound such as polyethylene glycol (PEG), polysaccharides, or dysopsonins (HSA), can increase the circulatory half-life from minutes to hours or days. Another

possibility is to reduce the particle size; however, despite all efforts, complete evasion of the RES does not seem feasible^[116] and unwanted migration to other areas in the body could cause toxicological problems. In addition to cancer treatment, magnetic NPs can also be used in anemic chronic kidney disease and disorders associated with the musculoskeletal system (i.e. local inflammatory processes, side effects). For those disorders, iron oxide NPs together with external magnetic fields, seem a suitable alternative for drug delivery to inflammatory sites by maintaining appropriate local concentrations while reducing overall dosage and side effects.^[117]

2.5.1 Amphiphilic micellar coatings

Oil-soluble magnetic NPs can be transferred to aqueous media by over coating them with amphiphilic ligands having both hydrophobic and hydrophilic regions. The process results in the formation of polymeric micelles. The strategy, first developed for quantum dots,^[118,119] has been successfully extended to magnetic NPs. The addition of amphiphilic ligands, such as tetradecylphosphonate and PEG-2-tetradecylether to NPs induces the formation micelles around the NPs^[120] with the hydrophilic PEG end of the ligand contributing to the water solubility. Similarly, water-soluble iron oxide nanoparticles are prepared through using a micellar coating of either amphiphilic PEG–phospholipids^[121] or poly(maleic anhydride-alt-1-octadecene)-PEG block copolymers.^[122] Encapsulation of several magnetic NPs into each amphiphilic micelle is also possible. Owing to hydrophobic interactions, multiple MNPs are confined in the micelles formed by using the amphiphilic polystyrene–poly(acrylic acid) (PS-PAA) block copolymer (**Figure 2.13a**).^[123] Similarly, evaporation of organic solvents containing polylactide– PEG block copolymers generate micelles of approximately 50 nm size with a hydrophobic interior containing MNPs and a hydrophilic shell (**Figure 2.13b**).^[96]

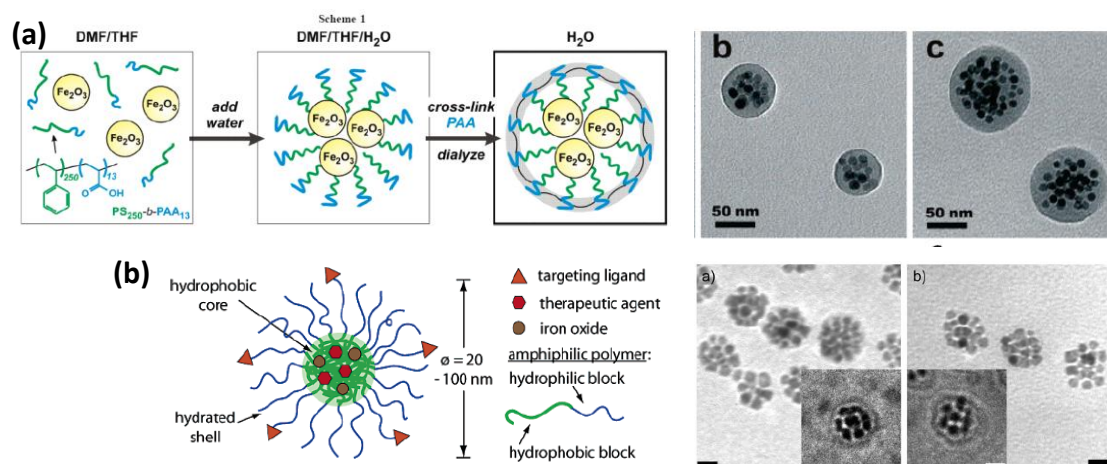


Figure 2.13 (a) Synthesis scheme and TEM image of polystyrene–poly(acrylic acid) (PSPAA) block copolymer micelles encapsulating several MNPs. (b) Schematic and TEM image of poly(d,l-lactide)–PEG block copolymer micelles encapsulating several MNPs and a therapeutic agent. Copyright 2005, American Chemical Society.[123,96]

2.5.2 Magnetic nanoparticles encapsulated in polymer for small molecules drug delivery

Recently, the application of multifunctional particles containing magnetic NPs for drug delivery applications has been the employment to provide imaging functionality, cell-specific targeting, and controlled drug release.^[124] Although it offers an extensive body of literature on the incorporation of iron oxide NPs into microbeads,^[125,126] the development of multifunctional nanocarriers has only been achieved recently for drug delivery applications. Magnetic NP-based drug delivery vehicles provide MRI contrast enhancement as well as the ability to be guided physically by a magnetic field gradient for enhanced and localized drug delivery.^[127-129] A novel multifunctional polymeric micelle was developed by Nasongkla et al. to specifically target and deliver doxorubicin (DOXO) to cancer cells with up-regulated $\alpha\beta3$ integrin expression via cRGD ligands.^[96] By means of a solvent-evaporation method, monodisperse 8-nm SPIOs were co-loaded with DOXO into an amphiphilic block copolymer micelle consisting of maleimide-terminated

PEGblock-PLA and methoxy-terminated PEG-block-PLA. The overall size of the multifunctional constructs was approximately 45 nm as confirmed by TEM and dynamic light scattering. Control over maleimide surface density ranging from 0 to 16% of PEG chains was achieved by adjusting the ratio of the two block copolymers. Importantly, pH-dependent release of DOXO was achieved because of the ionizable amine groups in DOXO and the amorphous nature of PLA, such that higher concentrations of DOXO were found in the cell nuclei compared to other studies utilizing more crystalline poly(ϵ -caprolactone).

Additionally, iron oxide NPs to micelle loading density was as high as 50% by weight, which enabled a significant improvement in the T2 relaxivity allowing for *in vitro* detection of nanomolar concentrations of multifunctional micelles. In cells, micelles with 16% cRGD surface density enhanced the MR image contrast (cells appeared darker due to the accelerated decay of the T2 signal by magnetic NPs) to a greater degree than micelles lacking the targeting ligands. It should be noted that control experiments indicated that at higher micelle concentrations, nonspecific uptake was observed. The presence of 16% cRGD in the micelles had an approximately 2.5-fold increase in cell uptake and 7-fold decrease in cell growth over non-cRGD containing micelles. Along these lines, Hyeon et al. recently designed a multifunctional PLGA nanostructure incorporating 15-nm monodisperse SPIOs for MR imaging, 3-nm QDs for fluorescence visualization, and DOXO as a therapeutic agent.^[130] The 100–200 nm multifunctional NPs were formed by an oil-in-water emulsion using a nonionic amphiphilic surfactant under sonication followed by solvent evaporation. For cancer specific targeting, poly(l-lysine)- poly(ethylene glycol)-folate (PLL-PEG-FOL) ligands were electrostatically adsorbed onto the NPs, increasing the zeta potential from -32 to $+22$ mV. Nanoconstructs lacking folate

ligands and DOXO were shown to have little effect on cell viability, whereas incorporation of both components into the NPs lowered cell viability to approximately 70%. To improve therapeutic efficacy, a synergistic targeting strategy was facilitated by the incorporated SPIOs, wherein the nanoconstructs were manipulated by a magnetic field and concentrated near cancer cells *in vitro*, which correspondingly further decreased cell viability from ~70 to 40% (**Figure 2.14**).

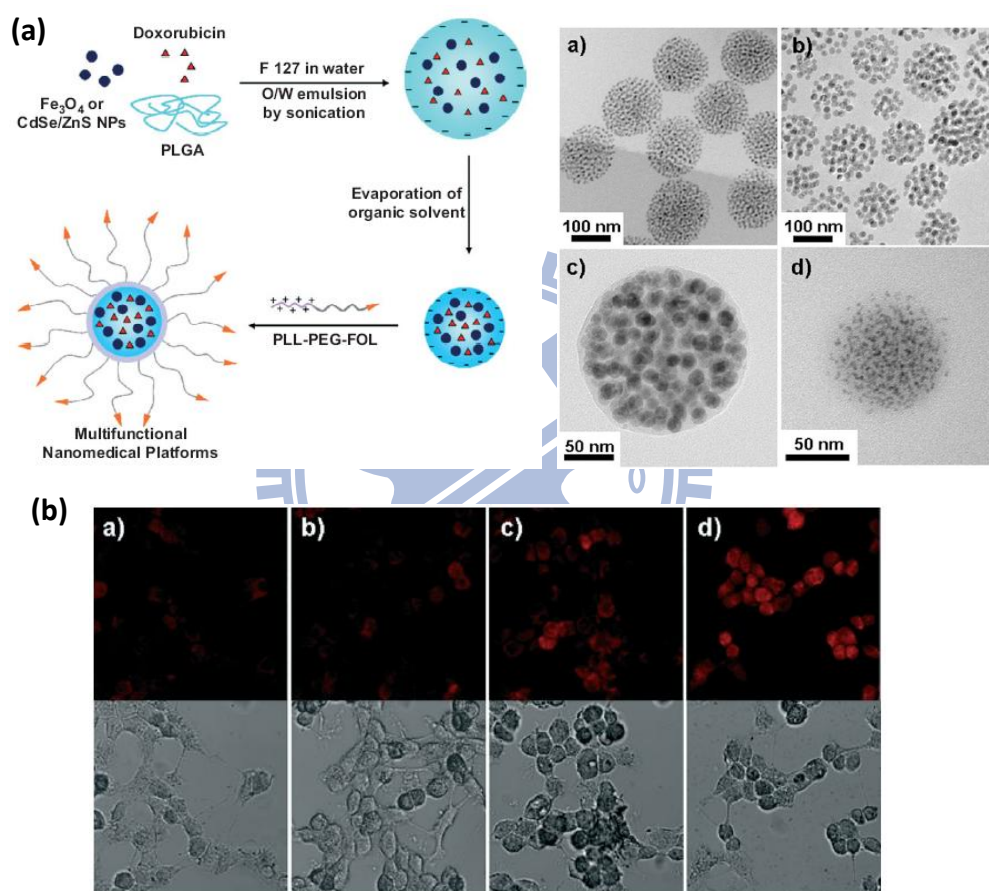


Figure 2.14 (a) Synthetic procedure for the multifunctional polymer nanoparticles. TEM images of nanoparticles. (b) CLSM of DOXO fluorescence and optical images in KB cells treated with a) naked PLGA(MNP/DOXO), b) PLGA(MNP/DOXO)-PEG, c) PLGA(MNP/DOXO)-FOL nanoparticles, and d) PLGA(MNP/DOXO)-FOL nanoparticles under an external magnetic field, respectively. Copyright 2008, WILEY-VCH Verlag GmbH & Co. KGaA, Weinheim.[130]

2.5.3 Magnetic nanoparticles encapsulated in silica for drug delivery

The multifunctional NP was investigated by using mesoporous silica.^[131] In

Figure 2.15, this work presented the ability to simultaneously image (via fluorescence and MRI) and deliver water-insoluble therapeutics to tumors using multifunctional mesoporous silica-magnetic NP platforms. Hydrophobic 20-nm monodisperse iron oxide NPs were synthesized via high-temperature organic phase methods and transferred into the aqueous phase with the amphiphilic surfactant CTAB upon evaporation of the organic phase. A 100–200 nm thick mesoporous silica shell was grown around the water solubilized iron oxide NPs using TEOS within a controlled temperature range (65–80°C). Afterward, FITC dye was conjugated to the pore walls and particle surface to provide fluorescence functionality. To prevent NP aggregation during hydrophobic drug loading, surfaces were modified with trihydroxysilylpropyl methylphosphonate to inhibit interparticle hydrogenbonding between the surface silanol groups. Using a clinical MRI instrument, the aqueous NPs at a concentration of 1 mg/mL produced hypo-intense (negatively enhanced) T2-weighted MR images. It is likely that such a high NP concentration is needed to achieve MRI contrast enhancement because of the low magnetic NP loading density and the thick silica shell which reduces the interaction between magnetic NPs and water molecules. To demonstrate drug loading and deliverability, the water-insoluble anti-cancer drugs camptothecin (CPT) and paclitaxel (TXL) were utilized. UV/vis spectroscopy indicated 4% of the stored drug leached out in aqueous solution after 6 h, whereas all of the stored drug (~30 nmol per 1 mg silica NPs) were released in DMSO or methanol, suggesting slow release kinetics could be achieved in vivo. Cytotoxicity and targeted delivery were studied using pancreatic cancer cell lines PANC-1 and BxPC3, which indicated that the observed cytotoxicity was attributed to the drugs and not the silica NPs for the concentrations used. In this study, folic acid was chosen as a targeting ligand due to the over-expression of folate receptor in PANC-1 and not human foreskin fibroblast (HFF) cancer cell lines. A two-fold increase in NP uptake

was observed in PANC-1 cells due to folate modification and not in HFF, although both cell lines exhibited baseline levels of NP uptake. Cytotoxicity studies illustrated the receptor-dependent cytotoxicity effect; HFF cells treated with NPs with and without folate had similar cell survival, whereas PANC-1 cells demonstrated increased cytotoxicity with folate modified NPs. It is likely that increased magnetic NP loading density can also improve MRI sensitivity of these silica NPs. (Figure 2.15)

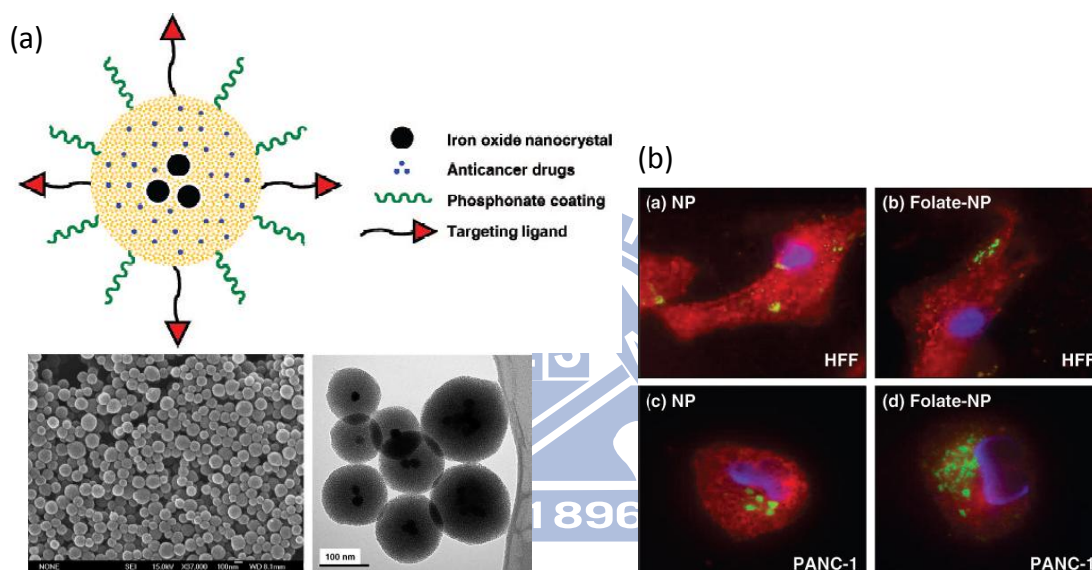


Figure 2.15 (a) Schematic illustration of multifunctional nanoparticles showing iron oxide nanocrystals encapsulated within mesoporous silica, hydrophobic anticancer drugs stored inside the pores, and surface modifications with phosphonate and folic acid targeting ligands. SEM and TEM images of the iron oxide incorporated within the mesoporous silica NPs. (b) Fluorescence microscopy images showing the effect of folic acid modification on the NPs (green fluorescence). The cell nuclei were stained with DAPI (blue fluorescence), and the membranes were stained with WGA (red fluorescence). Copyright 2008, American Chemical Society.

2.5.4 Magnetic nanoparticles for other therapy

Hybrid metal-alloy MNPs can have therapeutic capabilities in addition to MR imaging capabilities. As **Figure 2.16a** shown, when HeLa cells are treated with FePt@CoS₂ nanoparticles, cell viability is dramatically decreased.^[132] After cellular

uptake of FePt@CoS₂ nanoparticles the low pH value (ca. 5.5) of the cellular environment induces oxidation of Pt and the subsequent release of Pt²⁺ ions, which causes DNA damage and cell apoptosis. The cytotoxic effect of FePt@CoS₂ can be confirmed by changes in cell morphologies and dosedependent cell viability.

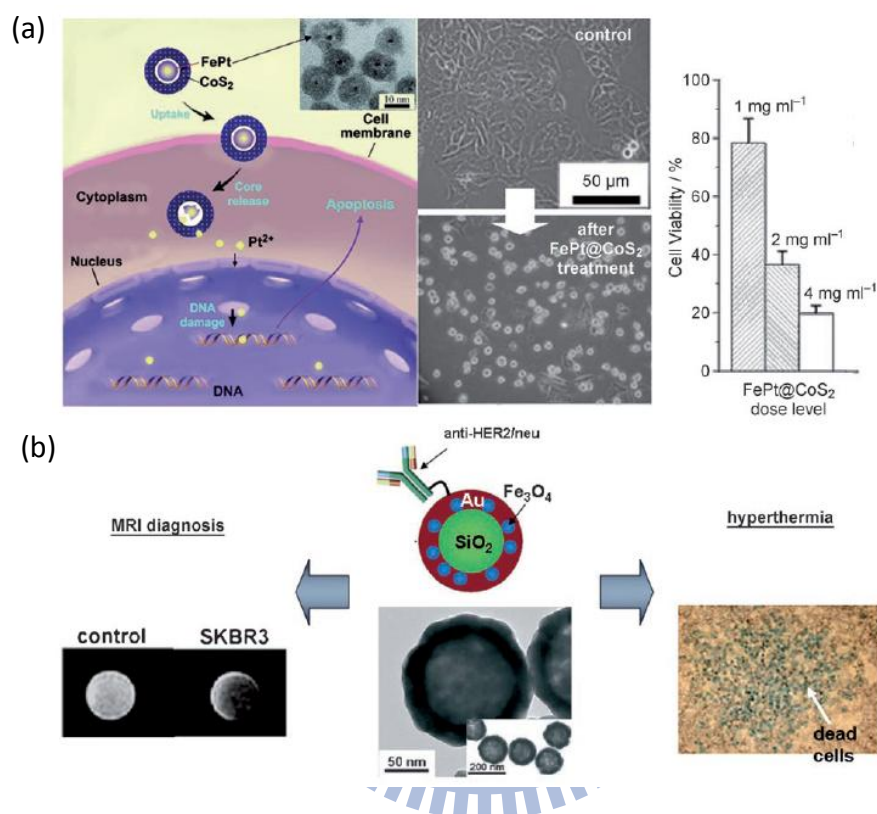


Figure 2.16 (a) Therapeutic applications of hybrid FePt@CoS₂ metal-alloy MNPs. Left: the lethal effect of the hybrid MNPs on cells. Middle: optical detection of changes in cell morphology of untreated HeLa cells (top) and the MNP-treated HeLa cells (bottom). Right: dose-dependent cell viability (from Ref. [132]), b) hybrid iron oxide nanoparticles consisting of SiO₂@Fe₃O₄@Au and anti-HER2/neu antibody for simultaneous MRI diagnosis and laser-assisted hyperthermia therapy (from Ref. [133]).

Hybrid nanoparticles of SiO₂@Fe₃O₄@Au can be used for molecular MR imaging and cancer therapy (**Figure 2.16b**). [97] After conjugation with an anti-HER2/neu antibody and subsequent treatment to breast cancer cells, a dark MR contrast is observed for the cells in the T₂-weighted MRI, indicating successful HER2/neu targeting. Upon irradiation by a continuous-wave (CW) laser, the targeted

cells are killed by hyperthermia effects arising from the Au shells.

2.5.5 Magnetically triggered release for composite membrane

Todd et al. reported that a composite membrane fabricated by multiple engineered magnetic NPs which enabled rapid, repeatable, and tunable drug delivery upon the application of an external oscillating magnetic field.^[134] As shown in Figure 2.11a, the membrane consisted of thermosensitive poly(N-isopropylacrylamide) (PNIPAM)-based nanogels (the switching entity). To facilitate effective *in vivo* triggering, the nanogels were engineered to remain swollen (i.e., in the “off” state) at physiological temperature by copolymerizing N-isopropyl-acrylamide (NIPAM) with N-isopropylmethacrylamide (NIPMAM) and acrylamide (AAm). The ratio between the monomers was chosen to maximize the size change from the swollen to the collapsed state, in order to optimize membrane pore opening when triggered. The ability of the membrane constituents and the composite membrane to trigger at physiologically relevant temperatures was evaluated using both thermal and magnetic stimuli. Nanogels in free suspension in PBS underwent a ~400 nm change in diameter upon heating from physiological temperature to 50 °C, with >90% of the total deswelling transition completed at 43 °C. Thermal triggering of the nanogel-containing membrane was tested by placing it between two chambers of a glass flow cell submerged in a water bath and evaluating the flux of sodium fluorescein across the membrane (i.e., between the chambers) as a function of time and temperature. A ~20-fold higher flux of sodium fluorescein occurred at temperatures exceeding the volume phase transition temperature (~40 °C) of the nanogels (**Figure 2.17a**). The fluorescein flux could be switched on and off over multiple thermal cycles with high reproducibility, suggesting that the nanogel phase transition inside the membrane pores was fully reversible. **Figure 2.17b** shows the

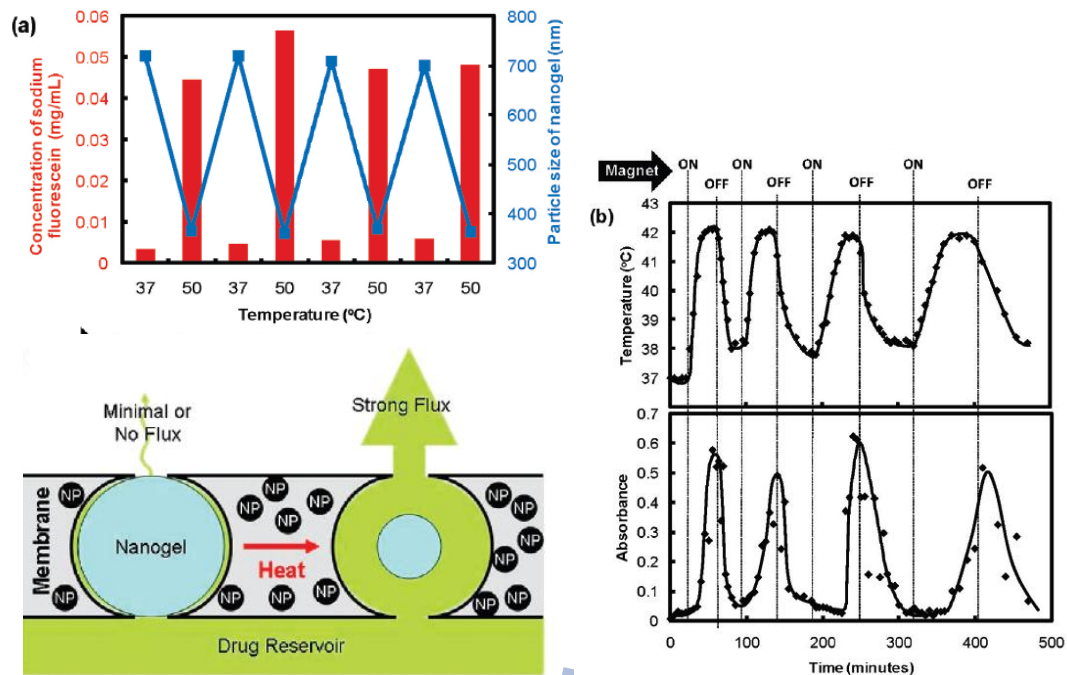


Figure 2.17 Stimulus-responsive membrane triggering in vitro: (a) temperature-triggering, comparison of nanogel particle size in suspension (blue data, right y-axis) and differential flux of sodium fluorescein through the nanogel-loaded membranes (red data, left y-axis) as a function of temperature; (b) magnetic triggering, temperature profile in the sample chamber and differential flux of sodium fluorescein out of membrane-capped devices as a function of time over four successive on/off cycles of the external magnetic field.[134]

magnetic triggering of the composite membrane. The magnetic nanoparticles embedded in the membrane heated inductively when subjected to an external oscillating magnetic field, heating previously attributed to power absorption and subsequent magnetic relaxation of single-domain nanoparticles.⁴⁷ At the applied magnetic frequency and field amplitude, the water inside the semiadiabatic flow cell heated from 37 °C to ~42 °C over the course of ~10 min, at which point the temperature reached steady state. Heat generated by magnetite induction heating was transferred to the adjacent thermosensitive nanogels, causing the nanogels to shrink and permit drug diffusion out of the device. As a result, the drug flux returned back to a near-zero value (**Figure 2.17b**). As in the thermally activated experiments, a 10- to 20-fold differential flux was observed between the “off” and “on” states. Furthermore,

multiple on-off cycles could be performed without significantly changing the permeability of the membrane in the “off” state. This reproducibility suggests that magnetically triggered physical distortion of the device⁴² plays no significant role in accelerating drug release from the membrane-based devices.

2.5.6 Magnetic-vortex microdiscs for targeted cancer-cell destruction

Dong-Hyun et al. reported that the 60-nm-thick, 1- μ m-diameter 20:80% ironnickel (permalloy) discs, coated with a 5-nm-thick layer of gold on each side, were prepared by magnetron sputtering and optical lithography. When the biofunctionalized MDs selectively bind to cancer cells, this mechanical force is efficiently transduced to the membrane and further on to subcellular components (**Fig. 2.18a**).^[135] It demonstrated that a spatially uniform and time-varying magnetic field as small as tens of oersteds, with a frequency as low as a few tens of hertz and applied for only 10 min, is sufficient to achieve cancer-cell destruction in vitro. This antineoplastic activity is the combined result of the compromised integrity of the cellular membrane and magnetic-vortex-mediated initiation of programmed cell death.

The optical images show that untreated control cells (**Fig. 2.18b,d**) with well-organized chromatin structures have a blue fluorescence, whereas treated cells (**Fig. 2.18c,e**) are stained with a dark orange-brown dye owing to chromatin fragmentation. The largest number of TUNEL-positive cells (~60%) was observed for a 90 Oe -20 Hz field. The number of apoptotic cells decreased with further increase in the field strength. We attribute this observation to increasing numbers of necrotic cells at higher field strengths owing to more severe magnetomechanically induced membrane damage. Application of lower fields (30 Oe) still results in a noticeable (~20%) population of cells undergoing apoptosis. DNA denaturation at the terminal

stage of apoptosis is known to be catalysed by calcium-dependent endonucleases²⁸, and DNA fragmentation could only barely be directly achieved by the applied mechanical forces. When an alternating magnetic field is applied the microdisc vortices shift, creating an oscillation, which transmits a mechanical force to the cell. Because reduced sensitivity of cancer cells toward apoptosis leads to inappropriate cell survival and malignant progression, selective induction of apoptosis is of great importance for the anticancer therapeutic strategies. The spin-vortex-mediated stimulus creates two dramatic effects: compromised integrity of the cellular membrane, and initiation of programmed cell death. A low-frequency field of a few tens of hertz applied for only ten minutes was sufficient to achieve ~90% cancer-cell destruction *in vitro*.

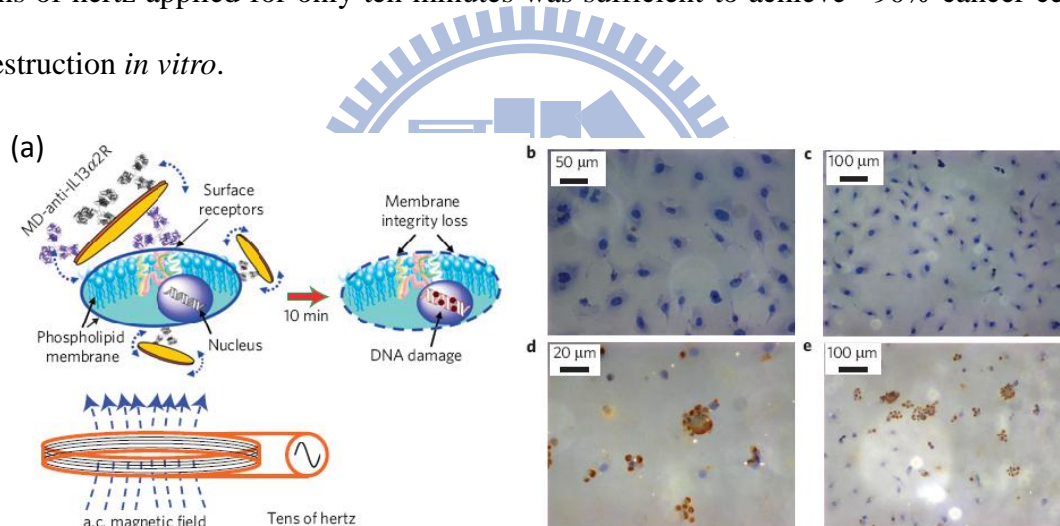
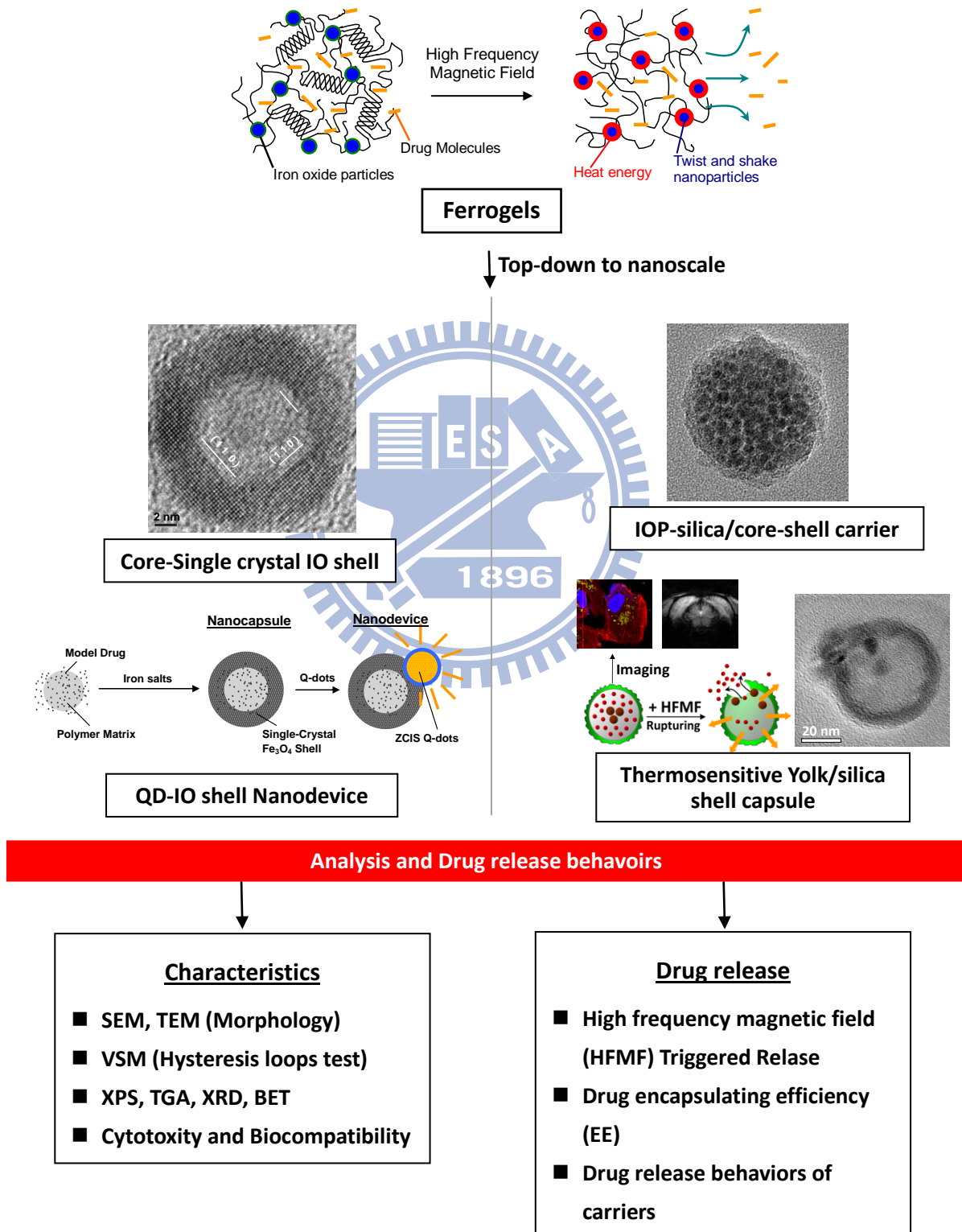


Figure 2.18 (a) The concept of targeted magnetomechanical cancer-cell destruction using disc-shaped magnetic particles possessing a spin-vortex ground state. The microdiscs are biofunctionalized with anti-human-IL13 2R antibody, specifically targeting human glioblastoma cells. When an alternating magnetic field is applied, the magnetic discs oscillate, compromising membrane integrity and initiating spin-vortex-mediated programmed cell death. (b,d) and MD-mAb-functionalized cells subjected to 20 Hz–90 Oe a.c. fields for 10 min and TUNEL stained 4 h after the magnetic-field exposure (c,e). The control cells with well-organized chromatin structures have a blue fluorescence, whereas the treated cells are stained with a dark orange–brown dye owing to chromatin fragmentation—an indication of apoptosis. Copyright 2009, Macmillan Publishers Limited.[135]

Chapter 3

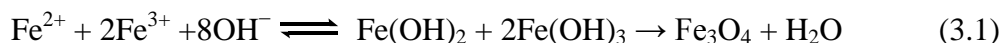
Experimental Procedures

3.1 Experiment overviews



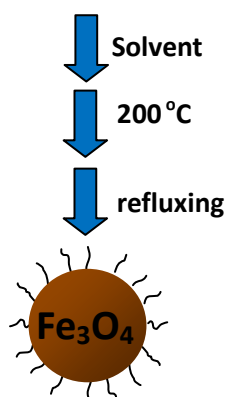
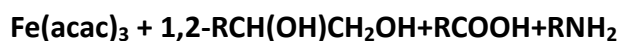
3.2 Synthesis of magnetic nanoparticles

Water-soluble iron oxide NPs: The coprecipitation technique is probably the simplest and most efficient chemical pathway to obtain magnetic particles. The traditional method of preparing iron oxide nanoparticles usually used the chemical co-precipitation of iron salts in the alkaline medium:



According to the thermodynamics of this reaction, complete precipitation of Fe₃O₄ should be expected at a pH between 8 and 14, with a molar ratio of 2:1 (Fe³⁺/Fe²⁺) in a non-oxidizing oxygen environment.

Oil-soluble iron oxide NPs: Monodisperse iron oxide nanoparticles were synthesized by a method developed by Sun et al.^[24] Briefly, 5 nm of iron oxide nanoparticles were synthesized by mixing 2 mmol Fe(acac)₃, 10 mmol 1,2-dodecanediol, 6 mmol oleic acid, 6 mmol oleylamine and 20 mL benzyl ether under a flow of nitrogen. The mixture was stirred magnetically and pre-heated to reflux (200 °C) for 60 minutes, and then, heated to 300 °C for another 3 hour under nitrogen atmosphere. The black-brown mixture was allowed to cool to room temperature and added 50 mL ethanol to precipitate. The products were collected by centrifugation at 6000 rpm for 10 minutes, and then washed with excess pure ethanol for 4 times. The product, iron oxide nanoparticles, was centrifuged to remove solvent, and redisperse into hexane.



3.3 Characterization

The morphologies of the hydrogel or nanoparticles were examined using field emission scanning electron microscopy (FE-SEM, JEOL-6500, Japan) and transmission electron microscopy (TEM, JEM-2100, Japan). For SEM analysis, the capsules were dried on 0.5×0.5 cm silicon wafers. After drying, the capsules were coated with an ultrathin metal layer using platinum sputtering to enhance the image quality. The magnetization of the NPs was measured using a superconducting quantum interference device (SQUID, MPMS-XL7) at 298 K and ± 8000 G applied magnetic field. Before SQUID analysis, the iron oxide nanoparticles and NPs were dried in a vacuum oven at 60 °C for 2 days. The relative amount of magnetic nanoparticles that were associated with the gelatin was determined using thermo-gravimetric analysis (TGA, Perkin Elmer). Samples were dried under vacuum for approximately 48 hours and analyzed in the platinum plate at a heating rate of 10 °C/min under an atmosphere of nitrogen. Differential scanning calorimetry (DSC, Perkin Elmer, Diamond DSC) with ultralow noise (<0.2 mW) was employed. Liquid samples weighing 50-70 mg were placed in a fluid-tight batch vessel and DI water was used as a reference. Cycling scans were performed with a scan rate of 5 °C /min. The high-frequency magnetic field (HFMF) was produced by a power supply with a functional generator, amplifier, and cooling water.

BET analysis (Quantachrome, NOVA 2000, USA) was conducted using N₂ gas absorption isotherms at 77K, and the pore size were calculated following the approach by Barrett, Joyner, and Halenda (BJH). The nanospheres were dried by 80°C in vacuum condition for 1 day before BET analysis, afterwards the sample was de-gassed for 150°C and 2 hours following BET analysis.

3.4 High frequency magnetic field (HFMF)

The strength of the magnetic field in these systems depends on the coils used; in this study, the coil had 8 loops with a frequency of 50 kHz and a magnetic field strength (H) of 2.5 kA/m. The temperature of the HFMF generator was controlled by cycling cooling water at 25 °C. The heating effects of magnetic nanoparticles submitted to high frequency magnetic fields (HFMF) are due to several types of loss processes (hysteresis losses, Néel and Brown relaxation), the relative contributions of which depend strongly on particle size. Nanoparticles with a core diameter less than 30 nm, as used here, are single-domain particles. Thus, their magnetization relaxation is governed by the combined effects of the rotational external (Brownian) and internal (Néel) diffusion of the particle magnetic moment.³⁹ Brown relaxation is due to thermal orientational fluctuations of the grain itself in the carrier fluid, the magnetic moment being locked onto the crystal anisotropy axis. The characteristic time τ_B for Brown relaxation is given by: $\tau_B = 3\eta V_H/kT$, where η is the viscosity of the carrier fluid, k , the Boltzmann constant, T , the temperature, and V_H , the hydrodynamic volume of the particle.^[137]

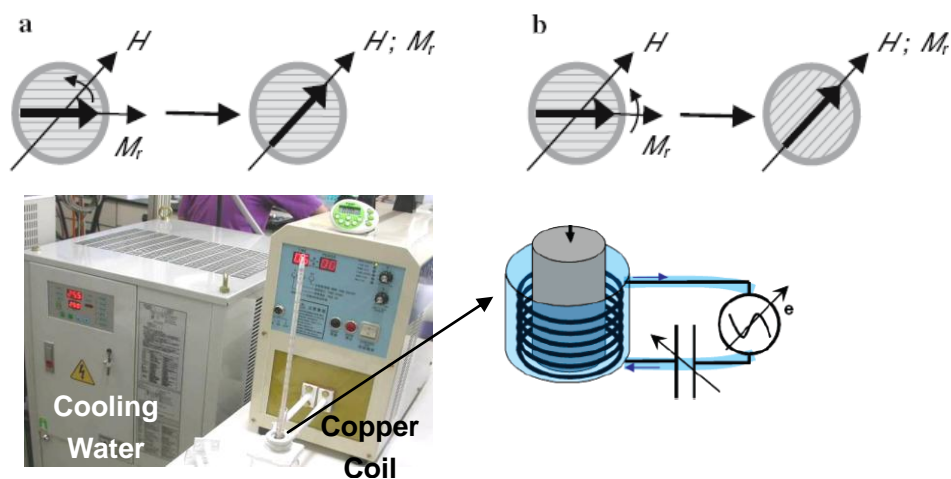


Figure 3.1 (a) Intrinsic (Néel) and (B) extrinsic (Brown) remagnetization mechanism (schematic). Equipment of high frequency magnetic field (HFMF).

Néel relaxation refers to the internal thermal rotation of the particle's magnetic

moment within the crystal, which occurs when the anisotropy energy barrier $E_a = KV$ is overcome; K is the anisotropy constant of the magnetic material, and V is the magnetic particle volume. The characteristic time τ_N for Néel relaxation is written as $\tau_N = \tau_0 \exp(E_a/kT)$, where τ_0 is of the order of 10^{-9} s. As the two relaxation mechanisms take place in parallel, the effective relaxation time τ is given by the relationship: $1/\tau = 1/\tau_N + 1/\tau_B$. Note that the shorter time determines the dominant mechanism of relaxation.

3.5 Drug loading efficiency and release

This study used vitamin B12 or ibuprofen (IBU) as a model drug to examine the drug loading efficiency and release behaviors of the NPs. After the drug loading process, the drug-containing capsules were separated from the aqueous solution by centrifugation at 10,000 rpm for 15 min. The drug concentration in the supernatant was analyzed using a UV-vis spectrophotometer (Agilent, 8453 UV-Visible spectrophotometer) at a wavelength of 264 nm, where there is a strong absorption band from the IBU. These measurements were performed in triplicate. The amount of drug in the NPs was calculated by subtracting the residual IBU in the supernatant from the total amount of IBU measured. The encapsulation efficiency (EE) was obtained as follows: $EE = (A - B) / C \times 100$, where A is the total amount of IBU, B is the amount of IBU remaining in the supernatant, and C is the weight of the capsules. For the drug release tests, the capsules were washed with phosphate buffered saline (pH 7.4) and then DI water. Ibuprofen-containing capsules were placed in PBS buffer solution for all drug-release experiments. A quantitative estimate of the IBU loading was obtained using UV-vis spectrophotometry, and the drug-release behavior of the capsules was measured using 20 mL of phosphate buffered saline solution (pH 7.4). To measure the concentration of released drug, 1.5 mL of the NPs-containing PBS

medium was centrifuged at 4000 rpm to remove the particles.

3.6 Release kinetics

Vitamin B12 (Sigma, V-2876) was used as model drug in this composite system because it is a water-soluble agent with low molecular weight, and its colorful nature allows a direct visual observation during the test, and almost shows negligible interaction with gelatin or MNPs. In the preparation of the drug-loaded NPs, the NPs were soaked in 1 % vitamin B12 of 50ml PBS solution for drug loading. Before conducting the drug release test, the drug-loaded NPs were first washed to remove the drug on the surface. The drug release behavior of the NPs was measured using 50 ml phosphate buffered saline per sponge cube (pH 7.4). UV-Visible spectroscopy (Agilent 8453) was used for characterization of absorption peak at 361 nm to quantitatively determine the vitamin B12.

To investigate the diffusion mechanism of the drug molecules in the gel, the drug released data were characterized using Eq. (3.2):^[138]

$$\frac{M_t}{M} = kt^n \quad (3.2)$$

where M_t is the mass of drug released at time t , M is the mass released at time infinity, and M_t/M is the fractional mass of released drug; k is a rate constant, and n is a characteristic exponent related to the mode of transport of the drug molecules. By taking logarithm on both sides of Eq. (3.2), Eq. (3.3) can be used to calculate the diffusion parameters (i.e., n and k) for $M_t/M < 0.6$.

$$\ln\left(\frac{M_t}{M}\right) = n \ln t + \ln k \quad (3.3)$$

The cumulative concentrations of released drug at time t and at the end of the experiment (to approximate the infinite time) were used to calculate M_t/M .

3.7 Cell culture

Three cell lines were used as normal cell models: retinal pigment epithelium (RPE) cells, ARPE-19 cells, and a monolayer of hexagonal cells that separate the neural retina from the underlying choroidal vascular bed. The cells were cultured on 75 cm² flasks at a density of 10,000 cells/cm² and were maintained in culture until the plates reached >95% confluence. Cultures were fed Dulbecco's modified Eagle's medium-nutrient mixture F-12 (DMEM-F-12; GIBCO, Invitrogen Corporation, Grand Island, NY) supplemented with 10% fetal bovine serum, 100 U/μL of penicillin and 100 g/mL of streptomycin. Cells were cultured in complete medium at 37 °C in a humidified atmosphere of 5% CO₂ in air. In all experiments, cells were harvested from subconfluent cultures using trypsin and were resuspended in fresh complete medium before plating. The *in vitro* cytotoxicity of the NPs to the AREP-19 cells was tested with an external magnetic field treatment using an *in vitro* proliferation method with MTT. In brief, 1×10⁴ cells were plated in 96-well plates to allow the cells to attach. The cells were then exposed to 10 μL/cc of NPs at 37 °C. At the end of the incubation period, 20 μL of MTT solution was added and the cells were incubated for an additional 4 h. The medium was then replaced with 200 μL of DMSO and the absorbance was monitored using a Sunrise absorbance microplate reader at dual wavelengths of 570 and 650 nm.

To estimate the cellular uptake of NPs, green emitting fluorescein dye was attached to the nanoparticles (FITC-labeled nanoparticles). First, fluorescein isothiocyanate (FITC) was mixed with an ethanolic 3-aminopropyltrimethoxysilane (APTMS) solution for 24 h at room temperature to form N-1-(3-trimethoxysilylpropyl)-N-fluoresceyl thiourea (FITC-APTMS). In a separate flask, 5 mg of NPs were dispersed in 4 mL of 99.5% ethanol and 0.1 mL of 33% NaOH solution for

30 min. Following this, 40 μm of tetraethylorthosilicate (TEOS) and 10 μm of FITC-APTMS were slowly added to the mixture, which was then stirred for 12 h. After hydrolysis and condensation, the FITC-labeled silica was coated onto the NPs. The unreacted chemicals were removed by rinsing with DI water three times. The NPs were incubated with the cells for different times and then the cells were observed by confocal microscopy (Nikon, C1).



Chapter 4

Controlled Pulsatile Drug Release from a Ferrogel

4.1 Introduction

Stimuli-responsive controlled release drug from polymeric devices has been received great attention, as it provides advantages, such as better delivery efficiency and site-specific therapy over the conventional routes of drug delivery. By taking these advantages, a number of researches have been successfully proposed to integrate active drug molecules and host materials, to manipulate drug release desirably. A very recent achievement of a protein-containing hydrogel reported by Ehrick et al.,¹⁰ addressed the stimuli-sensitive hydrogel that can be triggered as a result of the conformational change of the embedded calmodulin protein interacting to bioactive agents. Such a transfer from sensing actuation to mechanical action is novel but it may be hard to reach high accuracy and sensitivity in therapeutic dosing as a burst-controlled drug delivery system. The use of a magnetic field to modulate drug release from polymeric matrices was previously developed.^[139,140] Saslawski et al. reported the alginate microspheres for pulsed release of insulin by an oscillating magnetic field.^[141] The release rate of insulin from the alginate-strontium ferrite microspheres was enhanced in the absence of a magnetic field. Recently, the polyelectrolyte microcapsule embedded with Co/Au used the external magnetic fields of 100-300 Hz and 1200 Oe to increase the permeability to macromolecules.^[142] In previous studies, a ferrogel with direct current (DC) magnetic-sensitive properties has been characterized and the amount of drug released from the ferrogel was effectively restricted while applying an external DC magnetic field.^[143,144] So far, little investigation has been addressed on the controlled drug release under high frequency magnetic fields (HFMF). A real-time burst release of drug needs a fast-responsive

drug release system to “inject” precise dose of drug when body needs and “stop” or “slow” releasing right after the injection, however, it is hard to easily achieve with traditional stimuli-responsive hydrogels. A controllable pulsatile-type drug delivery device with repeatable dosing ability in therapeutically effective precision is clinically desirable. Therefore, in this communication, a high frequency magnetic field (HFMF) triggered pulsatile drug delivery ferrogel with a mechanically reliable and flexible hybrid structure composed of gelatin and magnetic nanoparticles (nano-magnets) of 10 nm - 250 nm in diameter is reported. Furthermore, under cyclic exposures to the high frequency magnetic stimuli, a highly controllable and repeatable burst release with desirable precision from the ferrogels is achieved.

4.2 Fabrication of ferrogels

Gelatin (Sigma, USA, from bovine skin, type A, ~300 bloom) with pre-determined amount was first dissolved in the D.I. water for 2 hours at 50°C. After gelatin was fully dissolved, 3 wt % Fe₃O₄ magnetic particles with different sizes and 0.03 wt % drugs (vitamin B₁₂, Sigma, USA), based on gelatin weight, were added into the solution under ultrasonication for 6 h to ensure the well dispersion of the magnetic particles in final suspensions. After then, 2 wt % chitosan dissolved in 1 (v/v) % acetic acid was blended with the gelatin suspension in order to form strong frames in which the resulting ferrogels interpenetrating. Genipin (GP, Challenge Bioproducts Co., Ltd., Taiwan) as a crosslinking agent was mixed with the suspension then, cast into a plastic vessel and incubated at 25 °C for 2 days to form ferrogel. The magnetic particles used in this study included: (1) 250 nm, larger magnetic particles, diameter ca. 150-500 nm, (Aldrich, USA). (2) 40 nm, middle magnetic particles, diameter ca. 40-60 nm, (Alfa Aesar, USA). (3) 20 nm, small magnetic particles, diameter ca. 20-30 nm, (Aldrich, USA). (4) 10 nm, which was synthesized using a co-precipitation method, outlined by Mikhaylova et al.^[20] In brief, FeCl₃·6H₂O and FeCl₂·4H₂O (The

molar ratio of $\text{FeCl}_2/\text{FeCl}_3$ was kept constant at 2:1) were dissolved into water with vigorous stirring at 80 °C under N_2 . Ammonium water, NH_4OH (33% (w/w)), was added to cause precipitation where the Fe_3O_4 nanoparticles were immediately formed in the solution, with a size of ca. 6-11 nm in diameter.

Vitamin B_{12} (Sigma, V-2876) is used as a model drug which is water soluble and has negligible interaction with gelatin or MNPs. In the preparation of the drug-carrying ferrogels, the drug with pre-determined amount was loaded upon ferrogel synthesis. Drug release test was carried out in a 20 ml phosphate buffered saline (pH 7.4) and the environment temperature was kept at 25 °C. UV-Visible spectroscopy (Agilent 8453) was used for characterization of absorption peak at 361 nm to determine the concentration of vitamin B_{12} released in the saline. Drug release behavior of the ferrogels was investigated using a high frequency magnetic field (HFMF) of 50-100 kHz and 15 kW applied externally. Because the HFMF generates heat around the coil during operation, it was kept at 25°C through a control of cooling water bath to prevent thermally-induced interference from environment.

4.3 Characteristics of ferrogels

Figure 4.1(a) illustrates the SEM images of one of the ferrogels shaping in cylindrical geometry, namely 40nm@GE ferrogel, where 40nm@GE represents the ferrogels with gelatin cross-linked with genipin, reinforced by 2 wt% chitosan, and 3% Fe_3O_4 magnetic nanoparticles (nano-magnets) of averaged 40 nm in diameters. As shown, the iron nanoparticles were embedded into the polymer matrix and the nano-magnets displayed a uniform spherical size and dispersed well in the ferrogel. TEM image, i.e Figure 4.1(b), exhibits that the gelatin was intimately attached to the surface of the nano-magnets, and the nano-magnet particles also percolated as a continuous phase, indicating the resulting ferrogels are virtually an interpenetrating network composites.

This also suggests that the physical or thermal interactions between these two closely-contact, interpenetrating phases can be easily triggered and accessible from one phase to the other at a nano-metric level. This also ensures fast-responsive properties of the ferrogels that can be achieved as disclosed in the forthcoming analysis.

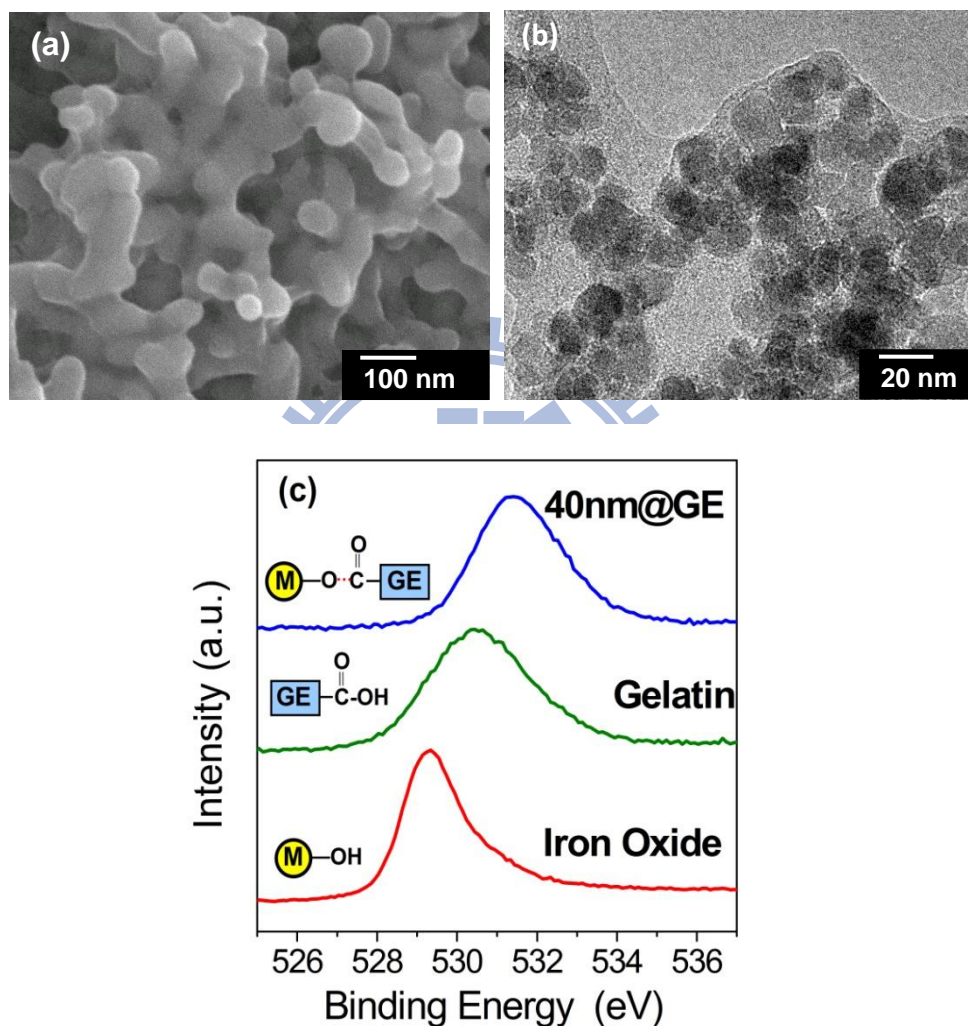


Figure 4.1 (a) SEM, (b) TEM and (c) XPS analyses of ferrogels composed by iron oxide nanoparticles and gelatin matrix.

The nano-magnets were essentially chemically bounded with the gelatin matrix to form the ferrogel, which further evidenced from XPS analysis, in Figure 4.1(c). The binding energy of O_{1s} is detected from 527.0 to 537.0 eV, and the peak of iron oxide was at 529.3 eV, which is reasonably consistent with literature report, i.e.,

528-531 eV. A peak at 530.4 eV for the gelatin indicates its carboxylic acid group; however, a shifting to higher energy region (531.4 eV) when the iron oxide particles were incorporated, implying that the carboxylic acid was chemically bonds or immobilized, onto the nano-magnet surface. The higher binding energy is believed to be a result of esterification between hydroxide moiety on the surface of the MNPs and carboxylic acid group of gelatin, forming a COO-Fe bonding, indicating an excellent chemical affinity between both participating phases and a mechanically strong solid network of the ferrogels is achieved.

4.4 Drug release triggered by magnetic field from ferrogels

Upon magnetic manipulation, the drug (vitamin B₁₂) released from the ferrogels was demonstrated in the Figure 4.2(a). The ferrogels with different particle sizes of the nano-magnets showed different release rates even though they possessed the same concentration of the nano-magnets. In comparison, pure polymer gelatin showed faster drug release rate than that of the ferrogels, indicating the nanoparticles are acting as physical barriers to inhibiting the diffusion of the drug molecules. After the initial time period (50 min) of slow release, the high frequency magnetic field (HFMF) was applied to the ferrogels for 10 minutes, and then was removed. The amount of drug release from the 40nm@GE ferrogel burst to a level as high as about 63 %, compared to 12% during the first 50-min release in the absence of the HFMF. The finding strongly indicates that the applied HFMF accelerated considerably the drug release from the ferrogels of 40nm@GE composition by as large as 5 times. More specifically, the amounts of drug release from the ferrogels with different particle size were increased in the order of 40nm@GE > 20nm@GE > 250nm@GE > 10nm@GE > pure gelatin under the same magnetic stimulus. However, the release profiles after the 10-min burst, restored almost completely right after removal of the high-frequency magnetic stimulus, and behaved almost exactly the same as those at the initial 50-min period. A real-time, fast-responsive drug delivery ferrogels can be achieved and the

faster responsivity of the ferrogels with respect to the HFMF stimulus offers greater potential for an in-time drug release device for medical applications.

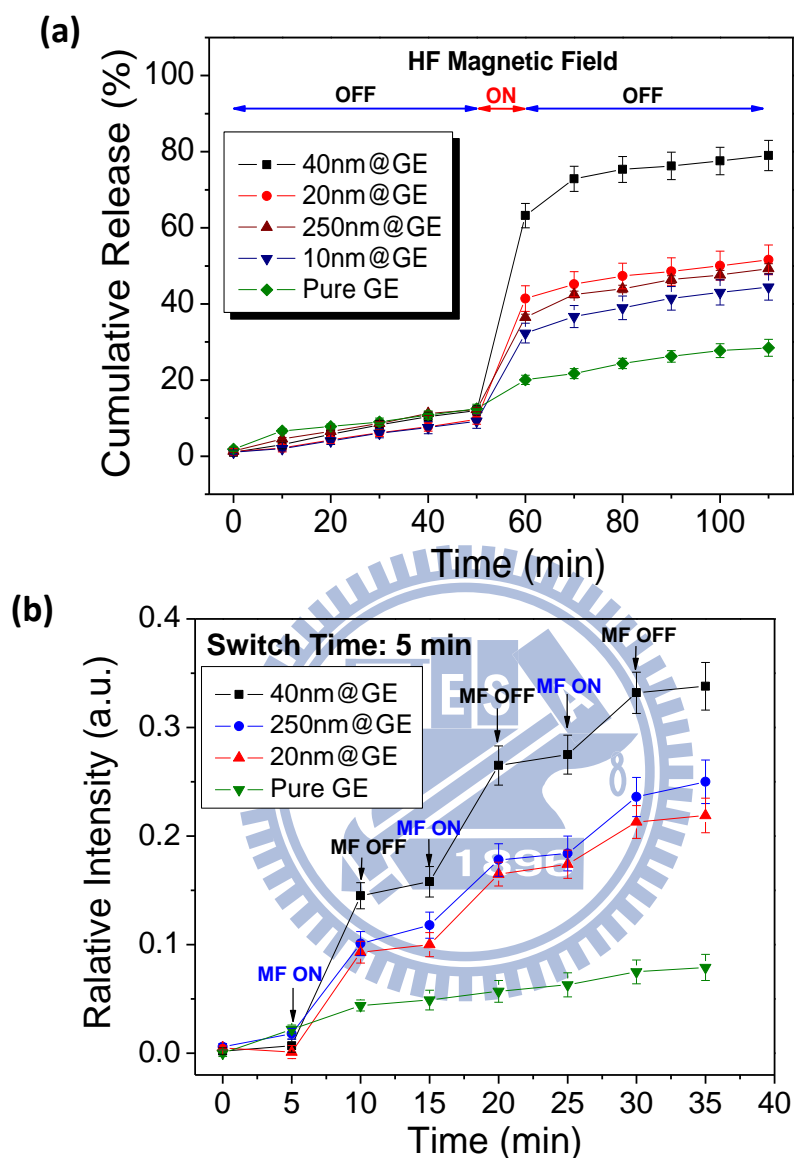


Figure 4.2 (a) Drug release behaviors of the ferrogels under the 10 minutes exposing of high frequency magnetic field (HFMF) and (b) The on-off switch operations of high frequency magnetic field (HFMF) manipulated the cumulative drug release of the ferrogels with different sizes of the nano-magnets.

Upon tripled on-off operations of the HFMF to the ferrogels, Figure 4.2(b) shows that reproducible slow-to-burst release profiles while consecutively applying the magnetic stimulus at a 5-min switching time period and the release profile restored immediately when the stimulus was removed. The findings imply two important

characteristics underlying the drug release pattern of the high-frequency-induced ferrogels: first, under a short time “on-off” exposure of the magnetic stimulus, the ferrogels followed exactly the signals switching from burst to slow release of the drug instantly and second, the amounts of drug bursting from the ferrogels maintained accurate dosing under cyclic on-off operations of the HFMF. The latter suggests the ferrogels prepared deformed elastically and showed potential anti-fatigue behavior, whilst the former indicates a fast-acting response of the ferrogels that can be technically achieved with desirable stimuli-sensitive control of drug delivery through the incorporation of 40 nm nano-magnets in average diameter.

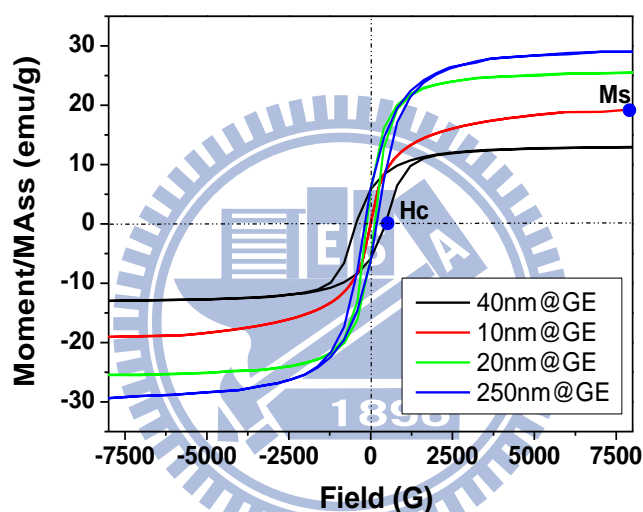


Figure 4.3 Vibrating sample magnetometry measurements for the ferrogels with various iron oxide nanoparticles sizes.

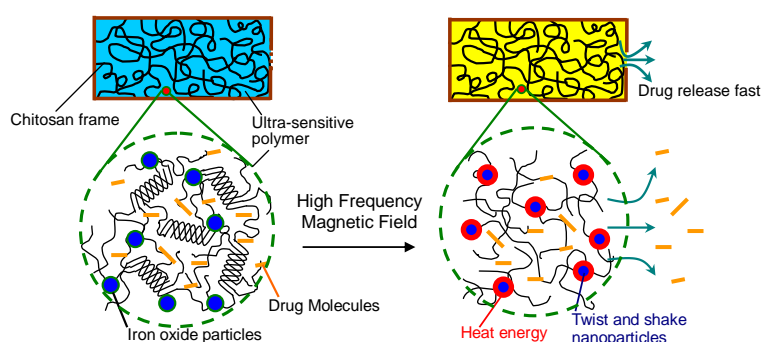


Figure 4.4 Schematic drawing of structures of ferrogel which exhibited a triple-helix structure to restrict the drug molecules to release. While applying the high frequency magnetic field (HFMF), the magnetic nanoparticles provides the heat energy to loose the structures, and twist and shake the polymer molecular chains to effectively accelerate drug release rate.

The bursting release of the drug from the ferrogels is indicative of a mixture of mechanical actions imposed by the ferrogels, which may include (1) an “open” configuration of the network structure and (2) an elastic deformation (i.e., contractile deformation) of the ferrogels, while subjecting instantly to the HFMF stimulus. Under HFMF, the nano-magnets were activated kinetically and possibly thermally (for larger nanoparticles), and transformed the structural or molecular configuration of the ferrogels upon microstructural deformation (shrinking) of the gelatin matrix. Gelatin is considered as a thermosensitive polymer since its conformation is a coil in the warm water ($>40^{\circ}\text{C}$) but turns into a gel structure involved a triple-helix sequences on cooling.^[145,146] Among the ferrogels prepared, magnetization evaluation (see the Supporting Information, Figure S4.1) showed 40nm@GE composition exhibiting the broadest hysteresis loop compared to the others, indicating more energy can be generated instantly under the high frequency magnetic stimulus. In other words, the 40nm@GE ferrogel was effectively thermally activated, where a rapid change in molecular conformation of the gelatin matrix from denser to looser configuration, as schematically illustrated Fig. 4.3, is expected in the ferrogels by a high-frequency magnetically-induced thermal variation near the nano-environment surrounding the nano-magnets.

4.5 Cyclic drug release rates of ferrogels

For a long HFMF switching duration, i.e., 180 minutes, Fig. 4.4 illustrates a series of bursts started after a first 3-h slow release, under a 5-min duration of HFMF stimuli, where a gradual reduction in the burst release rate was detected with time. Even though the longer switching time period of the high frequency magnetic stimulus ensures a kinetically favorable drug migration, the insufficient drug amount in the ferrogel can hardly sustain the same burst release rate. However, a relatively slow to near-zero release rate was detected immediately after removal of the HFMF

and kept relatively constant during the time duration, i.e., 180 minutes, between each stimulus. Same scenario of burst and slow release profiles repeated accurately for a time period of 840 minutes of drug release operation proved that the ferrogels exhibited an excellent elastic deformation property. This allows a consecutive operation for a continuously controlled burst release of drug into patient's body to maintain a therapeutically effective dose in body for a longer period of time to efficiently treat the disease locally or systemically. One clinically important advantage of this high-frequency-modulated fast-acting drug delivery ferrogel over other existing drug delivery devices is that it can potentially meet immediate urgent physiological needs and with dosing compatibly match chronological changes in patients' body.

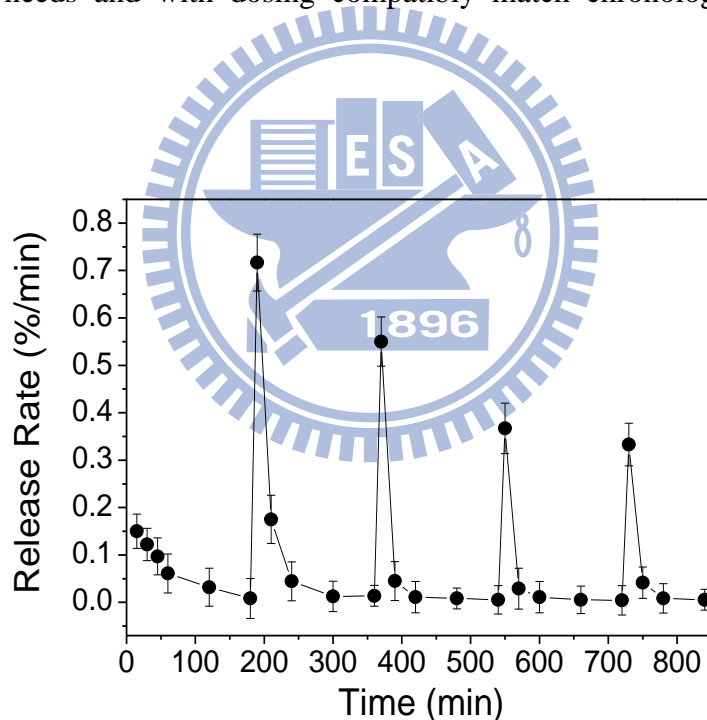


Figure 4.5 Cyclic drug release rates of 40nm@GE ferrogels under a 5-min period of HFMF stimuli and a long 180-minute switching duration, where a longer switching time period ensures the drug to reach a kinetically favorable distribution in the ferrogel for a subsequent burst release.

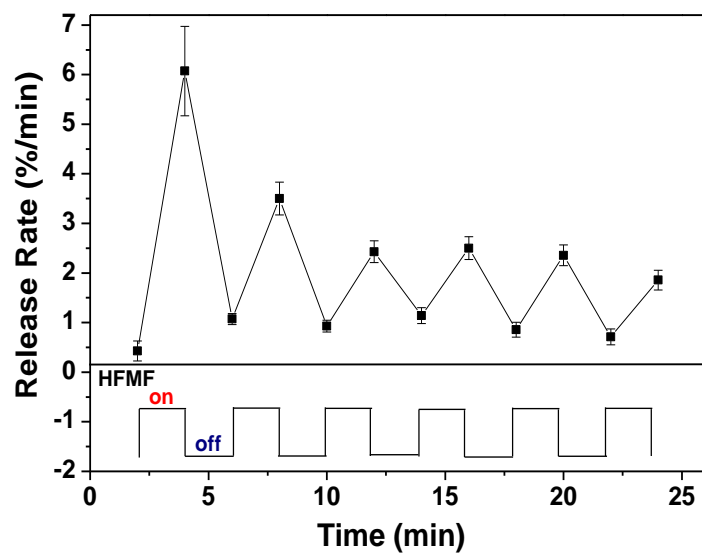


Figure 4.6 Cyclic drug release rates of 40nm@GE ferrogels (a) under a 2-minute period of HFMF stimuli and a short 2-min switching duration.



Chapter 5

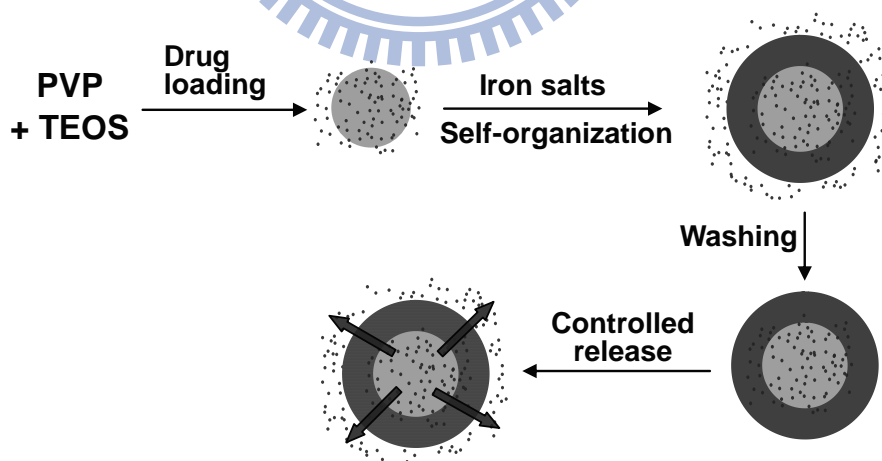
Core/Single-Crystal-Shell Nanospheres for Controlled Drug Release via a Magnetically Triggered Rupturing Mechanism

5.1 Introduction

Recently, superparamagnetic iron oxide nanoparticles with enhanced functionality through surface modification or combining with functional materials have been widely used in a variety of biological applications such as drug/gene delivery, bioseparation, magnetic resonance imaging and hyperthermia therapy. In contrast, there was only a limited number of reports addressed the use of magnetic nanoparticles for controlled drug delivery. Most of the drug-containing magnetic nano-carriers comprise magnetic nanoparticulate “cores” with an organic or inorganic “shell”, where therapeutic drugs are encapsulated within the shell structure. Drug released from these magnetic core-shell nano-carriers can easily be triggered by an external magnet, which has been known as “magnetic motor effect” for site-specific drug delivery applications. However, it is impossible to provide “zero release” capability before the drug-containing nano-carriers reached the targeted sites because the nature of diffusion of drug molecules from the nano-carriers to the environment is virtually thermodynamically unavoidable in the presence of a concentration gradient of drug. Once being triggered, the dose of drug which is originally designed to treat the targeted disease will be changed, sometimes, in an un-expected manner, to reduce therapeutic efficiency. Therefore, a novel design for a nano-carrier to eliminate undesirable drug release before reaching the target sites will be more interesting and practically desired. In the meantime, it is more than critical if the drug can be truly released after reaching the target by a controllable manner via external stimuli.

Magnetic field provides a non-contact nature, which permits remotely

manageable dosing, over those required a physical or chemical contact in order to trigger drug release action on practical applications. However, nanoparticulate drug carrier with accurate and fast response to the magnetic field has not been achieved. Here, we report a novel core-shell nano-carrier with a drug-containing silica core surrounding with a single crystalline iron oxide shell. With such a unique core-shell configuration, we believe that biomolecules encapsulated in the core with an outer single-crystalline thin iron oxide shell can be protected from damages by harsh environment and as one major objective of this study, eliminating un-controllable release due to natural diffusion of molecules upon delivery in, for instance, patient's body. On the other hand, the magnetic nano-shell displays ultra-fast response and sensitivity under exposure of high-frequency magnetic field (HFMF), where the highly magnetic-sensitive property of the nanometric shell allows a controlled burst release of drug in a quantitative manner. In comparison, such a novel core-shell PVP-modified silica/Fe₃O₄ nanosphere is expected to provide much greater advantages in biomedical uses than existing alternatives.



Scheme 5.1 Schematic of the stimuli-responsive delivery system (PVP-modified Silica/Fe₃O₄ core-shell nanospheres) based on silica-PVP nanospheres coated with iron oxide shells. The controlled release of PVP-modified Silica/Fe₃O₄ core-shell nanospheres is based on applying high-frequency magnetic field (HFMF).

5.2 Preparation of core/single-crystal-shell nanospheres

In this study, a sol-gel process was used to encapsulate the fluorescence molecules within the silica matrix. First, 2 wt% polyvinylpyrrolidone (PVP; 0.06 ml; $M_w \sim 10,000$) was dissolved in the D.I. water under stir. 0.04 ml tetraethoxysilane (TEOS) was added into the 25 ml ethanol, and 5 ml of 2 wt% polyvinylpyrrolidone (PVP) was mixed into the solution and pre-heated to 80 °C. Then, the fluorescence molecules was dissolved in the D.I. water and added into the solution and mixed for 6 hours. Under nitrogen atmosphere, 100 μ L ammonia solution (33 wt %) was introduced to the pre-hydrolyzed TEOS solution. After 24 hr, the ethanol was used to wash the silica nanoparticles to remove the surfactant and unreacted chemicals for three times. The dye-loaded silica nanoparticles were dispersed in ethanol solution. Under nitrogen, $\text{FeCl}_3 \cdot 6\text{H}_2\text{O}$ and $\text{FeCl}_2 \cdot 4\text{H}_2\text{O}$ with a $\text{FeCl}_2/\text{FeCl}_3$ molar ratio of 2:1 were dissolved into water, and then mixed with the PVP-modified silica nanoparticles with vigorous stirring at 80 °C under nitrogen atmosphere. After 4 hr, the iron salts were adsorbed on the PVP-modified silica nanoparticles, the ammonium water (33%) was slowly dripped into the mixed solution. Addition of 2 ml ammonium water (NH_4OH , 33%) caused precipitation where iron oxide shells were immediately formed on the surface of PVP-coated silica nanoparticles, forming a self-assembly core-shell nanosphere. The precipitated powders were collected through the centrifuge at 6000 rpm, removed from the solution, and washed by D.I. water for four times. The PVP-modified silica/ Fe_3O_4 core/shell nanospheres were separated by centrifugation, and the average diameter of the core-shell nanospheres is about 20 nm.

The morphologies of core-shell nanospheres were examined using transmission electron microscopy (TEM, JEM-2010, Japan). X-ray diffractometer (XRD, M18XHF, Mac Science, Japan) was applied to identify the crystallographic phase of

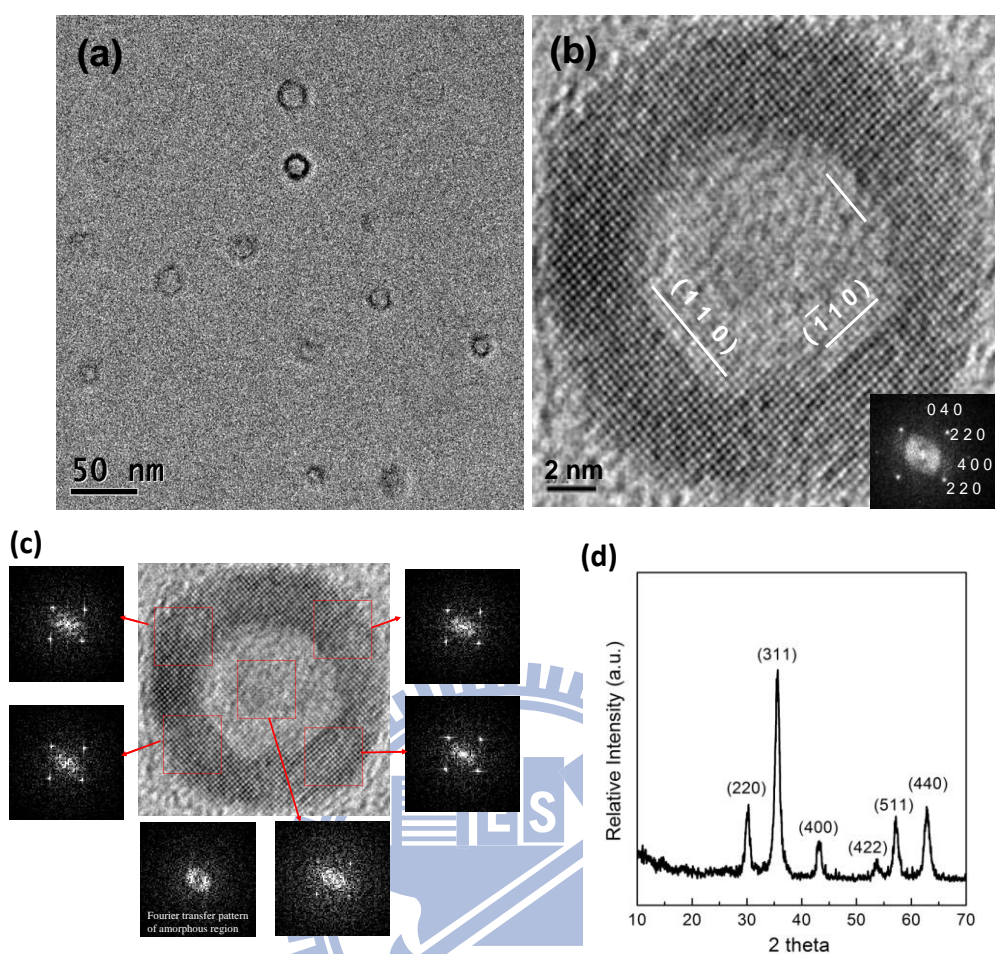


Figure 5.1 (a) TEM images and (b) HR-TEM of PVP-modified Silica/Fe₃O₄ core-shell nanospheres. Local Fourier transfer patterns indicate that the crystallographic structure is extremely uniform and homogenous through the shell. Some facet {1 1 0} planes are observed inside the nanosphere, and the Fourier transform pattern indicates that the shell is oriented at $z = [0\ 0\ 1]$. (c) Local Fourier transfer patterns indicate that the crystalline is uniform and homogenous through the particle. (d) X-ray diffractometer verified the crystallographic phase, at a scanning rate of $6^\circ\ 2\theta$ per minute, as Fe₃O₄ (magnetite, according to JCPDS [85-1436]).

nanospheres, at a scanning rate of $6^\circ\ 2\theta$ per min over a range of 2θ from 10° to 70° . The high frequency magnetic field (HFMF) with 50-100 kHz was applied to the magnetic silica nanospheres to investigate the drug release behavior. HFMF was set up from power supply, functional generator, amplifier, and cooling water. The strength of the magnetic field depended on the coils. In this study, the coil is 8 loops,

frequency is 50 kHz and the strength of magnetic field (H) is 2.5 kA/m. The temperature of HFMF generator was controlled by cycling cooling water at 25 °C. The drug release behavior from the magnetic silica nanospheres was measured in a 20 ml phosphate buffered saline (pH 7.4). PL spectroscopy (PL, Fluorescence Spectrophotometer F-4500, Hitachi, Japan) was used to characterize the release profile of the dye molecule by measuring the change in the intensity of the fluorescence dye before and after a high frequency magnetic field (HFMF) of 50 kHz was applied to the nanospheres with a concentration of 0.01 wt% dispersed in the water solution for a time period from 0, 30, 60, 90, 120, 150 to 180 sec under the HFMF exposure. BET analysis was measured using N₂ gas absorption isotherms at 77K, and the BET surface areas were calculated in the region 0.05-0.3 of relative pressures.

5.3 Nanostructure of core-single crystal shell nanospheres

The PVP-modified Silica/Fe₃O₄ core-shell nanospheres shown in the **Figure 5.1a** displayed a spherical geometry ranging from 15 to 23 nm in diameter. High-resolution transmission electron microscopy (HRTEM) image in **Figure 5.1b** confirmed the core and shell nanostructure which are clearly discernable with an amorphous silica core phase and a thin crystalline shell phase that completely enclosed the core. No observable crevices or cracks were visually detectable at the interface of these core-shell nanospheres, suggesting excellent physical integrity between two dissimilar phases. The thickness of the shell is about 4 nm in average, and the shell demonstrates a relatively dense, single-crystal nanoarchitecture with an orderly-arranged crystal lattice clearly shown in the HR-TEM image. The nano-shell presented with a crystal structure can be clearly identified as magnetite phase (Fe₃O₄). Such a highly order arrangement of the crystal lattice in the shell structure is relatively unique and is

suggesting to result from a self-assembly of the iron oxide salt in the presence of the PVP molecule. Although the actual mechanism for the growth of single-crystalline iron oxide shell is unclear at present, it is believed that with the adsorption of PVP on the surface of the silica cores, the iron ions can be efficiently anchored on the pyrrolidone ring of PVP, which promotes an epitaxially-like growth of the oxide to form single-crystal structure while increasing solution pH upon synthesis.

5.4 Triggered release of fluorescence dye from nanoparticles

To demonstrate the release behavior of the fluorescence dye (as model molecule encapsulated in the core phase) from the core-shell nanospheres under high frequency magnetic field, two cuvettes were charged with fluorescence-loaded nanospheres (100 mg each) dispersed in 15 mL water solution. After 24 hours (**Figure 5.2a**, right), the nanospheres with the green dye showed no sign of release from the nanospheres under UV detection, suggesting that the dye molecules were enclosed in the silica cores and effectively inhibited from diffusion to surrounding solution for a time period of 24 hours, where such a time period is far over the time duration required for a metabolic operation in healthy body. However, while applying a high frequency magnetic field (HFMF, 50 kHz and a power output of 15W) to the cuvette for 5 minutes (**Figure 5.2a**, left), a large amount of the dye molecule was detected in the water solution, indicating the molecules were released rapidly from the nanosphere under magnetic stimulus, indicating that the core-shell nanospheres are highly sensitive to HFMF stimulus and show outstanding remotely controlled release behavior.

A kinetic analysis was performed using PL spectroscopy to monitor the release of the dye molecules from the core-shell nanospheres under different time periods of HFMF exposure. **Figure 5.2b** shows the resulting PL spectra of the dye at different time periods, where the intensity of the fluorescence spectra is increased with time of

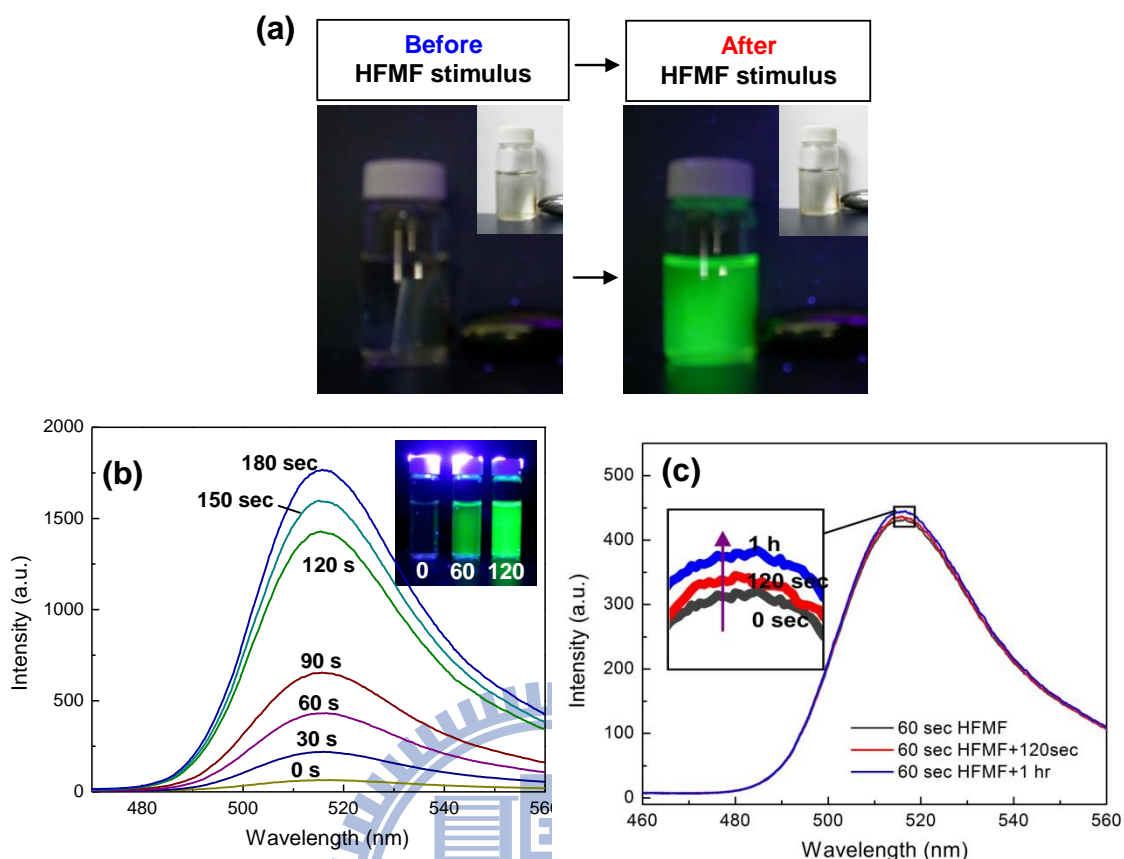


Figure 5.2 (a) Photographs of the cuvettes with fluorescence-loaded PVP-modified Silica/Fe₃O₄ core-shell nanospheres dispersed in water solution. Before HFMF exposure, fluorescence-loaded PVP-modified Silica/Fe₃O₄ core-shell nanospheres displayed no sign of fluorescence under the UV light (left); after exposure, green fluorescence released from the PVP-modified Silica/Fe₃O₄ core-shell nanospheres was clearly detected (right). (b) Emission spectra of PVP-modified Silica/Fe₃O₄ core-shell nanospheres (15 mg per 10 mL water) for applying HFMF from 30 s to 180 s. (c) Emission spectra of PVP-modified Silica/Fe₃O₄ core-shell nanospheres. Negligibly small amount of the dye molecule being further released from the nanospheres for a time period of 120 seconds in the absence of the stimulus.

MF exposure, till a maximum at 180 seconds. After which, no further increase in peak intensity was detected, indicating the dye molecules were completely released from the nanospheres after subjecting to 180-second HFMF exposure. Since the test is monitored at different time periods of on-off stimulation, the time-dependent peak intensity indicates that the dye was released only when the magnetic field was applying onto the nanospheres, and the release ceased right after removal of the field.

This observation suggests the action of magnetically-driven drug release from the core-shell nanosphere is reversible.

However, in order to further verify the reversibility of the open-close nature of the magnetic shell, we performed a simple test following a 60-second HFMF exposure, and kept the sample away from the field for another 120 seconds, the PL spectrum showed negligible change in the spectral intensity as the first test shown in **Figure 5.2c**, i.e., the same as the spectrum at 60-second exposure, indicating no or negligibly small amount of the dye molecules being further released from the nanospheres for a time period of additional 120 seconds in the absence of the stimulus. This simple test indicates the shell being reversibly closed right after the field was removed and the dye molecules were physically enclosed inside the core phase again where un-controllable diffusion is completely avoided.

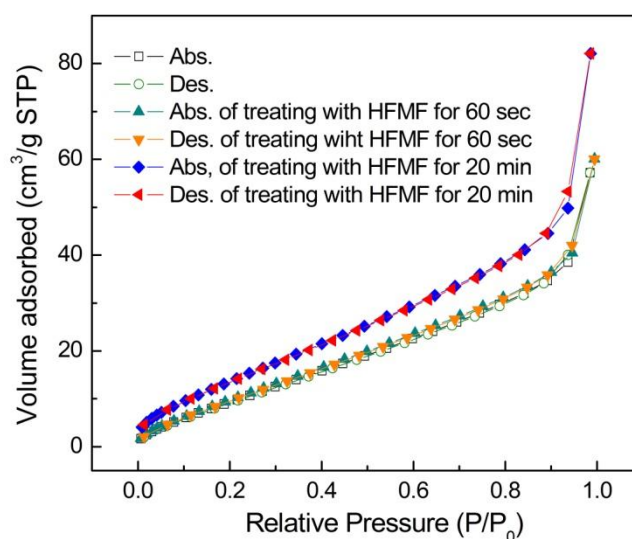


Figure 5.3 Nitrogen-adsorption spectra for the nanospheres before and after a 20-min HFMF exposure. BET measurements of silica nanospheres treated with HFMF for 0 sec, 60 sec and 20 minute.

5.5 BET analysis of core-shell nanospheres

Since the use of HFMF is able to induce vibration of the magnetic shell, it is conceivably believed that a short HFMF exposure of the core-shell nanospheres may

induce relatively small deformation of the shell structure and result in a reversible change of the nanostructure after the field was removed. However, it is conceivable that an irreversible change in the nanostructure of the core-shell nanospheres may occur if the physical deformation is large enough to cause permanent damage to the shell structure for a long-term HFMF exposure. To verify this concept, a nitrogen-adsorption measurement was performed in order to evaluate the subtle variation of the nanostructure under a longer-term HFMF stimulus. **Figure 5.3** shows the resulting nitrogen-adsorption spectra for the nanospheres before and after a 20-min HFMF exposure. The as-synthesized nanospheres have a specific surface area of $47 \text{ m}^2\text{g}^{-1}$ and total pore volume of $0.089 \text{ cm}^3\text{g}^{-1}$ and a considerably increase in the surface area and total pore volume of nanospheres to $61 \text{ m}^2\text{g}^{-1}$ (increased by ~30%) and $0.127 \text{ cm}^3\text{g}^{-1}$ (by ~40%), respectively was detected after the long-term exposure, suggesting that the nanoporous structure of the nanospheres is changed irreversibly after long-term exposure to HFMF. Since the shell is a relatively dense, single-crystalline structure covering the core surface, no accessible paths are available for nitrogen molecules ($\sim 30 \text{ \AA}^2$) to diffuse in, it is thus reasonably to believe that the specific surface area and pore volume measured of the as-synthesized nanospheres is the pore nature of the agglomerates of the nanospheres, i.e., the pore volume obtained is then a sum of the volume of inter-particle voids rather than the pore properties within the nanospheres. In contrast, the increment in specific pore volume and surface area of the nanospheres after long-term field stimulation is highly likely to be a contribution from within the porous structure of the nanospheres. In other words, the shell was structurally deformed or damaged, where defects were developed and accessible for the molecules to release out. This increase in both the surface area and pore volume may also result from the dissolution of the silica core, however, it seems not feasible for such a concern since the porosity of the silica core itself remained the

same after the test, i.e., 20-minute exposure. However, the change in these pore parameters is different from what was previously observed, where the nanoporous structure remained nearly unchanged for 60-sec HFMF exposure, albeit the fact that the test is a long exposure, rather than the short exposure illustrated in Figure 5.2b.

5.6 Nanostructural evolution

To further elucidate the mechanism behind the release and zero-release behaviors, the nanospheres were examined using HR-TEM under different time periods of stimulus, as illustrated in **Figure 5.4**, where a schematic drawing of the corresponding mechanism of controlled release is demonstrated. After a short exposure to the stimulus, i.e., 60 seconds, the single crystal nanoshell structure was under lattice deformation as a result of atomic rearrangement, forming nano-sized polycrystal of varying orientations. Boundaries between the nano-polycrystal were developed and it is highly likely that such boundaries (are prone to develop nano-crevices under continuing stimulus) provide conduits for the dye molecules (having dimensions estimated by software about 1.1 nm and smallest height is only 0.1 nm) to elute. In other words, while subjecting to the magnetic field for short-term period, crevices or cracks in a nanometric scale were evolved along the boundary regions of the thin shell, magnetically-induced vibration enlarges the nano-crevices, permitting dye molecules easy to release out and the change in the dimension of the nano-crevices is physically reversible to a certain degree upon a short-term field exposure. However, under long-term exposure, the nano-crevices further enlarges in scale, as a nanometric crack propagation along the spherical shell structure, and ultimately, forming irreversible deformation, i.e., rupture, of the shell while absorbing sufficient amount of the magnetic energy, resulting in an increase in both pore volume and surface area (Figure 5.3).

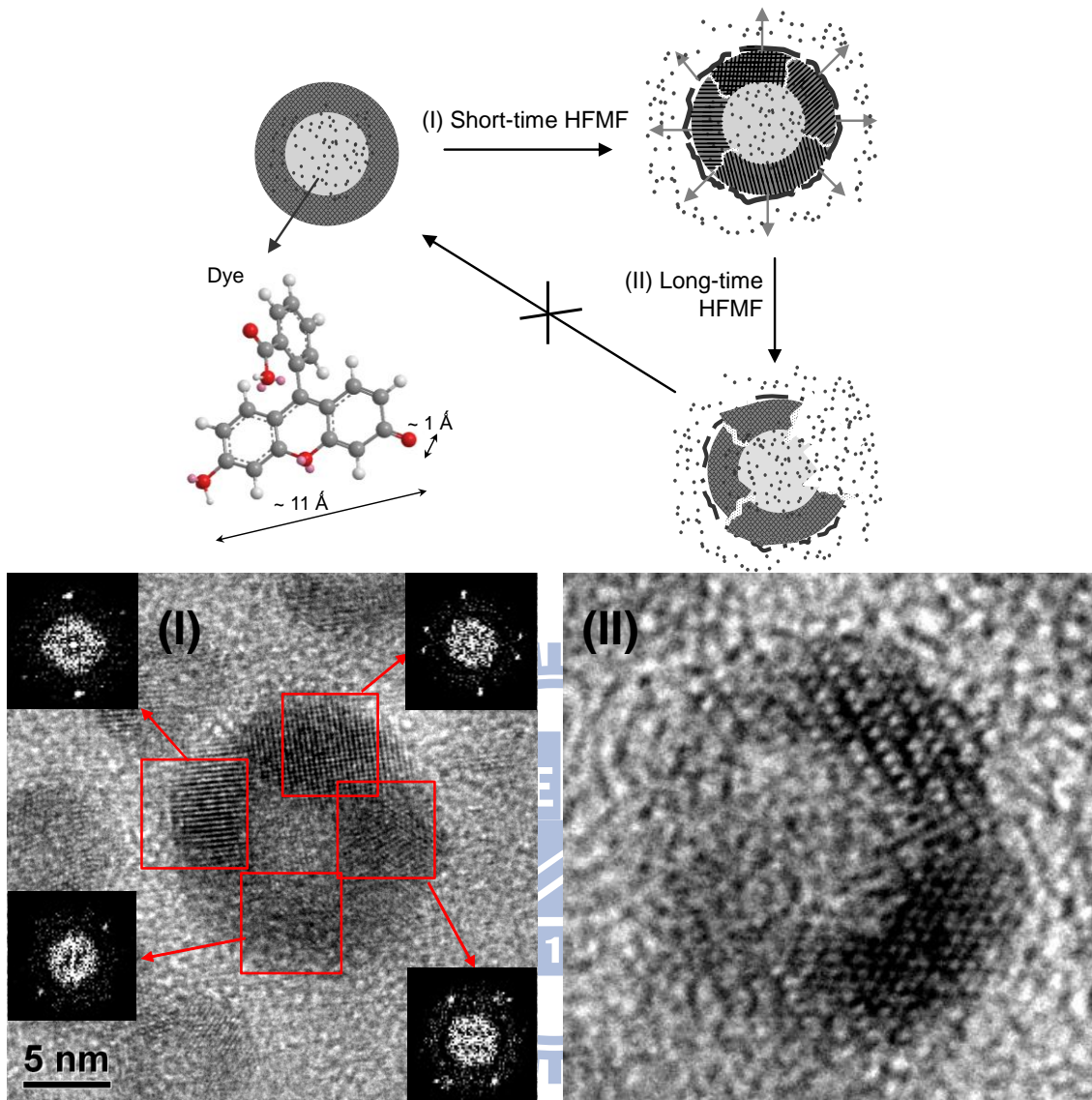


Figure 5.4 Schematic illustration of the thin shell with a proposed mechanism for control release of the fluorescence dye: (I) while applying HFMF, vibration enlarges the dimension of the nano-faults, making dye molecules easy to release out and the change in the dimension of the nano-faults is physically reversible upon a short-term field exposure. (II) under long-term exposure, the nano-faults received sufficient amount of the energy, vigorous energy (although not specifically identified yet in this communication) ruptures the thin shell permanently.

The variation of the shell lattice structure from single crystalline configuration, i.e., single crystal, to polycrystal formation is seemingly physically ir-reversible, but the magnetic-sensitive behavior appears to remain the same afterward for these nanospheres. This phenomenon does offer great interest of developing a “temporary

single-crystal shell” to protect and encapsulate molecules of interest more effectively for many types of specific delivery to diseased hosts without possible loss or damage of the molecules during the course of delivery. The variation of such a lattice change of the single-crystal iron oxide nanoshell upon magnetic stimulus may be a result of (a) thermal induced atomic re-arrangement where the free or surface energy of the single-crystal shell may be reduced by forming polycrystal of varying orientations, where some free or surface energy being reduced by formation of numerous inter-polycrystal boundaries and (b) magnetically-triggered mobility of the atoms along the direction of magnetification, to achieve a status of lower energy with enhanced structural stability, since the shell is essentially so thin and small in dimensions where surface energy should be relatively high and is structurally unstable.

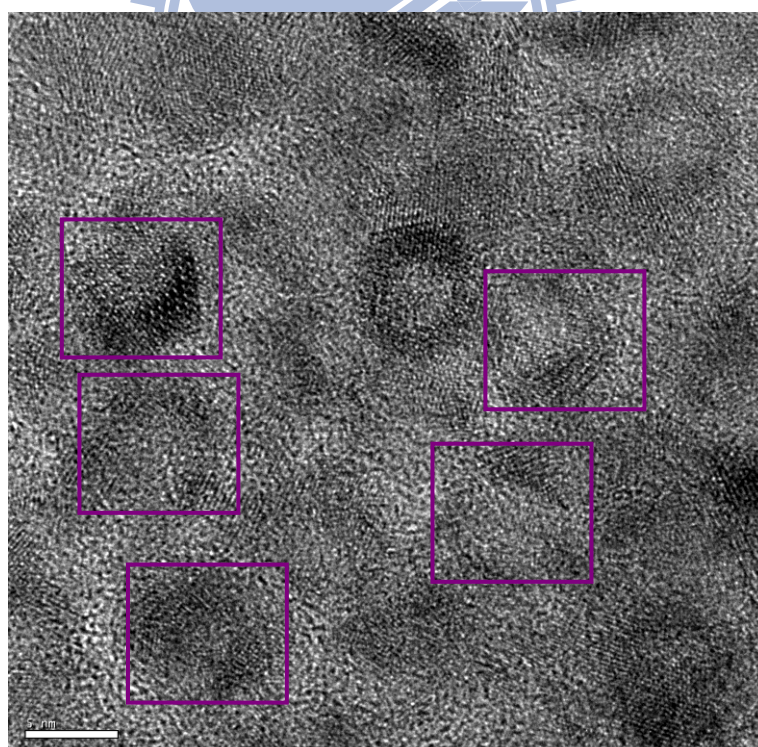


Figure 5.5 TEM images of long-term HFMF exposure, the nano-faults received sufficient amount of the energy, vigorous energy (although not specifically identified yet in this communication) ruptures the thin shell permanently.

5.7 *in vitro* controlled release

Since the core-shell nanospheres are able to provide precise control of release and non-release characters for the molecules, which provides greatest advantages for drug delivery uses, however, it is important to investigate the endocytosis following a magnetically-triggered drug release behavior of the nano-device within cells. To further elucidate such a behavior, HeLa (human cervical cancer) cells were incubated overnight with the magnetic nanospheres loaded with green fluorescence dye to allow the endocytosis of nanospheres to be optically examined. **Figure 5.6a** shows the optical and fluorescence images of the cell line before HFMF treatment where a relatively weak green fluorescence was observed. However, after 30 seconds of HFMF stimulus, green fluorescence was clearly observed within the cell bodies of these HeLa cells upon excitation at 494 nm (**Figure 5.6b**) which strongly indicates that the dye-loaded nanospheres were efficiently uptaken by the cells and were release rapidly under a well-controllable manner within the cells. The dye molecules were also illustrated a well-controlled non-release behavior during the time period of the test. Therefore, we envision from the appearance of healthy intact and the visibility of fully grown cells suggested that the nanospheres are biocompatible *in vitro* under experimental conditions and precisely released desirable molecule for therapeutic purposes.

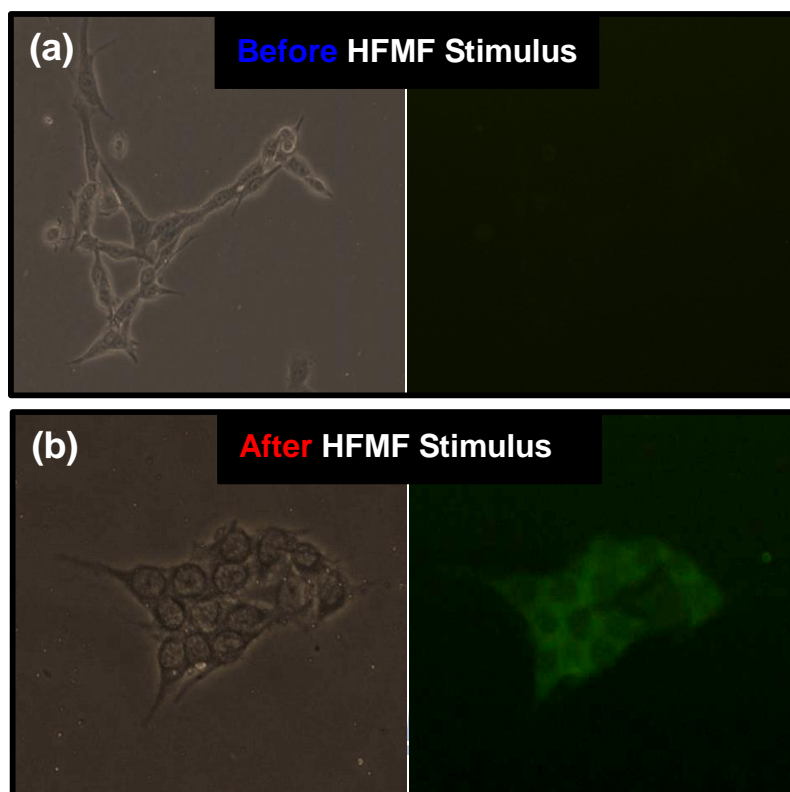


Figure 5.6 Fluorescence micrographs of HeLa cells after 10 hours incubation with fluorescence-loaded PVP-modified Silica/Fe₃O₄ core-shell nanospheres. (a) without HFMF treatment; (b) after 30 seconds of HFMF stimulus, green fluorescence was clearly observed within the cell bodies of these HeLa cells upon excitation at 494 nm.

5.8 Specific power absorption rate (SAR) of nanocapsules

Functional magnetic nano-capsules (f-MNCs) can provide dual effect to therapy cancer; one is to magnetically control drug release in specific site, and the other is hyperthermia treatment of cancer. When the magnetic nanoparticles were subjected to a high-frequency magnetic field (HFMF), the resulting eddy current, hysteresis, and Brownian rotational losses can produced a source of heat capable of imparting cell death. The ability to combine MRI contrast enhancement and therapy in the form of hyperthermia and controlled drug release as well as the possibility of functionalizing particles specific to biomarkers may further advance the use of magnetic nanoparticles in biomedical application. To further understand the ability of hyperthermia of f-MNCs, the different strength of high-frequency magnetic field

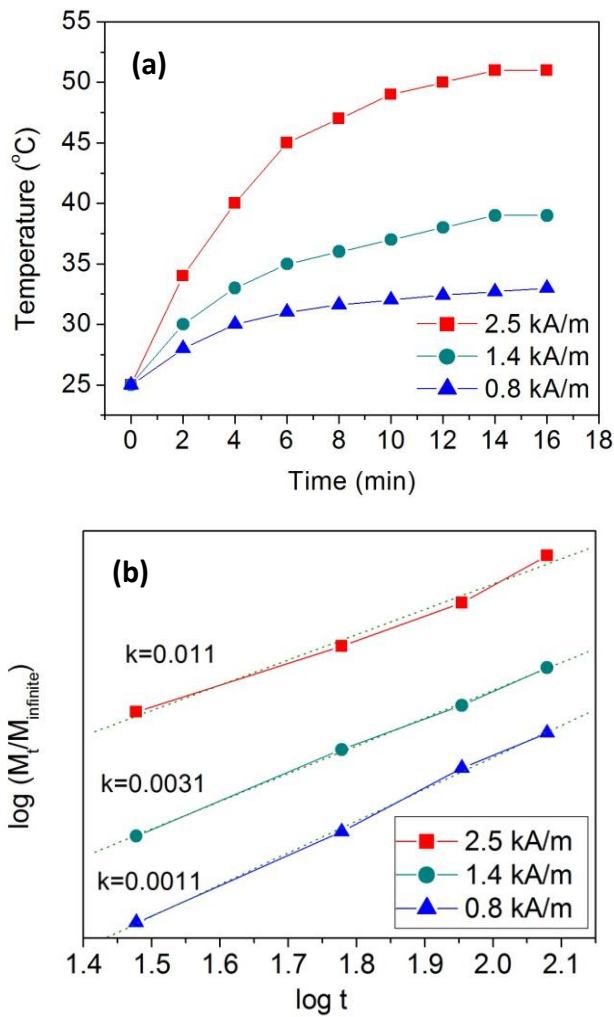


Figure 5.7 (a) Temperature curve of nanocapsules during application of HFMFs. (b) Drug release behaviors of nanocapsules under HFMFs, and their release rates (k).

was used. The heating field is always generated by AC typically in the radio-frequency (RF) range, $10^4 \sim 10^5$ Hz. Because an AC field can produce an eddy current, induction heating is always feasible for conductor, and it exhibits more efficient for a magnetic material in which magnetic hysteresis causes additional energy dissipation. To enhance the sum of eddy current heating and magnetic heating, the relative large magnetic coercivity (mainly due to the resistance to domain wall movement) is preferred. However, functional magnetic nano-capsules (f-MNCs) are superparamagnetic because of the single-crystalline and the particle size, it is a

Table 1 The specific power absorption rates (SAR) of functional magnetic nanocapsules (f-MNCs) under the specific strength of magnetic field. H is the strength of magnetic field with an alternating frequency of 50 kHz. dT/dt is the initial heating rate, and C is the specific capacity of f-MNCs.

H (kA/m)	dT/dt	C (J/gK)	SAR (W/g)	k	R ²
0.8	1.25	1.04	1.30	0.0011	0.986
1.4	2.00	1.04	2.07	0.0031	0.998
2.0	2.9	1.03	3.00	0.0061	0.998
2.5	3.75	1.04	3.89	0.011	0.998

single-domain ferromagnet free to switch following a quasi-state field without apparent coercivity. There is only little coercivity contribution, so the energy dissipation must come from some sort of internal or boundary “friction” which drags the magnetic moment letting it lag the AC field. In linear-response medium, the Debye theory describes this lag in terms of a relaxation time. Under magnetic heating, the temperature of the f-MNCs solution gradually rises reaching a steady of several to several tens of degrees of centigrade higher. At this temperature, the heat of f-MNCs absorption equals the heat loss at the external boundary (container, solution). The initial heating rate of magnetic dissipation is informative, the order of 0.1°C/s to 0.5°C/s for f-MNCs, which is depending on the strength of magnetic field. As shown in **Figure 5.7a**, while applying the magnetic-field strength of 2.5 kA/m, the temperature of the solution increased about 25 °C in 10 minutes. In order to compare the energy absorption and drug release behavior of f-MNCs induced by the high-frequency magnetic field, the specific power absorption rate (SAR) was calculated. The SAR values of magnetic fluids strongly depend on the alternating magnetic field and the magnetic fluids properties, such as particle size, size distribution, anisotropy constant, saturation magnetization. In our study, a high frequency magnetic field with different strength at 50 kHz was applied to the functional magnetic nano-capsules (f-MNCs). The SAR of a magnetic fluid is

determined by the initial linear temperature rise of a fluid measured after subjecting to the magnetic field:

$$SAR = C\left(\frac{\Delta T}{\Delta t}\right) \quad (1)$$

where C is the heat capacity of the sample and ($\Delta T/\Delta t$) is the initial slope of the temperature data. The SAR values were summarized in **Table 5.1** to further compare with the drug release behaviors. To investigate the release mechanism of the drug molecules in the f-MNCs, the drug released data were characterized using Eq. (2): [30]

$$\frac{M_t}{M} = kt^n \quad (2)$$

where M_t is the mass of drug released at time t, M is the mass released at time infinity, and M_t/M is the fractional mass of released drug; k is a rate constant, and n is a characteristic exponent related to the mode of transport of the drug molecules. By taking logarithm on both sides of Eq. (2), Eq. (3) can be used to calculate the diffusion parameters (i.e., n and k) for $M_t/M < 0.6$.

$$\log\left(\frac{M_t}{M}\right) = n \log t + \log k \quad (3)$$

The cumulative concentrations of released drug at time t and at the end of the experiment (to approximate the infinite time) were used to calculate M_t/M . To demonstrate the drug release behavior, the model drug (fluorescence dye) was encapsulated in the f-MNCs. While subjecting the f-MNCs to different strength of magnetic HFMF, the burst drug release was observed from the nanocapsules measured by PL spectroscopy. After 3-min period operation of HFMF, the cumulative release of f-MNCs can reach to 87 % under strength of 2.5 kA/m. With decreasing power of magnetic field to trigger drug release, the cumulative release of f-MNCs showed a relative lower amount, suggesting the release rate is high corresponding to the magnetic field power. More interestingly, the release profile of the f-MNCs

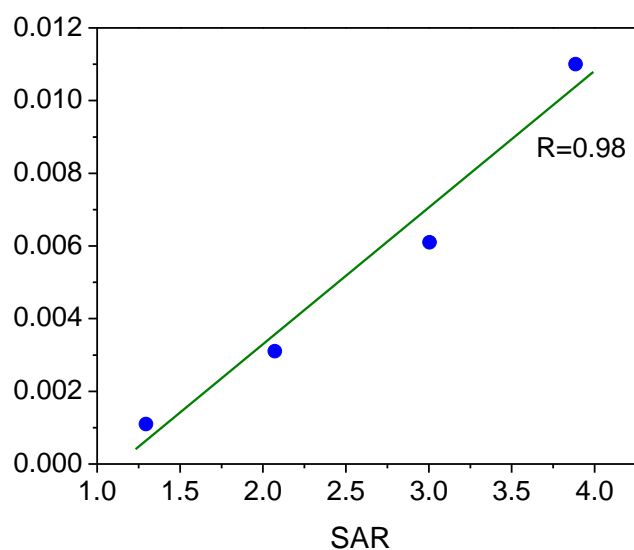


Figure 5.8 A near-linear relationship between the rate constant k and SAR values, with correlation coefficient as high as 0.98 can be obtained.

displayed a zero-order release pattern under the stimulus. In other words, the drug molecules released from the nanocarriers, albeit in a burst-like profile under HFMF stimulus, can still be well regulated with a controllable dosage. By taking Eq. (3), a kinetic analysis of drug release from the f-MNCs can be obtained, as shown in **Figure 5.7b**, where release kinetics under different strength of magnetic field treatment. Both exponent constant, n and rate constant k , are estimated. For the release kinetics, the exponent constant is in a range of 0.83-1.05, indicating the release mode under the high-frequency magnetic field (HFMF) treatment similar. However, the n values under the HFMF can not be explained by typical diffusion mode because an external energy powerfully controlled the release behaviors. The rate constant, k , for f-MNCs under strong magnetic field (2.5 kA/m) is apparently higher than others, indicating that the strength highly affects the burst release property. With the decreasing the strength of magnetic field, the rate constants relatively decreased. In order to compare the relation between strength of magnetic field and release rate, SAR values were defined as the energy that the external magnetic field donated to nanoparticles because SAR values can express the energy absorption of nanoparticles. The resulting

correlations of the magnetically-induced drug release rate are given in **Figure 5.8**, where a near-linear relationship between the rate constant k and SAR values, with correlation coefficient as high as 0.98 can be obtained. The finding strongly suggests, albeit the heating production and the drug release behavior were seemingly independent, that drug release rate from the f-MNCs can be correlated over a relatively high precision with SAR value. To this end, we can use the SAR values calculated by the energy absorption of f-MNCs to estimate the drug release rate in specific strength range of magnetic-field based on this newly-designed drug nano-carriers may also adopted for cellular or animal systems in the future.

Applying magnetic field to trigger drug release from nanocapsules is a convenient way because it is a non-contact energy for a specific-site therapy. However, the intensity of magnetic field is not easy to form uniformly in the magnetic coil, especially for large volume of magnetic field. For this reason, a 9-cm diameter of magnetic field was estimated to understand the different regions of magnetic strength and the relative drug release behaviors of nanocapsules in the cell. First, as shown in **Figure 5.9**, the magnetic field was divided into 5 regions from center defined by specific power absorption rates (SAR). The highest SAR is 3 W/g in the red region of center, and the magnetic strength gradually decreased from red region to the blue region of 1.4 W/g. The f-MNCs was uptaken through the endocytosis in the the A549 cell lines by incubating of 12 hours.

The possible mechanism of magnetically-triggered drug release from functional magnetic nanocapsules (f-MNCs) has been conjectured in our previous report. The high frequency magnetic field (HFMF) is able to induce vibration of the magnetic shell, resulting that an irreversible change of the core-shell nanostructure if the physical deformation is large enough to cause the permanent damage under long-term MF treatment. To further investigate the behaviors of the deformation or even rupture of the f-MNCs, the HFMF treatment and directly-heating the nano-capsules were

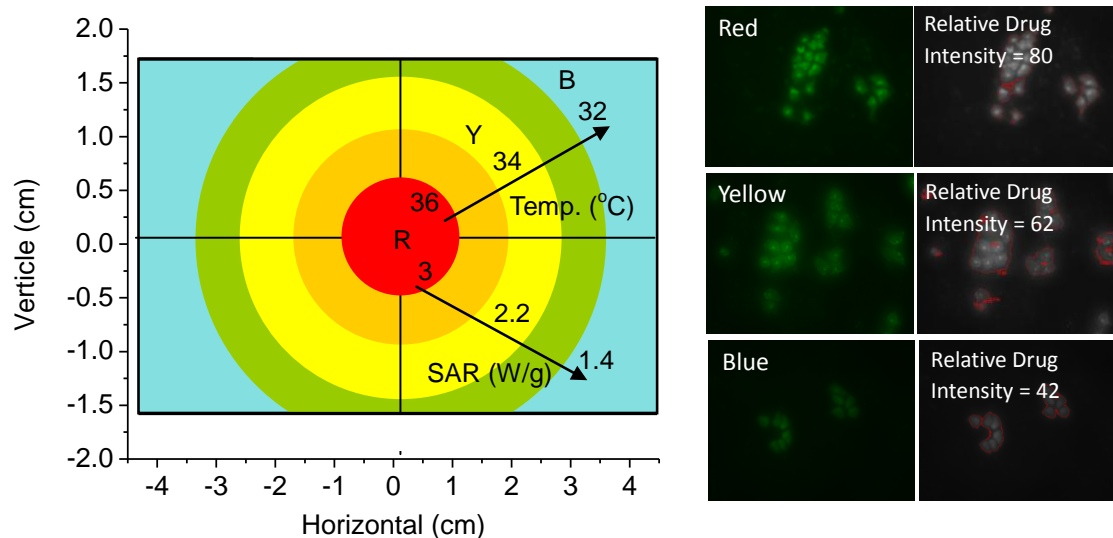


Figure 5.9 SAR effects on the different magnetic field regions. Drug release behaviors in cells are highly relative with the strength of SAR.

carried out individually in this study to interpret the effect of heat and magnetically-induced force to the nanostructure. To estimate the temperature of the f-MNCs after the HFMF treatment, the initial heating rate of magnetic dissipation is informative, the order of 0.1°C/s to 0.5°C/s for f-MNCs, which is depending on the strength of magnetic field. Since the energy input of the solution is entirely from the energy input of the magnetic nanoparticles, the temperature of the f-MNC should be calculated by the thermodynamic relationship, $\Delta H = m_w C_w \Delta T_w = m_m C_m \Delta T_m$. Here C_w and C_m are the specific heat capacity of water and the magnetic material, respectively, and m is the weight. If without any heat transport to the surrounding water, the temperature of the f-MNCs after subjecting the HFMF for 1 min can rise to 200°C under the strength of 2.5 kA/m . However, the high specific surface area of the nanocarriers would rapidly decrease their temperature through the heat transfer to the surrounding solution so the temperature of the particles should be much lower than the theory calculation. After subjecting the f-MNCs to the HFMF for 15 minutes, the crystallographic phase was examined by the X-ray diffractometer, at a scanning rate of 6° per minute. The X-ray diffraction patterns exhibited the similar crystalline

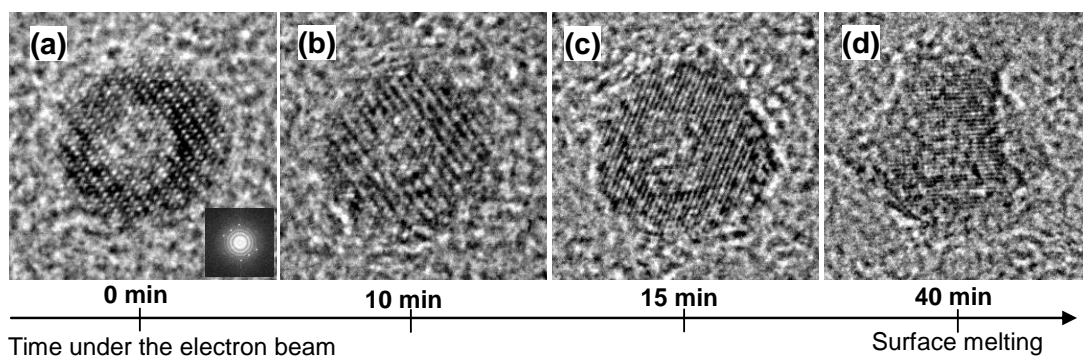


Figure 5.10 The TEM electron beam is focus on the nanocapsule for different time durations. While increasing the heating time to 40 minutes, the obvious deformation of melting was observed.

phases of f-MNCs with different time of HFMF treatment, which are Fe_3O_4 (magnetite, according to JCPDS [85-1436]). The finding demonstrated that the temperature of the f-MNCs under the HFMF is lower than the temperature of the iron oxide phase transition, indicating the f-MNCs still maintain low temperature even under the long-term of HFMF treatment. In order to understand the behaviors of the f-MNCs with heating, the high-resolution transmission electron microscopy (HR-TEM) was applied to continue focusing on the nanoparticles for 40 minutes, and the images were monitored as shown in **Figure 5.10**. In such high magnification of TEM images, the electron beam can rapidly heat the nanoparticles more than $200\text{ }^\circ\text{C}$ within 10 minutes. With continue focusing for 10 minutes, the morphology of the nanocapsule was still similar to the original one. However, in Figure 3c, increasing to 15 minutes of electron beam heating, the surface of nanocapsules starts to slight melt. While increasing the heating time to 40 minutes, the obvious deformation of melting was observed. These results demonstrated that the heat can only melt the nanocapsules, but not to crack the nanocapsules. The phenomena of heat melting and cracking inducing by HFMF are significantly different, suggesting that HFMF probably provided energy to induce some mechanical force in the inner structure of magnetic nanocapsules, and then to rupture the structures. Some sort of internal or

boundary “friction” were believed to drags the magnetic moment with the Néel relaxation which implied the magnetic moment rotates within the crystal.^[27] This inner energy can cause the unstable boundaries of nanocapsules to crack or even rupture, especially in the ultra-thin magnetic shells. Such a nanostructural evolution under HFMF stimulus surely enhances the burst release behavior from the magnetic nanocapsules.

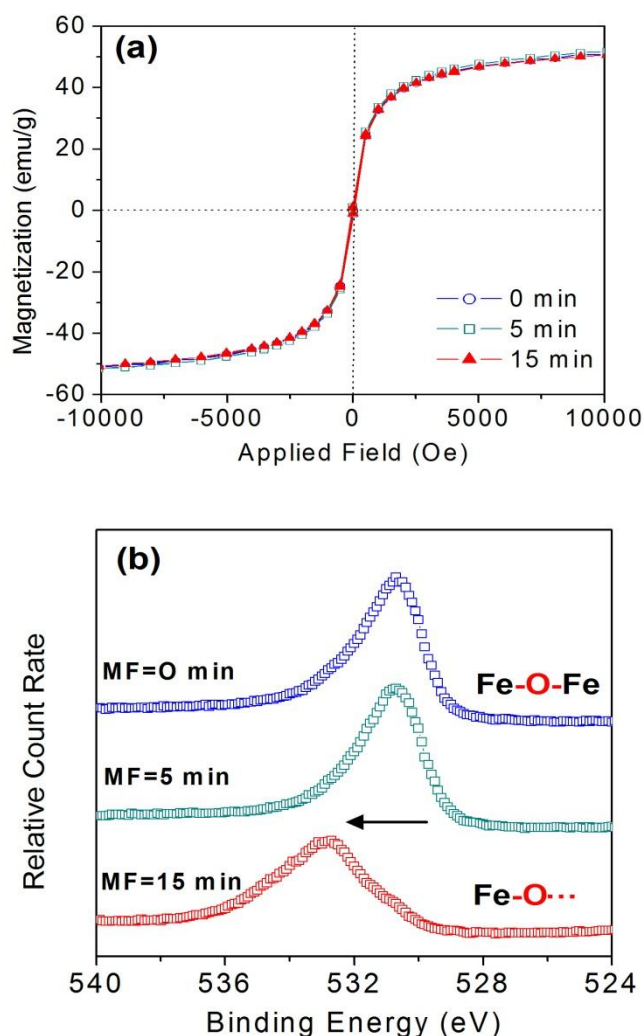


Figure 5.11 (a) Field-dependent magnetization curve and (b) XPS analysis of nanocapsules for different time of HFMF treatment.

The magnetic property of functional magnetic nanocapsules (f-MNCs) was estimated by SQUID at 298 K with the magnetic field sweeping from -10000 to +10000 G. **Figure 5.11a** shows the correlation of the magnetization with magnetic

field for functional magnetic nanocapsules (f-MNCs) with different duration time of HFMF treatments, where the curves show similar shape with negligible hysteresis. The result shows there is no obviously difference between magnetic properties with the HFMF treatment, indicating that the nanocapsules didn't change the crystal phase or chemical states. This finding is also corresponding to the XRD results as previous section discussion. In this duration of HFMF treatment, the nanocapsules can receive enough energy to rupture or crack but not to cause phase transfer, demonstrating the inner force produced by Néel relaxation leading a strong physical destruction. X-ray photoelectron spectroscopy (XPS) was employed to clarify surface chemistry of the f-MNCs after magnetic induction. A change in the binding energy spectrum of O 1s, **Figure 5.12b**, of the f-MNCs from 529 eV (before the stimulus) to 533 eV (after the stimulus) is clearly detected. The peak of iron oxide was at 529 eV, which is reasonably consistent with literature report, i.e., 528-531 eV. After applying HFMF for 15 minutes, some of the Fe-O-Fe bonds were broken, and different binding of oxide appeared, which represented the oxide binding to the hydroxide. The finding suggested that new interfaces between iron oxide shells and water produced after long-term HFMF treatment, in the other words, the nanocapsules cracked and then to cause these new interfaces.

In conclusion, we have demonstrated a novel functional magnetic nanocapsule (f-MNC) with polymer core following a functional deposition of a single-crystal iron oxide shell. Through an external high-frequency magnetic field, these f-MNCs offer an excellent controlled release behavior for molecules encapsulated inside the polymer core by a non-contact force. By the specific power absorption rate (SAR) values investigate previously, the precise drug release rate can be predicted in the body. It is envisioned that the drug of interest can be released in precise dosage in a remotely controlled manner or burst as the shell being ruptured when reached the diseased sites. On the other hand, the mechanisms of f-MNCs rupture were examined

through heating directly and applying magnetic field. The results demonstrated that the heat induced by HFMF only can melt the iron oxide but not to crack the nanostructures, indicating the HFMF provided an inner mechanical force to rupture the nanocapsules. From this study, we envision that these f-MNCs are expected to play a significant role in the development of new generation of site-specific controlled-release drug delivery nano-device.

5.8 Summary

In conclusion, we have demonstrated a novel core-shell nanosphere with PVP-modified silica core following a functional deposition of a single-crystal iron oxide shell. Such a core-shell nanosphere offers a surprisingly outstanding controlled release and non-release behavior for the molecules encapsulated inside the silica core. The dense, single crystalline shell is efficiently preventing the fluorescence dye from un-desired release, giving that an undesirable leakage of the molecule during the course of delivery is completely inhibited. More than that, the molecules encapsulated in the core can be released with a highly controllable manner, through the use of a magnetic stimulus. It is envisioned that the drug of interest can be released in précised dosage in a remotely controlled manner or burst as the shell being ruptured when reached the diseased sites. We also envision from this study that these core-shell nanospheres are expected to play a significant role in the development of new generation of site-specific controlled-release drug delivery nano-device.

Chapter 6

A Multifunctional Nanodevice capable of Imaging, Magnetically Controlling, and In-situ Monitoring Drug Release

6.1 Introduction

Surface modification with functional attachments is a widely used technical strategy to enhance biological, optical and chemical functionality of materials in a wide variety of biomedical applications, such as imaging, diagnosis, drug delivery, implants, and so on. Recently, the development of multifunctional, nanomedical platforms, through skillful combination of different nanostructured materials, has been proposed. Owing to the specific advantages of these nanomaterials, many studies have been done on multimodal imaging and simultaneous therapy. For example, magnetic nanoparticles were infused with fluorescent dye to construct multimodal imaging probes. Among the many nanoparticulate systems, semiconductor nanocrystals known as quantum dots (QDs) confer advantages over traditional fluorescent molecules, such as organic dyes. This is because of their unique optical properties, including narrow photoluminescence spectra, low photo-leaching, and high resistance to chemical degradation. QDs have also been reported to carry therapeutic agents for healing applications. The combination of both imaging and therapeutic functions in nanoparticles introduces an attractive advance in the field of biomedicine, diagnosis, and pharmaceuticals.

However, there has been little investigation into fast-response, controlled drug release from nano-platforms under magnetic stimulation, or monitoring of the release of therapeutic molecules in a quantitative manner. Therefore, an integration of these functions will be technically significant in developing a multifunctional nanodevice capable of simultaneous imaging, controlled drug delivery and in-situ monitoring of

drug release with molecular resolution.

In our earlier research, we developed a new type of magnetic core-shell nanocapsule which allows active molecules to be expelled in the presence of a remotely controlled magnetic field. The active molecules released from the nanocapsules can be finely tuned according to exposure time in the magnetic field. However, it would be desirable to further engineer the nanocapsules to monitor the release of active molecules at nanometric or cellular resolution. We also believe that a nanocapsule should be able to provide easily monitored, high-resolution optical information, viewable via simple spectroscopic methods, rather than conventional MRI imaging. On this basis, here, we designed a new drug delivery nanodevice by deposition of quantum dots (QDs), i.e., Zn-Cu-In-S (ZCIS) nanocrystals, onto the surface of a core-shell drug delivery nanocapsules recently developed, to form a nanometric multifunctional platform. The core-shell nanocapsule consists of a polymer core covered with a thin layer of single-crystal iron oxide shell. This unique core-shell structure offers great therapeutic potential for controllable drug release, with a dosage controlled via an external magnetic field. The quantum dots deposited on the surface of the magnetic nanoparticles are used for directly monitoring the release of the drugs. This is achieved by observing variations in the fluorescence intensity of quantum dots. The fluorescence intensity of quantum dots varies with absorption of thermal energy matching the excitation binding energy of QDs. Free carriers generated by exciton dissociation can tunnel between nearby QDs, causing a decrease in the fluorescence intensity. While the QDs are attached to the surface of the magnetic nanoparticles, the heat energy induced by the external HFMF can transfer from the magnetic shell to QDs via magnetic nanoparticles. Since this design is conceptually and technically achievable, it is further believed that the attachment of the ZCIS QDs on the surface of the nanocapsules may act not only as a strong

fluorescence-emitting agent, but also as a nanometric sensor to monitor drug release, in real-time, within a magnetic field.

6.2 Experimental section of multifunctional nanodevices

Preparation of the nanodevices. Synthesis of the PVP-Fe₃O₄ core/shell nanospheres was reported in the previous section. To encapsulate the model drug, fluorescence molecules, in the polymer matrix, 4 Wt. % Polyvinylpyrrolidone (PVP; Mw~10,000; Sigma) was dissolved in D.I. water and preheated to 80 °C. Then fluorescence molecules were added into the solution and mixed for 6 hours. In suitable concentrations, the PVP will assembly themselves as nanospheres in the solution, forming drug-loaded PVP nanoparticles. Under nitrogen atmosphere, FeCl₃·6H₂O and FeCl₂·4H₂O with a FeCl₂/FeCl₃ molar ratio of 2:1 were dissolved into water and mixed with the drug-loaded PVP nanoparticles under vigorous stirring at 80 °C. After 4 hr, the iron salts were deposited on the surface of the drug-loaded PVP nanoparticles. This was achieved via slow addition of 2 ml of ammonium water (NH₄OH, 33%), causing precipitation so that iron oxide shells were immediately formed on the surface of PVP nanoparticles. At this stage, a drug-loaded PVP core-iron oxide shell nanosphere exists in the solution. Precipitated powders were collected by centrifugation at 6000 rpm, removed from the solution, and washed in D.I. water four times. The PVP-Fe₃O₄ core/shell nanospheres were separated by the centrifugation. The average diameter of the core-shell nanospheres was about 12-20 nm.

To grow the ZCIS quantum dots on the surface of the PVP-Fe₃O₄ core/shell nanospheres, they were re-dispersed in trioctylphosphine (TOP, 90%, technical grade) with diethyldithiocarbamic acid zinc salt, [(C₂H₅)₂NCSS]₂Zn. The solution was diluted with octadecene (ODE, 90%, technical grade) to form Solution 1. Then, CuCl

and InCl_3 were dissolved in oleylamine at 50°C to form Solution 2. The two solutions were mixed and heated to 140°C in a nitrogen atmosphere for several minutes. Deposition of quantum dots (QDs) on the surface of the PVP/ Fe_3O_4 core-shell nanospheres caused the solution to turn yellow.

Characterization. X-ray photoelectron spectroscopy (XPS) was performed in an ESCALAB 250 (Thermo VG Scientific, West Sussex, UK), equipped with Mg $K\alpha$ at 1253.6 eV at the anode. The chemical shifts of the XPS peaks were standardized with respect to C 1s peak at 284.6 eV.

Cell Culture and In-Situ Monitoring of Drug Release. HeLa, human cervical cancer cells, were maintained in Dulbecco's modified Eagle's medium (DMEM) with 10% fetal bovine serum, 100 units/mL penicillin, and 100 $\mu\text{g}/\text{mL}$ streptomycin. Cells were cultured at 37°C in a humidified atmosphere of 5% CO_2 in air. The nanodevices were incubated with the cells for 12 hours. The cells were then subjected to a high frequency magnetic field (HFMF) for 0, 90 and 180 sec. Results were observed by PL microscopy (Nikon TE-2000U, Japan). Digital analysis software (Nikon, Japan) was used to analyze the fluorescence intensities of the model drug and the nanodevices. The conditions of exposure were the same for each color channel. Analysis was done by Nikon C1 software, which defined the fluorescence intensity from 1 to 255. The range of the fluorescence intensities were: Blue channel (60-255), Green channel (40-255), and Red channel (30-255).

6.3 Structures of multifunctional nanodevices

The procedure for synthesis of magnetic nanocarriers is schematically illustrated in **Figure 6.1a**. Poly-(N-vinyl-2-pyrrolidone) (PVP) nanoparticles containing a test molecule, such as fluorescent dye, were prepared through a self-assembly process in benzyl ether. After self-assembly, the PVP molecules are aggregated into a micelle

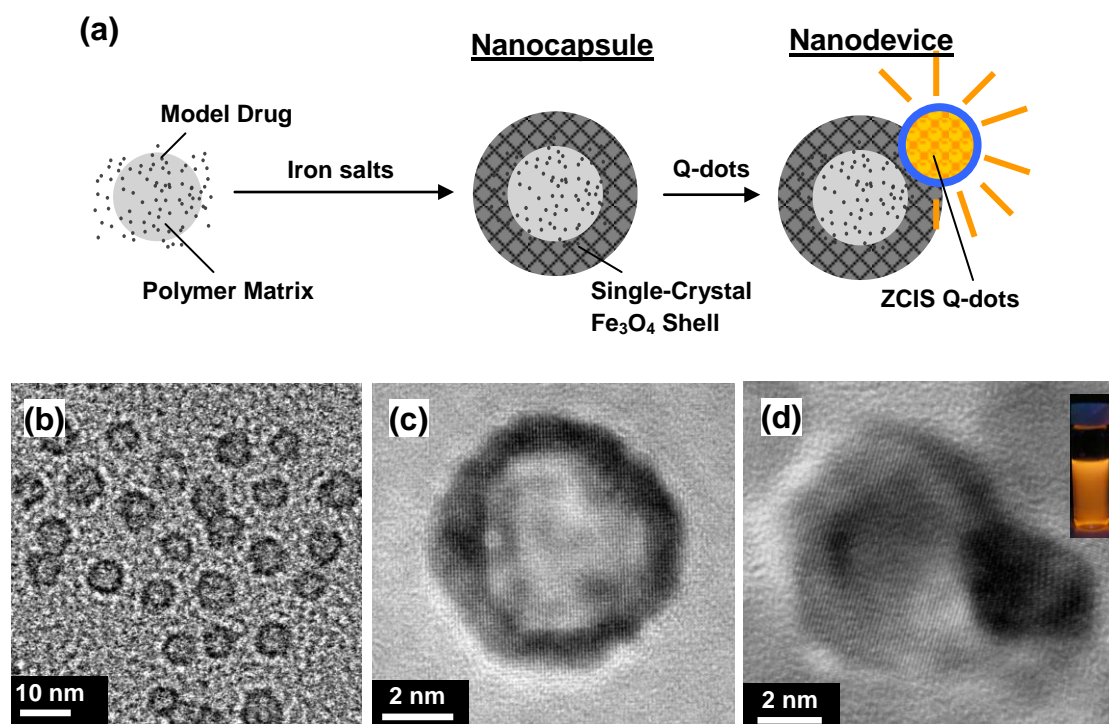


Figure 6.1 (a) Schematic of the stimuli-response nanodevice delivery system where quantum dots were deposited on the shell of the PVP/Fe₃O₄ core-shell nanospheres. Attachment of the ZCIS QDs on the surface of the nanospheres acts not only as a strong fluorescence-emitting agent, but also as a sensor to monitor the drug release in a real-time basis under magnetic induction. (b) TEM image and (c) HRTEM image of the PVP-Fe₃O₄ core-shell nanospheres. (d) HRTEM image of the ZCIS-doped nanospheres. After incorporation of the ZCIS QDs on the core-shell nanospheres, the suspension displayed a fluorescence character under the UV light (inset picture).

structure. Drug molecules are embedded within the amphiphilic nature of the PVP. Following micelle formation, a thin layer of iron oxide, is deposited on the core surface in single-crystal form. The resulting PVP-Fe₃O₄ core-shell nanocapsules, shown in **Figure 6.1b**, display a spherical geometry ranging from 10 nm to 15 nm in diameter. High-resolution transmission electron microscopy (HR-TEM), shown in **Figure 6.1c** and in the supporting information of **Figure 6.2**, confirms that the structure of the nanospheres is an amorphous core and a thin single-crystal shell which suggests self-organization of the iron oxide precursor upon nucleation and

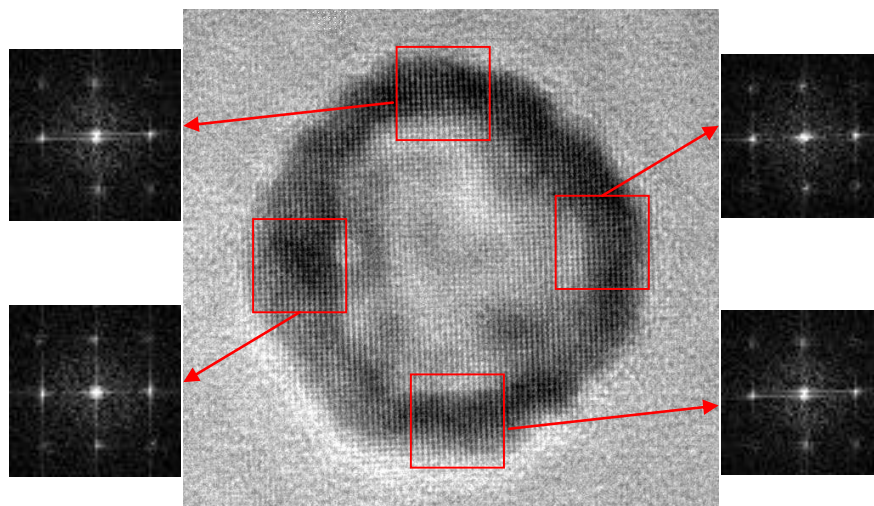


Figure 6.2 Local Fourier transfer patterns of single-crystal iron oxide shell indicate that the shell exhibits uniform and homogenous crystalline orderliness along the surface of the core phase.

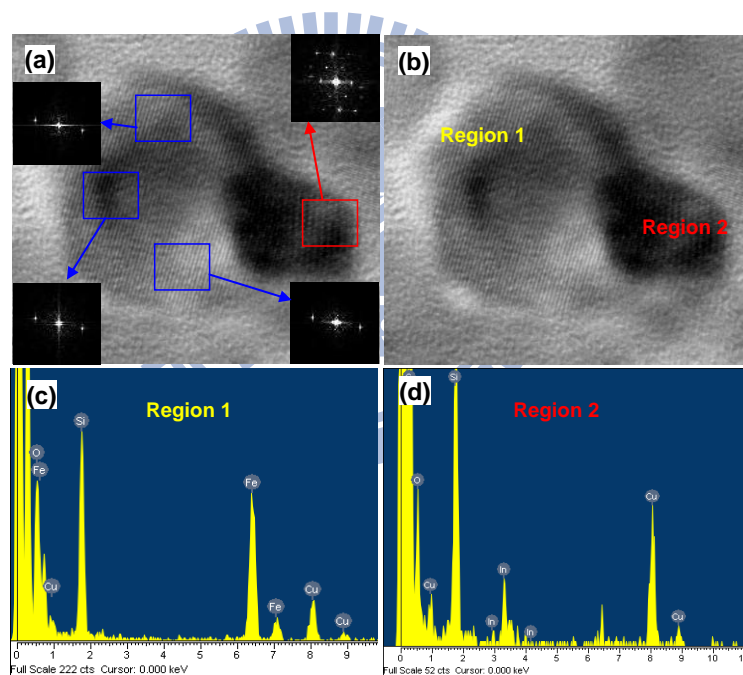


Figure 6.3 (a) The TEM image and local Fourier transfer patterns of ZCIS QD-Single crystal Fe_3O_4 shell nanoplateform. The local Fourier transfer pattern also demonstrated a high crystallinity of the ZCIS QD. (b) The HRTEM image of CIS QD-Single crystal Fe_3O_4 shell nanoplateform. The EDS investigated the Fe_3O_4 shell and ZCIS QD, corresponding to the regions 1 and 2 in the HRTEM image, respectively. HRTEM image shows the solid nanoparticle attaching the ring-like shell region being ZCIS QDs in the heterodimer. The energy dispersive X-ray spectrometer (EDS) analysis confirms that the ring-like region mainly consists of Fe and the small solid particle consists of Cu and Se.

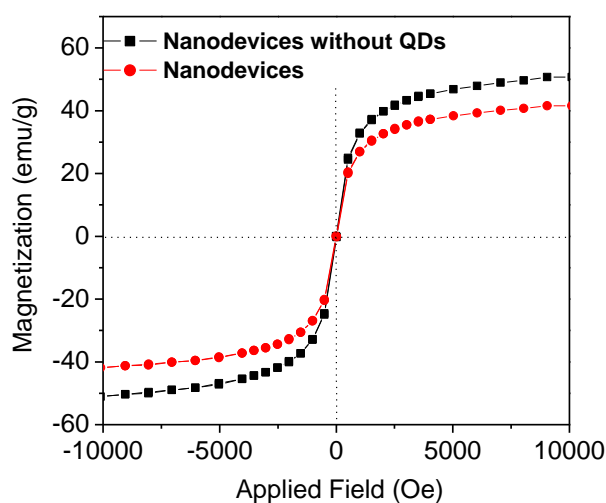


Figure 6.4 Field-dependent magnetization curve of nanodevices with and without quantum dots.

growth in the presence of the PVP. Although limited to metallic crystals, this agrees with an earlier study of a similar synthesis scenario. In the current core-shell system, iron ions can be efficiently anchored onto the pyrrolidone ring of PVP. This provides epitaxial-like growth of the oxide to form single-crystal structure. After the core-shell nanocapsules were synthesized, ZCIS quantum dots were prepared and grown on the shell surface. A procedure described by Nakamura et al. is used to form Fe_3O_4 shell-ZCIS heterodimers.^[147] An HRTEM image, shown in **Figure 6.1d**, shows the solid particle residing on the ring-like shell, corresponding to a ZCIS heterodimer. Energy dispersive X-ray spectrometer (EDS) analysis confirms that the ring-like region mainly consists of Fe and the small solid particle consists of Cu and S shown in the **Figure 6.3**. The local Fourier transfer pattern also demonstrates a high crystallinity of the ZCIS QD. After incorporation of the ZCIS QDs onto the shells, the resulting suspension shows a strong yellow appearance under UV exposure. This can be seen in the inset picture of Figure 1d and suggests that these ZCIS-modified nanocapsules (hereafter called nanodevices) can be used not only as drug nanocarriers,

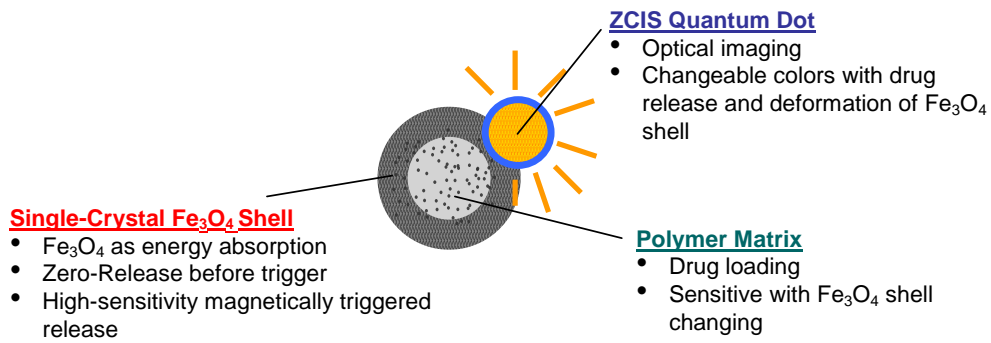


Figure 6.5 Schematic drawing showing multi-functionalities of each compartment from as-designed nanodevices for nanoimaging, controlled drug release, and in-situ motoring of drug release.

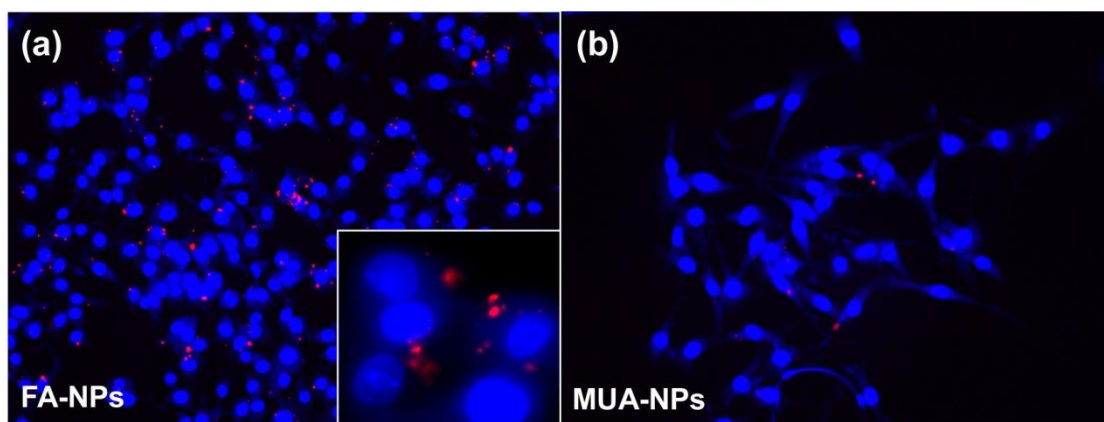
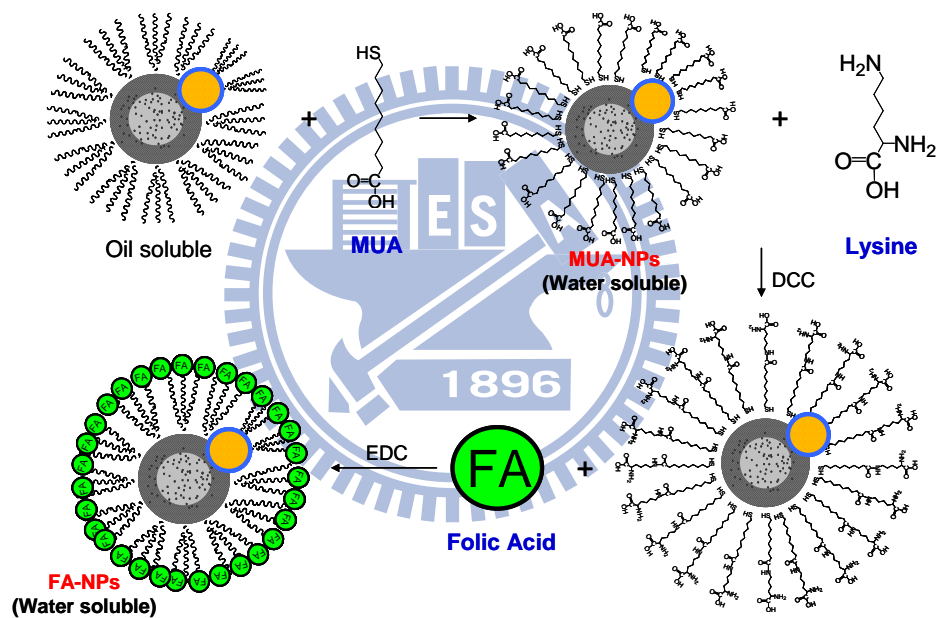


Figure 6.6 Cellular uptake of the nanodevice was evaluated using HeLa cells, by incubating the cell line with both mercaptoundecanoic acid-modified nanodevice (MUA-NDs) and folic

acid-modified nanodevice (FA-NDs). Both the MUA-NDs and FA-NDs were uptaken by the cells in 4 hours of period, probably through endocytosis, with different degrees of efficiency. In comparison, the majority of the FA-NDs can be clearly observed in the cytoplasm region of the cell, but only a few MUA-NDs was uptaken by HeLa cells, indicating that the folic acid-modified version promotes a stronger cell-specific intake by the HeLa cell line than that of the mercaptoundecanoic acid-modified version. The folic-acid-modified nanodevices showed excellent cell-specific uptake efficiency, through possibly endocytosis.

but also as nano-probes for imaging. (**Figure 6.5**) The magnetic properties of the nanodevices and nanocapsules were measured by SQUID at 298 K, with the magnetic field sweeping from -10000 to +10000 G. The correlation of magnetization with magnetic field for both the nanodevices and the nanocapsules, shown in **Figure 6.4**, demonstrates a similar shape with negligible hysteresis, showing superparamagnetic behavior. The saturation magnetization (M_s) of the nanodevices is smaller than that of the nanocapsules, due to dilution effect.

6.4 Drug release and in-situ monitoring abilities of the nanodevices

The nanodevices were surface-modified and conjugated with a targeting ligand, folic acid (FA), to cause hydrophilic behavior. The process is illustrated in **Figure 6.6**. After modification of the nanodevices, a stable aqueous suspension was prepared. The fluorescence spectrum of the ZCIS remained identical to the initial preparation, indicating that folic acid imparts no adverse effect on the optical properties of the ZCIS QDs. The suspension was subjected to a high frequency magnetic field (HFMF) for investigation of the drug release mechanism. Prior to magnetic stimulation, the green-fluorescence loaded nanocapsules showed no sign of release in 24 hours of storage in an ambient environment. This was confirmed via PL spectroscopic monitoring and suggests that the dye molecules are encapsulated in the core phase for a long period of time without any unwanted leakage. However, subjection to the

HFMF for varying lengths of time, as shown in **Figure 6.7a**, reveals an interesting phenomenon. The intensity of the dye emission peak at 517 nm increased with the duration of the magnetic field. In contrast, the intensity of the emission peak from the ZCIS QDs showed an opposite relationship, a decrease in emission intensity. The increase in peak intensity with time upon magnetic stimulation indicates a magnetically-induced release of dye molecules from the nanodevices. In a recent

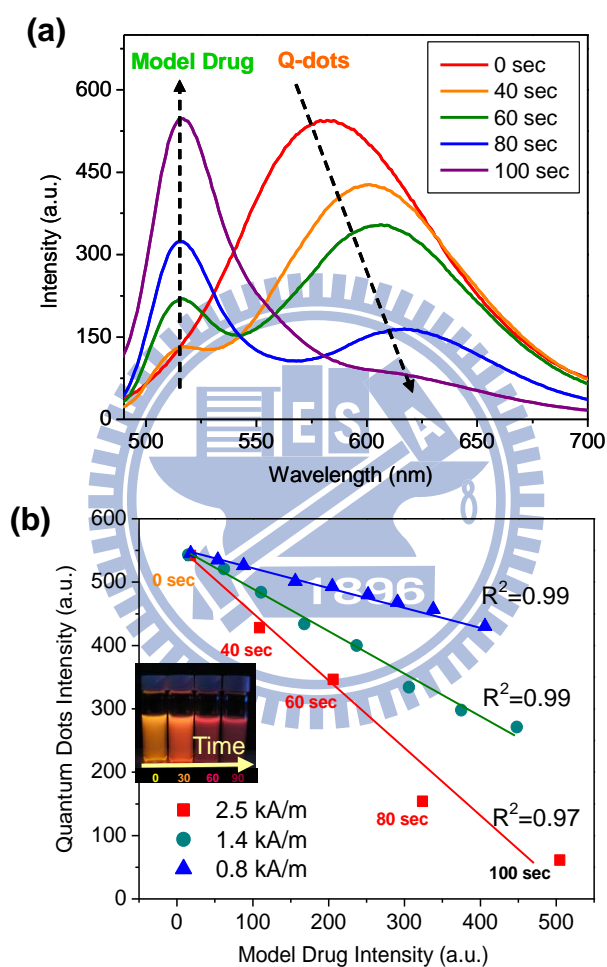


Figure 6.7 (a) Emission spectra of dye-loaded nanodevices (30 mg per 10 mL water) under HFMF treatment over a time period from 0 s to 100 s. Before HFMF exposure, the dye-loaded nanodevices displayed no sign of dye release, which causes green fluorescence at an emission wavelength of 517 nm, as determined by fluorescence spectrophotometer. However, a strong emission signal from the QDs after exposure, red fluorescence at an emission wavelength of 581-614 nm, show that dye was released from the nanodevices. A degenerative green fluorescence appeared concurrently. (b) Model drug intensity versus quantum dot intensity curves originate from both the dye and ZCIS emitting spectra and show a near symmetrical profile under different magnetic field strengths.

study, such a release can be easily and precisely controlled with manipulation of the surrounding magnetic field; from a burst-like profile upon stimulation to a zero release profile immediately after removal of the magnetic field. The emission peak from the ZCIS quantum dots showed strong PL intensity at the beginning of the stimulus. However, as time elapsed, a gradual reduction in peak intensity together with a red shift of the PL spectra for the QDs was clearly detected over an operation time of 100 seconds. The peaks for the dye and QDs reacted oppositely under the same magnetic stimulus, implying a potential correlation of both spectra.

Bias may arise when determining whether the correlation is simply coincidence or a rule in this nanosystem. To avoid this, magnetic fields of varying intensities were applied. This aimed at determining whether the correlation of the spectra between drug release and quantum dot emission is sustainable over a range of operating intensities, from 0.8 kA/m to 2.5 kA/m in the current magnetic system. The resulting correlation in the magnetically-induced changes of spectra are given in **Figure 6.7b**. There exists a linear relationship between the spectral intensity of dye molecules and the QD emission. The correlation coefficient over a range of the data reaches 0.97-0.99 and can be obtained for different magnetic intensities. The quantity of drug released relied mainly on the strength of magnetic field under short-term induction. This implies that a weaker magnetic field results in the slower release of drugs. A linear relationship exists over the entire range of operating conditions. Although the emission spectra were measured from two independent sources, this finding strongly suggests that the drug release from the nanodevice can be quantitatively correlated with in-vitro, doped ZCIS QDs. to high precision. Dye release can be precisely monitored along with the spectral variation of the ZCIS QDs from the nanodevices. This finding is in agreement with the hypothesis that two independent mechanisms can be triggered simultaneously from a given magnetic field, and that the mechanisms

will also be quantitatively correlated. We believe that this highly correlated relationship may also be adopted for in-situ monitoring of cellular systems. This will be explained further.

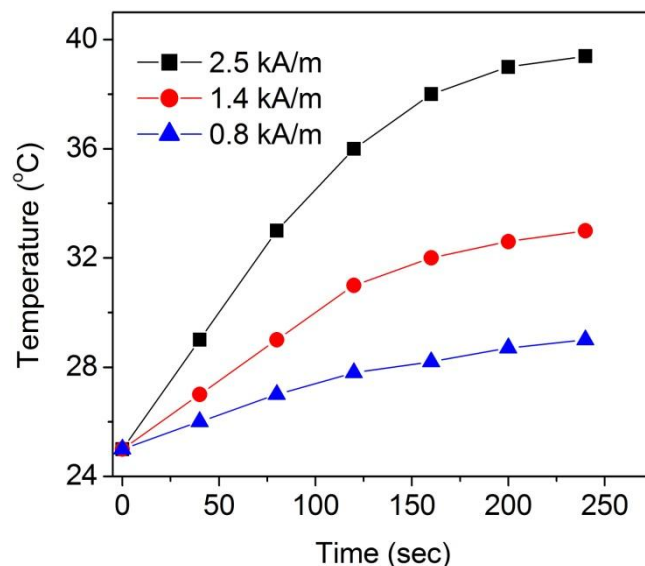


Figure 6.8 Temperature curve of nanodevices during application of HFMFs of different strengths.

6.5 Spectrum variation of the ZCIS QD under magnetic induction

The mechanism causing the spectral variation of the ZCIS QDs upon magnetic induction is of great interest. To further explore the possible causes, a separate photoluminescence test for the ZCIS QDs was performed in the same magnetic field; no detectable sign of change in the emitted spectrum was observed. This indicates an invariance in the spectral properties of the ZCIS QDs with respect to magnetic field. Since the variation of emitted spectrum for quantum dots has been proven to be associated with a change in the band energy structure or surface composition of the QDs, it is highly plausible that a number of factors cause changes in the resulting spectrum of the ZCIS QDs. These changes may include magnetically-induced heating, surface adsorption of the dye molecules, and/or surface corrosion due to the presence of water. However, according to experimental observation, the above factors have to

be rapidly responsive and probably interdependent since the decrease in the emission intensity and a red shift of the spectra occurred relatively quickly, in less than 20 seconds, in the presence of the magnetic stimulation at 2.5 kA/m. More interestingly, it is evident that the spectral variation has experimentally proven to be irreversible. These observations suggest that a permanent change in either chemical or physical structure has been induced rapidly on the ZCIS QDs while the nanodevices were subjected to magnetic stimulus.

To further explain the reasons behind the spectral degeneration of the QDs under short-term induction, nanodevices not carrying the dye molecules were prepared and exposed to the same magnetic field. The resulting emission spectra were identical to the case of the nanodevices with the dye. This indicates that dye molecules exerted little or no influence on resulting PL emission spectra of the ZCIS QDs. The PL spectrum of the dye molecules remained identical in shape and emission peak position to that given in Fig. 6.2, suggesting that the dye molecules, after release into an aqueous environment, remained chemically and physically stable. There is a magnetically-induced temperature rise, or hot spot, on the shell of the nanodevice due to magnetic energy dissipation from single-domain particles, such as a Brown and/or Neel relaxation, where this has been verified in a number of recent studies.^[137] From experimental observation, the temperature of the solution that contained the nano-devices gradually rises. As shown in **Figure 6.8**, while applying a high strength magnetic field of 2.5 kA/m, the temperature of the solution increased to about 40°C in 4 minutes. *Since the temperature rise of the solution is solely resulting from the energy dissipated from the magnetic nanodevices, the temperature of the nanodevice itself should be much higher and can be calculated by the thermodynamic relationship, $\Delta H = m_w C_w \Delta T_w = m_m C_m \Delta T_m$. C_w and C_m are the specific heat capacity of water and the magnetic material, respectively, and m is the weight. Neglecting any heat loss to the*

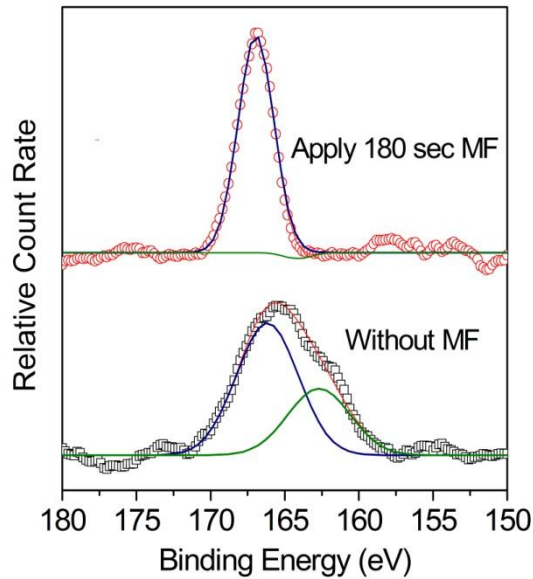


Figure 6.9 Binding energy of S 2p of the nanodevices with and without exposure to a high frequency magnetic field (HFMF) for a time period of 180 seconds. XPS results indicate the binding energy shift of the S 2p line from 162.3 eV - 166.2 eV before the stimulus to a single, strong binding-energy peak at 167 eV after the magnetic exposure. This could be attributed to S^{2-} from ZnS, CuS, In_2S_3 , or SO_4^{2-} , SO_2 . The binding energy at 167 eV on the ZCIS surface is strongly associated with the presence of oxide groups including SO_4^{2-} , SO_2 , etc on the surface. This demonstrates a rapid oxidation of the ZCIS QDs after a short period of magnetic induction.

surrounding water, the temperature of the nanodevices, after subjection to the HFMF for 1 min, can raise to approximately $200^{\circ}C$ in a field strength of 2.5 kA/m. Heat transfer from the shell to adjacent QDs occurs rapidly, causing quick equilibration with the water environment. However, once the QDs were heated, free carriers of exciton dislocations in QDs tunnel to the surrounding environment causing a deterioration of the emitted fluorescence intensity. Therefore, temperature rise of the QDs may cause a certain degree of thermal corrosion, such as surface oxidation or thermally-induced structural variation of the ZCIS QDs. This would permanently change the surface structure of the ZCIS. This change has been confirmed by X-ray photoelectron spectroscopy (XPS), as shown in **Figure 6.9**. A change in the binding energy spectrum of the S 2p peak of the ZCIS QDs, from 162.3 eV before the

stimulus to 167 eV after the stimulus, is clearly detected. For the latter, the binding energy is associated with the presence of oxide groups such as SO_4^{2-} or SO_2 , which strongly suggests a rapid oxidation occurred on the ZCIS surface under short-term magnetic induction. The associated, thermally-induced emission deterioration of both mechanisms mentioned above explains the degeneration of emission behavior and spectral shift of the ZCIS QDs upon magnetic stimulation. However, it is difficult to clearly differentiate the degenerative contribution in a quantitative manner from either mechanism. We simply consider the degeneration of both as a single event for the following discussion.

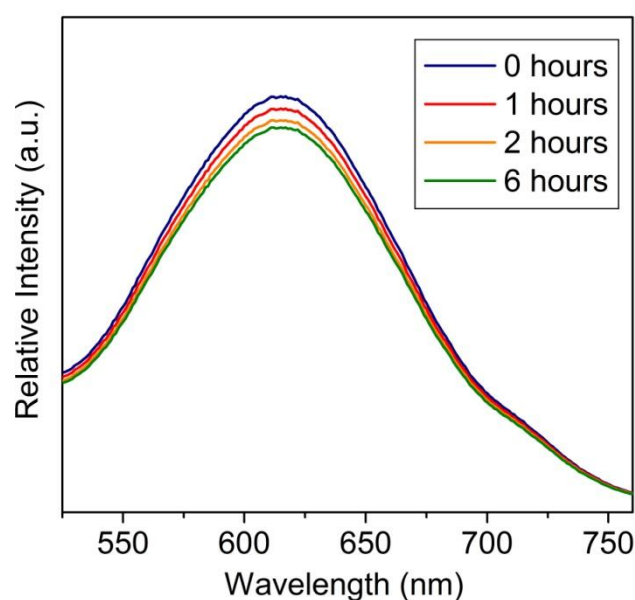


Figure 6.10 PL emission spectrum at various time intervals of nanodevice incubation in PBS solution.

An important concern for practical applications of this nanodevice is whether the emission degeneration of the attached QDs occurs spontaneously without the presence of the magnetic field over a reasonable time period in a physiological environment. If spontaneous degeneration occurs, the correlation depicted in Fig. 6.7 becomes unreliable. To examine this possibility, a simple test was performed by incubating the nanodevices in PBS for a time period of 6 hours, followed by measuring the PL

emission spectrum at various time intervals, as shown in **Figure 6.10**. Fortunately, the resulting PL spectrum of the QDs remained identical over the timespan of evaluation. This confirms the reliability of the linear relationship given in Figure 3 and further substantiates the correlation between two optical spectra as sustainable in vitro. However, it is more technically important from the current research that both spectral variations, the one from dye spectrum and the PL emission of the ZCIS, are able to work independently but are well correlated. In other words, the attached ZCIS QD can act as a nanometric sensor to monitor the quantity of drug released from the drug-carrying nanodevice. This multi-functional assembly, imaging, drug delivery controller and in-situ monitor, when integrated onto the nanodevice, may enable new pathways to advance nano-therapeutic technology.

6.6 Operation mechanism of the nanodevice

Based on the mechanism of degeneration of the emission spectrum of the ZCIS QDs and the deformation mechanism of the shell, outlined in a previous investigation, we propose an operation mechanism for the nano-device in a magnetic field. **Figure 6.11a** shows a schematic drawing of the mechanism of drug release and shell deformation associated with the structural degeneration of the attached QDs. Accordingly, after 60 seconds of exposure to the stimulus, the single crystal nanoshell structure was subjected to lattice deformation, forming nano-sized polycrystals of varying orientations, shown in **Figure 6.11b**. Nanometric scale boundaries between the nano-polycrystalline domains formed and provided numerous nano-conduits that allow leaking of the dye molecules to the environment. In other words, for short-term induction, extremely small cracks or crevices were formed along the boundary regions of the thin iron oxide shell and are kept open by the presence of the magnetic field. Extended magnetic stimulus enlarged the nano-crevices until permanent rupturing

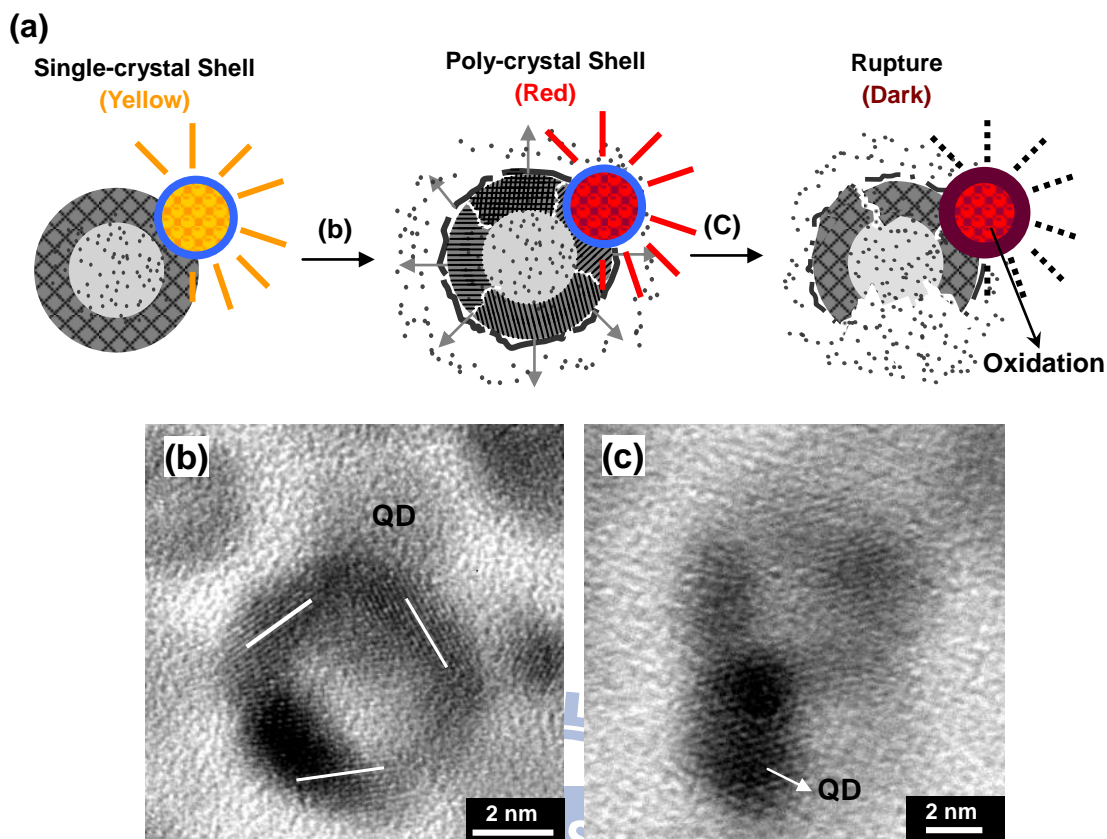


Figure 6.11 (a) Schematic illustration of the nanodevice with a proposed mechanism for controlled release of the dye molecules, as well as the degeneration of fluorescence intensity of the ZCIS QDs (b) Shell vibration causing enlargement of the dimensions of nano-crevices along the deformed single-crystal shell, rendering dye release upon short-term magnetic stimulation. (c) After long-term exposure, the deformed shell has received a sufficient amount of the energy to cause a final, permanent, mechanical rupture. Meanwhile, a rapid surface oxidation altered the surface structure of the QDs, leading to substantial degeneration of the fluorescence intensity.

of the shell occurred. At this time, the dye molecules were released from the nanodevice easily and completely, as shown in **Figure 6.11c**. Meanwhile, the energy structure of the ZCIS QDs altered considerably as a result of thermally-induced photo-leaching along with surface oxidation. This resulted in degeneration of the fluorescence intensity. While the shell was undergoing permanent rupture, the bandgap structure of the QDs was irreversibly altered, turning a dark red after about 100 sec at a magnetic field strength of 2.5 kA/m.

6.7 In-situ-monitoring of drug release in cancerous cells

To understand the optical behavior of the nanodevices within cells, they were modified using mercaptoundecanoic acid (MUA) followed by cross linking with lysine to form a hydrophilic layer exhibiting both carboxyl and amine groups on its

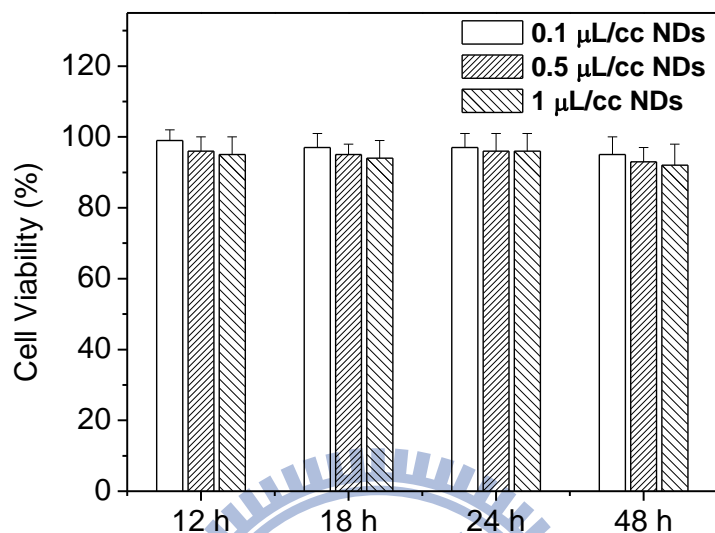


Figure 6.12 Cell viability of HeLa cells after 12 to 48 hours of incubation with increasing amounts of folic acid modified nanodevices (FA-NDs). Cell viability was measured using an MTT assay.

surface.^[148] Folic acid molecules were attached to the functional layer on the surface using carbodiimide chemistry to form bioconjugates. Folate receptors (FR) act as cancer-cell targeting ligands due to overexpression in many human cancerous cells, including mammary gland, lung, kidney, colon, prostate and throat cells.^[149] However, they are only minimally distributed in normal cells. Folic acid exhibits high affinity to FR and is expected to allow the nanodevice to efficiently attach on or enter into cancerous cells via receptor mediated endocytosis. Incubation of the HeLa cell line with the MUA modified nanodevices (MUA-NDs) and folic acid modified NDs (FA-NDs) were completed separately. Both the MUA-NDs and FA-NDs were incubated with the cells for a period of 4 hours. The majority of the FA-NDs can be clearly observed in the cytoplasm region of the cell, but only a few of the MUA-NDs were attached or taken by HeLa cells, indicating that the folic acid-modified version

promotes cellular uptake, as shown in the Supporting Information, Figure S5. It is expected that higher attachment or cellular uptake due to folic acid modification imparts enhanced therapeutic potential for the nanodevices. **Figure 6.12** shows the results of the MTT (3-(4,5-dimethylthiazol-2-yl)-2,5 diphenyl Tetrazolium Bromide) assay, as a measure of metabolic competence of the cell with FA-NDs of different concentrations. The difference in the cytotoxicity over an incubation period of 12 to 48 hours is negligibly small. At the highest concentration of 1 $\mu\text{L}/\text{cc}$ FA-NDs, the cell viability remained at approximately 96 %. The results suggest that the nanodevices show minimal toxicity for the HeLa cells.

After cellular uptake, controlled drug release and real-time, in-situ monitoring of the ZCIS QDs were performed in a magnetic field with a strength of 2.5 kA/m. As illustrated in **Figure 6.13 and 6.15**, an increase in the duration of the field from 0 to 180 sec caused the dye molecules (Green channel) to be released rapidly within the cells, while the corresponding fluorescence intensity of the ZCIS QDs (Red channel) decreased. Digital software (Nikon, Japan) was used to analyze the fluorescence intensities of both the dye molecules and ZCIS Qds. B_{sum} , G_{sum} and R_{sum} represent the total intensity of the blue channel, the green channel and the red channel in the images, respectively. The blue fluorescence was due to the DAPI dyed nuclei and was expected to be relatively similar for each cell. Therefore, the intensity of the blue channel was assumed to be standard for each image. G_{sum} and R_{sum} are from drug release and quantum dots respectively. $G_{\text{sum}}/B_{\text{sum}}$, the ratio of the green channel intensity to the blue channel intensity, is indicative of the relative concentration of the dye molecules in each cell. Similarly, $R_{\text{sum}}/B_{\text{sum}}$ is the value of the relative intensities of the nanodevices in each cell. After measurement, statistical analysis of fluorescence intensities exhibited a strong correlation between dye release and spectral variation of the ZCIS within the cells, shown in **Figure 6.14**. The ratios of $G_{\text{sum}}/B_{\text{sum}}$ and

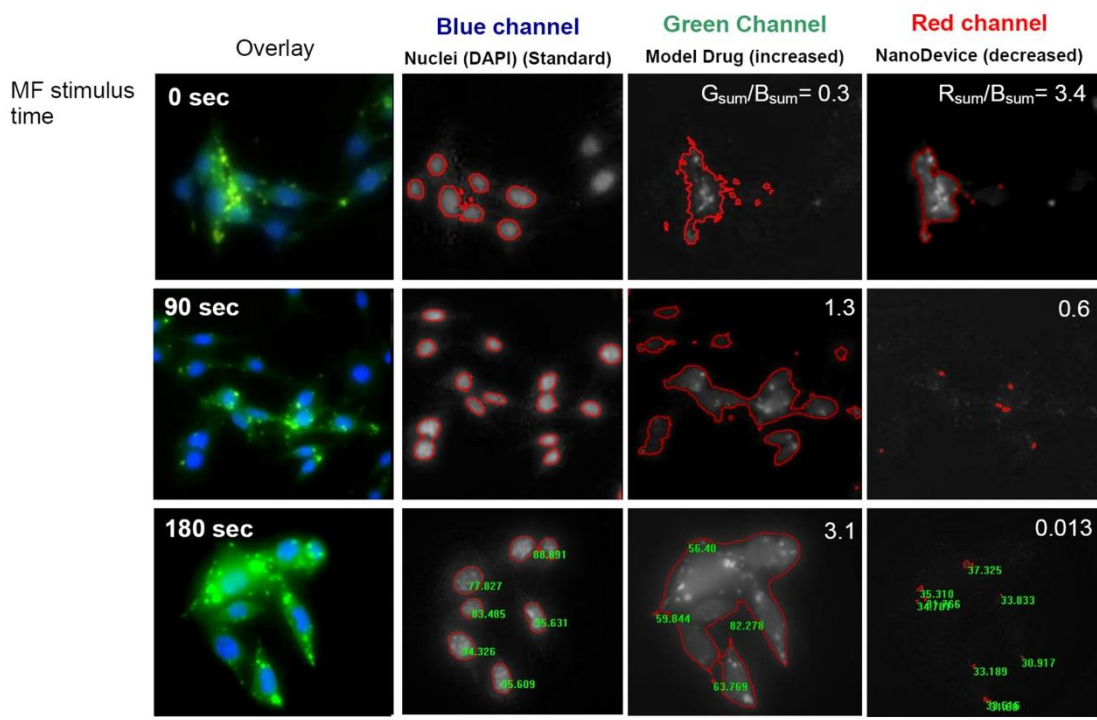


Figure 6.13 Fluorescent combination of the HeLa cells with the dye-loaded nanodevices after 12 hours incubation. With increasing duration of HFMF treatment, both the controlled release of the dye molecules (green channel intensity increased) and the associated real-time, in-situ monitoring capability of the doped ZCIS QDs (red channel intensity decreased) can be manipulated simultaneously to single-cell resolution. This implies that dye release can be precisely monitored by the variation of the ZCIS QDs from the nanodevices. G_{sum}/B_{sum} represents the ratio of the green channel intensity to blue channel intensity, and is indicative of the relative concentration of the model drug in each cell. R_{sum}/B_{sum} is then defined as the relative intensities of the nanodevices in each cell.

R_{sum}/B_{sum} versus duration of the magnetic field in the cells gives rise to two separate curves. These curves show that the relative drug concentration, represented by G_{sum}/B_{sum} , in the cells increases with the duration of stimulus. The fluorescence intensity of the nanodevice, originating from the ZCIS QDs and represented by R_{sum}/B_{sum} , decreased in proportion at the same time. There are two purposes of the cell culture test. The first purpose is a test of the short-term cyto-compatible nature of the nanodevice, where the HeLa cells appeared to be viable over the duration of the culturing step. The second and most critical purpose is the test of the in vitro

monitoring capability of the nanodevices, where drug dosage can be quantitatively traced within a single cell.

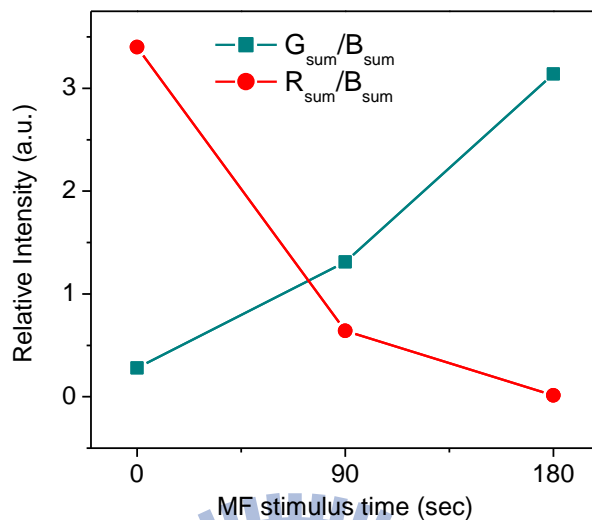


Figure 6.14 The ratio of G_{sum}/B_{sum} and R_{sum}/B_{sum} versus the duration of magnetic stimulus in the cells gives rise to two curves. The results demonstrate the relative drug concentration, represented by G_{sum}/B_{sum} , in the cells with increasing duration of stimulus. The fluorescence intensity originating from the ZCIS QDS, represented by R_{sum}/B_{sum} , decreased in proportion at the same time.

6.8 Summary

The multifunctional drug delivery nanodevice makes use of quantum dots to successfully image, target, and deliver drugs via remote control. The devices also have the capability to monitor the in-situ drug release within a model cancerous cell line, HeLa cells, to cellular resolution. These nanodevices offer outstanding control of release and retention for the molecules encapsulated inside their polymer core. The dense, single-crystalline shell prevents the fluorescence dye from escaping prior to the desired release. Furthermore, the nanodevices are able to monitor real-time drug dosage through corresponding variation in emission spectrum of the quantum dots within the HeLa cells. The nanodevices have great potential advantages as a cell-specific drug delivery system for nanotherapeutic applications. With the in-situ monitoring capability of the nanodevice, we believe that both target-oriented therapy

and diagnosis can be integrated and managed within a single cell. Multifunctional nano-platforms are expected to open a new avenue in the development of multifunctional therapeutic nanosystems. An in-vivo analysis is currently underway to treat brain tumors in mice.

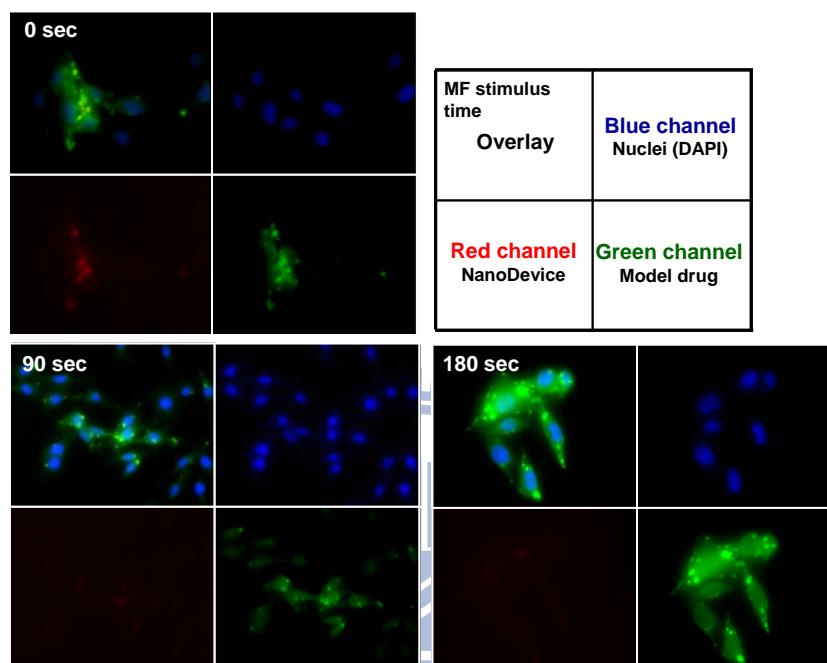


Figure 6.15 Fluorescent morphologies of HeLa cells after 12 hours incubation with drug loaded nanodevices. With increasing the time duration of HFMF treatment, the control of drug release associated with a real-time self monitoring of the ZCIS QDs from the nanodevices were manipulated simultaneously. The digital analysis software (Nikon, Japan) was use to analyze the fluorescence intensities of model drug and nanodevices. The conditions of the exposure are the same for each color channels. The analyzed areas were determined by the software which defined the fluorescence intensity from 1 to 255. The ranges of the fluorescence intensities: Blue channel (60-255), Green channel (40-255), and Red channel (30-255).

Table 6.1. The statistic data of fluorescence intensity was calculated by digital analysis software (Nikon, Japan). We employed the blue channel as a standard value because the fluorescence intensities of blue channel (DAPI) were assumed identical for each cell. G_{sum}/B_{sum} represents the ratio of the green channel intensity to blue channel intensity, and is indicative of the relative concentration of the model drug in each cell. In such a way, R_{sum}/B_{sum} is then defining as the value of the relative intensities of the nanodevices in each cell.

MF stimulus time	Blue channel Nuclei (DAPI)		Green channel Model drug		Red channel NanoDevice		G_{sum}/B_{sum}	R_{sum}/B_{sum}
	Mean	Sum	Mean	Sum	Mean	Sum		
0 sec	75	1.24×10^6	63	3.52×10^5	53	4.21×10^6	0.28	3.40
90 sec	78	1.39×10^6	68	1.82×10^6	44	89320	1.31	0.64
180 sec	89	1.94×10^6	74	6.10×10^6	33	25570	3.14	0.013



Chapter 7

PVA-Iron Oxide /Silica Core-Shell Nanocarriers for Magnetically Controlled Drug Release and Cancer Cell Uptake Efficiency

7.1 Introduction

Control release of therapeutic agents from nanometric carriers has been receiving increasingly interest because it provides numerous advantages, such as high delivery efficiency and site-specific therapy, compared to traditional dosing techniques. Owing to these advantages, many researches proposed to integrate active drug molecules with host materials, aimed at manipulating drug release profile. It is desirable that drug release behavior can be optimized with either a slow, zero-order release pattern or a burst fashion mimicking natural release of biological molecules, such as hormones like insulin or thyroxine formed in endocrine glands, in the body. Real-time release upon a short-time stimulus is also hard to achieve for traditional stimuli-responsive polymeric materials, which is especially critical for a certain clinical complications. Therefore, a practical development of a desired drug carrier should possess real-time responsive to the stimuli when an urgent need is required for disease control and/or slow, sustained release to meet different clinical complications.

The use of a magnetic field to modulate drug release through magnetic nanoparticles from drug carriers was previously developed. Recently, the core/single-crystal iron oxide shell nanospheres for magnetically triggered release were also developed by our team. However, nano-carriers with controllable drug release property is highly desirable because such small carriers can be designed to deliver drug to a specific site of disease, and then, drop the therapeutic molecules in a right position at a right time with a therapeutically effective dose. It is far from achievable under current drug delivery systems, especially those of particulate drug delivery nano-devices, and it seems to have a need to bring a successful marriage among the field of materials technology, biology, pharmaceuticals, and stimuli

environment.

It is more clinically desirable if a “zero or near-zero release profile” can be tailored as practically needed before the drug-containing nano-carriers reached the targeted sites because the nature of diffusion of drug molecules from the nano-carriers to the environment is virtually thermodynamically unavoidable in the presence of a concentration gradient of drug. Once such a mechanism was triggered right after administration, a risk of undesired clinical complications may result, included a reduction of therapeutic efficacy. Here, a novel nanodevice was designed and constructed by preparing a self-assembly iron oxide (SAIO) nanoparticles with drug molecules embedded in an ultra-thin silica nanoshell. A structurally dense silica shell has designed as a physical barrier to eliminate undesirable drug release before reaching the target sites appears to be practically desired. A mixture of magnetic nanoparticles and amphiphilic PVA was employed as a functional phase in the resulting nanocarriers which allow the response of the resulting drug carriers to be activated more dynamically and efficiently, aimed to achieve a real-time response to an immediate environmental change, i.e., magnetic field. In the meantime, the PVA phase provides not only a glue to assemble the nanoparticles, but also a matrix to immobilize therapeutical active agents of either hydrophilic or hydrophobic nature within. It is more interesting to know that high-frequency magnetic field, in the range of tens to hundreds of KHz, allows a pulsatile release of drug to be easily achieved on a real-time responsive base without undesirable delay in dosing accuracy under administration and more desirably, restores to zero or near-zero release immediately after removal of the high-frequency magnetic field. In addition, the cell uptake efficiency of these novel SAIO@SiO₂ nanocarriers was examined.

7.2 Experimental section

Materials: The synthesis was carried out under airless processes and using commercially available reagents. Absolute ethanol (99.5%), benzyl ether (99%), 1,2-hexadecanediol (97%), oleic acid (90%), oleylamine (>70%) and Iron(III) acetylacetonate were purchased from Aldrich Chemical Co. Polyvinyl alcohol (PVA, Mw: 72k) were purchased from Fluka Chemical Co. Tetraethylorthosilicate (TEOS) and 3-aminopropyltrimethoxy silane (APTMS) were purchased from Merck. Fluorescein isothiocyanate (FITC, Sigma) were used to label, which help nano-carriers visualization under fluorescence microscope. Ibuprofen (IBU, Fluka) was used as the model drug.

Synthesis of Magnetic nanoparticles: Monodisperse iron oxide nanoparticles were synthesized by a method developed by Sun et al. Briefly, 5 nm of iron oxide nanoparticles were synthesized by mixing 2 mmol Fe(acac)₃, 10 mmol 1,2-dodecanediol, 6 mmol oleic acid, 6 mmol oleylamine and 20 mL benzyl ether under a flow of nitrogen. The mixture was stirred magnetically and pre-heated to reflux (200 °C) for 30 minutes, and then, heated to 300 °C for another 1 hour under nitrogen atmosphere. The black-brown mixture was allowed to cool to room temperature and added 50 mL ethanol to participate. The products were collected by centrifugation at 6000 rpm for 10 minutes, and then washed with excess pure ethanol for 4 times. The product, iron oxide nanoparticles, was centrifuged to remove solvent, and redispersed into hexane.

Synthesis of self-assemble iron oxide nanoparticles/silica core-shell (SAIO@SiO₂) nanocarriers: To prepare the self-assembly iron oxide nanoparticles (SAIO), 10 mg of iron oxide nanoparticles were centrifuged at 6000 rpm for 10 minutes, and then redispersed in 4 mL chloroform to form an uniform organic phase. 200 mg of polyvinyl alcohol (PVA) as a polymer binder was dissolved in 10 mL D.I. water at 70 °C. After PVA totally dissolving in the solution, the clear solution was cooled to room

temperature. Then, organic phase was added into the PVA solution. The mixture was emulsified for 5 minutes with an ultrasonicator at 100 W. Under the ultrasonicating, the mixture was heated and evaporated the organic solvent. The mixture was stirred magnetically and heated again to 50 °C on hot plate to ensure the organic phase removing. After evaporation of organic solvent, the products were washed by D. I. water for 3 times, and centrifuged at 6000 rpm to collect the products. The precipitates were redispersed in water, and the diameter of the redispersed particles (hereinafter termed as SAIO) is about 77 nm. Once the solvent was removed, a mixture of PVA and iron oxide nanoparticles was formed where the iron oxide nanoparticles appeared to assemble in a somewhat uniform and regular configuration in the resulting SAIO phase. A silica ultra-thin shell was then coated on the SAIO nanoparticles by a modifying Stöber method. In brief, 5 mg of SAIO were dispersed in the 4 mL of 99.5 % ethanol and 0.1 mL of 33 % NaOH₄ for 30 minutes. 40 μm of Tetraethylorthosilicate (TEOS) was slowly added to the mixture and stirred for 12 hours. After hydrolysis and condensation, a silica nanoshell was coated on the SAIO nanoparticle to form a resulting PVA/iron oxide/silica core-shell (termed as SAIO@SiO₂) nanocarriers.

Drug Loading and Release: In this investigation, ibuprofen (IBU) was used as a model drug to estimate the drug release behaviors of the SAIO@SiO₂ nanocarriers, loading in nanocarriers through an in-situ process. First, the 4% IBU was dissolved in the chloroform with iron oxide nanoparticles to form the organic phase. This organic phase was used to prepare the self-assembly iron oxide nanoparticles (SAIO). Ibuprofen can be encapsulated in the SAIO nanoparticles through the amphiphilic polyvinyl alcohol (PVA). Then, the process of constructing SAIO and silica shells was also applied to prepare drug-loading SAIO@SiO₂ nanocarriers. Before drug release test, the nanocarriers were washed by the phosphate buffered saline (pH 7.4),

following by washing with D.I. water. Ibuprofen-containing nanocarriers were used in PBS buffer solution for all the drug-release experiments. Quantitative estimate of the IBU loading was obtained by UV-vis spectrophotometer. The drug release behavior from the nanocarriers was measured in a 20 ml phosphate buffered saline per sponge cube (pH 7.4). To measure the concentration of drug release, 1.5 ml PBS medium with the dispersed nanospheres was taken out, and separated by centrifuge with 4000 rpm. The clear solution without nanospheres was used to estimate the concentration of drug release UV-Visible spectroscopy (Agilent, 8453 1UV-Visible spectrophotometer) was used for characterization of absorption peak at 264 nm (I_{\max} of free IBU). The nanocarriers were absent and did not affect the measurements.

Cell Culture: HeLa (human cervical cancer) cells were maintained in DMEM (Dulbecco's modified Eagle's medium) containing 10% fetal bovine serum, 100 units/mL penicillin, and 100 $\mu\text{g}/\text{mL}$ streptomycin. Cells were cultured with complete medium at 37 °C in a humidified atmosphere of 5% CO_2 in air. For all of the experiments, cells were harvested from subconfluent cultures by use of trypsin and were resuspended in fresh complete medium before plating. A comparison of in vitro cytotoxicity of SAIO@SiO₂ nanocarriers with different concentrations and times was performed on HeLa cells with an in vitro proliferation method using MTT. Briefly, 1×10^4 cells were plated in 96-well plates to allow the cells to attach, and then, exposed to the serial concentrations of SAIO@SiO₂ nanocarriers at 37 °C. At the end of the incubation, 20 μL of MTT solution was added and incubated for another 4 hours. Then, the medium was replaced with 200 μL of DMSO and the absorbance was monitored using a Sunrise absorbance microplate reader at dual wavelengths of 570 and 650 nm.

In order to estimate the cellular uptake of the nanocarriers, green emitting fluorescein dye was attached SAIO@SiO₂ nanocarriers (FITC-SAIO@SiO₂) for the

study. First, fluorescein isothiocyanate (FITC) was mixed with ethanolic 3-aminopropyltrimethoxysilane (APTMS) solution for 24 h at room temperature to form N-1-(3-trimethoxysilylpropyl)-N-fluoresceyl thiourea (FITC-APTMS). Separately, 5 mg of SAIO were dispersed in 4 mL of 99.5 % ethanol and 0.1 mL of 33 % NaOH for 30 min. 40 μ m Tetraethylorthosilicate (TEOS) and 10 μ m FITC-APTMS was slowly added to the mixture, and then, stirred for 12 hours. After hydrolysis and condensation, the FITC-silica was coated on the SAIO to form FITC-SAIO@SiO₂ nanocarriers. The un-reacted chemicals were removed by rinsed with DI water for 3 times. The SAIO@SiO₂ nanocarriers were incubated with the cells for different time, and then, observed by PL microscopy.

7.3 Preparation of SAIO@SiO₂ nanocarriers

Synthetic procedure of the SAIO@SiO₂ nanocarriers is schematically illustrated in **Figure 7.1**. The first step is to synthesize the monodispersed superparamagnetic iron oxide nanoparticles (Fe₃O₄) via a high-temperature decomposition of Fe(acac)₃.^[24] Two key steps were employed to form these monodispersed nanoparticles: firstly, the growth of nuclei was carried out at 200 °C, then, raising the reaction temperature to 300 °C, permitting the iron oxide nanoparticles to grow to uniform size. The iron oxide nanoparticles show an average diameter of 5 nm, **Figure 7.2a**, and well suspended in benzyl ether. In the second step, the nanoemulsion method using polyvinyl alcohol (PVA) as a binder was applied to prepare the SAIO nanoparticles, **Figure 7.2b**. The iron oxide nanoparticles appeared to assemble uniformly and pack regularly throughout the PVA nanomatrix, and it is believed to be resulting from possible interactions such as hydrogen bonding or dipole-dipole interaction between the functional groups on the iron oxide surface and hydroxyl groups of the PVA, wherein a PVA-induced structural alignment of the iron oxide

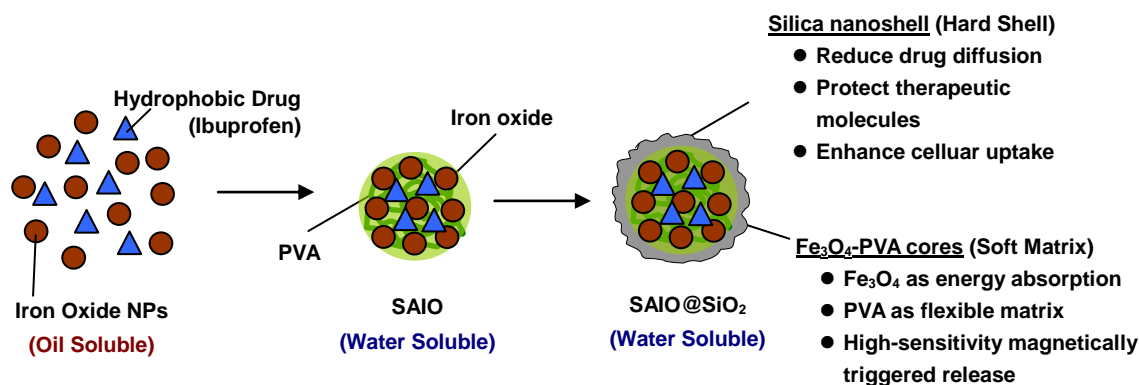


Figure 7.1 Schematic illustration of the synthesis and structure of the self-assemble iron oxide /silica core-shell (SAIO@SiO₂) nanocarriers for magnetically controlled drug release.

nanoparticles can be evolved. The SAIO nanoparticles having a diameter about 77 nm measured by dynamic light scattering (DLS, **Figure 7.2f**) displayed a well-dispersed behavior in water solution, without the need of any surfactant for stabilization. Then, the SAIO was coated with a thin silica shell by hydrolysis and condensation of TEOS to obtain final core-shell SAIO@SiO₂ nanocarriers, **Figure 7.2c**. The SAIO@SiO₂ nanocarriers with a diameter about 86 nm (**Figure 7.2g**) possessed an ultra-thin layer of dense silica shell of about 5 nm in thickness, and no observable crevices or cracks were microscopically detectable in the regions between the SAIO and silica shell, implying a compatible interface between the core and shell phases. The resulting core-shell nanocarriers showed again an excellent suspension character in both PBS solution and cell-culture solution without further chemical modification on the surface for stabilization purpose. Such a surfactant-free nanocarrier should be advantageous for many clinical practices and potential development since it not only reduces adverse effect possibly originated by some surfactant agents but also allows further surface modification by specific functional or biological molecules for enhanced functionality and performance, as will be further elucidated in later section. The ultra-thin silica shell was designed as a physical barrier for eliminating undesirable

drug release and in the meantime, to regulate desirable release in a controllable manner. Upon the synthesis, organic fluorescence dye was incorporated onto the silica shell through the co-condensation method for cell imaging (to be discussed later).

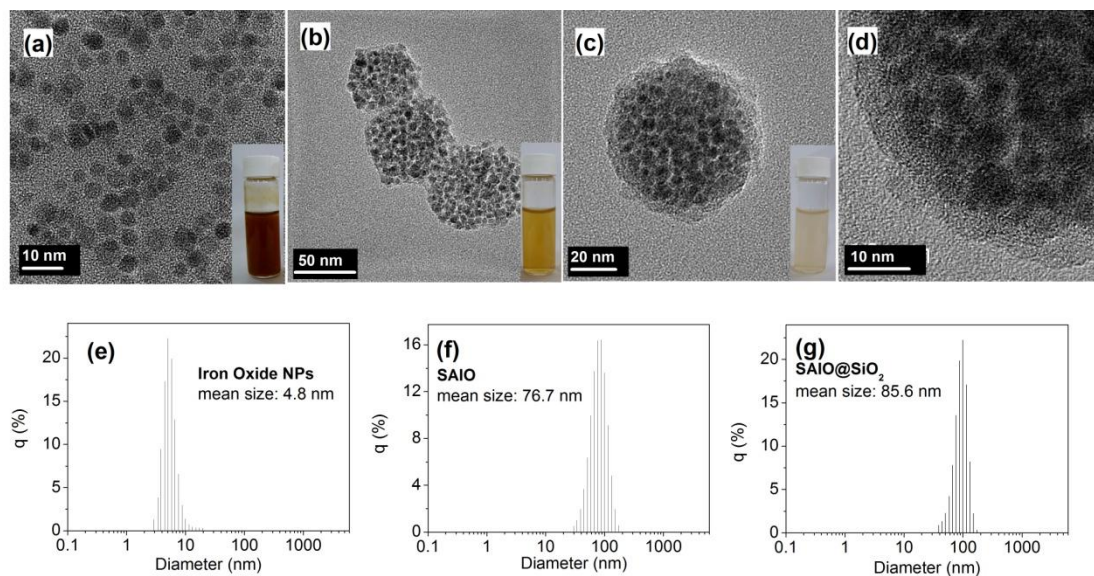


Figure 7.2 TEM images of (a) iron oxide nanoparticles, (b) self-assemble iron oxide (SAIO) nanospheres, and (c, d) self-assemble iron oxide /silica core-shell (SAIO@SiO₂) nanocarriers. The thickness of silica shells coated on the SAIO nanoparticle is 4-5 nm. The inside pictures displayed the solution color for different particles. (e-g) The size distributions of iron oxide nanoparticles, SAIO nanoparticles and SAIO@SiO₂ nanocarriers were measured by dynamic light scattering (DLS).

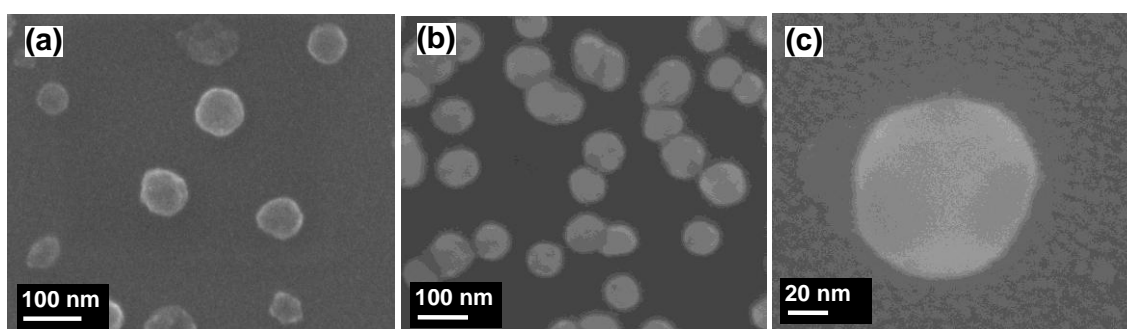


Figure 7.3 The SEM images of (a) SAIO and (b) SAIO@SiO₂ nanospheres. (c) After 4 minutes, the SAIO@SiO₂ nanospheres did not show obviously cracks under the SEM analysis.

7.4 Characterization of SAIO@SiO₂ nanocarriers

X-ray diffraction (XRD) analysis showed that the crystalline phases of iron oxide nanoparticles is Fe₃O₄ (magnetite), **Figure 7.4a**. Six diffraction peaks at $2\theta = 30.1^\circ$, 35.6° , 43.3° , 53.5° , 57.2° , 62.9° assigned as the characteristic peaks of standard Fe₃O₄ crystal plane were observed (according to Fe₃O₄ (JCPDS [85-1436])). Although PVA is a semi-crystalline polymer, the XRD pattern of iron oxide nanoparticles and SAIO is much similar, suggesting that the PVA/Fe₃O₄ ratio was negligibly small. After the SAIO was embedded by the silica layer, the relative diffraction intensity of the Fe₃O₄ peaks became weaker because the introduction of the silica phase diluted to a certain extent the concentration of iron oxide. In addition to the diffraction peaks of iron oxide, a broad and weak peak at $20\sim 23^\circ$ was observed and identified as the semi-crystalline silica. The magnetic property of Fe₃O₄ nanoparticles, SAIO and SAIO@SiO₂ nanocarriers was estimated by SQUID at 298 K with the magnetic field sweeping from -10000 to +10000 G. **Figure 7.4b** shows the correlation of the magnetization with magnetic field for the Fe₃O₄ nanoparticles, SAIO and SAIO@SiO₂ nanocarriers, where the curves show similar shape with negligible hysteresis. The presence of PVA and silica dilutes the concentration of Fe₃O₄ nanoparticles, resulting in a less saturation magnetization (M_s) of the SAIO and SAIO@SiO₂ nanocarriers than that of the pure Fe₃O₄ nanoparticle. The magnetic property of the SAIO@SiO₂ nanocarriers was also tested by applying a magnet near the cuvette, where the SAIO@SiO₂ nanocarriers were completely attracted to the side of the cuvette nearest to the magnet, as displayed in Figure 3b, suggesting the nano-carriers themselves possess magnetic property.

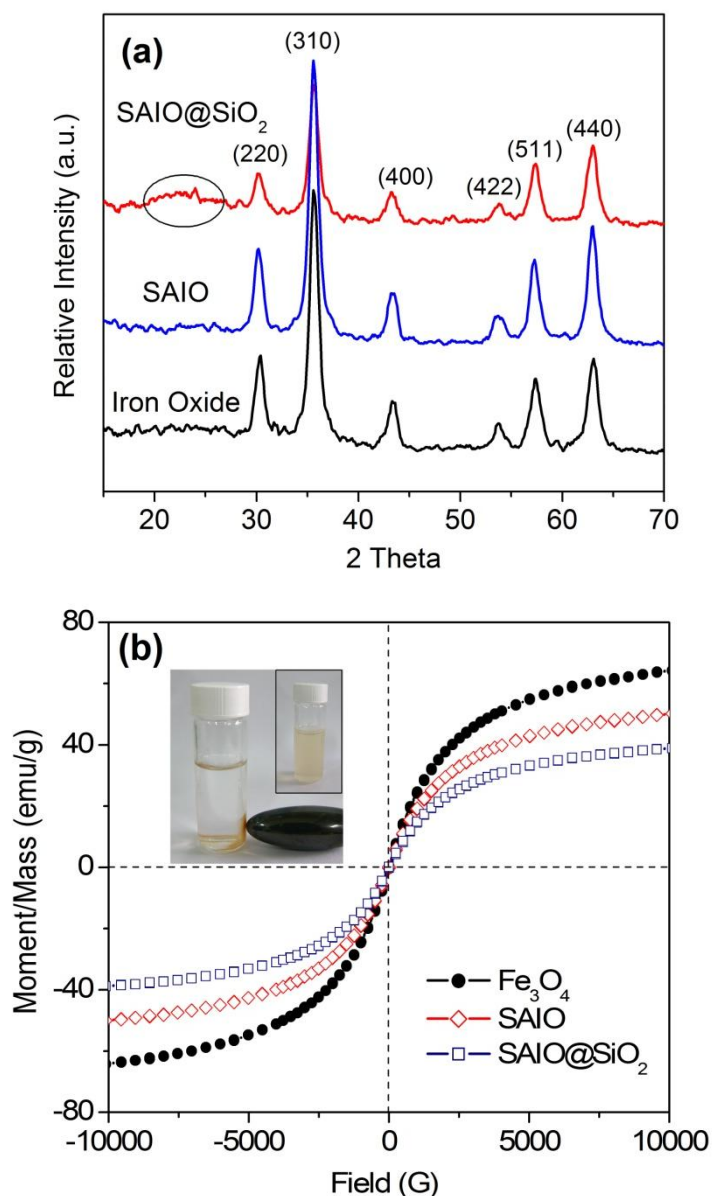


Figure 7.4 (a) X-ray diffraction patterns of iron oxide nanoparticles, SAIO and SAIO@SiO₂. (b) Field-dependent magnetization curve of iron oxide nanoparticles, SAIO and SAIO@SiO₂ nanocarriers. The inside pictures: the SAIO@SiO₂ nanocarriers were attracted by an external magnet.

7.5 Drug release of SAIO and SAIO@SiO₂ nanocarriers

Figure 7.5 shows the cumulative drug release of the SAIO and SAIO@SiO₂ nanocarriers in the PBS buffer solution of pH 7.4. The diagram clearly proves that both systems exhibit sustained release behavior, but the release rates are apparently different. The amount of IBU released from the SAIO reaches 90% in 48 hours; which,

together with a corresponding release rate, is much higher than that from the SAIO@SiO₂ nanocarriers. The difference in release rate should mainly be attributed to the presence of silica shells, acting as a physical barrier, limiting the outward diffusion of the IBU. The IBU, a hydrophobic drug, has limited solubility in PBS buffer so it stays readily in the SAIO. However, concentration gradient gives rise to a driving force causing outward diffusion of the IBU through the SAIO carriers without any physical barrier to regulate the release kinetic. However, for the SAIO@SiO₂ nanocarriers, the release profile is highly regulated and shows a zero-order kinetic, where the rate of release is relatively slow, reaching only 8 % over a time period of 48 hours. This clearly indicates that the silica shell, albeit with a thickness of as small as 5 nm, acts as an effective barrier to block the IBU molecules to a considerable extent from passing through. This finding also suggests that the ultra-thin silica shell is structurally compact with full coverage over the entire surface of the SAIO core, as evidenced in Figure 7.2c, wherein no observable defects were detected along the regions of the thin shell and sub-surface regions, indicating a well-compatible interface between the silica and core phase. In comparison with these two nano-carriers, the addition of ultra-thin silica shell are apparently highly capable of achieving a relatively slow release pattern, which is advantageous for preserving and protecting the drug molecules within the nano-carrier from undesirable leakage and damage as well.

To investigate the diffusion mechanism of the drug from the nanocarriers, the drug release kinetics can be characterized using the equation:

$$M_t/M = kt^n,$$

where M_t is the mass of drug released at time t , M is the mass released at infinite time, k is a rate constant, and n is a characteristic exponent related to the mode of transport of the drug molecules. The diffusion parameters (i.e., n and k) were

calculated through a log-log analysis of above equation under the condition of $M_i/M < 0.6$. The values of rate constant k for the nanocarriers were then determined and found that the k values decreased in the order of SAIO ($k=0.10$) > SAIO@SiO₂ nanocarriers ($k=0.01$), indicating a lower diffusion rate by a factor of 10 for the SAIO@SiO₂ nanocarriers. This finding strongly ascertains the efficient inhibition effect of the nano-metric silica shell for drug release from the SAIO@SiO₂ nanocarriers.

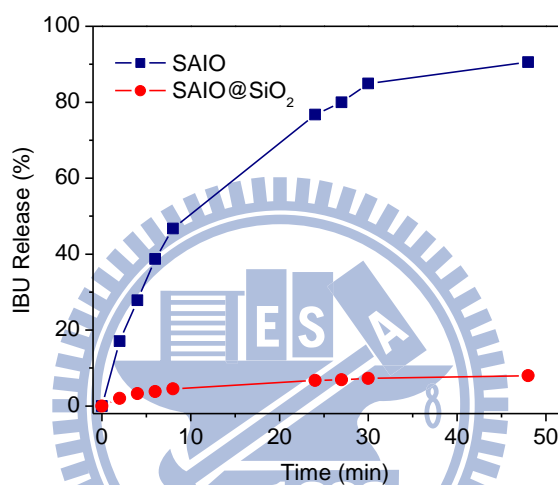


Figure 7.5 Cumulative drug release of SAIO and SAIO@SiO₂ nanocarriers. Coated with silica shells, the SAIO@SiO₂ nanocarriers exhibited relatively smaller amount of cumulative drug release than SAIO nanoparticles.

7.6 Magnetic-sensitive drug release behavior

Under magnetic stimulus, the release profile of IBU for both the SAIO and SAIO@SiO₂ nanocarriers is demonstrated in **Figure 7.6**, where a significant increase in the release profile was detected for both compositions, compared to those in the absence of the stimulus, Fig. 7.5(a). For the SAIO nanoparticles, the cumulative release amount is increased from 0.4 % to about 5.5 % over a 4-min stimulus. The slow-to-burst release profiles were also observed while applying the consecutively magnetic stimulus at 1-min and 2-min durations. With different time durations of the stimulus, the amount of drug released from the nanocarriers showed a linear

increment with the stimulus time. This finding indicates that the applied HFMF controlled the amounts of release through the operation time. However, the release profile from the SAIO nanoparticles could hardly be restored right after removal of the stimulus, moreover, the release rate was increased considerably compared to that of the as-prepared SAIO nanoparticles without subjecting to any HFMF treatment. This finding suggests that the SAIO nanoparticles can be physically and ir-reversibly deformed in structural integrity.

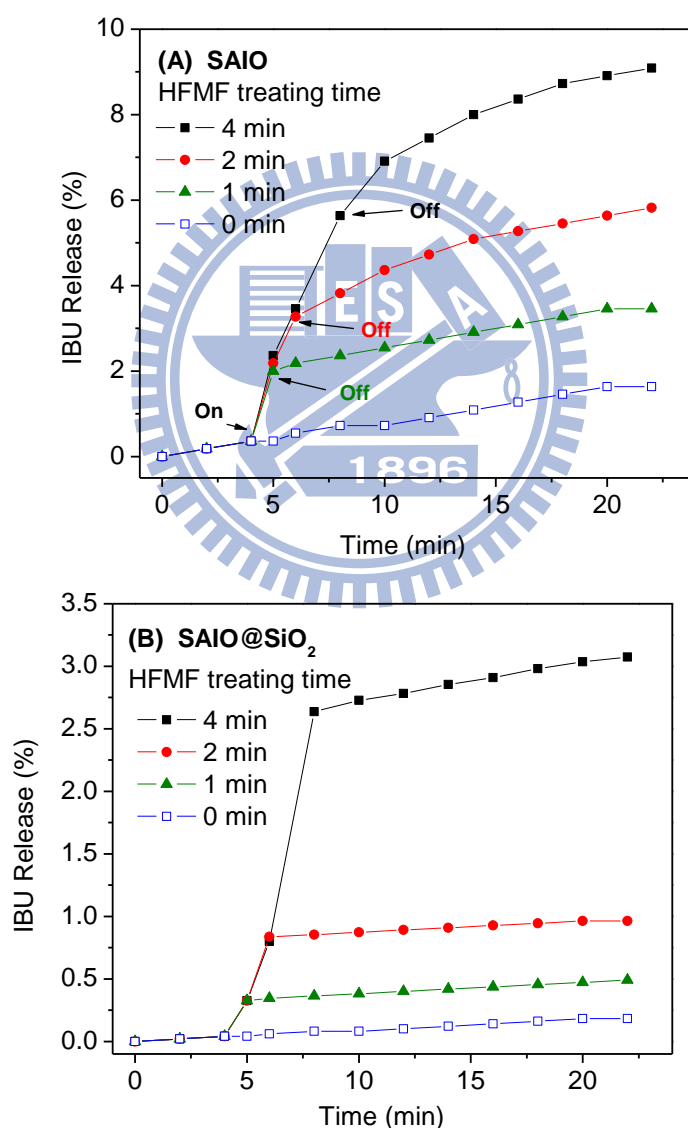


Figure 7.6 Cumulative drug release profiles of ibuprofen (IBU) from (a) SAIO and (b) SAIO@SiO₂ nanocarriers were triggered by 1 to 4 minutes of high frequency magnetic field.

For the SAIO@SiO₂ nanocarriers, **Figure 7.6(b)** shows a slow-to-burst release profile while subjecting to HFMF, similar to the release behavior of the SAIO nanoparticles. However, a closer look at the drug release profiles of the SAIO@SiO₂ nanocarriers under magnetic stimulus, the cumulative release amount after 4-min period operation increased from 0.1 % to 2.7 %, which is smaller by a factor of 2 than that from the SAIO nanoparticles (5.5 %), suggesting the silica shell effectively regulated the IBU release from the SAIO@SiO₂ nanocarriers. The amount of IBU from the SAIO@SiO₂ nanocarriers was much smaller in amount compared to those from the SAIO nanoparticles. More interestingly, the release profile of the SAIO@SiO₂ nanocarriers possessed a zero-order release pattern even under the stimulus. In other words, the IBU released from the SAIO@SiO₂ nanocarriers, albeit in a burst-like profile under HFMF stimulus, can still be well regulated with a controllable dosage. While removing the stimulus, the drug release profile restored immediately to original pattern, i.e., a relatively slow and zero-order release profile. Such a fast-acting and precise dosing response of the SAIO@SiO₂ nanocarriers relative to the given HFMF is believed to be easily manageable in practical operation and it is highly expecting to apply for magnetic-sensitive drug delivery manipulation.

7.7 Nanostructure evolution under magnetic treatment

To investigate the mechanism of release, especially under stimulus, the nanostructural evolution of the SAIO@SiO₂ nanocarriers subjecting to HFMF were monitored, as shown in **Fig. 7.7(a) and 7.7(b)**. Although the fast-response to the magnetic stimulus causing burst release was carried out under HFMF for a 4-min duration, the nanocarriers remained intact in structural integrity, indicating that the drug molecules, having a size less than 1 nm, have been accelerated considerably in passing across the silica shell. The rigid silica shell coated on the SAIO@SiO₂

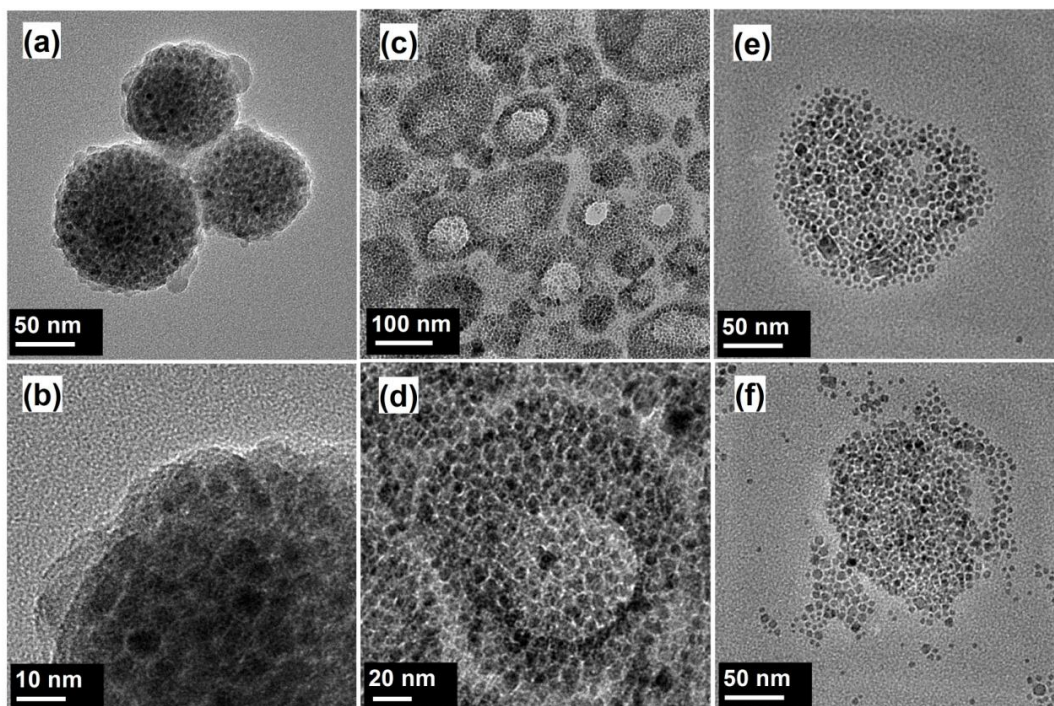


Figure 7.7 TEM images of nanostructures of (a, b) SAIO@SiO₂ nanocarriers, and (c) to (f) SAIO after 4-min duration of HFMF treatment. (a, b) SAIO@SiO₂ nanocarriers displayed no obviously crack after HFMF treatment. (c-f) SAIO without silica shells showed obvious cracks or deformation after applying HFMF.

nanocarriers is acting like a framework to keep the integrity of the SAIO core phase from physical deformation or damage under extensive magnetic stimulus. After subjecting to HFMF treatment, **Figure 7.7(b)** displayed no observable cracks or defects developed on the thin silica shells when the IBU molecules was releasing.

In order to estimate the structural evolution of the core phase of the SAIO@SiO₂ nanocarriers under the HFMF, the nanostructural evolution of SAIO core phase without the silica shells was examined. From TEM analysis, the morphological structure of the as-synthesized SAIO nanoparticles in the absence of HFMF treatment displayed excellent structural integrity, wherein the magnetic nanoparticles were well distributed with the PVA phase. However, after 4-min HFMF stimulus, the stresses induced by HFMF caused two types of structural deformation on the SAIO nanoparticles. First, nano-cavities of 20-60 nm in size were developed on the core

SAIO nanoparticle, as shown in **Figure 7.7(c) and (d)**, however, some nanoparticles seemingly remained structurally intact. Second, the stress-induced serious structural deformation of the SAIO nanoparticles exhibited in **Figure 7.7(e) and (f)**. These nano-cavities are probably resulting from the dissolution of the PVA in aqueous solution under magnetic-induced heating. Because the HFMF is able to induce heat energy from the magnetic nanoparticles at a faster rate, some “hot-spots” are believed to cause structural dissociation of the SAIO core, since it has well recognized that the heat generation, governed by the mechanism of magnetic energy dissipation for single-domain particles (Brown and Néel relaxations), is sensitive to the crystal size and the materials.^[28] The temperature of the solution (5 mg/cc water) will increase about 12 °C, from 24 °C to 34 °C. Once the energy induced by HFMF increased the temperature of SAIO nanoparticles, the PVA molecular chains became more flexible (glass transition temperature of PVA is about 80 °C), as they are subject to an aqueous and heating environment, causing the IBU molecules to diffuse more easily in the flexible and soft SAIO nanoparticles, whereupon a physical deformation of the SAIO nanoparticle was detected, as depicted in **Figure 7.7(e) and 7.7(f)**.

To investigate the weight loss of PVA after HFMF stimulus, thermogravimetric analysis (TGA) was used. After 4-min period of HFMF treatment, as given in Table 7.1, the PVA lost 7% and 2% by weight for the SAIO nanoparticles (also as a core phase for the core-shell nanocarrier) and SAIO@SiO₂ nanocarriers, respectively, indicating substantially large portion of the PVA phase still stayed within the core phase, especially for those covered with a silica shell. However, the findings suggest that the weight loss of the PVA in the core phase is a result of outward diffusion due to the presence of surface defects such as nanopores along the silica shell. This seems to provide a reasonable explanation of the burst-like release behavior. However, what is interestingly observed from the release behavior, Fig. 7.6(b), is that the release

profile behaved as a near zero-order kinetic even under HFMF stimulus, which further substantiates that the regulating effect of the shell structure remained the same. In other words, while subjecting to the HFMF, the nanostructural perturbation of the inner core phase accelerated considerably the movement of the IBU molecules due to the dissociation of the PVA phase and in the meantime, thermally-induced diffusion, a significant increase in the collision frequency of the IBU to the silica shell by a factor of est. 10 was observed. In consequence, a burst-like release behavior for the SAIO@SiO₂ nanocarrier was detected. However, once the stimulus was removed, the inner core phase must restore rapidly to original status, where the PVA solidified and thermal perturbation due to superparamagnetic nature of the nano-metric iron oxide nanoparticles ceased. The nanostructural integrity of the silica shell remained intact, where the regulating effect kept identically effective, as evidenced in the release profiles upon several “on-off” operations, Figure 7.6(b).

Mechanical motion of iron oxide nanoparticles within the core phase under HFMF gives rise to an alternative contribution to the burst release pattern of the SAIO@SiO₂ nanocarriers. The degree and speed of deformation of the SAIO core phase depended on the interactions among the nanomagnets and PVA phase, where both phases are intimately contact in a nanometric confinement. Magnetic nanoparticles in the magnetic field subject to stretch along the direction of the field due to the magnetostatic energy,

$$E_{ms} = 1/2(N_{//}-N_{\perp})M^2V \quad (1)$$

where $N_{//}$ and N_{\perp} are demagnetizing factors in the directions parallel and perpendicular to the magnetic field. E_{ms} is the energy of magnetic interaction of the magnetic moment M of the nanoparticles with magnetic field H . V is the volume of magnetic nanoparticles. While applying a magnetic field, magnetostatic interactions

induced by magnetic field will cause an appearance of demagnetizing field inside the SAIO core. Owing to this magnetostatic interaction, the magnetic particles in the core phase will tend to move, resulting in establishing stresses inside the nanostructures. Such stresses may act a factor accelerating the formation of the nano-cavities and deformation of SAIO nanoparticles as shown in Figure 7.7(c) to 7.7(f). From experimental observations, it suggests that such a HFMF-induced nanostructural evolution involves following four stages: (i) heating of the SAIO core locally, (ii) causing certain degree of relaxation of polyvinyl alcohol which further combines with (iii) the mechanical motions of iron oxide nanoparticles, following (iv) defect formation, which is especially pronounced for SAIO nanoparticles. Such a nanostructural evolution under HFMF stimulus surely enhances the burst release behavior from within the core phase for the SAIO@SiO₂ nanocarriers.

7.8 Cell Uptake

Cellular uptake of the FITC-labeled SAIO@SiO₂ nanocarriers was investigated by PL microscopy and flow cytometry. After 24 hours of HeLa cell incubation, which is employed as a cancer cell model, cells treated with FITC-SAIO@SiO₂ nanocarriers for various time durations were monitored. **Figure 7.8a to 7.8d** show that the nanocarriers subjected to the cells with time duration from 30 minutes to 4 hours were gradually uptaken by the cells, probably through endocytosis. The green fluorescence dye can be observed in cytoplasm clearly. The green FITC-nanocarriers appear localized as discrete dots, suggesting the nanocarriers without any detectable leaching. For a duration of 30 minutes, some of the nanocarriers appeared to rapidly attach on the surface of the cell membranes, Figure 7.8a, and further increase to a time point of 1 hour, Figure 7.8b, large amount of the labeled nanocarriers adsorbed onto the cells and some appeared to residing in the cells. After 2 hour of incubation, Figure 7.8c

show that the nanocarriers largely migrate to the cytoplasm region, where some light spots can be clearly visually detected in their cytoplasm. With 4 hours of incubation, considerable regions of the cytoplasm displayed strong green fluorescence illuminance as shown in Figure 7.8d, indicating that the nanocarriers are efficiently localized within the cell. It is also illustrated a relatively fast cellular uptake efficiency for the SAIO@SiO₂ nanocarriers, the absence of un-desirable surfactant and highly biocompatible, textured silica shell may take responsible for such an ultra-fast cell uptake behavior.

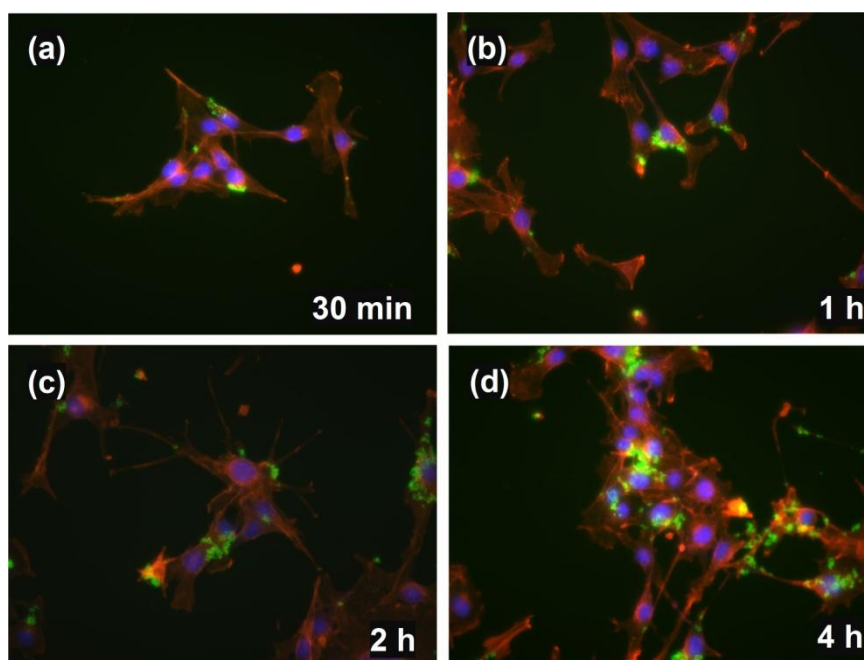


Figure 7.8 Time-course PL microscopy images of HeLa cells labeled with FITC- SAIO@SiO₂ nanocarriers, the cell skeleton was stained with rhodamine phalloidin (red), and cell nucleus with DAPI (purple). Cells were incubated with FITC- SAIO@SiO₂ nanocarriers for (a) 30 min, (b) 1 h, (c) 2 h, and (d) 4 hour.

Figure 7.9a showed the results of the MTT (3-(4,5-dimethylthiazol-2-yl)-2,5-diphenyl Tetrazolium Bromide) assay, as a measure of metabolic competence of the cell with SAIO and SAIO@SiO₂ nanospheres with different concentrations. The difference in the cytotoxicity at 12 to 48 hours of incubation is negligibly small. At

highest concentration of 5 $\mu\text{L}/\text{cc}$ SAIO, the cell viability also maintained at about 100%. The results suggest that the microcapsules were low in toxicity with respect to the HeLa cell line. Flow cytometric spectra, **Fig. 7.9b**, also indicate that the FITC-SAIO@SiO₂ nanocarriers are capable of penetrating the HeLa cells efficiently. Although flow cytometry cannot clearly define the surface-bound and intracellular nanocarriers, PL image strongly suggests the nanocarriers being largely uptaken by the cancer cells over a relatively short time period of contact. With increasing incubated time from 30 min to 2 hour of the nanocarriers, the fluorescence intensity

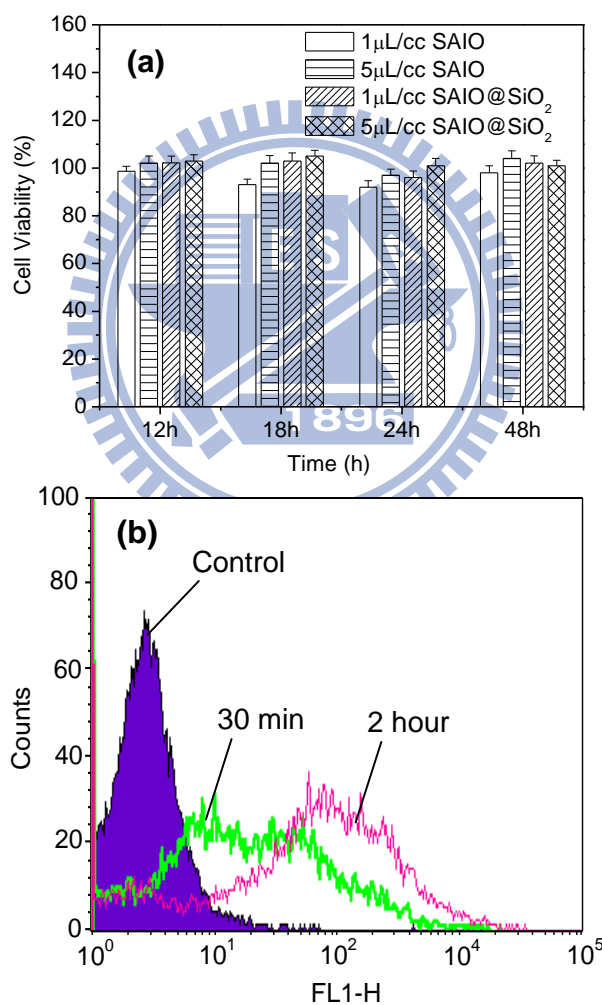


Figure 7.9 (a) Cell viability of HeLa cells after 12 to 48 hours of incubation with increasing amounts of SAIO and SAIO@SiO₂ nanospheres. Cell viability was measured using an MTT assay. (b) Flow cytometry analysis for the FITC- SAIO@SiO₂ nanocarriers accumulated in HeLa cells for incubation of 30 min and 2 hours.

measured by flow cytometry increased proportionally, further indicating that cellular uptake of the FITC-SAIO@SiO₂ nanocarriers can be efficiently and rapidly occurred. This finding indicates that the SAIO@SiO₂ nanocarriers showed little cytotoxicity to the HeLa cells, suggesting excellent biocompatible character and should accordingly be highly compatible to healthy cells. As a critical requirement for anti-cancer drug delivery strategy, reduction of the cytotoxicity of drug carrier itself can be satisfied and a further minimize the cytotoxicity of the drug can be accompanied. To our surprise is the ultra-fast cellular uptake of the nanocarriers within dozens of minutes, which, associated with a rapid and precise dosing corresponding to external stimulus, provides an avenue for a cellular-based control drug delivery and also offers a potential advantage for cellular imaging.

7.9 Summary

Self-assemble iron oxide/silica core-shell (SAIO@SiO₂) nanocarriers were fabricated as multi-functional drug vectors. The core-shell nanocarriers are able to well-disperse easily in an aqueous solution without using any interfacial molecules for stabilization, which provides great advantage for practical medical uses such as forming a suspension for injection or oral administrations. The ultra-thin, 4-5 nm, outer silica shell coated on the SAIO core, a mixture of iron oxide nanoparticles and PVA, blocked the drug molecules effectively from therapeutically undesirable release from the core phase before subjecting to magnetic stimulation. Under high-frequency magnetic field (HFMF) treatment, the SAIO@SiO₂ nanocarriers displayed a fast-acting and precise stimulus-time-dependent dosing response to the environment and restored to original state, i.e., a relatively slow and zero-order release profile, immediately after removal of the stimulus. In addition, the surfactant-free SAIO@SiO₂ nanocarriers were allowed a high efficiency uptake by HeLa cells within

dozens of minutes and have been shown to exhibit excellent cytocompatibility, implying the nanocarriers are potentially capable of offering high-efficient cellular-based delivery following a fast-acting, accurate release of therapeutic agents for anti-cancer applications.

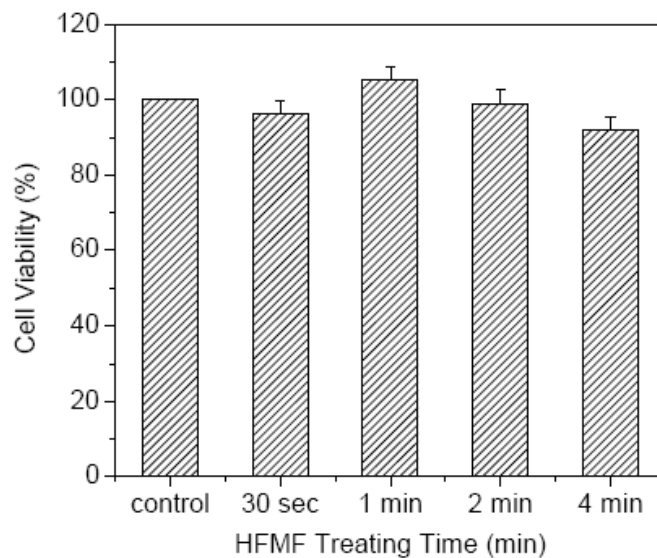


Figure 7.10 After the HeLa cells took up the SAIO@SiO₂ nanospheres, the HFMF subjected to these cells for 30 seconds to 4 minutes. The cytotoxicity with short time of HFMF treatment is small, indicating that the heat produced by nanospheres could not kill most of the cancer cells.

Chapter 8

Thermosensitive Yolk/Shell Capsules for Magnetically-Triggered Drug Release

8.1 Introduction

Biocompatible yolk/shell capsules are core/shell colloidal particles that can be remotely activated to rupture, making them attractive for their potential applications in drug delivery systems. The dense shells of these particles provide both chemical and physical shielding from the surrounding environment, which can reduce undesired drug release.^[150] Yolk/shell structures also have a cavity that allows for efficient delivery of proteins and nucleic acids.^[151-153] Finally, the interior of these particles can be functionalized by encapsulating guest species, allowing them to be tuned to obtain a variety of desired properties.^[154,155]

One possible approach to making these capsules is to use a composite material made of a magnetic nanoparticle inside a thermosensitive polymer. This particle can then be covered with a dense silica layer as a barrier to release. The thermosensitive polymer serves as a soft-template core that varies in size according to temperature. Self-heating of the magnetic nanoparticles in response to an external magnetic stimulus triggers the deformation and collapse of the capsules, causing the solid shell to rupture and the inner substances to be released, which in this application would be drug molecules. Drug release via physical rupture exhibits several advantages; for example, drug molecules are not covalently bound to the drug carriers avoiding the need to alter the molecule's original properties and for chemical treatment to cleave bonds. However, to the best of our knowledge, the synthesis of yolk/shell capsules possessing a cavity and their application for remotely triggered drug release has not yet been studied. Obtaining functional capsules that show an acceptable

biocompatibility, fast actuation, high drug-loading efficiency and an activation temperature near physiological temperatures will require careful design of the material constituents.

A major challenge in designing drug release systems involves the precise control of drug release, both spatially and temporally. Optimizing drug-release behavior to enable pulsatile release mimicking the natural release of biomolecules is also desirable. The reports have principally studied micro- or nano-scale structures and drug reservoirs. Many focal diseases require local drug release systems that can act at a specific site, thus reducing the side effects of a toxic drug molecule or enhancing a drug's therapeutic efficiency. Functional nanomaterials have recently been used as an energy-induced media to trigger drug release for cancer therapy. For example, the photothermal effects of gold nanostructures, nanocages and carbon nanotubes can be activated by irradiation with near-infrared (NIR) light for tumor therapy.^[156,157] These materials are effective at increasing the local temperature using NIR light, but the short penetration depth of NIR lasers may require the injection of an invasive optical-fiber into the tumor tissue to treat deep-seated cancer cells. Using a magnetic field in place of these NIR systems would allow for remote management to trigger drug release from the magnetic drug carriers.

A high frequency magnetic field can cause an increase in the temperature of magnetic nanoparticles, which could be a useful for creating local hyperthermia and as an approach to cancer therapy. However, such high temperature is not suitable for treatment of non-cancerous tissues or for normal drug release, as the high temperatures will likely kill healthy cells and destroy the activities of drug molecules. This activity would be a particular problem when delivering biomolecules like proteins. Therefore, there is a strong need for technologies that can achieve magnetically-triggered drug release at a low temperature. To address this technical

challenge, the thermosensitive polymer poly (ethylene oxide)-poly (propylene oxide)-poly (ethylene oxide) (PEO-PPO-PEO, known as Pluronic^[158]), was added to the magnetically-triggered yolk/shell capsules to optimize the operating temperature of the magnetic field and induce triggered release. To achieve a low-temperature trigger, rapid drug release under a remotely-applied magnetic stimulus and good encapsulation of the drug molecules in the capsules, we have designed particles containing several components, including a magnetic core composed of iron oxide nanoparticles, a thermally responsive PEO-PPO-PEO polymer and an ultra-thin silica shell that can efficiently regulate the drug release behavior before and after the magnetic trigger. The integration of these functions is critical for the development of a novel yolk/shell capsule that can be broadly applied as a drug and protein delivery vehicle for biomedical applications. These capsules would not only protect the drug molecules before release, but would also enable magnetically-triggered drug release at a well-tolerated temperature.

8.2 Experimental section

Synthesis of Thermosensitive Yolk/shell Capsules: To prepare the self-assembled magnetic nanoparticles and functional polymers, 5 mg of iron oxide was centrifuged at 6000 rpm for 10 min and then re-dispersed in 4 mL of a 1% ibuprofen (model drug) chloroform solution. Different ratios of PVA/F68 as shown in **Table 8.1** were heated in 10 mL of DI water at 70 °C until the solids had completely dissolved, and this clear solution was then cooled to room temperature. Next, the chloroform solution was added to the polymer solution and the resulting mixture was emulsified for 5 minutes with a 100 W ultrasonicator. The mixture was then stirred magnetically at room temperature to evaporate the organic solvent. After the evaporation of the organic solvent, the products were washed 3 times with DI water and centrifuged at 6000 rpm

to collect the desired products. An ultra-thin silica shell was then added to the nanospheres using the modified Stöber method. In brief, 5 mg of nanospheres were dispersed in 4 mL of 99.5% ethanol and 0.1 mL of 33% NH₄OH for 30 min. Following this, 50 μm of tetraethylorthosilicate (TEOS) was slowly added to the mixture and the mixture was stirred for 12 h. After hydrolysis and condensation, the silica shell was coated onto the nanocomposites (NCs) to form the yolk/shell capsules.

Table 8.1. Reagents used for the synthesis of thermosensitive yolk/shell capsules. The organic/inorganic ratios (*Org./Ino.*) and saturation magnetization (*Ms*) of yolk/shell capsules, and their encapsulation efficiency (*EE*) where the hydrophobic drug, ibuprofen, was used as a model drug.

sample	Weight Ratio			Org./Ino. (TGA)	Ms (emu/g)	Fe ₃ O ₄ (%)	EE (%)
	Fe ₃ O ₄	PVA/F68	TEOS				
Yolk/shell-1	1	5/1	2.5	66/34	7.9	12	73±5
Yolk/shell-2	1	5/2.5	2.5	72/28	6.7	10	70±4
Yolk/shell-3	1	5/5	2.5	79/21	4.9	8	65±4
Yolk/shell-4	1	5/10	2.5	85/15	3.1	5	58±5

Characterization: The relative amount of magnetic nanoparticles that were associated with the gelatin was determined using thermo-gravimetric analysis (TGA, Perkin Elmer). Samples were dried under vacuum for approximately 48 hours and analyzed in the platinum plate at a heating rate of 10 °C/min under an atmosphere of nitrogen.

Drug Loading Efficiency and Release: This study used ibuprofen (IBU) as a model drug to examine the drug loading efficiency and release behaviors of the yolk/shell capsules. After the drug loading process, the drug-containing capsules were separated from the aqueous solution by centrifugation at 10,000 rpm for 15 min. The drug concentration in the supernatant was analyzed using a UV-vis spectrophotometer (Agilent, 8453 UV-Visible spectrophotometer) at a wavelength of 264 nm, where

there is a strong absorption band from the IBU. These measurements were performed in triplicate. The amount of drug in the yolk/shell capsules was calculated by subtracting the residual IBU in the supernatant from the total amount of IBU measured. The encapsulation efficiency (EE) was obtained as follows: $EE=(A-B)/C \times 100$, where A is the total amount of IBU, B is the amount of IBU remaining in the supernatant, and C is the weight of the capsules. For the drug release tests, the capsules were washed with phosphate buffered saline (pH 7.4) and then DI water. Ibuprofen-containing capsules were placed in PBS buffer solution for all drug-release experiments. A quantitative estimate of the IBU loading was obtained using UV-vis spectrophotometry, and the drug-release behavior of the capsules was measured using 20 mL of phosphate buffered saline solution (pH 7.4). To measure the concentration of released drug, 1.5 mL of the capsule-containing PBS medium was centrifuged at 4000 rpm to remove the particles.

To estimate the cellular uptake of capsules, green emitting fluorescein dye was attached to the yolk/shell capsules (FITC-labeled yolk/shell capsules). First, fluorescein isothiocyanate (FITC) was mixed with an ethanolic 3-aminopropyltrimethoxysilane (APTMS) solution for 24 h at room temperature to form N-1-(3-trimethoxysilylpropyl)-N-fluoresceyl thiourea (FITC-APTMS). In a separate flask, 5 mg of SATN were dispersed in 4 mL of 99.5% ethanol and 0.1 mL of 33% NaOH solution for 30 min. Following this, 40 μ m of tetraethylorthosilicate (TEOS) and 10 μ m of FITC-APTMS were slowly added to the mixture, which was then stirred for 12 h. After hydrolysis and condensation, the FITC-labeled silica was coated onto the capsules. The unreacted chemicals were removed by rinsing with DI water three times. The capsules were incubated with the cells for different times and then the cells were observed by confocal microscopy (Nikon, C1).

8.3 Preparation of thermosensitive yolk/shell capsules

Figure 8.1a presents a schematic illustration of the synthetic procedure that was used to synthesize the yolk/shell capsules. The first step involved mixing the oil-soluble iron oxide nanoparticles and the hydrophobic drug in an organic solvent to form a uniform phase. Next, the mini-emulsion method was applied using blended polymers, polyvinyl alcohol (PVA) and pluronic F68 as a binder to fabricate the self-assembling nanocomposites (NCs). Because PVA and pluronic F68 are amphiphilic polymers, the hydrophobic segments of these polymers generated the driving force for the formation of iron oxide nanoparticles. While the organic solvent gradually evaporated, the polymers encapsulated the iron oxide nanoparticles and the hydrophobic drug within the composite. This encapsulation is believed to result from non-covalent interactions between the functional groups on the iron oxide surface and the hydroxyl groups of the PVA and F68. These groups may interact through hydrogen bonds or dipole-dipole interactions, resulting in an amphiphilic, polymer-induced structural self-assembly. Following this, the NCs were coated with a thin layer of silica by hydrolysis and condensation of TEOS to obtain the final yolk/shell capsules. Different ratios of PVA/F68 and iron oxide nanoparticles were used in this system as shown in **Table 8.1** to examine the effects of composition on thermosensitivity. **Figure 8.1b** presents the TEM image of the resulting yolk/shell-1. These capsules had an average diameter of approximately 76 nm and possessed an ultra-thin layer of dense silica, forming a shell approximately 7 nm in thickness. No observable crevices or cracks were detectable microscopically in the regions between the core structure and the silica shell, suggesting a compatible interface between these two materials. Furthermore, as shown in the TEM image, there were only 2-5 iron oxide nanoparticles per capsule, and the polymer matrix accounted for a large portion

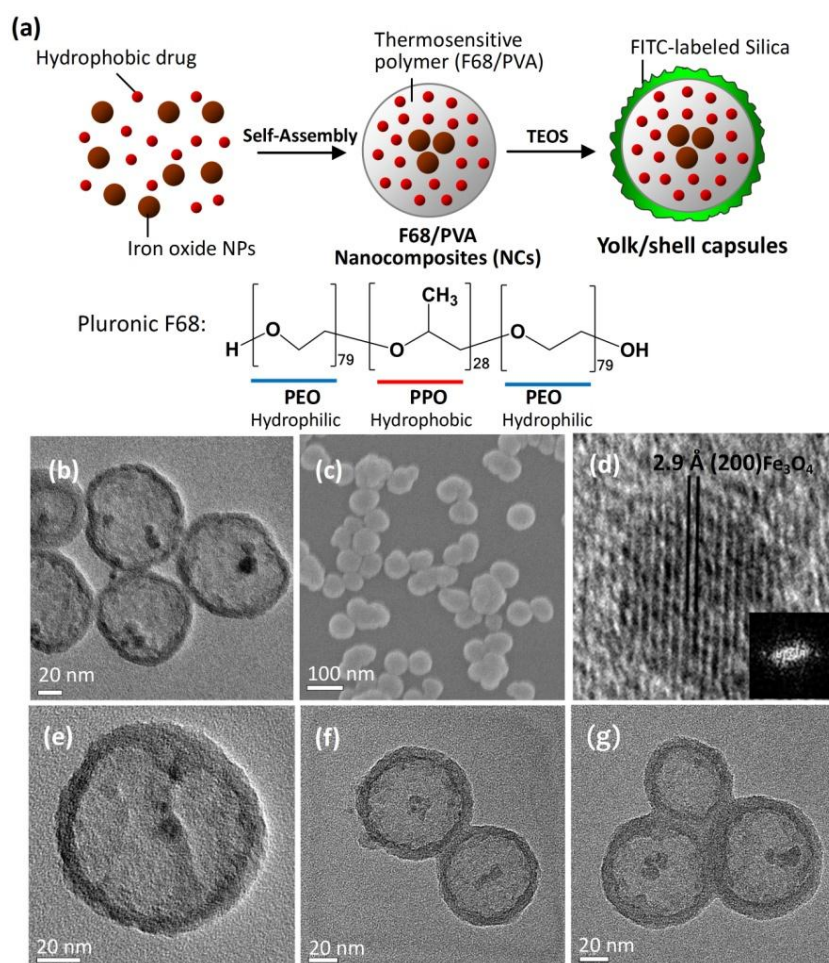


Figure 8.1 (a) Schematic illustration of the synthesis and structure of the thermosensitive yolk/shell capsules for magnetically-triggered controlled drug release. TEM images of (b) yolk/shell-1, (e) yolk/shell-2, (f) yolk/shell-3, and (g) yolk/shell-4. (c) The SEM images of yolk/shell capsules. (d) The TEM image of lattice structure of iron oxide nanoparticles in the capsules. The yolk/shell capsules with an average diameter about 76 nm possessed an ultra-thin layer of dense silica shell of about 7 nm in thickness.

of the capsule volume, providing sufficient space for drug loading. The resulting yolk/shell capsules showed excellent suspension characteristics in both PBS and cell-culture medium without any chemical modification to the surface required for stabilization. The scanning electron microscopy (SEM) image of the resulting yolk/silica shell capsules shown in **Figure 8.1c** reveals the surface structure and morphologies of the capsules. In this image, the capsules showed a spherical geometry and a smooth surface. The silica shells did not display any crevices or cracks in the SEM image, indicating that the core had a dense and continuous

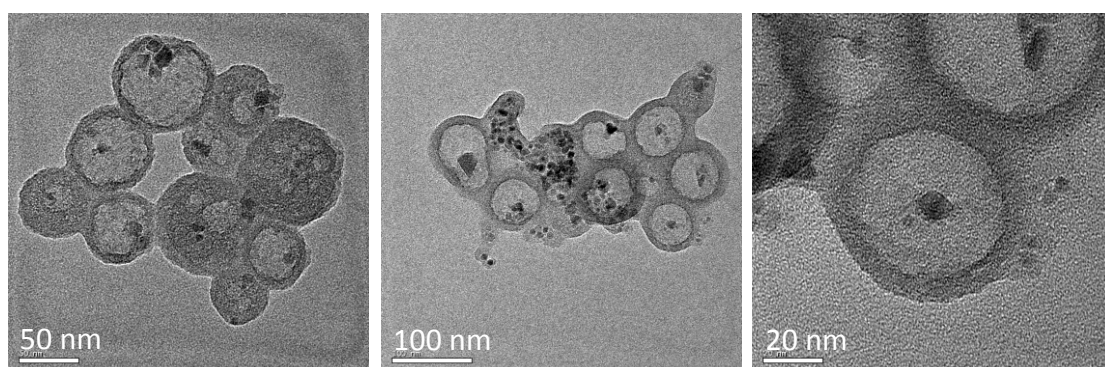


Figure 8.2 TEM images of yolk/shell capsules without PVA. Without PVA as a stabilizer, the nanocapsules displayed a un-uniform morphologies. Some magnetic nanoparticles were not encapsulated in the nanocapsules.

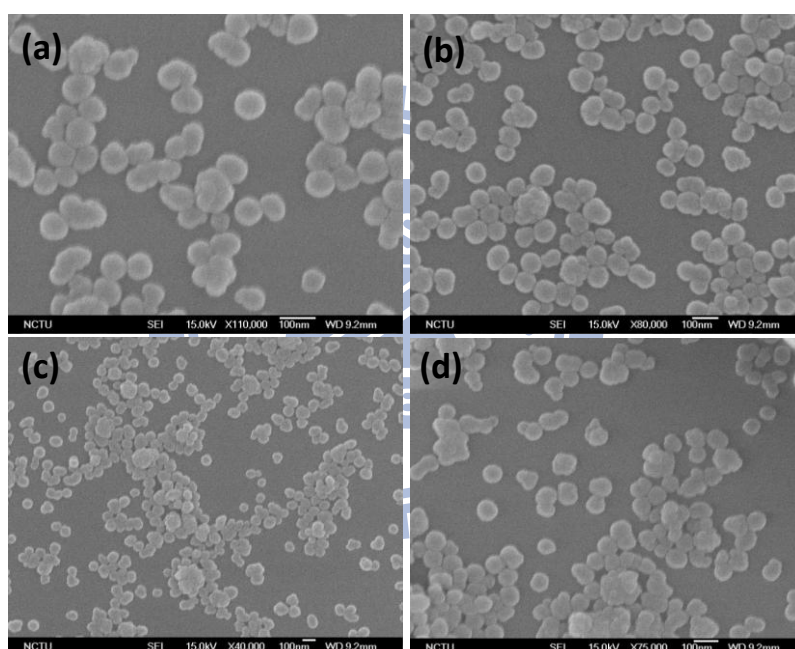


Figure 8.3 SEM images of (a) yolk/shell-1, (b) yolk/shell-2, (c) yolk/shell-3, and (d) yolk/shell-4.

structure. In the HR-TEM image shown in **Figure 8.1d**, the magnetic phase (Fe_3O_4) can be clearly identified as a crystalline structure. Yolk/shells-2, 3 and 4 with increasing F68/PVA ratios exhibited similar structures as seen in **Figures 8.1e** to **8.1g**, respectively. Silica shells approximately 7 nm in thickness, still covered the Fe_3O_4 /polymer core/shell nanocomposites (NCs). However, totally removing PVA

from this system resulted in yolk/shell capsules with non-uniform morphologies as observed by TEM analysis (**Figure 8.2**). This finding suggests that PVA plays an important role in stabilizing the core-shell structure and further in promoting the regular adsorption of the silica precursor on the surface. This could result from the high density of the hydroxide functional group in PVA, which forms strong hydrogen-bonding interactions with the -OH group on TEOS. Without the high-density -OH groups on the NCs, the silica would form nanospheres independently rather than coating the surface of the composite capsules. In addition, SEM images of yolk/shells-2, 3 and 4 displayed morphologies similar to those of yolk/shell-1, which had a spherical geometry (**Figure 8.3**). The ultra-thin silica shell was designed to be a physical barrier that could eliminate undesired drug release and regulate desired release in a controllable manner. Following the synthesis of these capsules, fluorescein isothiocyanate (FITC) was conjugated on the silica shell as a fluorescent dye for further cell imaging as discussed later.

8.4 Characterization of yolk/shell capsules

The magnetic properties of the yolk/shell capsules were investigated using a superconducting quantum interference device (SQUID) at 298 K with a magnetic field sweeping from -10000 to +10000 G. **Figure 8.4** shows the correlation of the magnetization with the magnetic field from yolk/shells-1 to -4, where the curves are similar for all yolk/shells and display negligible hysteresis. The increased polymer content from yolk/shell-1 to yolk/shell-4 dilutes the concentration of iron oxide particles, resulting in a decreasing saturation magnetization (M_s). The weight % (wt%) of iron oxide nanoparticles in the capsules shown in **Table 8.1** were determined by the relative intensities of saturation magnetization (M_s) between the Fe_3O_4 and the yolk/shell capsules (see supporting information, Figure S8.3). The wt% of iron oxide nanoparticles in the yolk/shell capsules ranged from 5-12%, suggesting a relatively

low concentration of these nanoparticles. Furthermore the weight ratios of organic substances in the yolk/shell capsules reported in **Table 8.1** ranged from 66-85% as estimated by TGA analysis (see supporting information, Figure S8.4). This could be advantageous for conjugating therapeutic molecules because a large proportion of organic material such as the polymer matrix can trap more therapeutic agents, thus increasing the payload in each capsule.

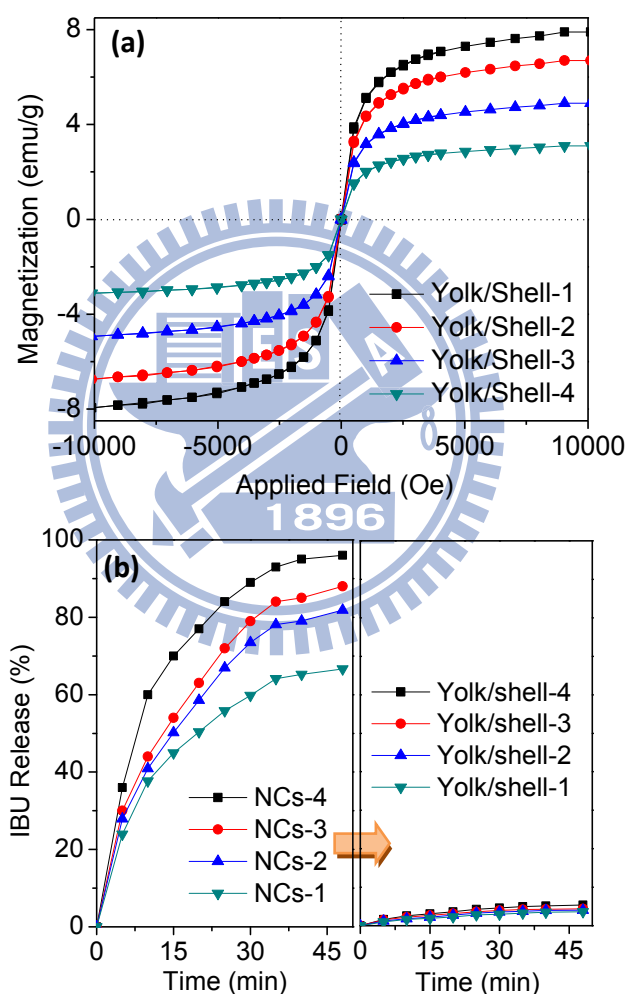


Figure 8.4 (a) Field-dependent magnetization curves of yolk/shell-1 to yolk/shell-4, showing the capsules are superparamagnetic. (b) Cumulative drug release of F68/PVA nanocomposites (NCs) and yolk/shell capsules. Coated with silica shells, the yolk/shell capsules showed relatively smaller amount of cumulative drug release than F68/PVA nanocomposites (NCs).

To investigate the drug-loading capacity of the yolk/shell capsules, the hydrophobic model drug ibuprofen (IBU) was loaded into the capsules. The encapsulation efficiency (EE) of IBU with different PVA/F68 ratios is shown in **Table 8.1**. The capsules encapsulate the drug molecules through a microemulsion process. This process enhances the drug loading efficiency because it gathers the hydrophobic substances like iron oxide nanoparticles and drug molecules into the oil-phase of the droplets. During evaporation of the organic solvent, the droplets form stable nanospheres that contain the hydrophobic molecules and nanoparticles. Furthermore, the hydrophobic chains of the amphiphilic polymer that are in the center of the nanospheres efficiently bind the hydrophobic drug through hydrophobic interaction. Because the hydrophobic drug has a low solubility in aqueous solutions, the drug molecules were preferentially encapsulated in the nanospheres rather than remaining in water. With an increase in the F68 ratio, the IBU encapsulation efficiency decreased from 0.73 to 0.58. The high encapsulation efficiency of IBU in the capsules resulted from three factors: first, the vast space of the polymer matrix in the yolk/shell capsules allows for a high payload. Second, PVA forms strong intrinsic hydrogen bonds, tightening the nanocomposites and making drug encapsulation more stable. Finally, silica shells are effective shielding layers to seal the drug molecules into the yolk/shell capsules and prevent leakage.

8.5 Drug release of yolk/shell capsules and F68/PVA nanocomposites

Figure 8.4a shows the cumulative drug release of the yolk/shell capsules and F68/PVA nanocomposites (NCs) in PBS at pH 7.4. The difference between these two systems is the absence or presence of the silica shell. Although both systems demonstrate sustained release, the drug release rates are markedly different between the two systems. Within 48 hours more than 60% of the IBU is released from the F68/PVA NCs, much higher than the amount released from the yolk/shell capsules. The main cause of this difference is the presence of the silica shells, which act as a

physical barrier, keeping the drug molecules inside the nanostructures and limiting their outward diffusion. The hydrophobic drug ibuprofen exhibits limited solubility (~0.5 %) in PBS and thus stays readily in the F68/PVA NCs. The driving force of the large concentration gradient and the flexible polymer structure give rise to an outward diffusion of the ibuprofen through the F68/PVA NCs in the absence of a physical barrier to regulate the release. The release from the yolk/shell capsules is predominantly regulated by the silica shells and show a zero-order kinetic reaction rate. In these systems, the rate of release is relatively slow, reaching only 6% over 48 h. This finding clearly indicates that the inorganic silica shell, although it is only 7 nm thick, acts as an effective barrier to block the drug molecules from passive diffusion due to its density and stability. This result also indicates that the ultra-thin silica shell is structurally compact, with full coverage over the entire surface of the F68/PVA NCs as shown in **Figures 8.1b to 8.1d**. These figures clearly demonstrate the presence of observable defects along the thin shell and sub-surface regions, indicating a compatible interface between the silica shell and core structure. In comparison to these two carriers, the ultra-thin silica shells have relatively slow release, which is advantageous for preserving and protecting the drug molecules within the nanostructures from undesirable leakage.

8.6 Thermosensitive behavior of the yolk/shell capsules

The thermosensitivity of these yolk/shell capsules is based on the well-known properties of PEO-PPO-PEO triblock polymers, commercially known as Pluronic, that manifest a range of critical micelle temperatures (CMT) for volume/hydrophobicity transitions.^[159] The capsule cores display thermosensitive behavior similar to that of the PEO-PPO-PEO polymer, including shrinkage above the CMT, which implies a hydrophobic/hydrophilic transition. The CMT of the volume change can be varied through chemical modification, enabling these polymers to be tailored to fit diverse drug release applications.^[160] To further investigate these

variations, the size of capsules without silica shells, i.e., F68/PVA nanocomposites (NCs), were measured by DLS at different temperatures. **Figure 8.5a** shows the size of F68/PVA NCs as a function of temperature, where a transition is revealed by the large change in size between 45 °C and 50 °C. The CMT of the F68/PVA series (47 °C) is higher than that of pure F68 (43 °C) because PVA introduces more hydrophilic functional groups to the nanostructures, resulting in stronger interactions such as hydrogen bonding between the PVA and F68. Compared to literature reports, the higher EO/PO ratio in F68 (5.24) compared to the lower ratio seen in F127 (3.08) result in a higher CMT (CMT = 26 °C), demonstrating that hydrophilic interactions can increase the CMT. Below the CMT, the size of the F68/PVA NCs increased significantly from 20 °C to 47 °C. The increase is caused by the interactions between the hydroxide moiety of PVA and the hydrophilic/hydrophobic transition of F68. Increasing the temperature below the CMT results in a gradual hydrophilic/hydrophobic transition where some of the hydrogen bonds of F68 transfer toward inner molecules, resulting in a hydrophobic surface. This causes repulsion between the hydrophilic hydroxide group of PVA and the hydrophobic backbone of F68. This repulsion readily increases the size of the nanocomposites with increasing temperature below the CMT. For example, NCs-1 with higher F68/PVA ratios exhibited a greater than 2.5-fold increase in size below the transition temperature (47 °C). DSC analysis was used to investigate the hydrogen bonding interactions between the two polymers, as shown in **Figure 8.5b**. An exothermic peak from pure F68 and F68/PVA NCs was detected in the cooling run due to the melting transition. With higher concentrations of PVA the liquefaction started at lower temperatures because PVA allows for more hydrogen bonding in the NCs, thus increasing the strength of the interactions between the two polymers and restricting the movements of polymer chains. The obvious peak shift is evidence of the strong interactions between the two polymers.

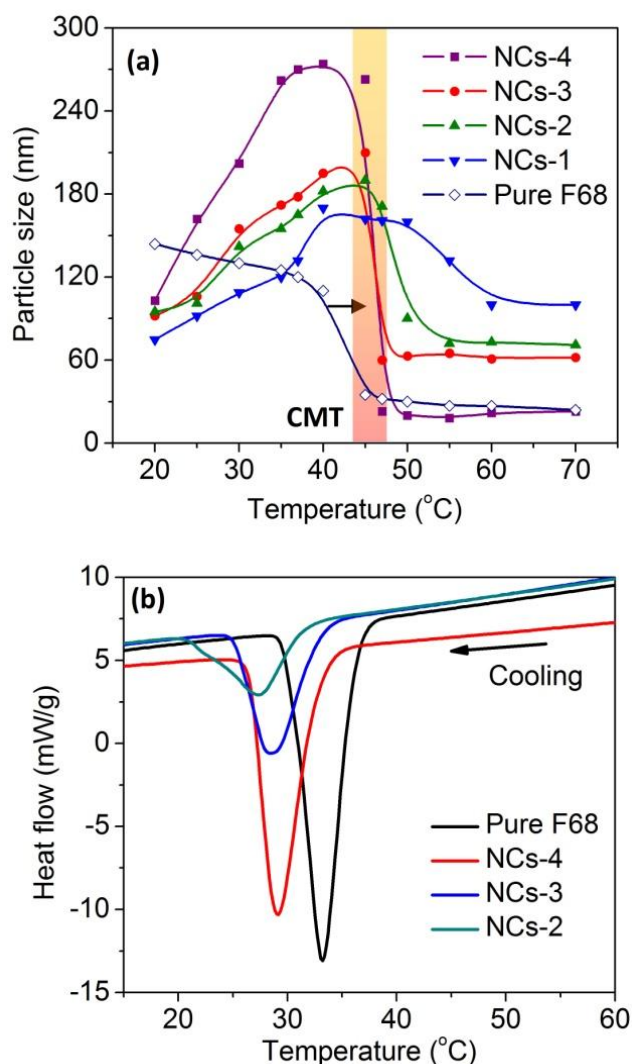


Figure 8.5 (a) Diameter of F68/PVA nanocomposites (NCs) measured by DLS decreased abruptly at about critically micellization temperature (CMT). (b) DSC cooling scans of F68 and F68/PVA nanocomposites (NCs).

The size ratio is defined as d_{max}/d_{min} , where d_{max} is the maximum particle diameter below the CMT at the lowest temperature and d_{min} is the minimum particle diameter above the CMT at the highest measurement temperature. The d_{max}/d_{min} of nanocomposites (NCs) obviously increased when the NCs possessed higher F68 ratios. For example, the d_{max}/d_{min} for NCs with a F68:PVA ratio of 10:5 is 11, much higher than the d_{max}/d_{min} ratio seen when the F68:PVA ratio is 1:5 ($d_{max}/d_{min} = 1.8$). This result was also compounded by the interactions of PVA and F68, as mentioned in previous paragraph, in that the F68:PVA=10:5 NCs possessed a larger d_{max} , so the d_{max}/d_{min}

dramatically increased. This finding also indicates the obvious shrinking that occurs once the temperature has crossed the CMT threshold, as shown in **Figure 8.5a**. Addition of PVA causes a clear decrease in the d_{\max} and an increase in the d_{\min} , so both the hydrophilic "swollen" state and the hydrophobic "shrunken" state appear to be constrained by the presence of PVA. NCs with PVA displayed larger volume/hydrophobicity transition properties than pure F68 nanospheres. Therefore, the ratio of PVA:F68 in this study is an important factor. Because the NCs with F68:PVA ratios of 5:10 through 1:5 were stable when forming silica shells and exhibited high variations in size ratios, these NCs were selected for the encapsulation of IBU for drug release studies.

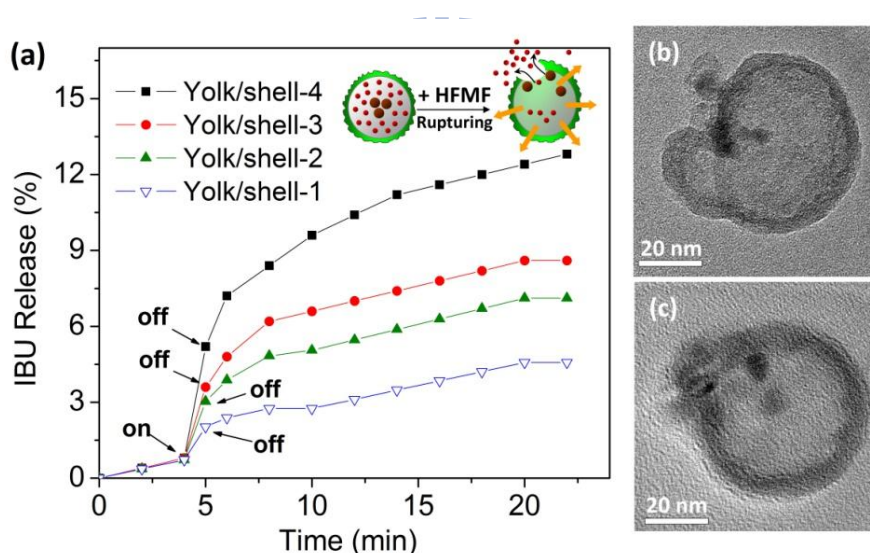


Figure 8.6 (a) Cumulative drug release profiles of ibuprofen (IBU) from yolk/shell capsules were triggered by 1 minute of high frequency magnetic field (HFMF) at fourth minute. Schematic illustration as shown in inside picture with a proposed mechanism for controlled drug release under HFMF. After the exposure to a magnetic field, the volume/hydrophobicity transition of cores produced a strong inner stress, making the capsules collapse or rupture as demonstrated in (b) and (c) TEM images.

8.7 Magnetically-triggered drug release from yolk/shell capsules

Figure 8.6a shows the IBU release profiles from yolk/shell capsules under magnetic fields of 2.5 kA/m at a frequency of 50 kHz. As these results show, a significant acceleration in release was observed in the fourth minute of subjection to

the magnetic field, which was not seen in the absence of the magnetic stimulus. For yolk/shell-1, the cumulative release amount increased to 2.0% over 1 min of exposure. With higher ratios of the thermosensitive polymer, the controlled release from yolk/shell-4 increased to 5.3% within 1 min of exposure to the stimulus. Furthermore, when the magnetic field was removed after five minutes, yolk/shell-4 maintained its accelerated drug release behavior and another rate increase was seen, increasing from 5.1% to 13% within 20 minutes. The release profile of the yolk/shell capsules was not restored right after the removal of the stimulus, and the release rate was considerably increased compared to that of the as-prepared yolk/shell capsules that were not subjected to any magnetic field treatment. This finding suggests that the nanostructures were physically and irreversibly deformed, thus maintaining their rapid release rate after removal of the stimulus. With different ratios of F68/PVA, the amount of drug released from the yolk/shell capsules after the removal of the magnetic field increased linearly with the F68 ratio, indicating that the drug release is a thermally activated process. To estimate the mechanism of drug release from the yolk/shell capsules under magnetic field treatment, the release kinetics can be characterized using the equation,

$$M_t/M=kt^n,$$

where M_t is the mass of drug released at time t , M is the mass released at infinite time, k is a rate constant, and n is a characteristic exponent related to the mode of transport of the drug molecules.^[138] This analysis was performed for $M_t/M < 0.6$, and the fitting parameters are listed in **Table 8.2**. Under magnetic induction the exponent constants (n) are all approximately 0.4, which is beyond the regime of the Fickian diffusion mode. This indicates that the rapid release may result from a strong driving force such as the rupture of the capsules that allows for effective diffusion of drug from the core. Accordingly, the diffusion of drug from yolk/shell capsules occurs along two paths after rupture. One path is from the core of the yolk/shell capsules, which would be

caused by the magnetic heating-induced volume/hydrophobicity transition that would pump the drug molecules from the polymer matrix toward the external environment. This path would have relatively fast release kinetics. The second path involves free diffusion towards the capsule outlet. Moreover, the rate constant (k) in Table 8.2 clearly shows that there is a systematic growth of k from yolk/shell-4 to yolk/shell-1. These results indicate that the drug release from the yolk/shell capsules is a thermally activated process, and the thermosensitive F68 polymer in the capsules plays an important role in accelerating the magnetically triggered release.

8.8 Nanostructure evolution under magnetic treatment

To further elucidate the mechanism behind the magnetically triggered release behavior, the yolk/shell capsules were examined using HR-TEM, as illustrated in **Figures 8.6b** and **8.6c**. After a short exposure to the stimulus (60 s), the silica shell of the capsules was deformed as a result of rapid shrinkage of the core phase, causing irreversible cracks in the silica shells. In other words, subjection to the magnetic field for a short period of time resulted in the evolution of nano-scale crevices or cracks along the thin shell. This could be caused by the rapid volume/hydrophobicity transition of the core. Thermosensitive cores showed a dramatic change in size and enlarged nano-scale crevices after magnetic heating, which permitted dye molecules to easily escape from the capsule and ultimately formed a severe crack and led to the irreversible deformation or rupture of the shell. Some silica nanocapsule shells collapsed after exposure to a magnetic field as shown in **Figure 8.6b**. In addition, other shells appeared to break (**Fig. 8.6c**). Clearly, these changes are highly disruptive and support the scenario depicted in **Figure 8.6a** in which the magnetic field induces structural rupture and thus a burst drug release. Closer observation demonstrates that the cracks in the shell are close to the magnetic nanoparticles, suggesting that the shell deterioration begins at these particles.

Table 8.2. Summary of fitting constants (n and k) for cumulative release under the magnetic field treatment. The F68/PVA nanocomposites (NCs) weight lost after 1 minute of magnetic stimulus, estimated by TGA.

Sample	n	K X 10 ³	Org./Ino. after MF (TGA)	F68/PVA Lost (%)
Yolk/shell-1	0.40	14	31/69	35
Yolk/shell-2	0.39	24	26/74	47
Yolk/shell-3	0.39	30	23/77	57
Yolk/shell-4	0.39	42	19/81	66

For practical application, application of a magnetic field should produce a large change in size ratio and then physical rupture. Such dramatic volume changes can "open" the yolk/shell capsules and then release the unharmed drug molecules, which means that the drug molecules would not require exposure to other active chemicals or heating that might destroy their drug properties. For the magnetically triggered drug-release system, the heat induced by the magnetic field triggers drug release. However, this heat might harm or denature the drug molecules or proteins. Because the magnetic field is able to rapidly produce heat energy from the magnetic nanoparticles, the nanoparticle "hot-spots" easily transfer their heat to the surrounding substances. Heat generation, governed by the mechanism of magnetic energy dissipation for single-domain particles (Brown and Néel relaxations),^[137] has been well documented. A 1 min treatment increase the temperature of the solution (5 mg/cc water) by approximately 2 °C, from 25 °C to 27 °C. However, the local temperature inside the magnetic nanoparticles becomes much higher than the solution. These yolk/shell capsules only contain 2 to 4 magnetic nanoparticles per capsule, which reduces the Brown relaxation of extrinsic remagnetization between particles. This means that the energy can be absorbed uniformly and dispersed in each capsule. This dispersive energy can readily decrease the "hot-spot" effect on drug molecules, meaning that these drug molecules would not be severely affected by magnetic heating, unlike those attached directly to the magnetic nanoparticles.

We also investigated the weight loss of F68/PVA after the magnetic field stimulus by thermogravimetric analysis (TGA). After a 1 min period of magnetic field treatment, the amount of F68/PVA decreased 35-66% from yolk/shell-1 to yolk/shell-4 as shown in **Table 8.2**, indicating that substantial portions of the core phase did not become permanently incorporated into the cores. This was especially true for capsules with high F68 ratios. These findings suggest that the weight loss of the F68/PVA in the core results from outward diffusion caused by the rupture of the capsules and the formation of large cracks. This provides a reasonable explanation of why the drug release remained rapid after the burst-like release behavior. However, the release behavior in **Figure 8.5b** also demonstrates a positive relationship between F68 concentration and the release rate after the removal of the magnetic field. This further supports the conclusion that the thermosensitive polymer regulates the rupture effect of the shells. In other words, subjection to the magnetic field perturbed the nanostructure of the inner core phase, considerably accelerating the movement of the IBU molecules due to the high stress of the core phase. Concurrently, thermally induced expansion and then shrinking of the core phase led to a significant release of IBU to the environment. This resulted in a burst-like release behavior for these yolk/shell capsules. However, once the stimulus was removed, the inner core phase could not be restored to its original state; thus, drug release continued following removal of the magnetic field. This increases the likelihood that the drug molecules will not be heated and harmed by magnetic heating, allowing them to reach high active concentrations in areas where release is triggered for local therapy.

8.9 Cell uptake and MR imaging

Cellular uptake of the FITC-labeled yolk/shell capsules was investigated using confocal microscopy. This study used a normal cell model of retinal pigment epithelium (RPE) cells (ARPE-19), which are from a monolayer of hexagonal cells separating the neural retina from the underlying choroidal vascular bed. **Figures 8.7a**

and **7b** show cells incubated with FITC-labeled yolk/shell capsules for 4 and 24 hours, respectively. For the 4 hour incubation, some of the capsules appeared as green dots that were attached to the surface of the cell membranes; however, most of the capsules were still dispersed on the plate. Increasing the uptake time to 24 hours, shown in **Figure 8.7b**, resulted in a greater adsorption of the FITC-labeled capsules onto the cells, and some capsules also appeared to reside inside the cells. This implies that the yolk/shell capsules were gradually taken up by the cells, probably through endocytosis. The green fluorescent dye can be clearly observed in the cytoplasm. The capsules appear to be localized as discrete dots, suggesting that there was no

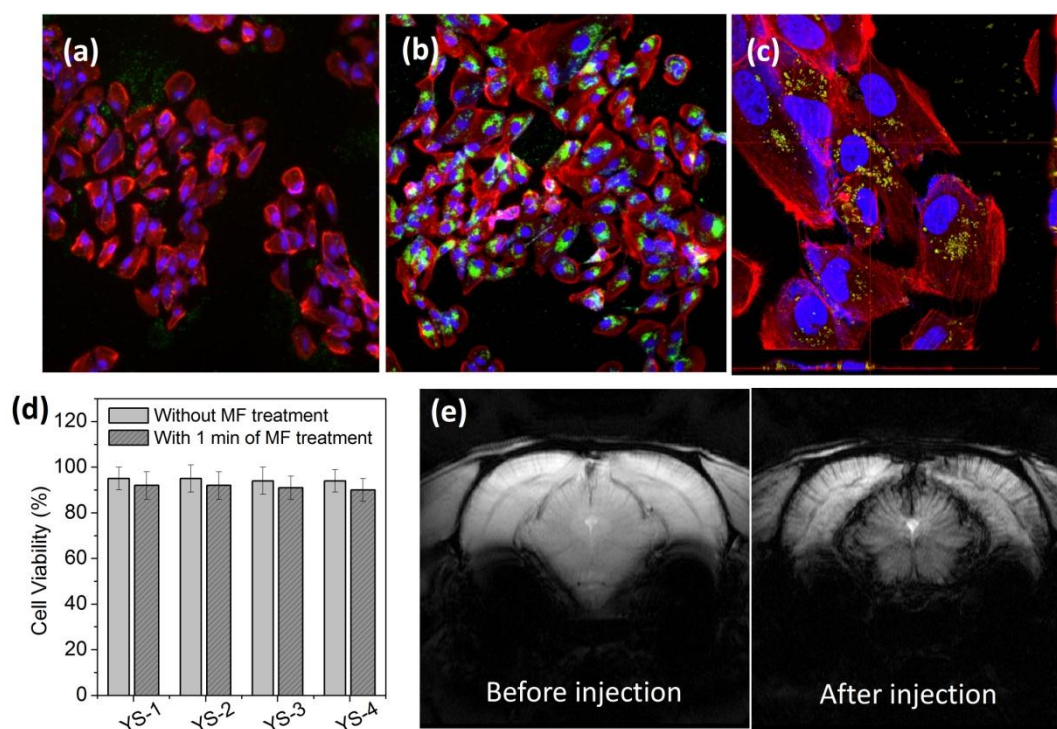


Figure 8.7 Time-course confocal images of ARPE-19 cells incubated with 10 FITC-labeled yolk/shell capsules (green dots) for (a) 4 and (b) 24 hours. The cells were stained with rhodamine phalloidin (red), and cell nucleus with DAPI (blue). (c) The cross section images of cells viewed by laser-scanning confocal microscope exhibited that the capsules are localized in cells. (d) ARPE-19 cell viability under the incubation of capsules for 24 hours with and without 1-minute of magnetic field treatment. (e) Magnetic resonance images of rat brain before and after the intravenous injection of yolk/shell capsules. The local hyperintensity generated by capsules was visualized using a 3 T small animal MR. Image was acquired pre-injection (Left) and 2 hr post-injection (Right).

detectable leaching of dye from the capsules. The cross-section of the confocal images in **Figure 8.7c** demonstrates considerable regions of the cytoplasm displaying strong green fluorescence, suggesting that the capsules are efficiently localized within the cell.

The MTT (3-(4,5-dimethylazol-2-yl)-2,5 diphenyl Tetrazolium Bromide) assay was used as a measure of the metabolic competence of the cells incubated with yolk/shell capsules, and the results are shown in **Figure 8.7d**. The nanocapsules were incubated with ARPE-19 cells for 24 hours and then subjected to a magnetic field for 1 min. The difference in the cytotoxicity seen before and after 1 min of magnetic field treatment is approximately 3% to 5%, and the cytotoxicity that was observed was likely caused by the magnetic heating. However, the magnetic field treatment is tolerable and the cell viability was still greater than 90%. These results demonstrate the relatively low cytotoxicity of these capsules under magnetic field treatment. However, decreasing the magnetic field exposure time required to trigger drug release could decrease the cytotoxic effect of magnetic heating. This is an important goal for future research because low cytotoxicity is a critical requirement for drug delivery vehicles.

The small effect of the capsules on cell viability led us to study the capsules in vivo as MR imaging agents as shown in **Figures 8.7e** and **8.7f**. Healthy rats were intravenously injected with yolk/shell capsules (12 mg/kg, 0.3 mL). Injection of the capsules enhanced the image contrast of MR images of rat brains and enabled the visualization of blood vessels, indicating that these yolk/shell capsules can serve as MRI contrast agents as well as drug delivery vehicles. These yolk/shell capsules provide an avenue for controlled drug delivery and offer a potential advantage for bioimaging and biomedical applications requiring drug release following physical rupture caused by external application of a magnetic field.

8.10 Summary

In summary, yolk/shell capsules have been prepared with a soft thermosensitive core and a thin but dense silica shell. The dense silica shell acts as a barrier that restricts undesired drug leakage before triggering. Incorporating a small amount of magnetic nanoparticles into the core leaves a vast space for encapsulation of drug molecules, and the thermosensitive polymer exhibits a hydrophilic-to-hydrophobic transition at a characteristic temperature (CMT) that triggers a size contraction as large as 10 fold. The thermal sensitivity of these yolk/shell capsules enables magnetic triggering of capsule rupture in response to the heat induced by the external magnetic field. In this system, the iron oxide nanoparticles act as the energy absorbers, achieving rapid triggered drug release that is not available from conventional yolk/shell particles and inorganic capsules. These capsules were efficiently taken up by healthy cell lines, and the cells maintain good viability under magnetic field treatment. In vivo MR imaging of rat brains showed that the yolk/shell capsules can clearly enhance image contrast after injection. Future development of this new class of functional yolk/shell capsules includes targeted imaging and therapy in vitro and in vivo, and we envision that this enabling technology will open exciting opportunities in nanomedicine and biotechnology.

Chapter 9

Conclusion

9.1 Ferrogels for magnetically-triggered drug release

1. Ferrogel fabricated by incorporating iron oxide NPs and gelatin/chitosan exhibited the fast response of drug release while applying a high frequency magnetic field (HFMF).
2. XPS and SEM demonstrated the strong interactions between carboxylic acid groups of gelatin and iron oxide NPs.
3. Burst release of drug from the ferrogels is optimized with the incorporation of 40 nm iron oxide nanoparticles under high-frequency magnetic field.
4. While applying cyclic short-time exposure of the ferrogels to HFMF, the stimulating response can be controlled and repeatedly reproduced as a result of a consecutive burst release profile of drug.

9.2 Core/single-crystal iron oxide shell nanospheres for drug delivery

1. Core-shell nanosphere with PVP-modified silica core following a functional deposition of a single-crystal iron oxide shell was fabricated.
2. The ultrathin iron oxide shell offers a surprisingly outstanding controlled release and non-release behavior for the molecules encapsulated inside the silica core.
3. The dense, single crystalline shell is efficiently preventing the fluorescence dye from un-desired release, giving that an undesirable leakage of the molecule during the course of delivery is completely inhibited.
4. The molecules encapsulated in the core can be released with a highly controllable manner, through the use of a magnetic stimulus.
5. The multifunctional drug delivery nanodevice was composed of core-iron oxide

shell carriers and quantum dots to image, target, and deliver drugs via remote control.

5. These nanodevices offer outstanding control of release and retention for the molecules encapsulated inside their polymer core.
6. Multifunctional nanodevices are able to monitor real-time drug dosage through corresponding variation in emission spectrum of the quantum dots within the HeLa cells.
7. With the in-situ monitoring capability of the nanodevice, we believe that both target-oriented therapy and diagnosis can be integrated and managed within a single cell.

9.3 Self-assemble iron oxide/silica (SAIO) core-shell carriers

1. The core-shell nanocarriers are able to well-disperse easily in an aqueous solution without using any interfacial molecules for stabilization.
2. The ultra-thin, 4-5 nm, outer silica shell coated on the SAIO core, a mixture of iron oxide nanoparticles and PVA, blocked the drug molecules effectively from therapeutically undesirable release from the core phase before subjecting to magnetic stimulation.
3. Under high-frequency magnetic field (HFMF) treatment, the SAIO@SiO₂ nanocarriers displayed a fast-acting and precise stimulus-time-dependent dosing response to the environment and restored to original state.
4. SAIO@SiO₂ nanocarriers were allowed a high efficiency uptake by HeLa cells within dozens of minutes and have been shown to exhibit excellent cytocompatibility, implying the nanocarriers are potentially capable of offering high-efficient cellular-based delivery following a fast-acting, accurate release of therapeutic agents for anti-cancer applications.

9.4 Thermosensitive yolk/shell capsules

1. The dense silica shell of capsules acts as a barrier that restricts undesired drug leakage before triggering.
2. Incorporating a small amount of magnetic nanoparticles into the core leaves a vast space for encapsulation of drug molecules, and the thermosensitive polymer exhibits a hydrophilic-to-hydrophobic transition at a characteristic temperature (CMT) that triggers a size contraction as large as 10 fold.
3. The thermal sensitivity of these yolk/shell capsules enables magnetic triggering of capsule rupture in response to the heat induced by the external magnetic field.
4. The iron oxide nanoparticles act as the energy absorbers, achieving rapid triggered drug release that is not available from conventional yolk/shell particles and inorganic capsules.
5. These capsules were efficiently taken up by healthy cell lines, and the cells maintain good viability under magnetic field treatment.
6. In vivo MR imaging of rat brains showed that the yolk/shell capsules can clearly enhance image contrast after injection.

Reference

- [1] A. C. R. Grayson, I. S. Choi, B. M. Tyler, P. P. Wang, H. Brem, M. J. Cima, R. Langer, *Nature Materials* **2003**, *2*, 767.
- [2] Z. Hu, X. Xia, *Adv. Mater.* **2004**, *16*, 305.
- [3] X. Z. Zhang, D. Q. Wu, C. C. Chu, *Biomaterials* **2004**, *25*, 3793.
- [4] M. Das, S. Mardiyani, W. C. W. Chan, E. Kumacheva, *Adv. Mater.* **2006**, *18*, 80.
- [5] M. R. Abidian, D. H. Kim, D. C. Martin, *Adv. Mater.* **2006**, *18*, 405.
- [6] B. G. De Geest, A. G. Skirtach, A. A. Mamedov, A. A. Antipov, N. A. Kotov, S. C. De Smedt, G. B. Sukhorukov, *Small* **2007**, *3*, 804.
- [7] H. J. Kim, H. Matsuda, H. Zhou, I. Honma, *Adv. Mater.* **2006**, *18*, 3083.
- [8] E. R. Edelman, J. Kost, H. Bobeck, R. Langer, *J. Biomed. Mater. Res.* **1985**, *19*, 67.
- [9] J. Kost, J. Wolfrum, R. Langer, *J. Biomed. Mater. Res.* **1987**, *21*, 1367.
- [10] J. Kost, R. Noecker, E. Kunica, R. Langer, *J. Biomed. Mater. Res.* **1985**, *19*, 935.
- [11] Z. vLu, M. D. Prouty, Z. Guo, V. O. Golub, C. S. S. R. Kumar, Y. M. Lvov, *Langmuir* **2005**, *21*, 2042.
- [12] D. Shi, H. S. Cho, Y. Chen, H. Xu, H. Gu, J. Lian, W. Wang, G. Liu, C. Huth, L. Wang, R. C. Ewing, S. Budko, G. M. Pauletta, Z. Dong, *Adv. Mater.* **2009**, *21*, 2170–2173.
- [13] J. Lee, J. Yang, H. Ko, S. J. Oh, J. Kang, J. H. Son, K. Lee, S. W. Lee, H. G. Yoon, J. S. Suh, Y. M. Huh, S. Haam, *Adv. Funct. Mater.* **2008**, *18*, 258–264.
- [14] J. Yang, J. Lee, J. Kang, S. J. Oh, H. J. Ko, J. H. Son, K. Lee, J. S. Suh, Y. M. Huh, S. Haam, *Adv. Mater.* **2009**, *21*, 4339–4342.
- [15] M. S. Yavuz, Y. Cheng, J. Chen, C. M. Cobley, Q. Zhang, M. Rycenga, J. Xie, C. Kim, K. H. Song, A. G. Schwartz, L. V. Wang, Y. Xia, *Nature Materials*, **2009**, *8*, 935–939.
- [16] Z. Liu, A. C. Fan, K. Rakhra, S. Sherlock, A. Goodwin, X. Chen, Q. Yang, D. W. Felsher, H. Dai, *Angew. Chem. Int. Ed.* **2009**, *48*, 7668–7672.
- [17] W. S. Kuo, C. N. Chang, Y. T. Chang, M. H. Yang, Y. H. Chien, S. J. Chen, C. S. Yeh, *Angew. Chem. Int. Ed.* **2010**, *49*, 2711–2715.
- [18] D. V. Volodkin, A. G. Skirtach, H. Möhwald, *Angew. Chem. Int. Ed.* **2009**, *48*, 1807–1809.
- [19] S. H. Hu, S. Y. Chen, D. M. Liu, C. S. Hsiao, *Adv. Mater.* **2008**, *20*, 2690–2695.
- [20] S. H. Hu, T. Y. Liu, D. M. Liu, S. Y. Chen, *Macromolecules* **2007**, *40*, 6786–6788.
- [21] H. Rosen, T. Aribat, *Nature Reviews Drug Discovery* **2005**, *4*, 381.
- [22] K. E. Uhrich, S.M. Cannizzaro, R. S. Langer, K.M. Shakesheff, *Chemical Reviews*, **1999**, *99*, 3181.

- [23] L.Y. Chu, Y. Li, J.H. Zhu, H.D. Wang, Y.J. Liang, *Journal of Controlled Release* **2004**, *97*, 43.
- [24] L. Chen, M.e Liu, H. Bai, P. Chen, F. Xia, D. Han, L. Jiang, *J. Am. Chem. Soc.* **2009**, *131*, 10467.
- [25] S. Q. Liu, Y. Y. Yang, X. M. Liu, Y. W. Tong, *Biomacromolecules* **2003**, *4*, 1784.
- [26] L. Bromberg, M. Temchenko, G. D. Moeser, T. A. Hatton, *Langmuir*, **2004**, *20*, 5683.
- [27] C. Alvarez-Lorenzo, S. Deshmukh, L. Bromberg, T. A. Hatton, I. Sández-Macho, A. Concheiro, *Langmuir*, **2007**, *23*, 11475.
- [28] K. Mortensen, *J. Phys.: Condens. Matter* **1996**, *8*, A13.
- [29] P. Alexandridis, et al., *Macromolecules* **1994**, *27*, 2414.
- [30] P. Alexandridis, et al., *Langmuir* **1995**, *11*, 1468.
- [31] S. H. Choi, J. H. Lee, S. M. Choi, T. G. Park, *Langmuir* **2006**, *22*, 1758.
- [32] A. I. Van D. Bulcke, B. Bogdanov, N. De Rooze, E. H. Schacht, M. Cornelissen, H. Berghmans, *Biomacromolecules* **2000**, *1*, 31.
- [33] T. Mitsumata, K. Ikeda, J.P. Gong, Y. Osada, D. Szabó, M. Zrínyi, *J. Applied Phys.*, **1999**, *85*, 8451.
- [34] P.M. Xulu, G. Filipcsei, M. Zrínyi, *Macromolecules* **2000**, *33*, 1716.
- [35] M. Zrínyi, D. Szabó, H.G. Kilian, *Polymer Gels and Networks*, **1998**, *6*, 441.
- [36] O. Saslawski, C. Weingarten, J.P. Benoit, P. Couvreur, *Life Science*, **1998**, *42*, 1521.
- [37] A.vK. Gupta, M. Gupta, *Biomaterials* **2005**, *26*, 3995.
- [38] T. Neuberger, B. Schöpf, H. Hofmann, M. Hofmann, B.V. Rechenberg, *J. Magn. Mat.* **2005**, *293*, 483.
- [39] J. Fricker, F. Writer, *Drug Delivery Today*, **2001**, *6*, 387.
- [40] T. Y. Liu, S. H. Hu, K. H. Liu, D. M. Liu, S. Y. Chen, *J. Magn. Magn. Mater.* **2006**, *304*, e397.
- [41] X. Z. Zhang, Y. Y. Yang, T. S. Chung, K. X. Ma, *Langmuir* **2001**, *17*, 6094.
- [42] T. D. Dziubla, M. C. Torjman, J. I. Joseph, M. Murphy-Tatum, A. M. Lowman, *Biomaterials* **2001**, *22*, 2893.
- [43] H. Storríe, D. J. Mooney, *Advanced Drug Delivery Reviews* **2006**, *58*, 500.
- [44] O. C. Farokhzad, R. Langer, *ACS nano* **2009**, *3*, 16.
- [45] M. Bruchez, Jr., M. Moronne, P. Gin, S. Weiss, A. P. Alivisatos, *Science* **1998**, *281*, 2013.
- [46] W. C. Chan, S. Nie, *Science* **1998**, *281*, 2016.
- [47] K. Balasubramanian, M. Burghard, *Small* **2005**, *1*, 180.
- [48] L. Lacerda, A. Bianco, M. Prato, K. Kostarelos, *Adv. Drug Delivery Rev.* **2006**, *58*, 1460.

- [49] L. R. Hirsch, A. M. Gobin, A. R. Lowery, F. Tam, R. A. Drezek, N. J. Halas, J. L. West, *Ann. Biomed. Eng.* **2006**, *34*, 15.
- [50] D. L. Thorek, A. K. Chen, J. Czupryna, A. Tsourkas, *Ann. Biomed. Eng.* **2006**, *34*, 23.
- [51] M. Ferrari, *Nat. Rev. Cancer* **2005**, *5*, 161.
- [52] P. Grodzinski, M. Silver, L. K. Molnar, *Expert Rev. Mol. Diagn.* **2006**, *6*, 307.
- [53] S. K. Sahoo, S. Parveen, J. J. Panda, *Nanomedicine* **2007**, *3*, 20.
- [54] K. B. Keys, F. M. Andreopoulos, N. A. Peppas, *Macromolecules* **1998**, *31*, 8149.
- [55] V. P. Torchilin, *Adv. Drug Delivery Rev.* **2006**, *58*, 1532.
- [56] J. Chen, H. Park, K. Park, *Proc. Int. Symp. Control. Rel. Bioact. Mater.* **1998**, *25*, 60.
- [57] W. Cai, X. Chen, *Small* **2007**, *3*, 1840.
- [58] S. Liu, R. Maheshwari, K. L. Kiick, *Macromolecules* **2009**, *42*, 3.
- [59] M. Arruebo, R. Fernández-Pacheco, M. R. Ibarra, J. Santamaría, *NanoToday* **2007**, *2*, 22.
- [60] S. J. Lee, J. R. Jeong, S. C. Shin, J. C. Kim, Y. H. Chang YH, et al. *J. Magn. Magn. Mater.* **2004**, *272*, 2432.
- [61] D. L. J. Thorek, A. Chen, J. Czupryna, A. Tsourkas, *Ann Biomed Eng* **2006**, *34*, 23.
- [62] C. H. Griffiths, M. P. Ohoro, T. W. Smith, *J. Appl. Phys.* **1979**, *50*, 7108.
- [63] C. B. Murray, D. J. Norris, M. G. Bawendi, *J. Am. Chem. Soc.* **1993**, *115*, 8706.
- [64] Z. A. Peng, X. G. Peng, *J. Am. Chem. Soc.* **2001**, *123*, 183.
- [65] L. H. Qu, Z. A. Peng, X. G. Peng, *Nano Lett* **2001**, *1*, 333.
- [66] M. A. Hines, P. Guyot-Sionnest, *J. Phys. Chem.* **1996**, *100*, 468.
- [67] X. G. Peng, M. C. Schlamp, A. V. Kadavanich, A. P. Alivisatos, *J. Am. Chem. Soc.* **1997**, *119*, 7019.
- [68] T. Hyeon, S. S. Lee, J. Park, Y. Chung, N. Bin, H. Na, *J. Am. Chem. Soc.* **2001**, *123*, 12798.
- [69] J. Park, K. J. An, Y. S. Hwang, J. G. Park, H. J. Noh, et al. *Nat. Mater.* **2004**, *3*, 891.
- [70] M. Green. *Chem. Commun.* **2005**, *24*, 3002.
- [71] U. Jeong, X. W. Teng, Y. Wang, H. Yang, Y. N. Xia, *Adv. Mater.* **2007**, *19*, 33.
- [72] T. Hyeon, *Chem. Commun.* **2003**, *8*, 927.
- [73] M. F. Casula, Y. M. Jun, D. J. Zaziski, E. M. Chan, A. Corrias A, et al. *J. Am. Chem. Soc.* **2006**, *128*, 1675.
- [74] S. G. Kwon, Y. Piao, J. Park, S. Angappane, Y. Jo, et al. *J. Am. Chem. Soc.* **2007**, *129*, 12571.
- [75] S. R. Dave, X. Gao, *Wiley Interdisciplinary Reviews: Nanomedicine*, **2009**, *1*,

583.

- [76] L. L. Muldoon, M. Sandor, K. E. Pinkston, E. A. Neuwelt, *Neurosurgery* **2005**, *57*, 785.
- [77] D. E. Sosnovik, M. Nahrendorf, R. Weissleder, *Circulation* **2007**, *115*, 2076.
- [78] H. S. Choi, W. Liu, P. Misra, E. Tanaka, J. P. Zimmer, et al. *Nat Biotechnol.* **2007**, *25*, 1165.
- [79] R. Weissleder, A.S . Lee, A.J . Fischman, P.Reimer , T.Shen, R. Wilkinson, R.J . Callahan, T. J. Brady, *Radiology* **1991**, *181*, 245.
- [80] J.W.M. Bulte, D.L. Kraitchman, *NMR Biomed.* **2004**, *17*, 484.
- [81] Y. X. J. Wang, S. M. Hussain, G. P. Krestin, *Eur. Radiol.* **2001**, *11*, 2319.
- [82] M. F. Bellin, *Eur. J. Radiol.* **2006**, *60*, 314.
- [83] R.W eissleder, A. Moore , U. Mahmood, R. Bhorade , H. Benveniste, E. A. Chiocca, J. P. Babilion, *Nat. Med.* **2000**, *6*, 351.
- [84] M. Zhao , D. A. Beauregard, L. Loizou, B. Davletov , K. M. Brindle, *Nat. Med.* **2001**, *7*, 1241.
- [85] J. Rockenberger, E. C. Sher, A. P. Alivisatos , *J. Am. Chem. Soc.* **1999**, *121*, 11595.
- [86] S. H. Sun, H. Zeng, D. B . Robinson, S. Raoux, P. M. Rice, S. X. Wang, G. X. Li, *J. Am. Chem. Soc.* **2004**, *126*, 273.
- [87] T. Hyeon, *Chem. Commun.* **2003**, 927.
- [88] J. Park, K. An, Y. Hwang, J. G. Park, H. J. Noh, J. Y. Kim, J. H. Park, N.M. Hwang, T. Hyeon, *Nat. Mater.* **2004**, *3*, 891.
- [89] N. R. Jana, Y. Chen, X. Peng, *Chem. Mater.* **2004**, *16*, 3931.
- [90] Y. Jun, J. Choi, J. Cheon, *Chem. Commun.* **2007**, 1203.
- [91] J. Cheon, N. J. Kang, S. M. Lee, J. H. Yoon, S. J. Oh, *J. Am. Chem. Soc.* **2004**, *126*, 1950.
- [92] A. H. Lu, E. L. Salabas, F. Schpth, *Angew. Chem. Int. Ed.* **2007**, *46*, 1222.
- [93] Y. Jun, Y. M. Huh, J. S. Choi, J. H. Lee, H. T. Song, S. J. Kim, S. Yoon, K. S. Kim, J. S. Shin, J. S. Suh, J. Cheon, *J. Am. Chem. Soc.* **2005**, *127*, 5732.
- [94] J. H. Lee, Y. M. Huh, Y. W. Jun, J. W. Seo, J. T. Jang, H. T. Song, S. Kim, E. J. Cho, H. G. Yoon, J. S. Suh, J. Cheon, *Nat. Med.* **2007**, *13*, 95.
- [95] W. S. Seo , J. H. Lee , X. Sun, Y. Suzuki, D. Mann, Z. Liu, M. Terashima, P. C. Yang, M. V. McConnell , D. G. Nishimura , H. Dai, *Nat. Mater.* **2006**, *5*, 971.
- [96] N. Nasongkla, E. Bey, J. Ren, H. Ai, C. Khemtong, J. S. Guthi, S. F. Chin, A. D. Sherry , D. A. Boothman , J. Gao, *Nano Lett.* **2006**, *6*, 2427.
- [97] Y. M. Huh, Y. Jun, H. T. Song , S. J. Kim, J. S. Choi, J. H. Lee, S. Yoon, K. S. Kim, J. S. Shin, J. S. Suh, J. Cheon, *J. Am. Chem. Soc.* **2005**, *127*, 12387.
- [98] H. T. Song, J. S. Choi, Y. M. Huh, S. Kim, Y. W. Jun, J. S. Suh, J. Cheon, *J. Am.*

- Chem. Soc.* **2005**, *127*, 9992.
- [99] M. P. Morales , S. Veintemillas-Verdaguer, M. I. Montero, C. J. Serna, *Chem. Mater.* **1999**, *11*, 3058.
- [100] E. V. Shevchenko, D. V. Talapin, A. L. Rogach, A. Kornowski, M. Haase, H. Weller, *J. Am. Chem. Soc.* **2002**, *124*, 11480.
- [101] C. W. Jung, P. Jacobs, *Magn. Reson. Imaging* **1995**, *13*, 661.
- [102] D. Hogemann, L. Josephson, R. Weissleder, J. P. Bacion, *Bioconjug. Chem.* **2000**, *11*, 941.
- [103] R. Weissleder, A. Moore, U. Mahmood, R. Bhorade, H. Benveniste H, et al. *Nat. Med.* **2000**, *6*, 351.
- [104] J. Sudimack, R. J. Lee, *Adv. Drug. Deliv. Rev.* **2000**, *41*, 147.
- [105] H. Choi, S. R. Choi, R. Zhou, H. F. Kung, I. W. Chen, *Acad. Radiol.* **2004**, *11*, 996.
- [106] J. H. Lee, Y. M. Huh, Y. Jun, J. Seo, J. Jang J, et al. *Nat. Med.* **2007**, *13*, 95.
- [107] Y. M. Huh, Y. W. Jun, H. T. Song, S. Kim, J. S. Choi, et al. *J. Am. Chem. Soc.* **2005**, *127*, 12387.
- [108] Y. W. Jun, Y. M. Huh, J. S. Choi, J. H. Lee, H. T. Song, et al. *J. Am. Chem. Soc.* **2005**, *127*, 5732.
- [109] A. K. Gupta, R. R. Naregalkar, V. D. Vaidya, M. Gupta. *Nanomedicine* **2007**, *2*, 23.
- [110] X. H. Gao, Y. Y. Cui, R. M. Levenson, L. W. K. Chung, S. M. Nie, *Nat. Biotechnol.* **2004**, *22*, 969.
- [111] T. Pellegrino, L. Manna, S. Kudera, T. Liedl, D. Koktysh, et al. *Nano Lett* **2004**, *4*, 703.
- [112] A. P. Philipse, M. P. B. Vanbruggen, C. Pathmamanoharan, *Langmuir* **1994**, *10*, 92.
- [113] Y. Lu, Y. D. Yin, B. T. Mayers, Y. N. Xia, *Nano Lett.* **2002**, *2*, 183.
- [114] M. Arruebo, et al., *Chem. Mater.* **2006**, *18*, 1911.
- [115] R. Duncan, *Materials Today* **2005**, *8*, 16.
- [116] U. Gaur, et al., *Int. J. Pharmacol.* **2000**, *202*, 1.
- [117] T. Neuberger, et al., *J. Magn. Magn. Mater.* **2005**, *293*, 483.
- [118] X. Wu, H. Liu, J. Liu, K. N. Haley, J. A. Treadway, J. P. Larson, N. Ge, F. Peale, M. P. Bruchez, *Nat. Biotechnol.* **2003**, *21*, 41.
- [119] X. Gao , Y. Cui, R. M. Levenson, L.W. K. Chung, S. Nie, *Nat. Biotechnol.* **2004**, *22*, 969.
- [120] D. B. Robinson, H. H. J. Persson , H. Zeng , G. Li, N. Pourmand, S. Sun, S. X. Wang, *Langmuir* **2005**, *21*, 3096.
- [121] N. Nitin, L. E. Laconte, O. Zurkiya, X. Hu, G. Bao, *J. Biol. Inorg. Chem.* **2004**,

- 9, 706.
- [122] W. W. Yu, E. Chang, C. M. Sayes, R. Drezek, V. L. Colvin, *Nanotechnology* **2006**, *17*, 4483.
- [123] B. S. Kim, J. M. Qiu, J. P. Wang, T. A. Taton, *Nano Lett.* **2005**, *5*, 1987.
- [124] J. Yang, C. H. Lee, J. Park, S. Seo, E. K. Lim, et al. *J. Mater. Chem.* **2007**, *17*, 2695.
- [125] T. R. Sathe, A. Agrawal, S M. Nie, *Anal. Chem.* **2006**, *78*, 5627.
- [126] N. Insin, J. B. Tracy, H. Lee, J. P. Zimmer, R. M. Westervelt, et al. *ACS Nano* **2008**, *2*, 197.
- [127] A. S. Lubbe, C. Alexiou, C. Bergemann, *J. Surg. Res.* **2001**, *95*, 200.
- [128] A. S. Lubbe, C. Bergemann, H. Riess, F. Schriever, P. Reichardt, et al. *Cancer Res.* **1996**, *56*, 4686.
- [129] A. S. Lubbe, C. Bergemann, J. Brock J, D. G. McClure, *J. Magn. Magn. Mater.* **1999**, *194*, 149.
- [130] J. Kim, J. E. Lee, S. H. Lee, J. H. Yu, J. H. Lee, et al. *Adv. Mater.* **2008**, *20*, 478.
- [131] M. Liong, J. Lu, M. Kovoichich, T. Xia, S. G. Ruehm, A. E. Nel, F. Tamanoi, J. I. Zink, *ACS Nano* **2008**, *2*, 889.
- [132] J. Gao , G. Liang, B. Zhang , Y. Kuang, X. Zhang , B. Xu, *J. Am. Chem. Soc.* **2007**, *129*, 1428.
- [133] J. Kim, J. E. Lee , J. Lee , Y. Jang, S. W. Kim, K. An, J. H. Yu, T. Hyeon, *Angew. Chem. Int. Ed.* **2006**, *45*, 4789.
- [134] T. Hoare, J. Santamaria, G. F. Goya, S. Irusta, D. Lin, S. Lau, R. Padera, R. Langer, D. S. Kohane, *Nano Lett.* **2009**, *9*, 3651.
- [135] D. H. Kim, E. A. Rozhkova, I. V. Ulasov, S. D. Bader, T. Rajh, M. S. Lesniak, V. Novosad, *Nat. Mat.* **2010**, *9*, 165.
- [136] S. Sun, H. Zeng, D. B. Robinson, S. Raoux, P. M. Rice, S. X. Wang, G. Li, *J. Am. Chem. Soc.* **2004**, *126*, 273.
- [137] J. P. Fortin, C. Wilhelm, J. Servais, C. Ménager, J. C. Bacri, F. Gazeau, *J. Am. Chem. Soc.* **2007**, *129*, 2628.
- [138] P. L. Ritger, N. A. Peppas, *J. Control. Release* **1987**, *5*, 37.
- [139] J. Kost, J. Wolfrum, R. Langer, R. *J. Biomed. Mater. Res.* **1987**, *21*, 1367.
- [140] E. R. Edelman, J. Kost, H. Bobeck, R. Langer, *J. Biomed. Mater. Res.* **1985**, *19*, 67.
- [141] O. Saslawski, C. Weingarten, J. P. Benoit, P. Couvreur, *Life Sci.* **1988**, *42*, 1521-1528.
- [142] Z. Lu, M. D. Prouty, Z. Guo, V. O. Golub, C. S. S. R. Kumar, Y. M. Lvov, *Langmuir* **2005**, *21*, 2042.
- [143] T. Y. Liu, S. H. Hu, T. Y. Liu, D. M. Liu, S. Y. Chen, *Langmuir* **2006**, *22*, 5974.

- [144] Ting-Yu Liu, Shang-Hsiu Hu, Kun-Ho Liu, Dean-Mo Liu, San-Yuan Chen, *J. Controlled Release*, **2008**, *126*, 228.
- [145] V. Crescenzi, A. Francescangeli, A. Taglienti, *Biomacromolecules* **2002**, *3*, 1384.
- [146] A. I. V. D. Bulcke, B. Bogdanov, N. D. Rooze, E. H. Schacht, M. Cornelissen, H. Berghmans, *Biomacromolecules* **2000**, *1*, 31-38.
- [147] H. Nakamura, W. Kato, M. Uehara, K. Nose, T. Omata, S. Otsuka-Yao-Matsuo, M. Miyazaki, H. Maeda, *Chem. Mater.* **2006**, *18*, 3330.
- [148] W. Jiang, S. Mardiyani, H. Fischer, W. C. W. Chan, *Chem. Mater.* **2006**, *18*, 872.
- [149] P. S. Low, W. A. Henne, D. D. Doorneweerd, *Acc. Chem. Res.* **2008**, *41*, 120.
- [150] A. Corma, U. Díaz, M. Arrica, E. Fernández, Í. Ortega, *Angew. Chem. Int. Ed.* **2009**, *48*, 6247.
- [151] Y. Lu, Y. Zhao, L. Yu, L. Dong, C. Shi, M. J. Hu, Y. J. Xu, L. P. Wen, S. H. Yu, *Adv. Mater.* **2010**, *22*, 1407.
- [152] Y. Yin, R. M. Rioux, C. K. Erdonmez, S. Hughes, G. A. Somorjai, A. P. Alivisatos, *Science* **2004**, *304*, 711.
- [153] Y. Sun, Y. Xia, *Science* **2002**, 2176.
- [154] X. J. Xu, D. Xu, *J. Am. Chem. Soc.* **2009**, *131*, 2774.
- [155] X. J. Xu, D. Xu, *Adv. Mater.* **2010**, *22*, 1516.
- [156] J. Yang, J. Lee, J. Kang, S. J. Oh, H. J. Ko, J. H. Son, K. Lee, J. S. Suh, Y. M. Huh, S. Haam, *Adv. Mater.* **2009**, *21*, 4339.
- [157] M. S. Yavuz, Y. Cheng, J. Chen, C. M. Cobley, Q. Zhang, M. Rycenga, J. Xie, C. Kim, K. H. Song, A. G. Schwartz, L. V. Wang, Y. Xia, *Nature Materials*, **2009**, *8*, 935.
- [158] S. H. Choi, J. H. Lee, S. M. Choi, T. G. Park, *Langmuir* **2006**, *22*, 1758–1762.
- [159] T. Y. Liu, K. H. Liu, D. M. Liu, S. Y. Chen, I. W. Chen, *Adv. Funct. Mater.* **2009**, *19*, 616.
- [160] Y. Tian, P. Ravi, L. Bromberg, T. A. Hatton, K. C. Tam, *Langmuir* **2007**, *23*, 2638.

Shang-Hsiu Hu, Ph. D. Candidate

Add: 1001 Ta Hsueh Road, Hsinchu, Taiwan 30049, ROC

Phone: +886-3-5712121#55394

E-mail: sshow210.mse93g@nctu.edu.tw

● **Education**

- Visiting Scholar, Department of Bioengineering, University of Washington, USA, 2009.5~2010.5.
- Ph.D., Material Science and Engineering, National Chiao Tung University, Taiwan, ROC, 2006~2010.
- M.S., Material Science and Engineering, National Chiao Tung University, Taiwan, ROC, 2004~2006.
- B.S., Chemical Engineering, National Chung-Hsin University, Taiwan, ROC, 2000~2004.

● **Research Interests**

1. Novel process development and controlled drug release in nano-biomaterial composites such as iron oxide nanoparticles, quantum dots and mesoporous silica.
2. Multifunctional nanomaterials for bioengineering and bioimaging.
3. Controlled rupture of novel core-shell spheres for drug delivery system which is able to be remotely controlled its rupturing behavior upon an external stimulation.

● **Selected Publications**

1. **Shang-Hsiu Hu**, and Xiaohu Gao, "Nanocomposites with Spatially Separated Functionalities for Combined Imaging and Magnetolytic Therapy", **J. Am. Chem. Soc.**, 2010, 7234-7237.
2. **Shang-Hsiu Hu**, San-Yuan Chen, Chi-Sheng Hsiao and Dean-Mo Liu, "Core/Single-Crystal-Shell Nanospheres for Controlled Drug Release via a Magnetically Triggered Rupturing Mechanism", **Adv. Mat.**, 2008, 20, 2690-2695.
3. **Shang-Hsiu Hu**, Wei-Lin Tung, Chen-Fu Liao, Dean-Mo Liu and San-Yuan Chen, Surfactant-free, "Self-Assemble PVA-Iron Oxide /Silica Core-Shell Nanocarriers for High-Sensitive Magnetically Controlled Drug Release and Ultra-high Cancer Cell Uptake Efficiency", **Adv. Func. Mat.**, 2008, 18, 2946-2955.
4. **Shang-Hsiu Hu**, Kuan-Ting Kuo, Dean-Mo Liu, and San-Yuan Chen. "Synthesis of Drug Delivery Nano-device capable of Imagining, Targeting, and Self-Monitoring of Drug Release in Cancerous Cells", **Adv. Func. Mat.**, 2009, 19, 3396.

5. **Shang-Hsiu Hu**, Ting-Yu Liu, Dean-Mo Liu and San-Yuan Chen, "Controlled Pulsatile Drug Release from a Ferrogel by a High-Frequency Magnetic Field", **Macromolecules**, 2007, 40, 6786-6788.

● **Honors**

1. Silver medal of "National Innovation Award" for Biotechnology and Medicine Industry, 2008, Taiwan. (2008 國家新創獎 第二名)
2. Gold medal of "Creative Design and Implementation Competition on Biomedical Engineering", 2008, Taiwan. (2008 醫學工程創意競賽 優勝)
3. Gold medal of "Taiwan Nano-Image Competition", 2008, Taiwan. (2008 台灣奈米影像攝影競賽 第一名)
4. Gold and copper medal of "Taiwan Nano-Image Competition", 2009, Taiwan. (2009 台灣奈米影像攝影競賽 第一名、第三名)
5. Silver medal of "National Innovation Award" for Biotechnology and Medicine Industry, 2007, Taiwan. (2007 國家新創獎 第二名)
6. 交大創意思源競賽 優勝

● **News Reports**

- a. News by **Material Views** (2009-04-28): Magnetic Triggering of Drug Release with Precise and Localised Dosage. <http://www.materialsviews.com/matview/display/en/352/TEXT>
- b. News by **Material Views** (2008-08-07): Magnetically Controlled Drug Release. <http://www.materialsviews.com/matview/display/en/739/TEXT>
- c. News by **NPG Asia Materials** (2008-09-24): Magnetic precision <http://www.natureasia.com/asia-materials/highlight.php?id=261>

● **Publications**

1. **Shang-Hsiu Hu**, and Xiaohu Gao, "Nanocomposites with Spatially Separated Functionalities for Combined Imaging and Magnetolytic Therapy", **J. Am. Chem. Soc.**, 2010, 7234-7237.
2. **Shang-Hsiu Hu**, and Xiaohu Gao, "Stable Encapsulation of QD Barcodes with Silica Shells", **Adv. Func. Mat.**, 2010, Accepted.
3. Kuan-Ting Kuo, **Shang-Hsiu Hu**, Dean-Mo Liu, and San-Yuan Chen. "Magnetically-induced Synthesis of Highly-Crystalline Ternary Semiconductor Chalcopyrite Nanocrystals via a Magnetic Doping at Ambient Conditions", **Journal of Chemistry Materials**, 2010, 20, 1744-1750.
4. **Shang-Hsiu Hu**, Kuan-Ting Kuo, Wei-Lin Tung, Dean-Mo Liu, and San-Yuan Chen. "Synthesis of Drug Delivery Nano-device capable of Imaging, Targeting, and Self-Monitoring of Drug Release in Cancerous Cells", **Adv. Func. Mat.**, 2009, 19, 3396.
5. Wei-Chen Huang, **Shang-Hsiu Hu**, Kun-Ho Liu, San-Yuan Chen and Dean-Mo Liu. "A Flexible Drug Delivery Chip for Magnetically-Controlled Release of Anti-Epileptic Drug", **Journal of Controlled Drug Release**, 2009, 139, 221-228.
6. Ting-Yu Liu, **Shang-Hsiu Hu**, Dean-Mo Liu, San-Yuan Chen, and I-Wei Chen, Biomedical

- Nanoparticle Carriers with Combined Thermal and Magnetic Responses, **NanoToday**, 2009, 4, 52-69 (invited review).
7. **Shang-Hsiu Hu**, Ting-Yu Liu, Hsin-Yang Huang, Dean-Mo Liu, and San-Yuan Chen, "Stimuli-Responsive Controlled Drug Release from Magnetic-Sensitive Silica Nanospheres", **J. Nanosci. Nanotechnol.**, 2009, 9, 866-870.
 8. **Shang-Hsiu Hu**, Chia-Hui Tsai, Chen-Fu Liao, Dean-Mo Liu and San-Yuan Chen, "Controlled Rupture of Magnetic Polyelectrolyte Microcapsules for Drug Delivery", **Langmuir**, 2008, 24, 11811–11818.
 9. **Shang-Hsiu Hu**, Wei-Lin Tung, Chen-Fu Liao, Dean-Mo Liu and San-Yuan Chen, Surfactant-free, "Self-Assemble PVA-Iron Oxide /Silica Core-Shell Nanocarriers for High-Sensitive Magnetically Controlled Drug Release and Ultra-high Cancer Cell Uptake Efficiency", **Adv. Func. Mat.**, 2008, 18, 2946-2955.
 10. **Shang-Hsiu Hu**, San-Yuan Chen, Chi-Sheng Hsiao and Dean-Mo Liu, "Core/Single-Crystal-Shell Nanospheres for Controlled Drug Release via a Magnetically Triggered Rupturing Mechanism", **Adv. Mat.**, 2008, 20, 2690-2695.
 11. Ting-Yu Liu, **Shang-Hsiu Hu**, Kun-Ho Liu, Dean-Mo Liu and San-Yuan Chen, Instantaneous Drug Delivery of Magnetic/Thermal Sensitive Nanospheres by a High Frequency Magnetic Field, **Langmuir**, 2008, 24, 13306-13311.
 12. Ting-Yu Liu, **Shang-Hsiu Hu**, Kun-Ho Liu, Dean-Mo Liu and San-Yuan Chen, "Study on controlled drug permeation of magnetic-sensitive ferrogels: Effect of Fe₃O₄ and PVA ", **Journal of Controlled Drug Release**, 2008, 126, 228-236.
 13. **Shang-Hsiu Hu**, Ting-Yu Liu, Hsin-Yang Huang, Dean-Mo Liu and San-Yuan Chen, "Magnetic-Sensitive Silica Nanospheres for Controlled Drug Release", **Langmuir**, 2008, 23, 239.
 14. Ting-Yu Liu, Li-Ying Huang, **Shang-Hsiu Hu**, Ming-Chien Yang and San-Yuan Chen, Core-shell magnetic nanoparticles of heparin conjugate as recycling anticoagulants, **J. Biomed. Nanotechnol.**, 2007, in press.
 15. **Shang-Hsiu Hu**, Ting-Yu Liu, Dean-Mo Liu and San-Yuan Chen, "Controlled Pulsatile Drug Release from a Ferrogel by a High-Frequency Magnetic Field", **Macromolecules**, 2007, 40(19), 6786-6788.
 16. **Shang-Hsiu Hu**, Ting-Yu Liu, Dean-Mo Liu and San-Yuan Chen, "Nano- Ferrosponges For Controlled Drug Release", **Journal of Controlled Drug Release**, 2007, 121 (3), 181-189.
 17. **Shang-Hsiu Hu**, Ting-Yu Liu, Chia-Hui Tsai, Dean-Mo Liu and San-Yuan Chen, "Preparation and Characterization of magnetic ferroscaffolds for tissue engineering", **Journal of Magnetism and Magnetic Materials**, 2007, 310(2), 2871-2873.
 18. Ting-Yu Liu, **Shang-Hsiu Hu**, Sheng-Hsiang Hu, Szu-Ping Tsai and San-Yuan Chen, "Preparation and characterization of thermal-sensitive ferrofluids for drug delivery application ", **Journal of Magnetism and Magnetic Materials**, 2007, 310 (2), 2850-2852.
 19. Ting-Yu Liu, **Shang-Hsiu Hu**, Tse-Ying Liu, Dean-Mo Liu and San-Yuan Chen," Magnetic-sensitive

- behavior of intelligent ferrogels for controlled release of drug," **Langmuir**, 2006; 22(14); 5974-5978.
20. Ting-Yu Liu, Hung-Chou Liao, Chin-Ching Lin, **Shang-Hsiu Hu**, and San-Yuan Chen, "Bio-functional ZnO nanorods arrays grown on flexible substrates," **Langmuir**; 2006; 22(13); 5804-5809.
21. Ting-Yu Liu, **Shang-Hsiu Hu**, Kun-Ho Liu, Dean-Mo Liu, San-Yuan Chen, "Preparation and characterization of smart magnetic hydrogels and its use for drug release," **Journal of Magnetism and Magnetic Materials**, 304, 2006, e397-e399.
22. Jiang-Jen Lin, Shi-Min Chen, **Shang-Hsiu Hu**, " Poly(oxyethylene) diamine- Derived Hydrophilic Copolymers for Emulsifying Diglycidylether of Bisphenol-A, " **Journal of Applied Polymer Science**, Vol. 94, 1797–1802 (2004).

● **Conference Papers**

1. **Shang-Hsiu Hu**, Ting-Yu Liu, Hsin-Yang Huang, Dean-Mo Liu, and San-Yuan Chen*, "Stimuli-Responsive Controlled Drug Release from Magnetic-Sensitive Silica Nanospheres," International Conference on Nanoscience & Technology, China 2007, June 4-6, Beijing, China.
2. **Shang-Hsiu Hu**, Chi-Sheng Hsiao, Dean-Mo Liu and San-Yuan Chen, A Novel Core-Shell PVP-silica/Fe₃O₄ nanosphere as Cancer Targeted and Drug Delivery System, 8th World Biomaterial Congress, 28 May-1 June, 2008, Amsterdam, Netherlands.
3. Chen-Fu Liao, **Shang-Hsiu Hu**, Chia-Hui Tsai, Dean-Mo Liu and San-Yuan Chen*, "Controlled Rupture of Magnetic Polyelectrolyte Microcapsules for Drug Delivery," 8th World Biomaterial Congress, 28 May-1 June, 2008, Amsterdam, Netherlands.
4. **Shang-Hsiu Hu**, Ting-Yu Liu, Chia-Hui Tsai and San-Yuan Chen*, "Preparation and characterization of magnetic ferroscaffolds for tissue engineering." The 17th International Conference on Magnetism (ICM) , Aug, 20-25, 2006, Kyoto, Japan.
5. Ting-Yu Liu, **Shang-Hsiu Hu**, Kun-Ho Liu, Sheng-Hsiang Hu, Dean-Mo Liu and San-Yuan Chen*, "Magnetic-sensitive characterization of the ferrogels and its use for drug release," 94 年度生醫材料暨藥物製放研討會，2005，新竹，清華大學。
6. **Shang-Hsiu Hu**, Ting-Yu Liu, Sheng-Hsiang Hu, Dean-Mo Liu and San-Yuan Chen*, "Preparation of characterization of smart magnetic bio-membrane and its use for drug release," International Symposium on Spintronics and Advanced Magnetic Technologies and International Symposium on Magnetic Materials and Applications (2005) .